



**University of
Nottingham**

UK | CHINA | MALAYSIA

Modelling the mechanical response of elastomers: the roles of the network, the filler and the deformation history

Vinotharan Annarasa
MEng

Thesis submitted to the University of Nottingham for the
degree of Doctor of Philosophy

March 2021

Abstract

The mechanical response of elastomers is influenced by a large range of factors including the elastomeric network, the deformation history (or Mullins effect) and the type and content of filler. The aim of this work is to develop modelling frameworks and models to capture the influences of these factors in selected elastomer systems. Several experimental studies were conducted to aid in the development and validation of the models.

The impact of the elastomer network on the mechanical response is explored using a set of soft custom-made cast ultraviolet light curable silicone-acrylate elastomers eventually intended for elastomer 3D printing. Five different compounds are explored, varying the silicone content from 30 to 70 wt%. Uniaxial tensile tests were performed on all of the compositions. The results from these tests suggest that varying the silicone content results in a systematic variation of the stress-strain response. To study the variation of the underlying network structure with the silicone content, an Edwards-Vilgis (EV) strain energy function was fitted to the stress-strain data. By examining the evolution of EV parameters with respect to the proportion of silicone in the system, it was shown that: 1) the network density increases with increasing silicone content, 2) the limiting extensibility decreases with increasing silicone content, i.e., smaller deformations are possible, and 3) the slip-link mobility increases, i.e., there is more freedom for the motion of topological constraints. Simple functions were fitted to quantify the evolution of EV parameters with composition. Based on the evolution of these parameters, a model was proposed to tune the mechanical properties of this class of materials. As these materials were developed for 3D printing, a printability assessment was carried out. It was also shown that further optimisation of the printing process is necessary to achieve mechanical response identical to that of the cast material.

A phenomenological constitutive model was developed and validated to

describe the impact of deformation history (or Mullins effect) on the mechanical response of an EPDM rubber compound. This model was inspired by recent experimental observations made on the uniaxial tensile cyclic stress-strain response. The third unloading-reloading loop after preconditioning was decomposed into elastic and viscous contributions. The viscous contribution was shown to form a master curve that was independent of the deformation history and only dependent on the effective network stretch. To the author’s knowledge, a constitutive model that incorporates a strain dependent viscosity has not been developed before. This model was shown to reasonably predict the stress in the third loop response, and provided an excellent prediction of the energy dissipated in this loop, making the model particularly useful for applications, such as vibration isolation where prediction of energy dissipation is vital. The initial loading case was underestimated by the model, and this is attributed to the time-dependent nature of the Mullins effect. The applicability of this model formulation to the deformation of CR and NBR rubber compounds was also explored. It was shown that the model was able to capture the response of NBR successfully but less so for CR. The failure was attributed to the inability of the strain energy function in capturing the upturn at small strains. Lastly, it was shown that the material requirement and the number of experiments required to parameterise the model can be reduced by utilising pseudo-cyclic tests.

An investigation on the impact of pre-deformation on the small strain dynamic response was also conducted. In this part of the study, the influence of filler type and filler content were explored in SBR compounds filled with three different filler types and amounts. A rheometer was used for both the quasi-static and the dynamic deformations. Uniaxial tensile tests were conducted for the pre-deformations, and oscillatory torsion was applied in the dynamic tests on the same specimens. Two test protocols were employed, and the Kraus model was used to study the small strain dynamic response (or Payne or Fletcher-Gent effect). The first protocol was concerned with the impact of pre-deformation on the small strain dynamic response. Prior to pre-deformation increasing the amount of filler and the surface area of the filler particles results in an increase in the storage modulus plateau at small strains G'_0 . As increasing pre-deformation is applied, G'_0 begins to decrease. Other parameters in the Kraus model, the strain γ_c at which half the van der Waals type interaction between aggregates are broken and the rate m at which it occurs, are approximately independent of pre-deformation, but are impacted by the filler type and content. The results indicate that it

may be possible to control the stiffness, and to some extent the onset of the Payne effect (or Fletcher-Gent effect), by a combination of filler selection and pre-conditioning. To the author's knowledge models describing the Payne effect have yet to incorporate the pre-deformation. To address this issue, an exponential function for G'_0 is proposed to link it to the pre-deformation. In the second test protocol, alongside pre-deformation, a static tensile strain was also imposed. In the shear strain range explored, for any given static strain, the storage modulus G' was independent of the shear strain. With increasing static strain, G'_0 was seen to increase. For a given filler type, G'_0 increased with increasing filler amount. However, unlike the first test protocol G'_0 , the behaviour between different filler types is more complex.

Several models are presented in this work to describe the roles of the network, of the filler and of the deformation history on the mechanical response of elastomers. Although the models were developed for the materials used in this work, much of the modelling framework is applicable to a range of different materials. These models and the modelling framework supplement existing models in the prediction of the mechanical response of elastomers and are of value to engineers in the design process of elastomeric components. Owing to their physical nature, these models could also be leveraged by scientists to better understand the behaviour of elastomer network.

Publications and presentations

Publications

- Annarasa, V., Popov, A. A. & De Focatiis, D. S. A., ‘*A phenomenological constitutive model for the viscoelastic deformation of elastomers*’, Mechanics of Time-Dependent Materials, 2020, DOI: <https://doi.org/10.1007/s11043-020-09452-2>.
- Foerster, A.*, Annarasa, V.*, Wildman, R., Hague, R., Irvine, D., Terry, A., Tuck, C. & De Focatiis, D. S. A., ‘*Development of UV-curable silicone with tuneable mechanical properties for 3D printing applications*’. Manuscript in preparation to be submitted in the peer-reviewed journal of Materials & Design.
- Annarasa, V., Popov, A. A. & De Focatiis, D. S. A., ‘*Influence of carbon black morphology and content on the Payne effect in shear in styrene butadiene rubber exposed to varying uniaxial tensile histories*’. Manuscript in preparation to be submitted in the peer-reviewed journal of Rubber Chemistry & Technology.

Conference proceedings

- Annarasa, V., Popov, A. A. & De Focatiis, D. S. A., ‘*A phenomenological constitutive model for the viscoelastic deformation of elastomers including the Mullins effect*’. 11th International Conference on Mechanics of Time-Dependent Materials, Milan, 2018.
- Annarasa, V., Popov, A. A. & De Focatiis, D. S. A., ‘*Influence of carbon black morphology and content on the Payne effect in shear in styrene butadiene rubber exposed to varying uniaxial tensile histories*’. International Rubber Conference, London, 2019.

Oral presentations

- Mechanics of Time-Dependent Materials, Milan, 2018. *‘A phenomenological constitutive model for the viscoelastic deformation of elastomers including the Mullins effect’*.
- Advanced Materials Research Group Seminar, The University of Nottingham, 2018. *‘A phenomenological constitutive model for the viscoelastic deformation of elastomers including the Mullins effect’*.
- International Rubber Conference, London, 2019. *‘Influence of carbon black morphology and content on the Payne effect in shear in styrene butadiene rubber exposed to varying uniaxial tensile histories’*.

Poster presentation

- Engineering Research Showcase, The University of Nottingham, 2018. *‘A phenomenological constitutive model for the viscoelastic deformation of elastomers including the Mullins effect’*.

One-slide presentations

- Engineering Research Showcase, The University of Nottingham, 2017. *‘Linear, or non-Linear, that is the question’*.
- International Rubber Conference, London, 2019. *‘Influence of carbon black morphology and content on the Payne effect in shear in styrene butadiene rubber exposed to varying uniaxial tensile histories’*.

என் அம்மாவுக்கும் அப்பாவுக்கும்

Acknowledgements

This work would not have been possible without the funding provided by the University of Nottingham. I would also like to extend my thanks to both the East Midlands Materials Society (EMMS) and the Institute of Materials, Minerals and Mining (IOM3) for supporting my attendance at various conferences.

I was fortunate enough to be blessed with two great supervisors, Dr. Davide De Focatiis and Prof. Atanas Popov, to guide me through this journey. I am grateful for their words of encouragement, inspiration, insightful intellectual discussions and for always keeping my best interest in mind. If (and it is a big if) I were to embark on another PhD project, I would choose you both again. I hope that I have been a reasonable PhD student and have produced work that both of you could be proud of.

I would also like to thank the p.lab research group: Gabriel Choong, Matthew Elsmore, Grace Owen and Michael Ward, and the Crypto Banter Boys: Matthew Carrington, Jaimie Daure, Ben Hanby, George Jackson, Alexander (Sandy) Lamond, George Jackson, Alexandre Sabard and Bryan Stuart. I am thankful for your support and banter; I owe my sanity (or insanity) partly to you guys.

The research process was full of stress-inducing (pun intended) challenges and days. At the end of each day, I knew I could always head to the dojang to kick a few paddles (or people) whilst screaming at the top of my voice without being judged. It was a great stress-reliever. This would not have been as fun if it were not for the people there. University of Nottingham Taekwondo club, I thank you for bringing everyone together. I would like to mention a few names here: Coleen Babilonia, Sokratis Charalampous, Lucy Colleer, Fredrik Salling Dausel, Gail Dechocha, Jasper Grant Estrañero, Arwa Hasan, Tarandeep Jhuti, Binh La, Paivyn Lee, Teo Loh (Grandmaster Loh), Wenqi Li, Thangaeswaran Nithirajah, Joseph Parsons, Alvin Setianto, Gary Skinner

(Mr S), Colin West and Kevin Zhan. Especial shoutout to Jasper Grant Estrañero: a big brother, a friend, a mentor and an OG Taekwonbro.

I have been fortunate enough to encounter many great souls throughout my life, all of whom have positively influenced my being, I would like to mention a few names here: Praekash Balendra, Aiden Bent, Luke Bradford, James Charlesworth, Sinneli Jayampathy, Nathalie Lekam, Thomas Lowbridge, Bhagya Samarakkody, Demi Sangowawa, Tharuka De Silva and Josh Vail. Especial shoutout to Praekash Balendra. You have been a brother, a friend and a mentor to me, I am truly blessed to have you in my life.

Lastly, I would like to thank my family for being my pillars and supporting me in everything I do. Sivagowri Annarasa, Annarasa Kanesapillai, Prasanna Annarasa and Anushiya Annarasa. Thank you. There is no one in this world that I love more than you. All my successes belong to you.

"வித்தை விரும்ப" - ஓளவையார்

"Long to learn" - Avvaiyar

Contents

Abstract	iii
Publications and presentations	v
Dedication	vi
Acknowledgements	viii
List of figures	xxvi
List of tables	xxix
Abbreviations	xxx
Symbols	xxxix
1 Introduction	1
2 Literature review	5
2.1 Elastomeric materials	5
2.1.1 Elasticity of a single chain	7
2.1.2 Phenomenology of the network	9
2.1.3 Reinforcement	12
2.1.4 Technical elastomers	14
2.2 Mullins effect	15
2.2.1 Softening effect	17
2.2.2 Permanent set	18
2.2.3 Anisotropy	18
2.2.4 Physical interpretations	20

2.3	Payne effect	24
2.3.1	Physical interpretation	25
2.4	Constitutive modelling	26
2.4.1	Network elasticity	26
2.4.2	Hyperelastic models	28
2.4.3	Viscoelasticity	30
2.4.4	Mullins effect models	31
2.4.5	Payne effect	37
2.5	Research opportunities	38
2.6	Aims and objective	39
3	The influence of network structure on the mechanical response	41
3.1	Introduction	41
3.2	Material preparation	42
3.2.1	Ink preparation	42
3.2.2	Casting setup	43
3.2.3	Jetting setup (3D printing)	44
3.3	Characterisation	45
3.3.1	Thermal characterisation	45
3.3.2	Metrology & mechanical characterisation	46
3.4	Results and discussion	50
3.4.1	Glass transition temperature	50
3.4.2	Uniaxial stress-strain response	51
3.4.3	Modelling	52
3.4.4	Evolution of EV parameters	54
3.4.5	Tuning mechanical properties	57
3.4.6	Influence of UV light intensity	60
3.4.7	Validation of 3D printing capabilities	62
3.5	Summary	64
4	The influence of deformation history on the mechanical response - part I	65
4.1	Introduction	66
4.2	Materials and methods	67
4.2.1	Materials and manufacturing	67
4.2.2	Mechanical testing	67
4.3	Experimental analysis	68

4.3.1	Extraction of elastic and viscous Contributions	68
4.3.2	Equilibrium contribution	70
4.4	Viscous contributions	72
4.5	Constitutive modelling	74
4.5.1	Model elements	75
4.5.2	Parameter evolution	75
4.5.3	Viscosity master curve	77
4.5.4	Determination of the linear spring modulus	78
4.6	Results	79
4.6.1	Simulation of the third loop response	79
4.6.2	Simulation of more complex deformation histories . . .	80
4.7	Discussion	82
4.7.1	Post-Mullins response	82
4.7.2	Pre-mullins response	84
4.8	Summary	88

5 The influence of deformation history on the mechanical response - part II **89**

5.1	Introduction	89
5.2	Materials and methods	90
5.2.1	Materials and specimen preparation	90
5.2.2	Mechanical testing	91
5.3	Analysis of experimental data	94
5.4	Constitutive modelling	97
5.4.1	EV parameter evolution	98
5.4.2	Viscosity master curve	100
5.4.3	Linear spring modulus	100
5.5	Results	101
5.5.1	Simulation of the third loop response	101
5.6	Discussion	102
5.6.1	Post Mullins response	102
5.6.2	Pre Mullins response	104
5.6.3	Transient portion	105
5.6.4	CR	108
5.6.5	Cyclic or pseudocyclic?	111
5.7	Summary	114

6	The influence of filler choice on the mechanical response	116
6.1	Introduction	117
6.2	Materials and methods	118
6.2.1	Materials	118
6.2.2	Compression moulding	118
6.2.3	Physical characterisation	120
6.2.4	Specimen preparation	122
6.2.5	Mechanical testing	123
6.3	Results and discussion	126
6.3.1	Frequency Sweep	126
6.3.2	Monotonic and cyclic uniaxial tensile tests	130
6.3.3	Reversible amplitude dependence	134
6.3.4	TP3	135
6.3.5	TP1	141
6.4	Summary	146
7	Conclusions	148
7.1	Conclusions	148
7.1.1	The influence of the network structure on the mechanical response	148
7.1.2	The influence of deformation history on the mechanical response	149
7.1.3	The influence of filler choice on the mechanical response	150
7.2	Recommendations for future work	151
7.2.1	UV curing and 3D printing	151
7.2.2	Extension to a fully three-dimensional model	152
7.2.3	The role of deformation history and choice of filler on the mechanical response of elastomers	152
	Bibliography	170
A	Appendices	171
A.1	Thickness measurement - Lebedev and Ufliand theory kernels	171
A.2	Thickness Measurement - Lebedev and Ufliand theory verification	174
A.3	Width measurement	175
A.4	Edwards-Vilgis - strain energy to stress	176
A.5	Viscosity master curve - normalisation of error	178

A.6	Linear spring modulus	179
A.7	Set rate dependent viscosity	180
A.8	EV parameter evolution	180
A.9	Heat transfer calculations - adiabatic heating	181
A.10	Heat transfer calculations - accounting for conduction and convection	182
A.11	Theoretical density of SBR compounds	185
A.12	Cyclic uniaxial tensile test	186
A.13	Reversible amplitude sweep	186
A.14	Filler volume fraction and effective surface area	187

List of Figures

2.1	(a) 1,4-polyisoprene monomer, and (b) rubber sap being collected from the Hevea Braziliensis tree. The image of the Hevea Braziliensis tree was obtained from Ji-Elle <i>via</i> Wikimedia Commons (CC).	6
2.2	A schematic of (a) thermoset, and (b) thermoplastic elastomer. The thermoset is constrained by chemical cross-links, whereas a thermoplastic elastomer consists of physical bonds i.e., “hard phase”.	7
2.3	A schematic of (a) rod-like zig-zag configuration highlighting important features of a single polymer chain, and (b) disordered configuration. The image for rod-like zig-zag configuration was adapted from [8].	8
2.4	A random configuration of a chain containing 10 bond. Adapted from [8].	9
2.5	Structural features of a network: (a) elastically active chain, (b) loop, (c) trapped entanglement, and (d) dangling chain. The black dots refer to both the chemical and physical cross-links. Adapted from [11]	10
2.6	The affine network model. The junction points are fixed, a macroscopic deformation results in an affine transformation of the components of the vectors representing the distance between the junction points.	11
2.7	The phantom network model. The junction points can fluctuate about a mean position; the fluctuation region is illustrated as dashed circles.	12

2.8	A schematic of the bound and occluded rubber concepts. The aggregates (made up of several filler particles) cluster to form agglomerates (made up of aggregates). The rubber interacts with the surface of the filler particles and are bound to the surface (illustrated in grey). The rubber trapped in the agglomerate is known as the occluded rubber. Adapted from [16].	13
2.9	Idealised Mullins effect curve	16
2.10	Stress-stretch response of a 50 phr carbon black filled SBR subjected to pseudo-cyclic and simple uniaxial tensile tests. The strains in the pseudo-cyclic test were incremented every 5 cycles. Adapted from [32].	17
2.11	A schematic of the test implemented by Mullins [34]. A sheet of rubber six inches square and one-tenth inch thick is clamped on both sides. A one-inch square is marked in the centre of the sheet. The specimen was stretched in direction A, held in position for 15 minutes. Following this the sample was allowed to rest for thirty minutes. The same protocol was implemented in direction B. The dimensions of the marked square were recorded after the rest period.	20
2.12	The response of carbon black filled rubber systems to dynamic oscillations. The complex modulus has been decomposed into its components, the a) storage and the b) loss modulus. Adapted from [62].	25
2.13	A Mooney plot of an elastomeric specimen subjected to a simple tension test. The results obtained from affine and phantom network models are compared with experimental data.[8] . . .	28
2.14	An illustration of the tube model concept. Entanglements form the tube and the centre of the tube is represented as dashed lines. The solid line represents a polymer chain that has been cross-linked at its ends. The hollow circles represent other polymer chains that are perpendicular to the surface of the page. Adapted from [80].	30
2.15	A representation of a) Kelvin, and b) Maxwell models.	31
2.16	The two idealisations of the Mullins phenomenon; a) the reloading response coincides with the unloading response and, b) the unloading and reloading responses differ. Adapted from [32] .	32

2.17	a) Experimental tensile data obtained by Mullins and Tobin [2], and b) the pseudo-elastic theory proposed by Ogden and Roxburgh [83] fitted to the experimental data using a non-linear least-squares solution. Adapted from [83].	33
2.18	The a) 3-chain network [86], b) 4-chain [87], c) 8-chain [79] and d) N -chain models [85]. A triangulated section of the sphere is provided for the N -chain model to illustrate the chains (in red). The 3, 4 and 8 chain diagram were adapted from [79], and the triangulated sphere diagram was adapted from [85].	35
3.1	Molecular structure of the UV curable ink components.	43
3.2	Description of the relevant parts of the driving pulse and its effect on the nozzle state.	44
3.3	A schematic of the problem of pressing a stamp of circular cross-section into an elastic layer.	47
3.4	The evolution of χ with p	48
3.5	a) The experimental setup used for the mechanical tests. One of the staple-like clips is left protruding out of the drums for illustration. b) A schematic of the counter-rotation of the drums with key dimensions, including the drum radius R , gauge length L and deflection angle θ . c) A representative example of the raw data obtained from the experiment. This particular data is for a 70/30 specimen.	50
3.6	The stress-strain response of the various silicone/acrylate systems explored. The error bars (± 2 standard errors) show variations encountered in the experimental data with different samples.	51
3.7	The glass transition temperatures T_g (± 2 standard errors) obtained for the various silicone/acrylate systems explored in the study.	52
3.8	A plot illustrating the impact of the various Edwards-Vilgis (EV) parameters. The legend entries are used in parallel with Table 3.2 to identify the magnitude of the individual EV parameters used to obtain a given curve.	56

3.9	The evolution of (a) slip-link density N_S , (b) slip-link mobility η , (c) cross-link density N_C and (d) chain inextensibility α with silicone weight fraction f_{PDMS} . The EV parameters are represented as crosses with ± 2 standard uncertainties. To describe the evolution of these parameters, simple functions (lines) are fitted to the experimental data. Large crosses are used to highlight the data points utilised in the fitting process.	59
3.10	The stress-strain response of the various silicone/acrylate systems explored. The error bars (± 2 standard errors) show variations encountered in the experimental data (symbols) with different samples. Edward-Vilgis EV model fits represented using solid lines.	60
3.11	The experimentally measured (symbols) (± 3 standard error) and model (line) predicted secant modulus as a function of composition for strain level of a) 50%, b) 100%, c) 150% and d) 200%.	61
3.12	A comparison of the stress-strain response of cast specimen of the 50/50 composition exposed to various intensities.	62
3.13	(a) The custom jetting setup used for 3D printing; and, (b) a printed 70/30 sample.	63
3.14	The stress-strain response of the 3D printed (solid line) and a cast (dashed line) 70/30 sample.	63
4.1	The stress-stretch response of selected EPDM specimens subjected to cyclic loading (displacement controlled, mixed mode) as shown in the inset to λ_{max} of 2, 3, 4, 5 and 6. The specimens are unloaded to a stretch corresponding to a load of 0.1 N ($\lambda_{0.1N}$) to prevent buckling. A virgin specimen was used for each test.	68
4.2	The experimental stress-stretch response (symbols) to cyclic tension to a λ_{max} of 3, showing only the pre-deformation and the third unload-reload loop. σ_e (dashed line) and σ_v (dot-dash line) are obtained from the mean and from half of the difference between the third loop unloading and reloading stress, respectively. The transient portion of the data (here indicated as a strain of 0.33 at each end of the deformation) and the data used in the procedure are highlighted.	70

4.3	The experimental σ_e (symbols) and model σ_{EV} (lines) equilibrium contributions as a function of stretch for five λ_{\max} levels between 2 and 6. The model is an EV function accounting for λ_{set}	71
4.4	(a) Viscous stress σ_v as a function of λ , and (b) the viscosity η_v as a function of λ_{eff} . When expressed as a function of λ_{eff} , the viscosity data overlay to form a master curve. A simple function is fitted to describe the viscosity master curve.	73
4.5	A modified viscoelastic standard linear solid (SLS) model in series with a slider intended to represent permanent set. The SLS part of the model consists of an Edwards-Vilgis hyperelastic spring in parallel with a linear spring and a non-linear dashpot.	74
4.6	The evolution of (a) slip-link density N_S , (b) slip-link mobility η , (c) chain inextensibility α , and (d) permanent set λ_{set} with pre-deformation λ_{\max} . The parameters extracted from the elastic contributions are shown as circles. The corresponding uncertainties (95% confidence interval) are also shown. To describe the evolution of these parameters, simple functions (lines) are fitted to the extracted parameter values as functions of for $\lambda_{\max} \geq 2.5$ (larger circles).	76
4.7	(a) The experimental third loop response (symbols) for a pre-deformation λ_{\max} of 2.5 and the model elastic contribution σ_{EV} (line). (b) Viscous contribution obtained by subtraction of the elastic stress obtained from the EV model (symbols) from the total experimental stress, as a function of the effective stretch. The Maxwell model response σ_M (line) is obtained by solving numerically the governing equation for the non-linear Maxwell element (eq. 4.8) and optimising for the spring stiffness E . The vertical dashed lines are used to identify the transition between transient and steady state portions of the data.	79
4.8	Comparison of experimental (symbols) and model (lines) third loop response for five pre-deformation λ_{\max} levels between 2 and 6. The inset shows the deformation history imposed on the specimens, the third unload-reload loop is shown in blue.	80

4.9	A comparison between the experimental and model responses for TP5. The protocol consists of three uniaxial load/unload cycles, followed by five reload/unload loops and a reload/unload cycle, as shown in the inset. The dashed line in the inset represents the data that has been omitted from the plot.	81
4.10	A comparison between the experimental and model responses for TP6. The protocol consists of two uniaxial load/unload cycles, a reload step, four unload/reload loops, and lastly an unload/reload cycles and an unload step, as shown in the inset. The dashed line in the inset represents the data that has been omitted from the plot.	82
4.11	A comparison of the experimental E_C^{exp} and model E_C^{mod} energy dissipated by the third loop.	83
4.12	Comparison between the dissipated energy obtained from experimental E_C^{exp} and model E_C^{mod} loops in complex loading histories TP5 (square) and TP6 (triangle).	84
4.13	The evolution of (a) flow stress $\sigma_{f,\text{set}}$ and (b) set rate $\dot{\lambda}_{\text{set}}$ with stretch.	85
4.14	The evolution of viscosity associated with set with increasing stretch λ . A constant η_{set} is utilised within the constitutive model for simplicity and is represented as a dashed line on the plot.	86
4.15	A comparison of the experimental and model initial (or virgin) loading behaviour. The model stress is obtained by the summation of σ_{EV} , σ_{M} and $\sigma_{f,\text{set}}$	87
4.16	An illustration of a compression moulded specimen being peeled off. The key parameters required to calculate the deformation are highlighted on the diagram.	87
5.1	(a) The deformation history used for the cyclic tests consisting of four load-unload cycles. The specimen are unloaded to a stretch corresponding to a load of 0.1 N ($\lambda_{0.1\text{N}}$) to prevent buckling. A virgin specimen was used for each test. The stress-stretch response of selected (b) CR, (c) EPDM2, and (d) NBR specimens subjected to cyclic loading.	92

5.2	The stress-stretch response of a EPDM2 specimen subjected to pseudocyclic loading, as shown in the inset, to ten linearly spaced λ_{\max} values between 1.5 and 6 inclusive. At each λ_{\max} increment the specimen is subjected to four load-unload cycles. To prevent buckling the specimens are unloaded to a stretch corresponding to a load of 0.1 N ($\lambda_{0.1N}$).	93
5.3	The stress-stretch response of a EPDM2 specimen subjected to pseudocyclic loading, as shown in the inset, to ten linearly spaced λ_{\max} values between 1.5 and 6 inclusive. At each λ_{\max} increment the specimen is subjected to four load-unload cycles. A ten minute pause is implemented prior to transitioning onto the next λ_{\max} increment. To prevent buckling the specimen is unloaded to a stretch corresponding to a load of 0.1 N ($\lambda_{0.1N}$).	94
5.4	The experimental σ_e (symbols) and model σ_{EV} (lines) equilibrium contributions as a function of stretch for EPDM2 subjected to (a) cyclic tests, (c) a pseudocyclic test, and (e) a pseudocyclic test with pauses. The model is an EV function accounting for λ_{set} . The viscosity η_v as a function of λ_{eff} for EPDM2 subjected to (b) cyclic tests, (d) a pseudocyclic test, and (f) a pseudocyclic test with pauses. When expressed as a function of λ_{eff} , the viscosity data overlay to form a master curve. A simple function is fitted to describe the viscosity master curve.	96
5.5	The experimental σ_e (symbols) and model σ_{EV} (lines) equilibrium contributions as a function of stretch for (a) CR and (c) NBR. The model is an EV function accounting for λ_{set} . The viscosity η_v as a function of λ_{eff} for (b) CR and (d) NBR. When expressed as a function of λ_{eff} , the viscosity data overlay to form a master curve. A simple function is fitted to describe the viscosity master curve.	97

5.6	The evolution of (a) slip-link density N_S , (b) slip-link mobility η , (c) chain inextensibility α , and (d) permanent set λ_{set} with pre-deformation λ_{max} for an EPDM2 specimen subjected to a pseudocyclic test with a pause. The parameters extracted from the elastic contributions are shown as circles. The corresponding uncertainties (95% confidence interval) are also shown. To describe the evolution of these parameters, simple functions (lines) are fitted to the extracted parameter values as functions of λ_{max} for $\lambda_{\text{max}} \geq 2$ (larger circles).	98
5.7	The evolution of (a) slip-link density N_S , (b) slip-link mobility η and (c) chain inextensibility α with pre-deformation λ_{max} for NBR specimens. The parameters extracted from the elastic contributions are shown as circles. The corresponding uncertainties (95% confidence interval) are also shown. To describe the evolution of these parameters, simple functions (lines) are fitted to the extracted parameter values as functions of λ_{max} for $\lambda_{\text{max}} \geq 1.6$ (larger circles).	99
5.8	Comparison of the experimental (symbols) and model (lines) third loop response for EPDM2 ((a) cyclic, (b) pseudocyclic and (c) pseudocyclic with pause) and (d) NBR. In each instance, five different pre-deformation levels λ_{max} out of ten have been highlighted.	101
5.9	Viscosities obtained for the EPDM2 sample subjected to a pseudocyclic test with pauses. The λ_{set} utilised here corresponds to the λ_{set} obtained from fitting to the pseudocyclic EPDM2 case. In this instance the viscosities are seen to form a master curve.	103
5.10	Comparison of the energy dissipated in the experimental and model third loop response for (a) EPDM2 (cyclic (circles), pseudocyclic (triangles), and pseudocyclic with pause (squares)) and (b) NBR.	104
5.11	Comparison of the experimental (symbols) and model (lines) initial loading response for (a) EPDM2 and (b) NBR. For EPDM2, the models corresponding to cyclic, pseudocyclic and pseudocyclic case with a pause correspond to the solid, dashed and dash-dot lines, respectively.	105

5.12	Comparison of the change in (a) RMS error, (b) confidence interval for λ_{set} , (c) elastic contribution (at $\lambda_{\text{max}} = 6$) and (d) viscosity η_v (at $\lambda_{\text{max}} = 6$) with varying amounts of strain discarded to account for transients. This data corresponds to the cyclic EPDM2 test.	106
5.13	The change in relaxation time τ against stretch λ for (a) EPDM2 and (b) NBR. It is assumed that the transients are over in a time equivalent to three relaxation times, hence 3τ is used here.	107
5.14	η_v as a function of λ_{eff} . A qualitative approximation for the λ_{set} was used to obtain the corresponding λ_{eff} . A formation of a master curve can be observed.	110
5.15	The evolution of (a) strain energy W and (b) temperature rise as a function of stretch for an EPDM2 specimen subjected to a pseudocyclic test.	114
6.1	TEM images of (a) N234, (b) N330 and (c) N600 carbon black filler particles. These images were provided by Dr Lewis Tunnicliffe of Birla Carbon. As the magnification was different for each micrograph, the images have been resized to allow for the same size scale bar and scale for comparative purposes.	118
6.2	Compression moulding setup. An image of a rolled sheet of rubber of dimensions similar to that of the mould cavity, above two stainless steel layers is also illustrated here. The stainless steel surface in contact with the rubber is polished.	119
6.3	Rectangular specimen preparation.	123
6.4	A schematic of the test procedure.	125
6.5	A plot of the storage modulus $G'(\gamma)$ against frequency for (a) the full frequency range explored and (b) for frequencies between 0.1 and 0.5 Hz.	128
6.6	A comparison between the uniaxial tensile tests conducted on CR specimen using an Instron tensile tester and an Anton Paar Rheometer.	131
6.7	A comparison of stress-stretch response obtained by conducting uniaxial tensile tests on SBR compounds containing 50 phr of N234, N330 and N660.	132
6.8	The stress-stretch response of uniaxial cyclic tensile test of selected SBR compounds utilised in this study.	133

6.9	The stress-stretch response of uniaxial cyclic tensile test of SBR N234 (a) 50 phr and (b) 60 phr compounds. For these compounds, the stress value is seen to reduce when the filler amount is increased from 50 to 60 phr.	134
6.10	A plot of storage modulus against dynamic shear strain demonstrating the reversibility of the Payne effect.	135
6.11	a) Typical cyclic tensile response and b) amplitude sweep following the cyclic history of SBR compound filled with 50 phr of N330 carbon black. The different strain histories explored in the experimental protocol are marked in the same colour.	136
6.12	A comparison of the model fits (lines) obtained by a) individually fitting modified Kraus models to amplitude sweeps for SBR filled with 50 phr of N330 filler for each tensile strain history, and b) simultaneously fitting modified Kraus models with a single value of γ_c and m for all datasets. Colours are used to highlight the different strain histories explored and the experimental data is represented by symbols. The RMS errors for the individual and simultaneous fits are 0.34 and 0.41 MPa, respectively.	137
6.13	Values of a) γ_c and b) m obtained <i>via</i> fitting modified Kraus models to experimental amplitude sweep data (± 1 standard uncertainty) for the SBR with 50 phr of N330 carbon black filler. Also shown as horizontal dashed lines are values of a) γ_c and b) m obtained by simultaneous fitting of all amplitude sweeps.	138
6.14	The evolution of G'_0 obtained by fitting Kraus models to amplitude sweep data for TP3 as a function of tensile pre-deformation for SBR systems filled with a) N234, b) N330 and c) N660 type carbon black. For each system three different filler contents are explored, 40, 50 and 60 phr, and are indicated by red, blue and black colours, respectively. The uncertainties (± 1 standard uncertainty) associated with each plot are also shown. The lines are for guidance only.	138
6.15	The evolution of γ_c and b) m with increasing filler content for SBR systems filled with N234, N330 and N660 type carbon black, represented by square, circle and triangle symbols, respectively. The uncertainty (± 1 standard uncertainty) associated with each plot are also shown.	139

6.16	The evolution of G'_0 with (a) filler volume fraction, and (b) effective surface area. The lines are a guide to the eye.	140
6.17	A comparison of the model fits (lines) obtained from employing Eq. 6.6 alongside Eq. 6.5, and the experimental data (symbols) for the SBR N330 50 phr compound for all the strain histories explored. RMS error of 0.55 MPa was obtained.	141
6.18	The impact of varying the static strain on the resulting dynamic response for a SBR N330 50 phr compound. The dynamic strains are superimposed on the static strain, refer to TP1.	143
6.19	The evolution of G'_0 obtained by fitting Kraus models to amplitude sweep data obtained for TP1 as a function of tensile static strain for SBR systems filled with a) N234, b) N330 and c) N660 type carbon black. For each system three different filler contents are explored, 40, 50 and 60 phr, and are indicated by red, blue and black colours, respectively. The uncertainty (± 1 standard uncertainty) associated with each plot are also shown. The lines are a guide to the eye	145
6.20	Evolution of the normalised G'_0 for TP1 as a function of tensile static strain for SBR systems with N234 (circles), N330 (squares) and N660 (triangles) type of carbon black. For each system three different filler contents are explored, 40 (solid line), 50 (dotted lines) and 60 (dashed lines) phr. For any given system, the normalisation was carried out with respect to the corresponding G'_0 value at zero% static strain. A theoretical value (red line) was obtained <i>via</i> Rivlin's [9] theory.	146
A.1	A thickness versus force plot for different silicone/acrylate compositions. A linear model (red line) has been fitted to the experimental data (black symbols). The thickness values obtained via the Lebedev and Ufliand theory [122] have been highlighted using blue symbols.	174
A.2	A dumbbell shaped specimen cut for uniaxial tensile testing. The image was scanned using a HP Scanjet G4010 scanner at 1200 dpi.	175
A.3	a) The calibration of a scanned image by using a scale of known length, and b) the determination of the width of the specimen by drawing straight lines on the calibrated image.	176

A.4	A comparison of the model (lines) viscosity curves obtained due to the different minimisation schemes utilised.	179
A.5	Experimental (symbol) and model (line) third loop transient response for all values of λ_{\max} explored.	188
A.6	The evolution of viscosity associated with set with increasing λ . A polynomial model of the fourth order is fitted to η_{set} and is represented as a solid red line on the plot.	189
A.7	A comparison of the experimental and model initial (or virgin) loading behaviour. The model stress is obtained by the summation of σ_{EV} , σ_{M} and $\sigma_{\text{f,set}}$. A variable η_{set} was utilised in the determination of $\sigma_{\text{f,set}}$	189
A.8	The evolution of (a) slip-link density N_{S} , (b) slip-link mobility η , (c) chain inextensibility α (d) permanent set λ_{set} with pre-deformation λ_{\max} for EPDM2 specimen subjected to cyclic tests. The parameters extracted from the elastic contributions are shown as circles. The corresponding uncertainties (95% confidence interval) are also shown. To describe the evolution of these parameters, simple functions (lines) are fitted to the extracted parameter values as functions of λ_{\max} for $\lambda_{\max} \geq 2$ (larger circles).	190
A.9	The evolution of (a) slip-link density N_{S} , (b) slip-link mobility η , (c) chain inextensibility α (d) permanent set λ_{set} with pre-deformation λ_{\max} for EPDM2 specimen subjected to a pseudocyclic test. The parameters extracted from the elastic contributions are shown as circles. The corresponding uncertainties (95% confidence interval) are also shown. To describe the evolution of these parameters, simple functions (lines) are fitted to the extracted parameter values as functions of λ_{\max} for $\lambda_{\max} \geq 2$ (larger circles).	191
A.10	A flow diagram highlighting the key steps involved in the solution implemented on MATLAB to determine the amount of heat dissipated via conduction through the grips and via convection to the environment.	192
A.11	The region of the specimen that will be gripped using the tensile tester clamps (a) prior to clamping, and (b) post clamping.	193
A.12	The change in temperature ΔT experience by a specimen during a pseudocyclic tests when (a) conduction and (b) convection are accounted for.	193

A.13	The stress-stretch response of uniaxial cyclic tensile test of the SBR compounds omitted from the main body of chapter 6. . .	194
A.14	Plot of the storage modulus against dynamic shear strain demonstrating the reversibility of the Payne effect for the SBR compounds omitted from the main body of chapter 6.	195

List of Tables

2.1	Physical interpretations for the Mullins effect. Adapted from Diani <i>et al.</i> [32].	21
3.1	Numerical values for χ	48
3.2	The EV parameters used to illustrate the impact of each parameter on the resulting stress-strain response on Figure 3.8. Test IDs are used to identify the corresponding curve.	55
3.3	Estimate ± 1 standard uncertainty for the coefficients of equations 3.11 - 3.14 describing the evolutions of the EV parameters: slip-link density N_S , slip-link mobility η , cross-link density N_C and chain inextensibility α , as a function of silicone weight fraction f_{PDMS}	58
4.1	Estimate ± 1 standard uncertainty for the coefficients of equations 4.9 - 4.13 describing the evolutions of the elastic parameters: slip-link density N_S , chain inextensibility α , slip-link mobility η , and of the permanent set λ_{set} , and of the viscosity η_V , as a function of maximum stretch λ_{max}	77
5.1	Modulus (± 2 standard uncertainty) of the linear spring in the modified SLS model.	100
5.2	A summary of the amount of data that must be discarded from the initial $\epsilon_{\text{discard,initial}}$ and final $\epsilon_{\text{discard,final}}$ portion of the strain range explored to account for transients, and the amount of data available $\epsilon_{\text{available}}$ for the fitting process once the transients is accounted for, for a given λ_{max} value. The data provided below corresponds to EPDM2 and NBR.	109

6.1	Vulcanisation time t_v required for the various SBR compounds explored in this study. The vulcanization time corresponds to the time required to reach 90% cure plus five minutes. The cure time was determined <i>via</i> a moving die rheometer by Dr Lewis Tunnicliffe of Birla Carbon.	120
6.2	The density ρ (± 1 standard error) in $\text{g}\cdot\text{cm}^{-3}$ of the cured and uncured styrene-butadiene rubber (SBR) systems. The data provided below is based on three repeats. The theoretical density is also provided.	121
6.3	The glass transition temperature T_g (± 1 standard error) in $^{\circ}\text{C}$ of the cured SBR compositions calculated using the inflection-point method.	122
A.1	Numerical values of the kernel $K(\nu)$	172
A.2	Numerical values of the kernel $\Omega(T)$	173
A.3	Estimate ± 1 standard uncertainty for the coefficients of equation 4.13 describing the evolution of η_v as a function of λ_{eff}	179
A.4	The optimised value for the linear spring modulus E for all cases of λ_{max} explored.	180
A.5	Estimate ± 1 standard uncertainty for the coefficients of equations 4.9 - 4.13 describing the evolutions of the elastic parameters: slip-link density N_S , chain inextensibility α , slip-link mobility η , the permanent set λ_{set} , and the viscosity η_v as a function of maximum stretch λ_{max} . These values are associated with EPDM2 cyclic test data.	181
A.6	Estimate ± 1 standard uncertainty for the coefficients of equations 4.9 - 4.13 describing the evolutions of the elastic parameters: slip-link density N_S , chain inextensibility α and slip-link mobility η , the permanent set λ_{set} and the viscosity η_v as a function of maximum stretch λ_{max} . These values are associated with EPDM2 pseudocyclic test data.	182
A.7	Estimate ± 1 standard uncertainty for the coefficients of equations 4.9 - 4.13 describing the evolutions of the elastic parameters: slip-link density N_S , chain inextensibility α and slip-link mobility η , the permanent set λ_{set} and the viscosity η_v as a function of maximum stretch λ_{max} . These values are associated with EPDM2 pseudocyclic test including pauses.	183

A.8	Estimate ± 1 standard uncertainty for the coefficients of equations 4.9 - 4.13 describing the evolutions of the elastic parameters: slip-link density N_S , chain inextensibility α and slip-link mobility η , the permanent set λ_{set} and of the viscosity η_v as a function of maximum stretch λ_{max} . These values are associated with NBR cyclic test data.	183
A.9	The ingredients and the corresponding values for parts, density ρ , volume V , volume fraction ϕ_{comp} and $\rho \times \phi_{\text{comp}}$ for the SBR compounds explored in this study.	186

Abbreviations

1D	one-dimensional
AM	additive manufacturing
BR	Butadiene rubber
CI	Confidence interval
CR	Chloroprene rubber
EHA	2-ethyl hexyl acrylate
EPDM	Ethylene propylene diene rubber
EPDM1	Ethylene propylene diene rubber DIK
EPDM2	Ethylene propylene diene rubber J-Flex
EV	Edwards-Vilgis
FE	Finite element
FT	Fourier transform
NBR	Acrylonitrile-butadiene rubber
NR	Natural rubber
PDMS	Polydimethylsiloxane
PDMS-MA	Methacryloxypropyl terminated polydimethylsiloxane
phr	parts per hundred rubber
RMS	root-mean-square
SBR	Styrene-butadiene rubber
SCA	Silane coupling agent
SLS	Standard linear solid
SRF	Solid rectangular fixture
TEM	Transmission electron microscopy
UV	Ultraviolet

Symbols

$\langle r^2 \rangle_0$	Unperturbed mean square end to end distance
$\langle r^2 \rangle$	Mean square end to end distance
A_0	Initial Nominal cross-sectional area of the specimen
A_{cond}	Conductive surface area
A_{conv}	Convective surface area
A_{el}	Elastic free energy of a single chain
C_1	Mooney-Rivlin parameter
C_2	Mooney-Rivlin parameter
C	Torsional constant of a rectangular cross-section
$E_{1\%}$	Tensile modulus at 1% strain
E_C^{exp}	Experimental value for energy dissipated
E_C^{mod}	Model prediction of energy dissipated
$E_{s,100\%}$	Secant modulus at 100% strain
E_s	Secant modulus
E	Stiffness of the linear spring
$G''(\gamma)$	Strain dependent loss modulus
G''_{∞}	Loss modulus at large strains
G''_{M}	Maximum loss modulus
G''	Loss modulus
$G'(\gamma)$	Strain dependent storage modulus
$G'_0(\epsilon_{\text{max}})$	Plateau storage modulus value at a given tensile strain history
G'_{∞}	Storage modulus at large strains
$G'_{0,0\%}$	Plateau storage modulus value of the virgin specimen
G'_0	Storage modulus at small strains
G'	Storage modulus
G_0	Shear modulus of the raw polymer
G_{affine}	Shear modulus of the affine network model

G_{phantom}	Shear modulus of the phantom network model
G	Shear modulus
I_p	Polar area moment of inertia of cross-section about axis of torsion
L_{cond}	Half the thickness of specimen post clamping on to the tensile tester. This is the distance that heat will have to travel to reach the clamps.
L	Length of the specimen (gauge)
M_w	Molecular weight
M	Torque
N_C	Cross-link density
N_S	Slip-link density
$P(r)$	The probability of any given distance r between the ends
P	The weight of the rubber thickness gauge probe
Q_{cond}	The energy gained or lost per unit volume via conduction
Q_{conv}	The energy gained or lost per unit volume via convection
R_0	Radius of curvature
R	SER3-P drum radius
T_g	Glass transition temperature
T	Absolute temperature
U	Internal energy
V_0	Nominal volume of the specimen
V	Volume
$W(\mathbf{F})$	Strain energy density function
W_C	Strain energy due to cross-links
$W_R(\mathbf{F})$	Reduced strain energy density function
W_S	Strain energy due to slip-links
W	Strain energy density
$\Delta A_{\text{el,affine}}$	Elastic free energy of an affine network
$\Delta A_{\text{el,phantom}}$	Elastic free energy of an phantom network
ΔT_{tol}	Allowable deviation in the temperature
$\Omega(\Xi)$	Kernal of the Lebedev and Ufliand function
$\Omega(T)$	Kernal of the Lebedev and Ufliand function
α_1	A constant related to the thickness and width ratio of a specimen, used in the torsion equation
α_{diff}	Thermal diffusivity
α	Measure of inextensibility
\tilde{G}	Dynamic shear modulus adjusted for an imposed static strain

β	A constant related to the thickness and width ratio of a specimen, used in the torsion equation
χ	A constant used in the Lebedev and Ufliand theory
\dot{Q}_{cond}	Rate at which energy is gained or lost due to conduction
\dot{Q}_{conv}	Rate at which energy is gained or lost due to convection
$\dot{\epsilon}_{\text{true}}$	True strain rate
$\dot{\epsilon}$	Strain experienced by the specimen
$\dot{\lambda}_{\text{eff}}$	Effective stretch rate
$\dot{\lambda}_{\text{set}}$	Rate of change of permanent set
$\dot{\lambda}$	Stretch rate
$\dot{\sigma}_{\text{M}}$	Rate of change of stress in the Maxwell element
ϵ_0	A constant utilised in the evolution of plateau modulus formula
ϵ_{max}	Historical maximum strain
ϵ	Strain experienced by the specimen
η_{loss}	Loss factor
η_{v}	Viscosity
η_{set}	Viscosity associated with the set flow stress
η	Measure of slippage
γ_{c}	Critical strain at which $G'_0 - G'_\infty$ reaches half its value
γ	Shear strain
λ_1	Stretch in the x direction
λ_2	Stretch in the y direction
λ_3	Stretch in the z direction
$\lambda_{0.1\text{N}}$	Stretch corresponding to a load of 0.1 N
λ_{eff}	Effective stretch, i.e., the stretch actually experienced by the network
λ_{max}	Historical maximum stretch
λ_{set}	Permanent set stretch
λ	Stretch
ν_{p}	Poisson's ratio
ν	Density of the chains in the network
ω_{d}	Damped natural frequency
ω_{n}	Natural frequency
ω	Frequency
ϕ'	Effective volume fraction
ϕ_{comp}	Volume fraction of the component

ϕ_{fun}	Functionality of a junction
ϕ	Volume fraction of filler material
ρ	Density of the material
σ_{EV}	Model equilibrium contribution
σ_{M}	Stress in the Maxwell element
σ_e	Elastic or equilibrium stress
$\sigma_{\text{f,set}}$	Set flow stress
$\sigma_{\text{n,max}}$	Maximum nominal stress
$\sigma_{\text{v,true}}$	True dissipative or viscous stress
σ_v	Dissipative or viscous stress
σ	Stress experienced by the specimen
τ_{cond}	Relaxation time
τ_{conv}	Relaxation time
τ	Relaxation time
\mathbf{F}	Deformation gradient
r	Distance between the ends of a polymer chain
t_s	Thickness of the specimen
$K(\nu)$	Kernal of the Lebedev and Ufliand function
SA_{eff}	Effective surface area
SA	Surface area
θ_1	Angle of twist
θ	SER3-P drum deflection angle
ξ	Cycle rank of the network
ζ	Damped ratio
a	A constant associated with the width to thickness ratio of a rectangular cross-sectional beam
b	A constant utilised in the evolution of plateau modulus formula
c	Specific heat
d	Damage variable
f_{PDMS}	Fraction of silicone
f	Force required to deform a polymer chain
h	Heat transfer coefficient
k	Boltzmann constant
m	Rate at which van der Waals type interactions are broken
p	A ratio of half the thickness of the rubber thickness gauge probe to the thickness of the elastic layer
s	Maximum power input (per unit mass)

$t_{s,0}$	The deformation caused by the weight of the thickness gauge
t_v	Time taken for vulcanisation process to complete
$\tan\delta$	Loss factor
t	Time
w	Width of the specimen
ΔT_{corr}	Corrective change in temperature to account for conduction or convection
ΔT	Change in temperature
Δt	Change in time

1. Introduction

Elastomers are used in a wide range of industrial applications, including tyres, dampers and seals, to name a few. The performance requirements for these materials have increased and will continue to increase in the coming years. For example, in the oil and gas industry, there is an increase in demand for deep-water exploration and production. Drilling oil wells at water depths approaching or exceeding 1500 m poses significant challenges. Elastomer seals leveraged in these applications must therefore be able to withstand high pressures and extreme temperatures and temperature changes. Similarly, in the tyre industry, owing to the need to curb greenhouse gas emissions, there is an increase in demand to reduce rolling resistance. Alongside this, there is also a need to reduce wear and increase the grip in the tyres. The elastomer compound therefore plays a vital role in the design process and must be selected accordingly.

Elastomers are made up of long entangled chains: imagine a bowl of spaghetti. It is likely that most people have experienced the act of unintentionally scooping up more pasta than necessary, as a result of entangled pasta strands. A polymer system is analogous to this. These systems are typically chemically bonded together (or cross-linked) *via* the vulcanisation process, creating an elastomer network that leads to the well-known resilience of elastomeric materials. The elastic properties of elastomeric materials are not just dependent on the molecular structure but on the length of the elastomeric chains, or the length of the pasta strand in the analogous system, between the cross-links. Therefore, this is a key design consideration.

For practical applications, elastomers that are reinforced with fillers are used, thus the name filled elastomers. This is due to the fact that incorporation of fillers leads to improvements in properties such as mechanical strength, abrasion resistance and wear resistance, and also leads to a cost reduction in the end part. Carbon black and silica are the two most popular

fillers. The primary filler particles can be between 5-350 nm wide. These particles have the tendency to clump together to form aggregates, the aggregates then clump together to form agglomerates, and the subsequent interactions between the agglomerates leads to the formation of filler networks. The size of the aggregates/agglomerates and the extent of the filler network depend on both filler type and amount of material. Many of the non-linear behaviour observed in filled elastomers can be attributed to the presence of fillers. The observed non-linearity can be controlled to a certain extent by carefully selecting the type and amount of filler.

Alongside the choice of the elastomer, filler type and filler amount, engineers must also consider the deformation history in the design process. This is due to the fact that the mechanical response of elastomers is dependent on the deformation history; the mechanical response of a virgin material will be different to that of a material that had been deformed before. This particular phenomenon was investigated intensively by Mullins and co-workers [1, 2, 3, 4]; hence this effect came to be known as the Mullins effect. The cause of this phenomenon is still a subject of on-going research.

It is evident that the performance requirements for elastomeric materials are on the rise. Amongst other factors, market demands and government regulations are the key driving forces for this. For any given application, the engineers will therefore need to select the appropriate elastomer, filler type, and filler amount. The deformation history also adds another dimension to the design process. Engineers often have to turn to computational tools such as constitutive models to aid the design process. This is due to the fact that it is often impractical or costly to carry out real-world experiments. Whilst there are numerous models that are available in the literature, owing to the complex non-linear behaviours exhibited by elastomeric materials, there still remains a number of challenges. Furthermore, there is still much debate in the academic literature regarding the physical origins of several aspects of the underlying material behaviour. Thus, there is a lot of scope in developing predictive models to capture the various aspects of elastomer behaviour. This thesis attempts to contribute to this area of research.

This thesis consists of seven chapters. Chapter 2 gives a critical overview of the relevant literature. A brief history of elastomeric materials is provided. This is followed by a description of the elasticity of the single chain and the elasticity of an elastomeric network. Subsequent sections delve into key phenomena pertaining to elastomeric materials, including the filler reinforcement, the Mullins effect and the Payne effect. The modelling frame-

works and models that exist in the literature to describe these phenomena are then explored. This section helps identify gaps in the research, and therefore opportunities for further research within the thesis. Lastly, the aims and objectives of this research are introduced.

Chapters 3 to 6 present the findings corresponding to this project. In chapter 3, the impact of the elastomer network on the mechanical response is examined. For this purpose, a set of soft custom-made cast ultraviolet light curable silicone-acrylate elastomers are used. The composition of these elastomers differ due to the differing ratios of silicone to acrylate. In elastomers, the change in the composition can impact the elastomer network. Aside from the simplicity by which compositional changes can be achieved, these elastomers are chosen as they are void of fillers. The focus is on the impact of the elastomer network and the fillers will add another dimension of complexity to the problem. Quasi-static tensile tests have been used to probe the mechanical response of these elastomers. The experimental data reveals that the elastomer network changes with varying silicone to acrylate ratio. These observations are used to develop a model for predicting the mechanical properties of the considered set of materials.

Chapter 4 studies the impact of deformation history on the mechanical response of elastomers. Sheet rolled, filled ethylene propylene diene monomer (EPDM) systems are used for this purpose. EPDM is chosen as it is used for a wide range of applications. A filled system is chosen due to the fact that most practical applications leverage filled elastomers. Specimens produced from sheet rolled EPDM material are subjected to uniaxial cyclic tensile test under various maximum deformation (or pre-deformation) levels. The uniaxial cyclic tensile data is then decomposed into elastic and viscous contributions. A physically motivated model is fitted to the elastic contribution. Curves are then fitted to the extracted model parameters, including permanent deformation, to describe their evolution with respect to pre-deformation. Once the permanent deformation is accounted for, the viscous contribution forms a pre-deformation independent and effective stretch dependent master curve. A model is fitted to describe this master curve. This chapter develops and validates a model based on the evolution of elastic parameters with pre-deformation and a viscous master curve.

Chapter 5 explores the applicability of the modelling framework developed in the previous chapter to other commonly used elastomeric materials. An effort is made to understand whether single pseudocyclic tests can be utilised instead of numerous cyclic tests.

In Chapter 6 , the impact of fillers on the mechanical response of elastomers is studied. For this purpose, styrene-butadiene rubber (SBR) compounds filled with three different amounts and types of carbon black fillers are used. SBR compounds are commonly employed in automotive tyres. Two test protocols have been adopted; each test protocol consisting of quasi-static and dynamic deformations. The impact of fillers is explored *via* the dynamic tests. The Kraus model is fitted to dynamic response for this purpose, and the variation in the parameters with varying filler type and content are explored. Alongside this, the impact of deformation history, i.e., the Mullins effect, on the small strain dynamic response, i.e., the Payne effect, is also explored. The Kraus model parameters are utilised for this purpose too. The observations made from this study are used to suggest a modified Kraus model to capture the impact of pre-deformation and filler type and amount.

A summary of the work and recommendations for future work are presented in chapter 7. Lastly, materials supporting the work in the main body of the text have been provided in the appendices.

2. Literature review

In this chapter, a review of the relevant topics pertaining to this thesis have been presented. In section 2.1, a brief overview of elastomeric materials has been presented, including a brief history, the theory pertaining to the elasticity of a single chain and that of a network, filler reinforcement, and technical elastomers. In section 2.2, a key phenomenon observed in elastomer materials, known as the Mullins effect, is discussed. The characteristic features of the effect are introduced, this is followed by physical interpretations of the phenomenon as suggested in the literature. In section 2.3, the Payne effect is introduced. This is another key phenomenon observed in filled elastomers. The corresponding physical interpretations are also discussed. The modelling of the elastic behaviour, the viscous behaviour and the various phenomena observed in elastomers are discussed, including the modelling approaches and key models, in section 2.4. The research opportunities are discussed in section 2.5. Lastly, the aims and objectives of this thesis is discussed in section 2.6.

2.1 Elastomeric materials

Elastomeric materials are characterised by the ability to deform to large strains when subjected to a mechanical load and return to their original shape (or close to) upon removal of the load. Their use dates back to 1600 B.C., when they were utilised by the Mesoamerican people for rubber balls, human figurines, and other items [5]. Nowadays elastomeric materials are used for a wide range of industrial applications, including tyres, dampers and seals, to name a few. The elastomeric materials used by the Mesoamericans were extracted from the sap of latex-producing trees. These materials are typically made up of monomeric repeat units, resulting in a polymer chain (long

molecule). 1,4-polyisoprene is an example of a naturally occurring monomer obtained from the sap of the tree *Hevea Braziliensis* as shown on Figure 2.1. Many synthetic variants exhibiting the rubberlike behaviour of 1,4-polyisoprene exist, such as 1,4-polybutadiene and poly(dimethyl siloxane).

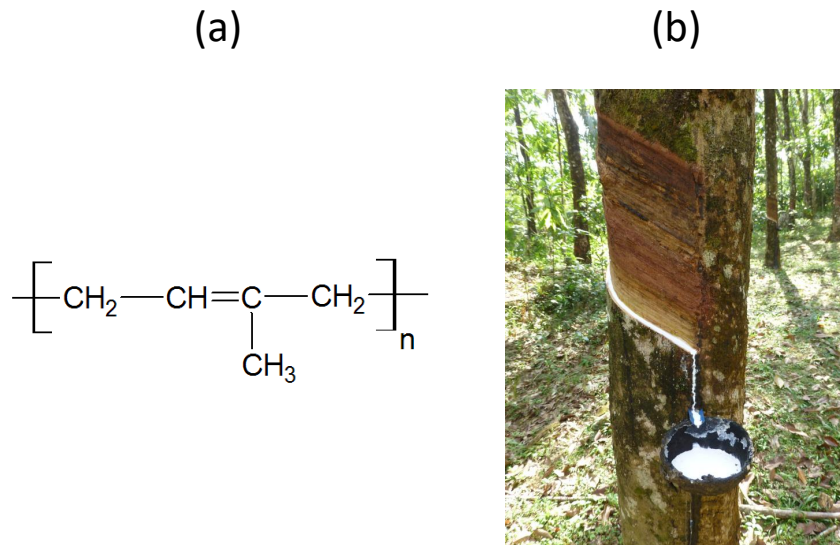


Figure 2.1: (a) 1,4-polyisoprene monomer, and (b) rubber sap being collected from the *Hevea Braziliensis* tree. The image of the *Hevea Braziliensis* tree was obtained from Ji-Elle *via* Wikimedia Commons (CC).

The discovery of the vulcanisation process by Charles Goodyear in 1841 was the next significant leap in elastomer technology. In this process, chemical bonds (or cross-links) are formed between macromolecules. Sulphur is the most commonly used cross-linking agent, accounting for 90% of all vulcanisation [6]. In the presence of heat, the sulphur reacts with the double-bonds in the polymer chains creating an elastomeric network. Peroxides are an alternative vulcanisation agent. The observed resilience of elastomers is due to the vulcanisation process. The most useful elastomeric products, such as tyres and seals, rely on vulcanisation. The chemically cross-linked elastomers are known as thermosets. This class of elastomers cannot be easily reprocessed.

Elastomers can also be thermoplastic. Thermoplastic elastomers are block copolymers, they consist of two different monomer segments. The monomer segments are chosen to be immiscible, hence copolymers exhibit

two distinct phases. There is a “soft” and a “hard” phase, the “hard” phase acts as a physical cross-link. Due to the physical bonds, the thermoplastics can be reshaped by exposing them to a temperature above that of the melting temperature of the hard phase. An illustration of chemically and physically cross-linked elastomers is shown on Figure 2.2.

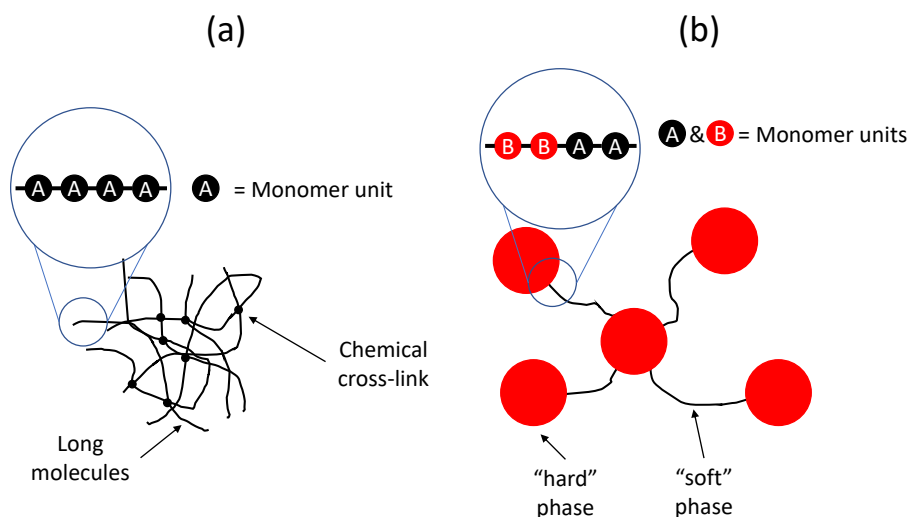


Figure 2.2: A schematic of (a) thermoset, and (b) thermoplastic elastomer. The thermoset is constrained by chemical cross-links, whereas a thermoplastic elastomer consists of physical bonds i.e., “hard phase”.

2.1.1 Elasticity of a single chain

Prior to exploring the rubber network, important features of a single chain will be explored briefly. A polymer chain is characterised by the bond angle, bond length and torsional angle. The length of a bond and the bond angle do not usually change much, unless very high forces act on them. The torsional angle fluctuates between three states (trans, gauche+ and gauche-) and takes on either a rod-like zig-zag (trans) or disordered configuration (gauche+ and gauche-) [7, 8] as shown on Figure 2.3. The rate of change between different states and configurations depends on the environment of the chain. For example, in a suitable solvent, the transition between the configurations occurs 10^{10} times per second [8].

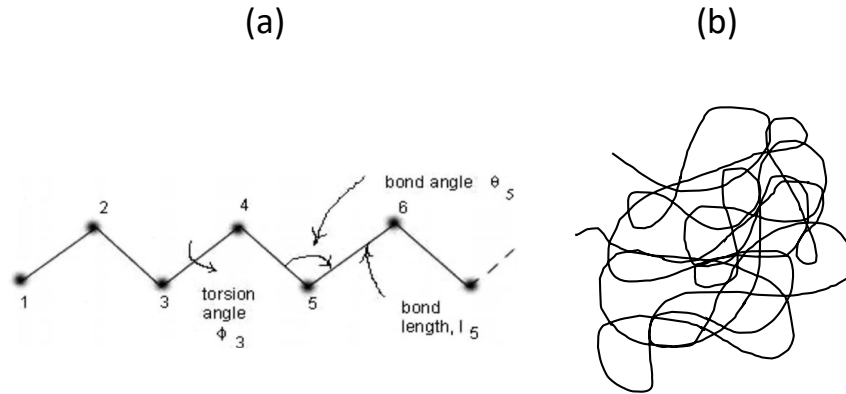


Figure 2.3: A schematic of (a) rod-like zig-zag configuration highlighting important features of a single polymer chain, and (b) disordered configuration. The image for rod-like zig-zag configuration was adapted from [8].

The properties of a single chain can be described statistically *via* the probability $P(r)$ of any given distance r between the chain ends. Figure 2.4 illustrates a random configuration of a chain of 10 bonds. The end to end vector r is highlighted on the figure. As stated previously, each bond in the chain can take three states. The number of configurations that this particular chain can exist in is therefore 3^{10} [8]. As the number configurations are large, typically an average measure such as the mean-square $\langle r^2 \rangle$ value of the distance between the ends of the chain r is used. $\langle r^2 \rangle$ can be determined by generating a number of random configurations, much like Figure 2.4, and averaging the determined r values. The Monte Carlo method can be used for the purpose of generating a large number of random configurations. The elastic free energy A_{el} of a single chain can then be determined by coupling $P(r)$ with the Helmholtz free energy and the Boltzmann relation.

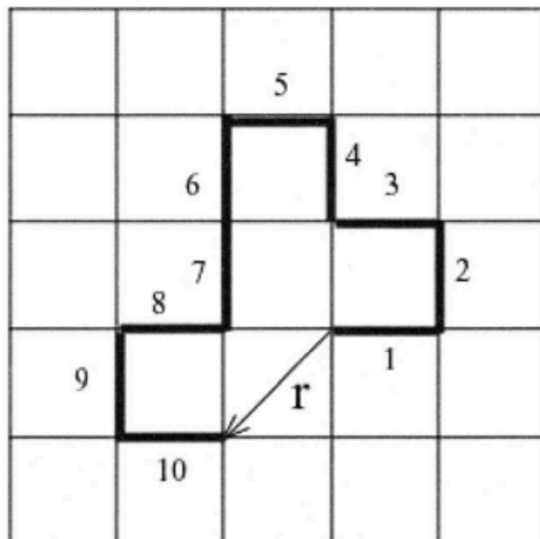


Figure 2.4: A random configuration of a chain containing 10 bond. Adapted from [8].

The elastic free energy A_{el} of a single chain forms the basis for many models describing rubber elasticity, and is given by

$$A_{el} = U - \left(\frac{3kT}{2 \langle r^2 \rangle_0} \right) r^2 \quad (2.1)$$

where U is the internal energy, k is Boltzmann's constant, T is the absolute temperature and $\langle r^2 \rangle_0$ is the unperturbed mean square end to end distance. The force f required to deform the chain can be determined by differentiating A_{el} with respect to r , and is given by

$$f = \frac{3kT}{\langle r^2 \rangle_0} r \quad (2.2)$$

This equation is the linear spring law, hence a single chain behaves like a linear spring. For an in-depth understanding of the theory, readers are referred to the text by Treloar [9] and the work by Erman [8].

2.1.2 Phenomenology of the network

An elastomeric network is formed by linking elastomer molecules together to form a three-dimensional macromolecular structure which contains elastically

active chains, loops, dangling chains and entanglements [8, 10]. Physical links include entanglements and crystal zones (formed *via* copolymerisation), and chemical links are formed *via* the vulcanisation process, see section 2.1).

Figure 2.5 highlights features of an elastomeric network. A chain whose ends are joined at two junctions is an elastically active chain. A chain whose ends are joined at a single junction is known as a loop. A chain that is connected only at one end is known as a dangling chain. Only active chains contribute to the elastic free energy of the network. If the network chains are sufficiently long, the entanglements may also contribute to the elastic free energy of the network [8].

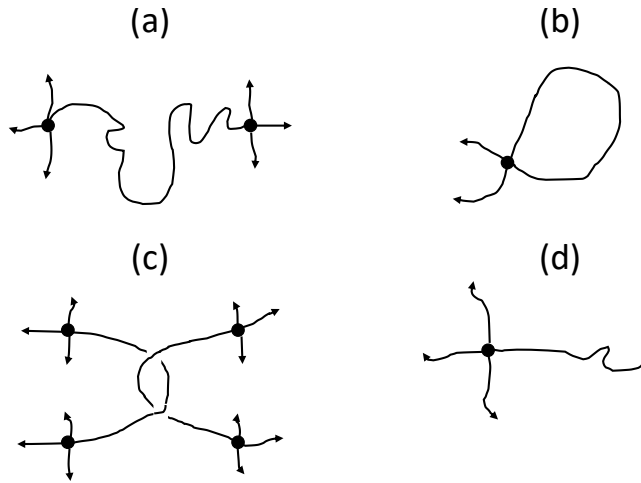


Figure 2.5: Structural features of a network: (a) elastically active chain, (b) loop, (c) trapped entanglement, and (d) dangling chain. The black dots refer to both the chemical and physical cross-links. Adapted from [11]

The affine and phantom models are the most basic models that describe the elasticity of a network. They are based on the assumption that the polymer chains can change shape without impacting the contour length. A macroscopic deformation is therefore associated with a change in conformation as a result of the varying torsion angle and bond angle. The affine model assumes that the network junction points are fixed, therefore macroscopic deformations lead to affine deformations between the junction points. The phantom model assumes that the junction points fluctuate about a mean position, unhindered by the presence of neighbouring chains. Figure 2.6 and

2.7 illustrate these concepts. The expression for the elastic free energy of affine $\Delta A_{el,affine}$ and phantom $\Delta A_{el,phantom}$ network models are given by eq. 2.3 and 2.4, respectively [8].

$$\Delta A_{el,affine} = \frac{\nu kT}{2}(\lambda_1^2 + \lambda_2^2 + \lambda_3^2 - 3) \quad (2.3)$$

$$\Delta A_{el,phantom} = \frac{\xi kT}{2}(\lambda_1^2 + \lambda_2^2 + \lambda_3^2 - 3) \quad (2.4)$$

where ν is the density of the chains in the network, k is the Boltzmann constant, T is the absolute temperature, ξ is the cycle rank of the network and λ_1 , λ_2 and λ_3 are the extensional ratios in the x, y and z-directions, respectively [8, 12]. ξ is related to ν via $(1 - 2/\phi_{fun})\nu$, where ϕ_{fun} is the functionality of a junction, i.e., the number of chains meeting at a junction. The free energy descriptors above are the free energies of the network, and are essentially the sums of the elastic free energies of single chains.

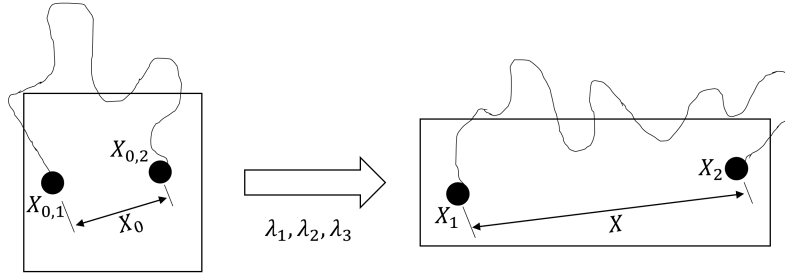


Figure 2.6: The affine network model. The junction points are fixed, a macroscopic deformation results in an affine transformation of the components of the vectors representing the distance between the junction points.

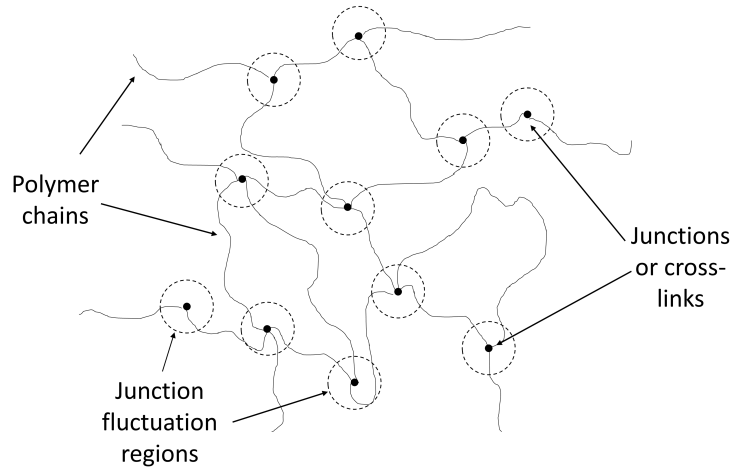


Figure 2.7: The phantom network model. The junction points can fluctuate about a mean position; the fluctuation region is illustrated as dashed circles.

2.1.3 Reinforcement

Unfilled elastomers do not possess the properties necessary for most commercial applications, hence most commercial elastomers contain substantial amounts of filler. Incorporating fillers into an elastomeric system can lead to improvements in mechanical strength, i.e., the maximum load that can be supported, abrasion resistance, wear resistance and fatigue resistance [13]. The inclusion of fillers leads to the reinforcement of some of the properties of elastomeric material, hence this process is also known as “filler reinforcement”. The inclusion of fillers also gives rise to a range of complex non-linear and hysteretic behaviours, such as the Payne and Mullins effect. These phenomena will be explored in detail in subsequent sections.

Carbon black is the most common reinforcing filler for commercial applications [14]. It offers improvements in mechanical strength, abrasion resistance, wear resistance and electrical properties. It is also low cost and is available in abundance. There are over 40 grades of carbon black mainly in use today, each grade has a different reinforcement capacity. Typically, carbon blacks with the largest surface area provide the highest reinforcement. Other fillers exist, including silica, graphite, carbon nanotubes and many more [13]. Particularly, silica is gaining prominence for tyre applications. This is due to the fact that it offers a lower rolling resistance and therefore

leads to an improvement in fuel economy [15].

The dynamics of the polymer chains in the vicinity of a particle are greatly altered. Polymer chains can interact with the reactive sites on the filler *via* chemisorption, physisorption or covalent bonding, causing the polymer chains to immobilize. These bonds are strong enough to resist dissolution in a solvent. The immobilized polymer is referred to as “bound rubber” and has a glassy behaviour. Alongside the interaction with the polymer chains, the filler particles also interact with each other to form aggregates (several particles fused together). With increasing filler loading, these aggregates cluster together to form agglomerates, and the agglomerates cluster together to form a network. The agglomerates or the filler network can encompass and trap rubber; this rubber is referred to as “occluded rubber”. The aggregates, agglomerates, bound rubber and occluded rubber concepts have been illustrated on Figure 2.8.

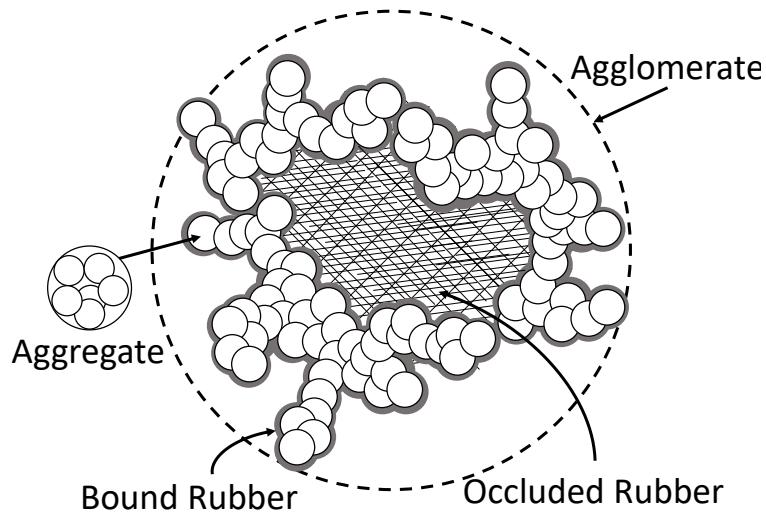


Figure 2.8: A schematic of the bound and occluded rubber concepts. The aggregates (made up of several filler particles) cluster to form agglomerates (made up of aggregates). The rubber interacts with the surface of the filler particles and are bound to the surface (illustrated in grey). The rubber trapped in the agglomerate is known as the occluded rubber. Adapted from [16].

The observed reinforcement of the properties of elastomeric materials from the addition of fillers is attributed to three factors: hydrodynamic effect, rubber-filler interactions and filler-filler interactions. The hydrodynamic

effect is the apparent increase in the modulus and viscosity due to the inclusion of fillers. The filler particles are significantly stiffer than the polymer; approximately three orders of magnitude stiffer. Thus, when the filled elastomers are deformed, the deformation is transferred to the polymer chains. This amplifies the strain of the polymer chains in the vicinity of the filler particles, i.e., the overall strain is less than the local strain. The amplification is described by Einstein-Smallwood [17] function, which is

$$\frac{G}{G_0} = 1 + 2.5\phi \quad (2.5)$$

where ϕ is the volume fraction of the filler material, G is the shear modulus of the filled elastomer and G_0 is the shear modulus of the unfilled elastomer. Eq. 2.5 is only valid for spherical particles with low loading and with a low reinforcement capacity, i.e., small surface area. Several authors have extended eq. 2.5 to account for some interaction between fillers and non-spherical particles [18, 19, 20, 21, 22].

At larger filler loadings, the hydrodynamic effect alone does not account for observed increase in modulus. This is due to the increase in prominence of the filler-filler and filler-polymer interactions, and several authors have extended eq. 2.5 to account for this. Medalia [23] proposed replacing ϕ with the effective volume fraction of filler ϕ' , to capture the impact of immobilized and occluded rubber. In this concept, the immobilized region, along with the occluded rubber and filler, behaves as the filler. For a detailed account of the contributing factors to reinforcement, the readers are referred to the review by Song *et al.* [24].

2.1.4 Technical elastomers

A multitude of elastomer composites are utilised in industry for various applications. The most common materials include natural rubber (NR), ethylene propylene diene rubber (EPDM), butadiene rubber (BR), acrylonitrile-butadiene rubber (NBR), chloroprene rubber (CR) and styrene-butadiene rubber (SBR) [25]. These materials are typically leveraged for the design of cable jacketing, dampers, gaskets, hoses, packers, sealing systems and tyres. As mentioned previously, fillers are typically incorporated into these materials to reinforce their properties. Most common fillers are carbon black and silica. Cords are also used as reinforcement for applications such as tyres,

conveyor belts and hoses [26]. Anisotropic properties can be present in compounds containing cords, depending on their layout. For example, in radial tyres the cords are placed at 90° to the direction of travel and in cross-ply tyres the cords are placed at an angle between -60° and 60° to the direction of travel [26]. Recently, silicone elastomers are gaining momentum for applications such as actuators [27, 28, 29] and biomedical devices [30]. In most cases, the silicone elastomers are based on polydimethylsiloxane (PDMS) and its copolymers.

2.2 Mullins effect

The mechanical properties of rubber and rubber-like materials are observed to change from the first extension as illustrated on Figure 2.9. The term stretch λ introduced on Figure 2.9 refers to one plus the strain ϵ . On initial loading, the stress-stretch response follows path AB. On unloading, the stress-strain response follows path BC. Upon reloading, a difference in the stress-stretch response from the initial loading case can be noted, the response follows path CD instead of path AB. This effect was initially reported by Bouasse and Carrière [31]. Subsequently, an extensive amount of investigation into this effect was carried out by Mullins and co-workers [1, 2, 3, 4], and therefore it came to be known as the Mullins effect (or Mullins phenomenon). The phenomenon is characterised by the observed softening, permanent set (stretch at C minus stretch at A), and induced anisotropy. The characteristics of the Mullins effect are illustrated on Figure 2.10. It should be noted that this phenomenon has been observed in various filled and unfilled materials, and for other modes of deformations [32], i.e., shear, equi-biaxial.

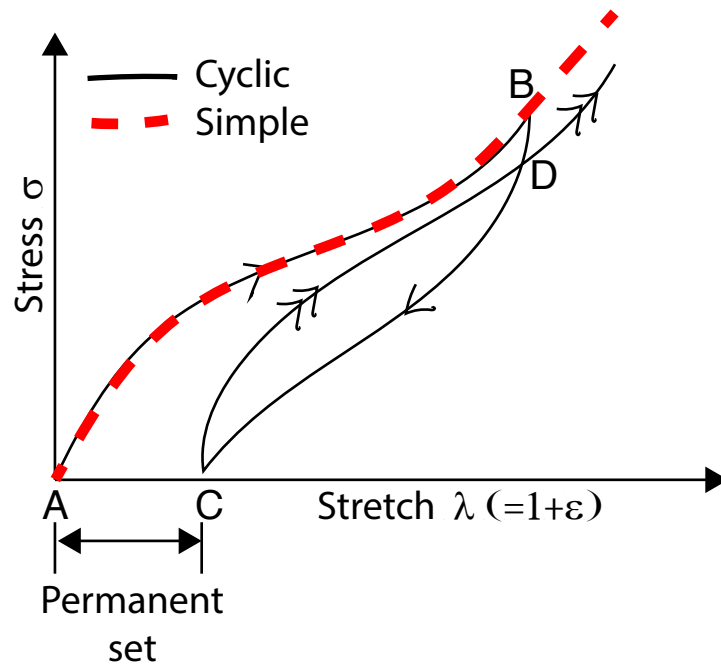


Figure 2.9: Idealised Mullins effect curve

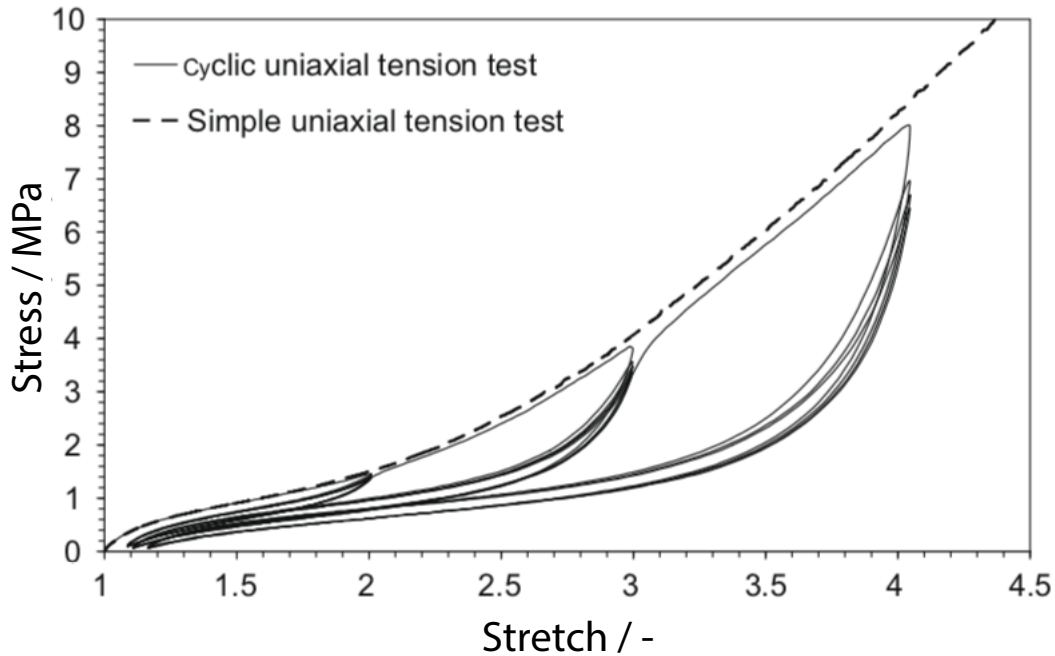


Figure 2.10: Stress-stretch response of a 50 phr carbon black filled SBR subjected to pseudo-cyclic and simple uniaxial tensile tests. The strains in the pseudo-cyclic test were incremented every 5 cycles. Adapted from [32].

2.2.1 Softening effect

A significant softening, characterised by a decrease in stress observed at a given stretch λ , is observed on reloading a given specimen. Minimal softening is observed with subsequent cycles as illustrated by the almost coinciding stress-stretch responses post reloading on Figure 2.10, provided that λ does not exceed the historical maximum stretch λ_{\max} seen by the specimen. When λ exceeds λ_{\max} , the stress-stretch response returns to that of the virgin uniaxial tensile test. The softening increases with increasing λ_{\max} . The aforementioned details can be observed on Figure 2.10.

Initially it was thought that fillers were required to observe the softening. However, Harwood and Payne [4] observed that some Mullins effect was present in pure gums. They argued that softening occurs when unfilled rubbers experience stress equivalent to those of their filled counter parts. This is the reason why the softening effect is often referred as the stress-softening

phenomenon. The incorporation of fillers in rubber greatly amplifies the softening; the amplification is dependent on the reinforcing effect of the filler [33]. Several expressions are proposed in literature to describe the amplification by studying the analogous problem of the increase in viscosity due to the suspension of solid particles [3, 33]. These expressions depend on the modulus of the rubbery matrix, the shape of the particle (i.e. spherical or asymmetric) and the volume concentration of fillers.

2.2.2 Permanent set

On unloading, the elastomer material do not always return to their original dimensions; and when this happens they are said to have been permanently deformed. The unrecoverable λ is termed permanent set stretch, λ_{set} . As illustrated on Figure 2.10, the permanent set is seen to increase with increasing λ . It should be noted that not all of the observed set is permanent, and given time some of the set can be recovered [34]. An increase in temperature will further increase the rate of recovery [34]. Although the illustration in Figure 2.10 is for uniaxial deformation, λ_{set} is also observed in other modes of deformation [35].

Fillers have a significant impact on the magnitude of λ_{set} ; the λ_{set} in unfilled vulcanizates is extremely small [34, 36]. The inclusion of fillers causes a significant increase in λ_{set} [34, 36]; increasing the filler content further increases λ_{set} [36]. Furthermore, for the same filler content per unit volume, Mullins [34] reported that greater set is observed in fillers that are known to give anisotropic properties.

2.2.3 Anisotropy

2.2.3.1 Deformation induced anisotropy

Mullins [1] carried out swelling tests on filled and unfilled natural rubbers to identify the degree of anisotropy that results after stretching. He identified that swelling was uniform for unfilled compounds, indicating that the softening that resulted from the stretching was uniform. Anisotropy produced due to stretching was pronounced for filled vulcanizates, and they were observed to be much softer in the direction of stretching. Recent swelling tests conducted by Fernandes [35] on various filled elastomers subjected to both uniaxial and equi-biaxial tests support the findings by Mullins.

An alternative approach to demonstrate anisotropy was conducted by Machado *et al.* [37] and Mai *et al.* [38] In both cases sheets of filled silicone elastomers were subjected to various strain histories; a set of sub-samples were then cut from these sheets at different angular orientations. These sub-samples were then subjected to uniaxial tensile tests. Machado *et al.* [37] used bulge and uniaxial tensile tests to pre-condition their sheets, whereas uniaxial, constant width and biaxial tests were utilised by Mai *et al.* [38] The bulge tests allows for a complex deformation history, equi-biaxial tension at the pole to planar tension at the border. However, the strain field achieved in this way is inhomogeneous. Nonetheless similar features were observed in both studies; the uniaxial loading responses post pre-conditioning were dependent on the pre-conditioning and orientation. The unloading curves were however independent of the pre-conditioning and the orientation indicating that the same state is attained after subsequent uniaxial loading. The influence of filler volume and the presence of silane coupling agent (SCA) on the induced anisotropy was also explored by Mai *et al.* [38] The induced anisotropy was shown to increase with increasing filler volume and in the presence of SCA.

2.2.3.2 Process induced anisotropy

The most common processes for manufacturing elastomers include compression moulding and rolling. It is well know that the manufacturing process imparts an initial anisotropy within the material. This initial anisotropy was studied by Mullins [34], and he associated the induced anisotropy with the permanent set. In his study, a square piece of filled vulcanizate was stretched in two different directions, direction A and direction B, see schematic on Figure 2.11. By recording the resulting dimensions, he shows that the set is always greater in the direction of stretching, be it direction A or direction B. Furthermore, the resultant sets in the direction parallel to the stretch, perpendicular to the stretch and through thickness are constant after six or more repeats. Most importantly, the difference in set in the directions parallel and perpendicular to the stretch are constant, suggesting that anisotropy present in the filled elastomers prior to the test remains after test.

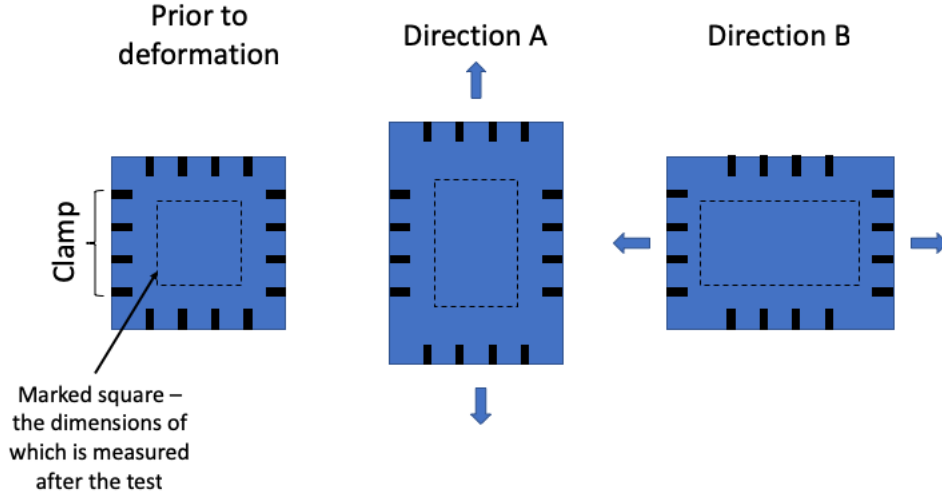


Figure 2.11: A schematic of the test implemented by Mullins [34]. A sheet of rubber six inches square and one-tenth inch thick is clamped on both sides. A one-inch square is marked in the centre of the sheet. The specimen was stretched in direction A, held in position for 15 minutes. Following this the sample was allowed to rest for thirty minutes. The same protocol was implemented in direction B. The dimensions of the marked square were recorded after the rest period.

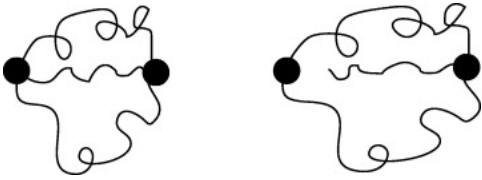
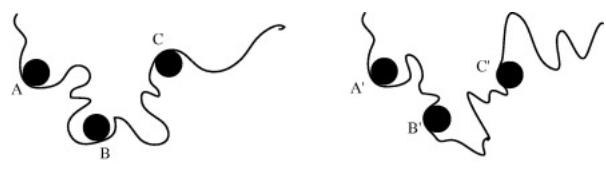
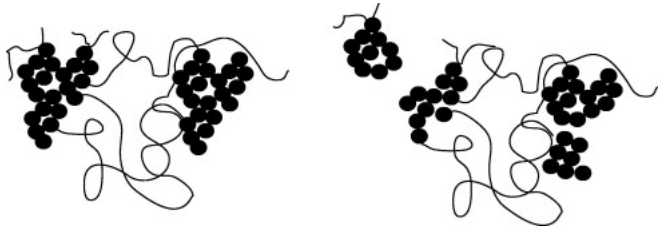
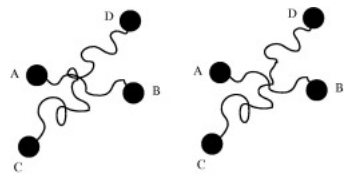
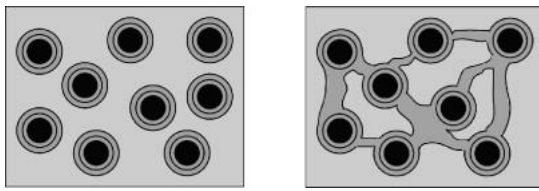
2.2.4 Physical interpretations

Numerous physical interpretations have been proposed in literature for the Mullins effect, including bond rupture, molecule slippage, filler rupture, disentanglement and double layer models. Sketches of these interpretations have been provided in Table 2.1. Diani *et al.* [32] provides a detailed summary of these interpretations, therefore only a brief description of each interpretation will be given here. This section also aims to highlight recent developments in support of the interpretations mentioned above.

Bond rupture

Blanchard and Parkinson [39], Bueche [40], and Govindjee and Simo [45] explained the Mullins effect based on bond rupture. This concept revolves around the rupture of both strong (chemical bonds) and weak bonds (physical bonds). Recently, Clough *et al.* [46] and Wan *et al.* [47] have shown

Table 2.1: Physical interpretations for the Mullins effect. Adapted from Diani *et al.* [32].

Physical Interpretation	Sketch
Bond rupture [39, 40]	
Molecule slippage [41]	
Filler rupture [42]	
Disentanglement [43]	
Double-layer model [44]	

that bond rupture also plays a role in the Mullins effect. Clough *et al.* [46] utilised mechanoluminescent cross-linkers to visualise the bond rupture with increasing strain levels. These cross-linkers emit light on rupture. In this experiment a total of 0.03% (10^{16}) of the mechanoluminescent bonds ruptured, this corresponds to approximately 4.4% of the total hysteresis energy. It should be noted here that other bonds were present in the material including C-C, Si-C and Si-O bond. Although larger dissociation energies correspond to these bonds, it is plausible that some of these bonds were also ruptured. Furthermore, the authors have also shown that bond scission is an anisotropic phenomenon. Wan *et al.* [47] utilised molecular dynamics to simulate a range of different systems to explore the cause of Mullins effect. Their simulation was able to reproduce key features of the Mullins effect. For filled systems with chemical interfacial interactions, the authors have shown that bonds on the chain backbone and bonds on the interface between the fillers and polymers are more likely to break and are responsible for the Mullins effect.

Several authors including Mullins have shown that at elevated temperatures the Mullins effect can be recovered [1, 48]. One argument which confutes the idea of bond rupture is the recovery of Mullins effect [49]. This is supported by the work of Wan *et al.* [47]; they showed that a complete Mullins recovery only occurs if there are no irreversible bond breakages, i.e. no chemical bond breakages. For systems where there is irreversible bond breakage, only a partial recovery is observed. Plagge and Klüppel [50] explored the impact of sulfur and peroxide curing systems on the recovery of Mullins effect, they illustrated that recovery occurs for sulfur cured systems but not for peroxide ones. Unlike chemical bonds, physical bonds can be readily created. Luo *et al.* [51] have observed that chain adsorption occurs at the surface of elevated temperatures *via* NMR.

Molecular slippage

Houwink [41] suggested the theory of molecular slippage, where during the first extension the molecules slip over the surface of the fillers and new bonds are instantaneously created along the chain. This causes a change of material entropy, which could be restored by a temperature increase as discussed above. Recent studies by Wan *et al.* [47], using molecular dynamics, illustrate that for lightly cross-linked systems and for filled systems with physical interfacial interactions molecular slippage is a significant contributor to the

Mullins phenomenon.

Filler rupture

Kraus *et al.* [42], after having conducted tests to confirm that network density and vacuole formation are not the primary cause of the Mullins effect, concluded that the primary cause of stress softening is due to the rupture of the carbon black structure. More recently, Tsujimoto *et al.* [52] implied a connection between the Mullins effect and fillers using Terahertz polarisation spectroscopy. The drawbacks of this theory include the recovery and induced anisotropy of Mullins effect, and the lack of anisotropy in unfilled rubber. By probing the conductivity and Mullins effect of a carbon-black filled SBR, Diaz *et al.* [53] showed that at elevated temperatures the Mullins effect recovered but the conductivity did not. This indicates that the filler network did not recover fully, and hence filler rupture cannot be solely responsible for the Mullins effect. Another supporting evidence is that the anisotropy in the conductivity is small in magnitude compared to the mechanical anisotropy observed as Mullins softening [54].

Disentanglement

Disentanglement theory is proposed by Hanson *et al.* [43]. In his early works, Mullins [55] also suggested that disentanglement played a role in the stress-softening phenomenon. In this theory the stress softening is associated with disentanglements in the direction of the strain. In this interpretation, the number of active chains stays the same, only the entanglement density changes. The recovery is aided by thermal motion which produces new entanglements. This theory accommodates the induced anisotropy. Recently, the characteristic features of Mullins phenomenon, including stress-softening, permanent set and recovery upon exposure to elevated temperature, have been reproduced by Ma *et al.* [56]. They utilised molecular dynamic simulations and argued that disentanglement of polymer chains is responsible for the observed behaviour. They reason that disentanglements are the only molecular interpretation that can explain the recovery of the Mullins phenomenon with exposure to elevated temperature.

A recent study by Song *et al.* [57] provides evidence stating that the Mullins effect is driven by disentanglement. They illustrated that once you account for the strain amplification which arises due to the presence of filler,

the non-affine tube model [58] parameters used to describe the Mullins effect form a master curve indicating that disentanglements are responsible for the stress-softening phenomenon.

Double-layer model

An interface model was suggested by Fukahori [44] in order to explain the mechanics and mechanisms of reinforcement and softening. This model represents the material as aggregates of particles, where a carbon aggregate or agglomerate is surrounded by two layers of uncrosslinked polymer of different molecular mobility. The inner layer is “glassy hard” and the outer layer is “sticky hard”, and these are embedded in a crosslinked rubbery matrix. During the initial loading, the sticky hard layers orient and extend and connect with other sticky hard layers forming a super-network. On unloading it is assumed that the sticky hard layers do not support the stress and instead the rubber matrix supports it. When reloading, if the stretch does not exceed the stretch previously seen, the rubber matrix continues to support the stress. When the current stretch exceeds the previously seen stretch the super-network returns to the previously extended state and supports the stress. Mullins recovery is attributed to the entropic forces in the super-network structure.

Although not a dominant cause of the Mullins effect, it is widely accepted that vacuole formation takes place in filled rubber systems [42, 59]. The formation of these voids does not dissipate significant energy, however they do bare some similarities with the Mullins effect. Zhang *et al.* [59] show that the formation of voids is strain/stress history dependent. Thus, they must contribute to the large energy dissipation observed on initial loading.

Overall, there have been some recent advances in this area. Based on the review above it is clear that a multitude of interactions are responsible for the different features observed. The prominence of one interpretation over another seems to be dictated by the elastomer system in question.

2.3 Payne effect

The Payne effect, also known as the Fletcher-Gent effect, describes the variation of the dynamic properties of rubber compounds with dynamic strains.

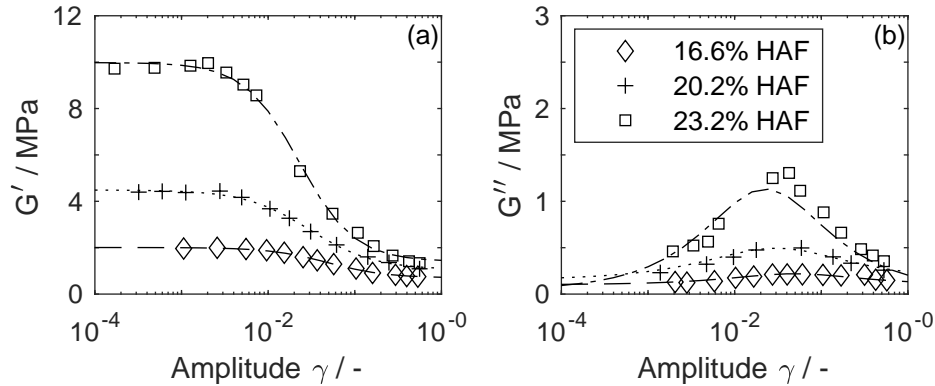


Figure 2.12: The response of carbon black filled rubber systems to dynamic oscillations. The complex modulus has been decomposed into its components, the a) storage and the b) loss modulus. Adapted from [62].

The effect is named so due to the extensive work carried out on this phenomenon by A. R. Payne [60, 61, 62, 63], W. P. Fletcher and A. N. Gent [64]. The Payne effect is characterised by a decrease in storage modulus from a zero amplitude plateau value to a large amplitude plateau value with increasing strain. The zero-amplitude plateau region is observed at small strains ($< 0.1\%$). A pronounced peak is observed in the loss modulus. The characteristic behaviour of the Payne effect has been illustrated on Figure 2.12. The Payne (or Fletcher-Gent) effect, unlike the Mullins effect, is a recoverable and reversible effect. It should be noted that this phenomenon is also observed for other composite systems [63, 65].

2.3.1 Physical interpretation

This phenomenon is primarily associated with the presence of fillers [63, 65]. Payne and Whittaker [63] also show that increasing vulcanization does not impact the difference between the zero amplitude and large amplitude plateau value of the storage modulus, demonstrating that the effect is not associated with the gum phase. Several interpretations for the cause of the Payne effect have been presented in the literature. Payne argued that this phenomenon occurs due to the breakdown and the reformation of van der Waals bonds within filler network structures [65, 66].

Alternatively, Maier and Göritz [67] suggested that the phenomenon oc-

curs due to rubber-filler interactions. Several studies provide experimental evidence to suggest that filler-filler interactions are not essential in order to observe the Payne effect. A study by Chazeau *et al.* [68] shows that agglomeration is not necessary for the Payne effect as a larger difference between the large and small strain storage modulus plateau was observed on a sample with higher dispersion and lower agglomeration, in comparison with a sample with more agglomeration. Yang *et al.* [69] show that regardless of the filler type and content, a normalised storage modulus forms a master curve once the strain amplification due to fillers is taken into account. A complete overlap of the loss modulus is not observed; the peak of the loss modulus increases with increasing filler amount. This is attributed to additional friction due to the presence of fillers. However, the peak occurs at a constant microscopic strain suggesting that this is a matrix-dominated process.

The Payne effect has also been interpreted using jamming physics. The jamming aspect relates to the progressive structural arrest occurring during filler particle flocculation and the Payne effect and recovery occurs due to the unjamming process. The jamming phenomenon is observed in a multitude of systems, including but not limited to granular media, colloidal suspensions, molecular structure, polymer-filler composites and traffic jams [70, 71]

2.4 Constitutive modelling

Constitutive models are a critical element in the design process of elastomeric products to simulate the in-service behaviour during their life cycle. Elastomers exhibit complex phenomena such as viscoelasticity, the Mullins effect and Payne (or Fletcher-Gent) effect; these pose a challenge in the development of constitutive models. Numerous models have been presented in literature to attempt to describe these phenomena; this section will review some relevant models.

2.4.1 Network elasticity

The affine and phantom models, as detailed in section 2.1.2, are the most basic models that describe network elasticity. However, these models are limited and the limitation of these models are best expressed by the Mooney plot whose axes are the reduced force $[f^*]$ ($= \sigma/(\lambda - \lambda^{-2})$, where σ is the stress) and $1/\lambda$. The reduced force can be obtained by resolving eq. 2.3 and

2.4 for the case of simple tension. Once the material incompressibility, i.e., $\lambda_1\lambda_2\lambda_3 = 1$, and symmetry of deformation are considered, the resulting deformations in the λ_1 , λ_2 and λ_3 directions are $\lambda^{-1/2}$, $\lambda^{-1/2}$ and λ , respectively [8, 9]. By substituting for λ_1 , λ_2 and λ_3 , and by applying the thermodynamic relation

$$f = \left(\frac{\partial\Delta A_{el}}{\partial L}\right)_T \quad (2.6)$$

for force f acting on a network can be determined. The subscript T in the above equation refers to constant temperature and L is the length of the specimen. σ is then determined by dividing by the nominal cross-sectional area A_0 . For an affine network, this results in

$$\sigma = \frac{\nu kT}{V_0}(\lambda - \lambda^{-2}) \quad (2.7)$$

where V_0 is the initial nominal volume of the specimen. It can be shown $\nu kT/V_0$ is equivalent to shear modulus G_{affine} of the affine network. Similarly, the shear modulus G_{phantom} of the phantom network can be shown to be $\xi kT/V_0$. $[f^*]$ is therefore equal to the shear modulus. For details, readers are referred to the text by Erman and Treloar [8, 9]. A Mooney plot for an elastomeric specimen subjected to a simple tension experiment is illustrated in Figure 2.13. The experimental data highlights that $[f^*]$ decreases with increasing extension and compression. At large extensions an upturn in the experimental data is noticeable. The affine and phantom models predict a constant $[f^*]$. The affine model prediction matches the experimental data at small extensions and compressions, whilst the value obtained from the phantom model produces a better approximation at larger extensions.

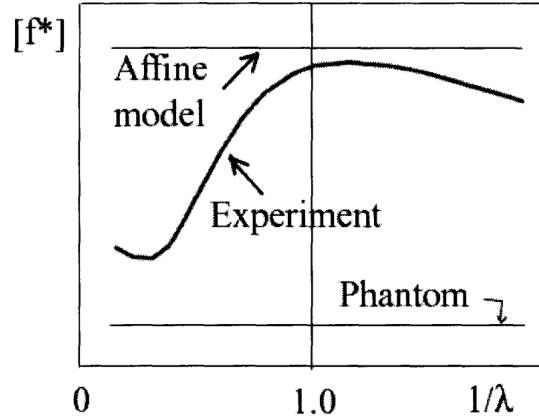


Figure 2.13: A Mooney plot of an elastomeric specimen subjected to a simple tension test. The results obtained from affine and phantom network models are compared with experimental data.[8]

2.4.2 Hyperelastic models

The affine and phantom models were obtained *via* statistical treatment of polymer chains [9]. These models have their limitations as presented in the previous section. Elastomers are also described using finite hyperelastic theory; the stress-strain relationships are derived from strain-energy density W functions. These functions are equivalent to or better at predicting the observed non-linearity than the affine and phantom models. The functions presented within assume that the material is incompressible and isotropic. Incompressibility is a typical assumption for many polymeric materials, as these materials can sustain deformations without noticeable change in volume [72]. Models describing anisotropy will be discussed in a subsequent section.

Several hyperelastic models have been proposed in the literature; however these are often phenomenological in nature. The phenomenological approach is primarily concerned with fitting mathematical equations to experimental data. Models of the phenomenological nature include the Ogden [73, 72, 74], Mooney-Rivlin [9, 72, 74, 75, 76, 77] and Yeoh [72, 74, 78] functions. The phenomenological models stated above reduce to the affine (or neo-Hookean) model for specific values of the constants. These functions are popular and widely used, and are often incorporated as standard in finite element software.

The models proposed by Arruda and Boyce [72, 74, 79], and Edwards

and Vilgis [80] are an alternative to the phenomenological approach. The Arruda-Boyce model is based on the statistical treatment of polymer chains, however, unlike the affine and phantom models this model is able to capture the finite chain extensibility of the chain. The finite chain extensibility refers to the maximum extension achievable by a polymer chain, at this point the force required for any further extension approaches infinity. The finite chain extensibility is included *via* the means of the Langevin function.

The Edwards-Vilgis (EV) [80] function is physically motivated; the EV parameters can be related back to the various features of the network including cross-links density, entanglements, entanglement mobility and finite chain extensibility. Unlike the aforementioned approaches, the EV function decouples the network density into cross-links and entanglements. To account for the entanglements, the simplified concept of slip-links is introduced. The slip-links can be pictured as a ring that traverse along the polymer chains. This was integrated into the theory by modifying the cross-links to allow slip-page along the arc length of a polymer chain. The finite chain extensibility is incorporated *via* the tube concept. The tube is formed from neighbouring chains that surround one particular chain as shown on Figure 2.14. The whole network can therefore be imagined as a system of tubes containing each polymer chain. The length of each tube (the primitive path) is determined using a random walk. During deformation, the tube length increase and approach the contour length of the corresponding polymer chain. The amount of slack, i.e., the difference between the contour and tube lengths, determines the maximum extension. The strain energy W of the EV function is given by

$$W = W_C + W_S \quad (2.8)$$

$$W_S = \frac{1}{2} N_S k T \left\{ \sum_{i=1}^3 \left\{ \frac{\lambda_i^2 (1 - \alpha^2) (1 + \eta)}{(1 - \alpha^2 \sum \lambda_i^2) (1 + \eta \lambda_i^2)} + \log(1 + \eta \lambda_i^2) \right\} + \log(1 - \alpha^2 \sum_{i=1}^3 \lambda_i^2) \right\} \quad (2.9)$$

$$W_C = \frac{1}{2} N_C k T \left\{ \frac{\sum_{i=1}^3 \lambda_i^2 (1 - \alpha^2)}{1 - \alpha^2 \sum_{i=1}^3 \lambda_i^2} + \log(1 - \alpha^2 \sum_{i=1}^3 \lambda_i^2) \right\} \quad (2.10)$$

where W_C is the strain energy density due to cross-links, W_S is the strain energy density due to slip-links, N_C is the density of cross-links, N_S is the



Figure 2.14: An illustration of the tube model concept. Entanglements form the tube and the centre of the tube is represented as dashed lines. The solid line represents a polymer chain that has been cross-linked at its ends. The hollow circles represent other polymer chains that are perpendicular to the surface of the tube. Adapted from [80].

density of slip-links, α is a measure of inextensibility, η is a measure of slippage and λ_i represents the principle stretches λ_1 , λ_2 and λ_3 in the x, y and z directions, respectively.

2.4.3 Viscoelasticity

Elastomers are viscoelastic in nature; the stress-strain response is strain rate dependent. Although the rubber elastic and hyperelastic models maybe sufficient to describe the elastic behaviour of the elastomer, they do not capture an elastomer's viscous nature. Viscoelasticity is characterised by:

- Creep - A gradual increase in strain over time in response to constant applied stress
- Stress relaxation - A gradual decrease in stress over time in response to a constant applied strain
- Hysteresis - Deviation in the load-unload response due to frictional effects, i.e. internal friction

The characteristic behaviour of a viscoelastic material can be described using idealised mathematical models based on combinations of springs and

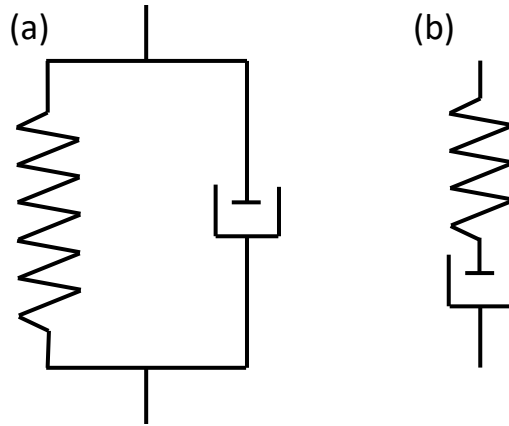


Figure 2.15: A representation of a) Kelvin, and b) Maxwell models.

dashpots. The dashpot represents the viscous component and the spring element represents the elastic component. One can generate the Kelvin and Maxwell models by the amalgamation of linear elements. They are the most basic linear viscoelastic models and can be observed on Figure 2.15. These models are insufficient to describe the characteristic viscoelastic behaviour, i.e. the Kelvin model is insufficient to describe stress-relaxation and the Maxwell model is insufficient to describe creep. However, they can be used as building blocks to form more complex models, including the standard linear solid (or Zener) model, and can include non-linear elements.

2.4.4 Mullins effect models

Several models have been proposed to describe the behaviour exhibited by the Mullins phenomenon. These can be categorised into phenomenological, physical and macromolecular models.

2.4.4.1 Phenomenological models

Phenomenological models are predictive models which are based on experimental outcomes and observations; there is no physical basis for these models. Many phenomenological models are based on Simo's [81] approach of multiplying the classic strain energy density (or hyperelastic) function $W(\mathbf{F})$ by a reducing parameter:

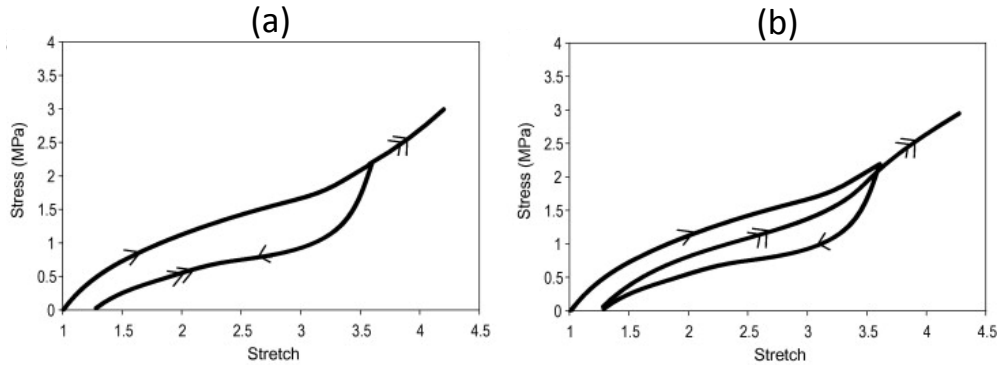


Figure 2.16: The two idealisations of the Mullins phenomenon; a) the reloading response coincides with the unloading response and, b) the unloading and reloading responses differ. Adapted from [32]

$$W_R(\mathbf{F}) = (1 - d)W(\mathbf{F}) \quad (2.11)$$

where \mathbf{F} is the deformation gradient, $W_R(\mathbf{F})$ is the reduced strain energy density function and d is the damage variable. The reduction factor $(1 - d)$ was first proposed by Kachanov [82] to model creep rupture of metals.

There are two different idealisations of the mechanical behaviour of rubbers subjected to Mullins softening:

- 1) Reloading response coincides with the unloading response
- 2) Reloading and unloading response differs

These behaviours have been illustrated on Figure 2.16. Following the naming convention of Diani *et al.* [32], these models will be referred to as the first and second class of models, respectively. Although elastomeric materials do exhibit differing reloading and unloading response, the first class of models are simpler and still describe the major dissipation mechanism and irreversible rearrangement of the structure [72].

2.4.4.1.1 First class of models

Ogden and Roxburgh [83] suggested a model based on the first idealisation. This model is a pseudo-elastic model; the strain energy function, alongside \mathbf{F} , is also governed by an additional scalar variable. The scalar variable which

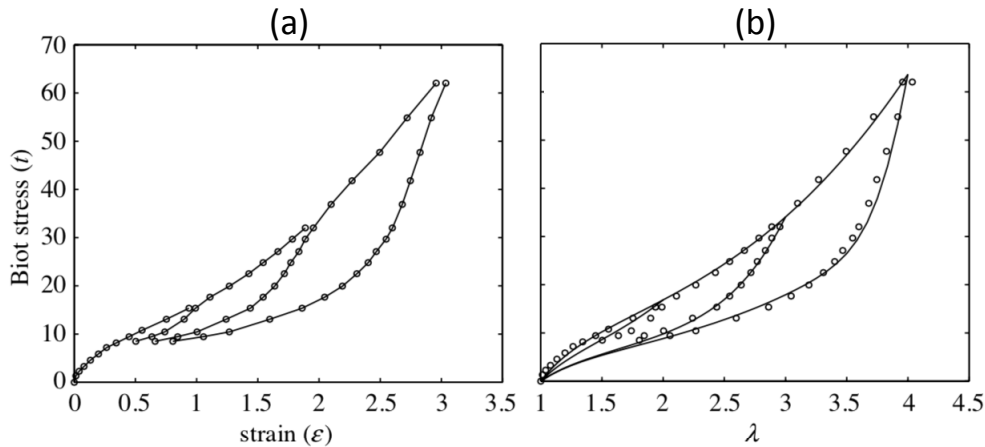


Figure 2.17: a) Experimental tensile data obtained by Mullins and Tobin [2], and b) the pseudo-elastic theory proposed by Ogden and Roxburgh [83] fitted to the experimental data using a non-linear least-squares solution. Adapted from [83].

is responsible for the damage sustained by the material is governed by the maximum energy state. Numerical studies were conducted to illustrate the response of their theory to pure shear and simple tension, the neo-Hookean and Ogden strain energy functions were used for this purpose. For the case of simple tension, the pseudo-elastic theory was fitted to the tensile data obtained by Mullins and Tobin [2] using a non-linear least-squares approach. It should be noted that the data had been adjusted by subtracting the permanent set from the length measurement. The results are illustrated on Figure 2.17. A good fit is obtained from the pseudo-elastic theory.

Qi and Boyce [84] proposed a model based on the concept suggested by Mullins and Tobin [2]. They conceived the concept of two phases; a hard phase and a soft phase. The hard phase consists of filler and occluded rubber, the release of which results in the softening behaviour. The strain energy function used in this instance is the 8-chain Arruda-Boyce model [79]. To capture the amplification due to rigid particle fillers an amplification factor was imposed on the material stretch, see section 2.1.3. The amplification decreases as the occluded rubber is released. The release of the occluded rubber commences when the amplified stretch exceeds the previous maximum. Once the amplified stretch reaches the limiting stretch of the chain, i.e. finite extensibility, the saturation point for occluded rubber is reached and no further evolution takes place. A model utilising the concept of oc-

cluded rubber was also implemented by Fernandes [35] to study the energy dissipated due to different modes of deformations. This model was simpler as a Gaussian strain energy function was utilised. However, unlike Qi and Boyce who obtain their parameters by fitting to data, the parameters obtained by Fernandes [35] were *via* experimental or theoretical means.

More recently, De Focatiis and Rahmeh [85] suggested a model where N -Langevin chains were mapped onto a unit sphere. The sphere is formed *via* triangulation, see Figure 2.18. An eighth of a triangulated sphere is utilised to highlight the chains (in red). The chains extend from center of the sphere to the centroid of the triangle. This model extends the ideas of the 3-chain [86], 4-chain [87] and the 8-chain [79] models. These models have also been illustrated on Figure 2.18. These models allow for the single chain idea to be translated numerically into 3D deformations. The 3, 4 and 8 chain models consist of two parameters: the number of chains per unit volume and the average number of links per chain. These models can be extended to capture the Mullins effect by the addition of evolving damage parameters. The model proposed by De Focatiis and Rahmeh [85] consists of three parameters: the number of chains per unit volume, the average number of links per chain and a distribution parameter. The damage criterion for the proposed model is simple, the chains break when they reach the finite extensibility of the given chain. This model is able to successfully capture some aspects of the Mullins phenomenon with a minimal number of parameters.

2.4.4.1.2 Second class of models

The second class of models have a differing reloading and unloading behaviour, they reflect the real behaviour of elastomeric materials. This behaviour is achieved by utilising a viscoelastic framework similar to that specified in section 2.4.3 with modifications. Numerous models have proposed models using this framework, including Miehe and Kech [88], Kaliske *et al.* [89], Lin *et al.* [90] and Diani *et al.* [91] to name a few. For these cases, the framework is modified by the replacing the linear spring element with of a spring element whose behaviour is described by a strain energy function $W(\mathbf{F})$. Largely, these authors have used strain energy functions that were described in the preceding sections. In some instances the linear viscous element has also been replaced with an alternative descriptor, i.e. a phenomenological non-linear viscoelastic function was implemented by Miehe and Kech [88]. For the aforementioned models, the damage is described by

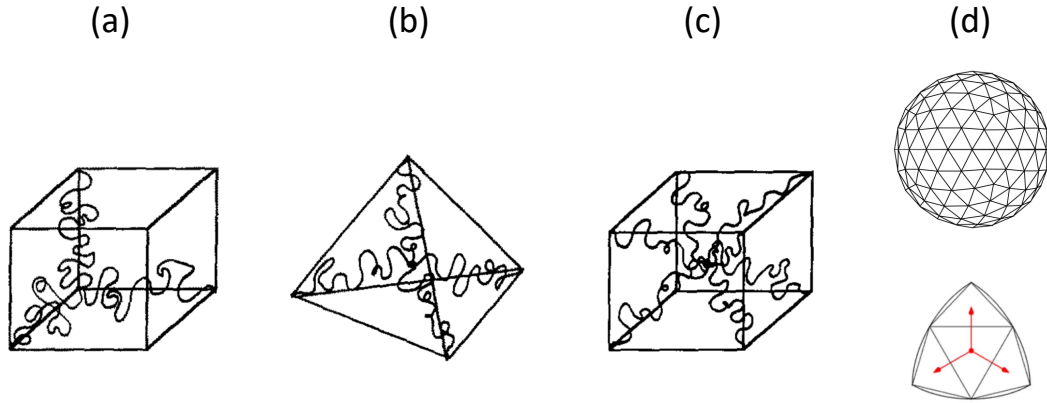


Figure 2.18: The a) 3-chain network [86], b) 4-chain [87], c) 8-chain [79] and d) N -chain models [85]. A triangulated section of the sphere is provided for the N -chain model to illustrate the chains (in red). The 3, 4 and 8 chain diagram were adapted from [79], and the triangulated sphere diagram was adapted from [85].

a continuous and a discontinuous variable. The driving force for damage is usually the maximum strain of the strain history. Several alternative definitions have been prescribed in literature to describe the evolution of the damage, these have been documented carefully by Diani *et al.* [32]. However, on a fundamental level, these variables can be traced back to the strain (or stretch).

An alternative approach was proposed by Besdo and Ihlemann [92] employing two curves. These curves were defined using the experimental data, and hence evolve with strain and cycles. Although simplistic, the model derived *via* this approach was able to reproduce many of the expected features.

2.4.4.2 Macromolecular models

Macromolecular models are based on physical interpretations, see section 2.2.4. Govindjee and Simo [45] proposed a constitutive model based on the bond rupture physical interpretation. The bonds that rupture are the bonds between the filler particle and the polymer chain as they assume that the carbon-carbon backbone of the polymer chain is much stronger. In their work, the strain energy was decomposed into the strain energy corresponding to a typical cross-linked network and the strain energy corresponding

to the polymer chains that interact with the filler particles. Although this model is based on a physical interpretation, the damage is achieved using a phenomenological parameter, the largest eigenvalue of the deformation gradient. Furthermore, this is an isotropic model and also does not account for the differing unloading-reloading response, i.e., idealised Mullins effect, or the residual strain. To account for anisotropy, Göktepe and Miehe [93] extended Govindjee and Simo’s model [45] by using 21 material directions, each with its own damage parameter.

Marckmann *et al.* [94] implemented a network alteration model based on bond rupture (i.e. weak integrations and cross-links). This model depends of two parameters; the average number of monomer segments N in a polymer chain and the average number of active chains n per unit volume. As the bond break, N increases as the number of junction points between the chains decreases. The parameter N is described by a linear function of the maximum pre-deformation seen by the network and is determined empirically. As N increases, the average number of active chains n decreases, causing a softening of the network. While this model is only dependent on two parameters, it does not account for the viscous effects and the residual strain.

Klüppel and Schramm [58] proposed an isotropic model based on the irreversible breakage of filler clusters. The breakage of filler clusters was incorporated *via* the concept pre-deformation dependent strain-amplification factor; the strain-amplification factor decreases exponentially with increasing pre-deformation. The elastomer network is captured using the tube model [95]. Unlike the aforementioned macromolecular models, this model uses the physical motivated strain-amplification factor as a damage variable. However, this parameter cannot yet be measured experimentally.

A model based on the molecular slippage theory was suggested by Kilian *et al.* [96]. They argued that reinforcement is due to the local strain of the rubber molecules trapped between the filler particles. The local strains are significantly larger than the macroscopic strains, i.e., strain amplification, this enforces the irreversible chain slippage. This model is capable of capturing the stress-strain response of elastomer under uniaxial tension and compression, and the residual strains. Twelve parameters are essential for this model and they are difficult to interpret.

Although the models presented above are based on physical interpretations, some of them still contain parameters which are phenomenological [45, 93]. Even in the instances where all the parameters are physically motivated, difficulties exist in obtaining a quantitative measure of these parameters [58],

i.e., the technology or the methodology to identify these parameters do not yet exist. In the instances where the parameters can be measured, the measured value do not always match the fitted value [94].

2.4.4.3 Permanent set

Alongside stress-softening, many elastomers exhibit a residual strain (or permanent set) upon load removal [34]. A number of different approaches have been proposed in the literature to capture the residual strain. One formulation is an extension of Simo's theory [81] and includes an additional reducing parameter. This approach was used by Dorfmann and Ogden [36], and by Peña [97]. Maher *et al.* [98] suggested an alternative approach where an additive split of stress tensor is used to introduce set. In this approach the stress is divided into a stress-softened damage tensor and an inelastic stress tensor (the tensor responsible for set). As the strain increases, the inelastic component becomes an additive negative stress, i.e. a negative stress is observed at a strain of zero; this is analogous to having a residual strain at zero stress. Lastly, the N -chain model recently proposed by De Focatiis and Rahmeh [85] (see section 2.4.4.1.1) naturally gives rise to a permanent deformation due to a distribution of broken chains and hence a shift in the equilibrium configuration.

2.4.4.4 Anisotropy

It is clear that both processing and deformation of elastomers leads to anisotropic behaviour. Few constitutive models have been proposed in literature to capture the induced anisotropy, and they primarily rely on the concept of material directions [85, 91, 93, 98, 99]. For these models, the damage incurred in each material direction depends on the experiment (test type and direction). This results in an anisotropic distribution of damage, hence an anisotropic material behaviour.

2.4.5 Payne effect

Several models have been proposed in literature to describe the Payne effect. Kraus [68, 100, 101] proposed a phenomenological model based on the breakdown and reformation of filler aggregates assuming van der Waals type

interaction between particles. The Kraus equation describing the storage and loss modulus is

$$\frac{G'(\gamma) - G'_\infty}{G'_0 - G'_\infty} = \frac{1}{1 + (\frac{\gamma}{\gamma_c})^{2m}} \quad (2.12)$$

$$\frac{G''(\gamma) - G''_\infty}{G''_M - G''_\infty} = \frac{2(\frac{\gamma}{\gamma_c})^m}{1 + (\frac{\gamma}{\gamma_c})^{2m}} \quad (2.13)$$

where γ is the shear strain, $G'(\gamma)$ and $G''(\gamma)$ are the strain dependent storage and loss modulus, respectively, G'_0 is the modulus at small strains, G'_∞ and G''_∞ are the storage and loss modulus at large strains, respectively, G''_M is the maximum loss modulus, γ_c is the critical strain at which $G'_0 - G'_\infty$ reaches half its value or the strain at which half the van der Waals type interaction between the filler aggregates have been broken, and m is a constant which describes the rate at which the van der Waals interactions are broken.

Huber *et al.* [66] proposed a model based on the assumption that the filler network is fractal and can be described by correlation similar to that of the percolation model. The resulting equations are identical to those of Kraus' model. However, in the Kraus model the exponent m was purely empirical, whereas in this model the parameter is determined by the structural properties of the filler network [65, 101].

Recently, Stöckelhuber *et al.* [102] proposed a model to describe the Payne effect by utilising the Schelling segregation model from game theory. This model simply utilises the work of adhesion between the filler particles and the polymer to explain the filler behaviour in polymers. The model illustrates that at low thermal energies the particles do not have enough driving force to move, as the thermal energy increases a network like structure is formed in a similar fashion to that observed for filled elastomers. Numerous other models exist in literature, some of which can be found in review by Heinrich *et al.* [65]

2.5 Research opportunities

The review presented in this chapter has highlighted that a significant amount of work has been invested in studying the different phenomena observed in elastomeric materials, namely the Mullins and Payne effect. On the basis of this review, one can appreciate that a host of reasons are responsible for the

observed phenomena and the prominence of a given physical interpretation depends on the system in question. Typically these phenomena are investigated in isolation and to the authors knowledge no worker has probed the interaction between the two phenomena, i.e. the impact of pre-deformation of the Payne effect. In this work, an effort has been made to understand the interaction between these phenomena, and how these interactions are influenced by the amount and type of fillers.

Numerous models have been proposed in the literature, these models are either phenomenological or macromolecular in nature. In most constitutive equations the fillers are coupled into the strain energy function. In some instances, a strain amplification factor is used to account for the presence of fillers. However, there are shortcomings to this approach as presented in the review above. The constitutive models usually focus on a given phenomenon, and in most cases do not capture all the characteristics of the phenomenon. For example, only a handful of the stress softening models can capture the permanent deformation and anisotropy induced by the phenomena. To this date, there are no models capable of capturing all the non-linearities exhibited elastomeric materials. Nonetheless, numerous insights obtained *via* thought and practical experiments await to be implemented as constitutive models. Although these avenues may not lead to a definitive solution, they may take us a step further.

Research into soft materials and additive manufacture of these materials is gaining momentum. The applications of target for these materials include actuators, sensors, conductors and biomedical devices. The opportunities here range from developing materials suitable for a specific application to the manufacturing process.

2.6 Aims and objective

The aim of this project is to contribute to the development of models and modelling frameworks suitable for predicting elastomer mechanical performance under a range of conditions. The particular aspects of focus are the influence of the elastomer network, of the deformation history (or Mullins effect) and of the choice of filler on the mechanical response of elastomers.

This is broken down into three objectives.

1. A set of novel unfilled silicone-acrylate elastomers will be used to study the impact of the elastomer network on the mechanical response of elas-

tomers. The silicone to acrylate ratio is varied in these materials. To understand the impact of the different ratios on the underlying network structure, a set of experiments will be performed, including simple uniaxial tensile tests. Subsequently, hyperelastic functions will be fitted to the experimental data to see how the function parameters vary with composition. The insights drawn from the experimental data, and subsequent analysis, will be utilised to develop a modelling framework and a model to predict the mechanical response of materials of this kind.

2. Sheet rolled ethylene propylene diene rubber (EPDM) specimens will be subjected to a range of uniaxial cyclic tensile tests to probe the impact of deformation history on the mechanical response of elastomers. The deformation history is applied during the initial loading portion of the cyclic test. The subsequent cycles, more specifically the elastic and viscous components of the third unload/reload cycle, will be utilised to study the impact of this pre-deformation on the mechanical response of elastomers. From the experimental findings, a modelling framework will be developed to predict the impact of deformation history on the mechanical response. The ability of such a modelling framework and a model to predict the mechanical response of other elastomers subjected to a deformation history will also be explored.
3. Styrene-butadiene rubber (SBR) compounds filled with different types and amounts of carbon black will be subjected to small strain dynamic mechanical tests to study the impact of fillers on the small strain dynamic response, i.e., the Payne effect. Alongside fillers, the impact of pre-deformation and static loading will be studied by combining dynamic torsional mechanical tests with uniaxial cyclic tensile tests. To better understand the experimental data, the well-known Kraus model will be fitted to the data and the evolution of the Kraus model parameters with fillers and pre-deformation will be studied in detail. The learnings will subsequently be used to develop models to predict the small strain dynamic response (or Payne effect) as a function of filler choice and pre-deformation.

3. The influence of network structure on the mechanical response

The aim of this chapter is to understand the impact of network structure on the mechanical response, and subsequently to model it. For this purpose, a set of simple novel unfilled silicone-acrylate elastomer systems are utilised. In these elastomers, the silicone to acrylate ratio is varied and this leads to a variation in the network structure. The impact of the different ratios on the key features of the network, including network density, entanglement mobility and finite chain extensibility, and therefore on the resulting mechanical response is studied. The physically motivated Edwards-Vilgis (EV) model is used for this purpose. The observations are then utilised to predict the mechanical properties, i.e., secant modulus, for a given silicon-acrylate ratio.

The material preparation process is presented in section 3.2. In section 3.3, the test protocols required for the mechanical and thermal characterisation of the prepared materials are presented. The experimental results and the model development are presented and discussed in section 3.4. Lastly, a summary of the most important findings are presented in section 3.5.

This work is to be submitted for publication in the peer reviewed Journal of Materials & Design.

3.1 Introduction

Developments in additive manufacturing (AM) technology, particularly jetting (three-dimensional (3D) printing), has invited research interests from the elastomer community due to the flexibility it offers over traditional manufacturing methods such as moulding [103, 104, 105, 106]. Jetting technique uses a layer-by-layer approach to produce complex structures, this technique

also allows for the deposition of different materials at each voxel [107, 108]. The challenges here include, and are not limited to, the development of suitable materials and the optimisation of the jetting process.

Silicone elastomers are members of the organosilicone compounds family and can be obtained by cross-linking functionalised PDMS in the presence of either a catalyst and high temperature, or a photoinitiator and ultraviolet (UV) light at room temperature. The chemical structure of silicone elastomers makes them useful for a wide variety of applications, including encapsulation of electronics, stretchable electronics, energy absorption and thermal insulation [109, 110, 111, 112]. Their softness and biocompatibility, i.e., interacting with living tissues in a safe manner, also makes them suitable for soft robotics [29] and biomedical [30] applications.

Several temperature cured silicone systems, compatible with AM techniques, have been investigated in literature [113, 114, 115]. The disadvantage of using a temperature cured system is with regards to its shelf life and processing, as even a small rise in temperature can cause a reaction, thus blocking the nozzle. UV cured silicone materials are an alternative. The main silicone suppliers such as Momentive, Novagard, Wacker, Bluestar Silicones, and Shin-Etsu are offering various types of UV curable silicones [116, 117, 118, 119, 120]. Commercially available silicone are restrictive as their structure cannot be altered to tune the mechanical properties for a given application.

In this chapter, a simple UV light curable silicone-based unfilled elastomer system for the purpose of 3D printing is developed. The variations in the mechanical properties when the composition, and consequently the structure of the material is varied is then explored. Subsequently, a model is developed to describe the variation in the mechanical properties with varying composition.

3.2 Material preparation

3.2.1 Ink preparation

In additive manufacturing, particularly in Jetting, the materials prior to cure are referred to as ink owing to their low viscosity. The ink used in this work were synthesised by Dr A. Foerster from the additive manufacturing group at the University of Nottingham. They were formed by react-

ing methacryloxypropyl terminated polydimethylsiloxane (PDMS-MA) with molecular weight M_w of 25000 g/mol with 2-ethyl hexyl acrylate (EHA) with a M_w of 184.27 g/mol in the presence of Irgacure 819 photoinitiator. Figure 3.1 illustrates the molecular structure of the acrylate monomer, silicone oligomer and the photoinitiator used in the formulations. EHA acts as a reactive diluent due to its low molecular weight and the presence of an acrylate group available for cross-linking with PDMS-MA. The PDMS-MA and EHA were mixed in different ratios, namely 30/70, 40/60, 50/50, 60/40 and 70/30, and 1 wt% of Irgacure was added. A simple novel UV curable silicone-based system, absent of fillers, has been presented herein.

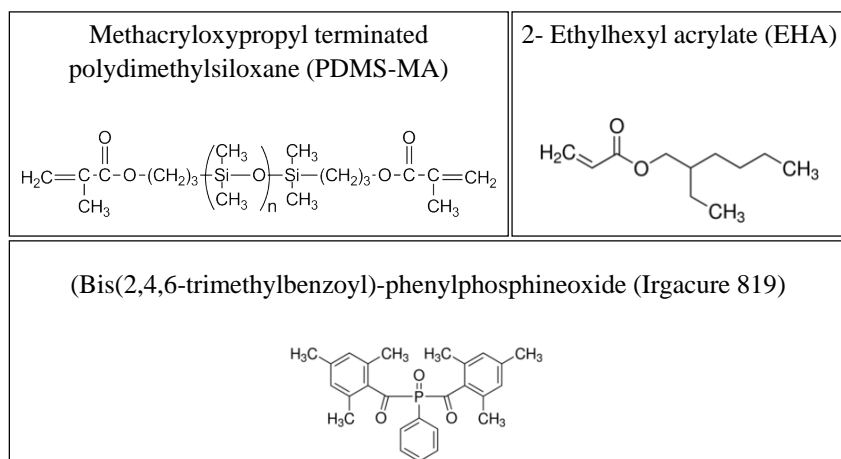


Figure 3.1: Molecular structure of the UV curable ink components.

3.2.2 Casting setup

Cast samples were prepared by transferring 0.3 ml of the pre-mixed ink into an aluminium mould of dimensions 40 mm \times 10 mm \times 1.5 mm (length \times width \times thickness) and cured for 30 seconds using Phiseon's FireEdge FE400 UV light set at 5% intensity. This UV light has a nominal flux density (radiant power per unit area) of 8 W cm⁻² at 100% intensity and a wavelength of 395 nm. The distance between the mould and the UV light was \sim 10 mm.

3.2.3 Jetting setup (3D printing)

Jetting is an additive manufacturing process that is similar to that of the typical inkjet printer. A low viscosity ink (or material) is deposited onto the build surface and cured one layer at a time. The ink is typically temperature or UV light cured. In this work, a custom setup was utilised for the jetting process, consisting of a movable stage synchronised with stationary Nordson EFD jetting valves. The jetting time is controlled by a PicoTouch controller (Nordson EFD). Compressed air is used to push the build material placed in the fluid container towards the nozzle and piezoelectric actuators are used to control the opening and closing of the nozzle.

Firstly, the fluid is pressurised up to 6 bars and injected onto the jetting chamber. Subsequently, the piezo-electrically driven ceramic rod terminated with a sealing ball is oscillated according to the printing signal (up to 500 Hz), opening and closing the nozzle as shown on Figure 3.2. The nozzle is open when the rod is in its upper position, allowing the pressurised fluid to flow through the nozzle. The nozzle is closed when the rod is in its lower position. The closing of the nozzle also provides the fluid with enough kinetic energy to allow it to break from the nozzle and travel towards the substrate, where it forms a dot. For the purpose of this work close, pulse and cycle times of 0.40 ms, 0.67 ms, and 5 ms respectively were utilised. These values are user defined and are based on the fluid properties.

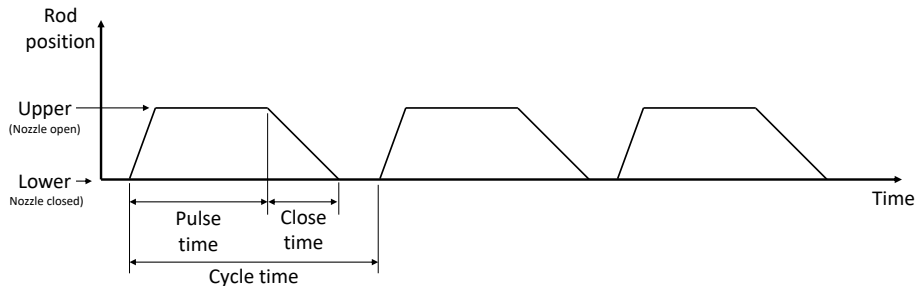


Figure 3.2: Description of the relevant parts of the driving pulse and its effect on the nozzle state.

During printing, the nozzle and the substrate is ~ 1 mm apart. The ink is deposited one drop at a time to form a layer, once a sufficient number of layers are achieved the stage is moved under the 395 nm UV lamp to cure the ink, with the lamp set at 100% intensity. The number of layers is dependent

on the application at hand and the corresponding thickness, for example, three layers results in a thickness of ~ 0.21 mm and ten layers results in a thickness of ~ 0.69 mm. The distance between the lamp and the curing layer is ~ 10 mm. Droplet spacing, which is the distance between adjacent droplets, is an important factor that determines the quality of the printed lines or films. The degree of droplet spacing is normally determined by the value of the droplet diameter. In this work, continuous printed lines were formed using $500\ \mu\text{m}$ drop spacing. To print and cure a sample $0.35\ \text{mm} \times 10\ \text{mm} \times 40\ \text{mm}$ in dimension took roughly one minute (including the 30 second cure time).

3.3 Characterisation

3.3.1 Thermal characterisation

The glass transition temperature T_g is an important thermal property of an elastomer. As the temperature transitions from below the T_g to above it, the material goes from a brittle “glassy” to a “rubbery” state. A significant change in the modulus is observed, transitioning from the GPa range in the glassy state to MPa range in the rubbery state. Typically rubber products are utilised above their T_g . Several methods exist to determine the T_g ; these include, but are not limited to, differential scanning calorimetry (DSC), dynamic mechanical analysis (DMA) and thermomechanical analysis (TMA) [121]. It should be noted here that the value of T_g is dependent on the experimental method [121].

T_g of the various compositions were determined using a Linkam DSC600 in conjunction with the LNP96 cooling system. The cooling system consists of a liquid nitrogen pump and a dewar. This setup was necessary to achieve a temperature of $-150\ \text{°C}$. Samples of ~ 5 mg were loaded onto aluminium pans and placed into the crucible. Following a purging process with nitrogen gas, the samples were cooled to $-150\ \text{°C}$. Subsequently, they were heated at a rate of $5\ \text{°C}/\text{min}$ to a temperature of $20\ \text{°C}$. A minimum of three samples were tested for each composition.

3.3.2 Metrology & mechanical characterisation

3.3.2.1 Metrology

Prior to performing the mechanical characterisation, the specimen needs to be prepared and measured. The specimens required were cut from cast compounds into $\sim 0.35 \text{ mm} \times 5.75 \text{ mm} \times 25\text{m}$ using sharp parallel blades. To measure the dimensions of the tensile specimen, a Hildebrand rubber thickness gauge and a calibrated HP Scanjet G4010 scanner was used to measure thickness t_s and the width w respectively.

The process used for the thickness measurement was complicated by the softness of the elastomers. The weight P ($= 0.276 \text{ N}$) of the rubber thickness gauge probe causes the material to deform significantly. For example, the thickness gauge will report a thickness value of 0.33 mm when the actual thickness is 0.35 mm . Typically, this is not an issue as the specimen stiffness is sufficient ($\sim >1 \text{ MPa}$) to prevent this from occurring. However, in this instance, the stiffness is smaller by an order of magnitude.

To calculate the actual thickness, the solution developed by Lebedev and Ufliand [122] to predict the deformations arising from a circular punch on a finite elastic layer is used. A schematic of the problem is provided on Figure 3.3. The actual thickness t_s is then obtained by summing the thickness measured by the thickness gauge and the deformation $t_{s,0}$ caused due to the thickness gauge as determined by the Lebedev and Ufliand [122] theory. For this purpose, five thickness measurements were taken per specimen. During each measurement, the sample was allowed to relax for two minutes. Thickness changes rapidly during the initial minute and only minimal changes are observed thereafter, thus a duration of two minutes was chosen. An average of the five measurements were used as the measured thickness in the solution proposed by Lebedev and Ufliand [122].

According to the Lebedev and Ufliand theory, the deformation $t_{s,0}$ caused by the thickness gauge (or probe) is determined as

$$t_{s,0} = \frac{P(1 - \nu_p)}{4a\chi G} \quad (3.1)$$

where ν_p is the Poisson's ratio, a is the radius of the circular probe, G is the shear modulus and χ is a constant. Lebedev and Ufliand [122] have provided numerical values for χ for ratios of p ($=a/t_s$) of up to 2. However, in this instance, the samples have a nominal thickness of $\sim 0.35 \text{ mm}$ and therefore χ

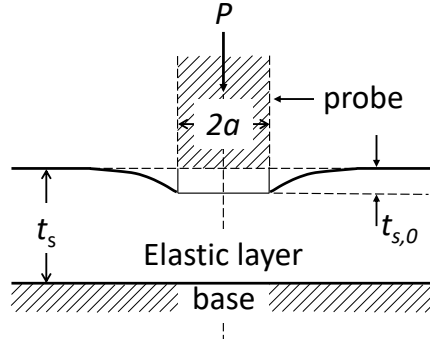


Figure 3.3: A schematic of the problem of pressing a stamp of circular cross-section into an elastic layer.

needs to be calculated for a p of 5.7. The framework to determine the value of χ has been provided by Lebedev and Ufliand [122].

To determine χ the numerical values of the kernels $K(\nu)$ and $\Omega(\Xi)$ are required and they are described as

$$K(\nu) = p \int_0^\infty \frac{A + e^{-A} \sinh A}{A + \sinh A \cosh A} \cos(pA\nu) dA \quad (3.2)$$

$$\Omega(\Xi) = 1 + \frac{1}{\pi} \int_0^1 [K(T + \Xi) + K(T - \Xi)] \Omega(T) dT \quad (0 \leq \Xi, T \leq 1) \quad (3.3)$$

The first step is to tabulate the numerical values for eq. 3.2 in the interval $0 < \nu < 2$ and $0 < p < 8$. The parameters ν and p were varied in increments of 0.1 and 0.5 respectively. The integration was carried out using the MATLAB *trapz* function [123]. Eq. 3.3 is resolved by approximating the integral using a quadrature formula, i.e. trapezium rule, the problem is now reduced to that of a system of linear equations. By substituting the numerical values obtained for $K(\nu)$ and solving the system of linear equations, the numerical values for $\Omega(T)$ can be obtained. The numerical values for $K(\nu)$ and $\Omega(T)$ are tabulated in Appendix A.1.

The constant χ is then determined by integrating $\Omega(T)$ for a given value of p as described by

$$\chi = \int_0^1 \Omega(T) dT \quad (3.4)$$

MATLAB *trapz* function [123] was utilised for the integration process. The numerical values obtained for χ for the range of values of p explored are given

Table 3.1: Numerical values for χ

p	0	1	2	3	4	5	6	7	8
χ	1.00	2.20	3.72	5.26	6.80	8.34	9.87	11.39	12.91

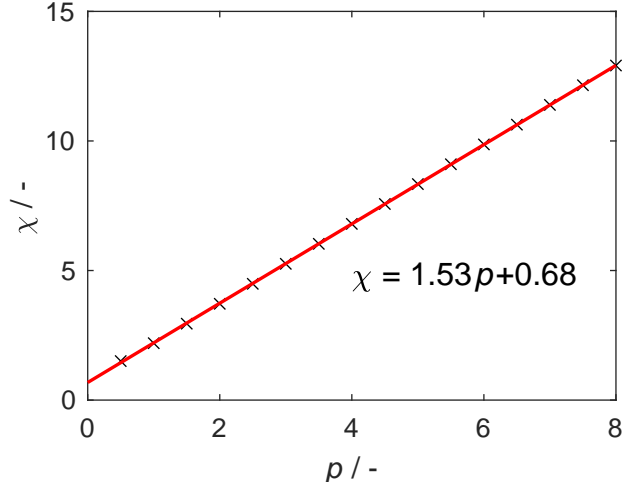


Figure 3.4: The evolution of χ with p .

on Table 3.1. χ and p form a linear relationship as illustrated on Figure 3.4. This relationship is described by the equation $\chi = 1.53p + 0.68$.

Sufficient information is now available to determine the true thickness t_s of the specimen using eq. 3.1. However, several iterations are required to determine t_s owing to the fact that G and t_s are related. The G value utilised for the first iteration is obtained, assuming isochoric deformation, *via* the relation $G = E_{1\%}/3$ [124]. $E_{1\%}$ is the tensile modulus at 1% strain and is obtained from the tensile stress-strain relationship, which in turn leveraged an incorrect thickness value. For this reason, at each iteration the value of $E_{1\%}$ is recalculated using the corrected thickness value. The actual thickness value t_s is only reached when the difference between the corrected thickness values for current and previous iterations are negligible. The first four decimal points are compared between the current and previous iterations in this work. The tensile modulus at 1% strain was chosen as the initial assumption was that the deformations caused by the thickness probe were in this region when compared to the actual thickness. This assumption is incorrect, the deformations are \sim in the 3-5% region. However, the resultant

measure of actual thickness is correct and is validated by an alternative experiment described below. This indicates that the modulus does not vary significantly in the 1-5% strain range.

To validate the Lebedev and Ufliand theory, parallel experiments were conducted. The experiments consisted of monitoring the deformation seen by the material as a result of varying the thickness probe force. The actual thickness of the specimen was then determined by extrapolating the data to the thickness at zero force. The thickness calculated *via* this method and *via* the Lebedev and Ufliand theory were in excellent agreement, the measurement were within 0.7% of each other in all cases. For further details on this method, please refer to Appendix A.2. Following the success of the validation experiments, the Lebedev and Ufliand [122] theory was leveraged extensively throughout to determine the actual thickness of the specimen as it produced the results without the need to conduct further time-consuming experiments.

For the width measurements, a HP Scanjet G4010 scanner and ImageJ software was used. As the specimen were sticky, they were transferred directly onto a microscope slide once they were cut to the required dimension and the thickness was measured. This also allows the samples to be stored easily. The slide was then placed in the scanner alongside a ruler; the ruler serves as a calibration tool for the image. The scanner lid remained open during the scan to prevent the lid from causing further deformation and skewing the measured dimensions. Instead, a black piece of card was used to cover the top and minimise light so that a good image is achieved. The details of this process are highlighted on Appendix. A.3.

3.3.2.2 Mechanical testing

Once the specimens were cut to shape and measured, they were attached to the SER3-P drums using staple-like clips and the strain was applied to the specimen by the counter-rotating drums as illustrated by Figure 3.5. The counter-rotating drums enable the sample to be stretched uniformly over the entire stretch area. Furthermore, a fixture with counter-rotating drums was chosen over fixtures with a single rotating drum as fixtures with a single rotating drum can potentially damage the host rheometer due to the resulting lateral forces. A small torque of $10 \mu\text{N}\cdot\text{m}$ was applied to ensure that the specimen was taut prior to the test. The tests were carried out at a rotation speed corresponding to a constant true strain rate $\dot{\epsilon}_{\text{true}}$ of 0.1 s^{-1}

at room temperature (20 ± 1 °C).

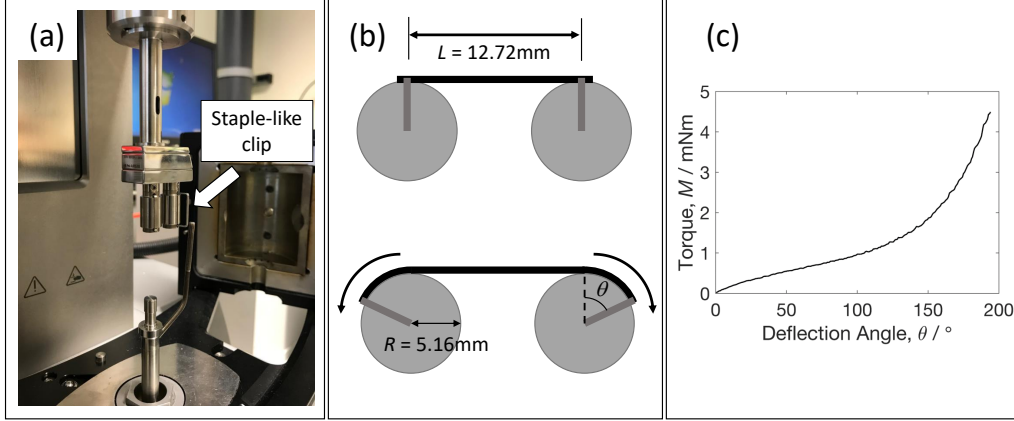


Figure 3.5: a) The experimental setup used for the mechanical tests. One of the staple-like clips is left protruding out of the drums for illustration. b) A schematic of the counter-rotation of the drums with key dimensions, including the drum radius R , gauge length L and deflection angle θ . c) A representative example of the raw data obtained from the experiment. This particular data is for a 70/30 specimen.

The raw data obtained from the tests can be utilised to determine the nominal strain ϵ and the nominal stress σ [125]. The former is defined as

$$\epsilon = \exp(\dot{\epsilon}_{\text{true}}t) - 1 \quad (3.5)$$

where t is the time, and the latter is defined as

$$\sigma = \frac{M}{2t_s w R \lambda \exp(-\dot{\epsilon}_{\text{true}}t)} \quad (3.6)$$

where M is the torque, t_s is the thickness of the specimen, w is the width of the specimen, R is the radius of the SER3-P drums and λ is the stretch ($=1+\epsilon$). The stress-stretch response has been illustrated on Figure 3.6

3.4 Results and discussion

3.4.1 Glass transition temperature

Several methods are available to analyse the DSC data, most of which have been outlined on BS ISO 11357-2:2014 [126]. These include half-step-height

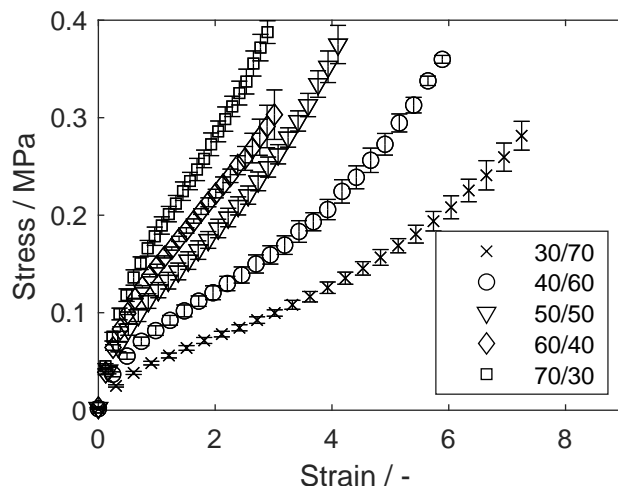


Figure 3.6: The stress-strain response of the various silicone/acrylate systems explored. The error bars (± 2 standard errors) show variations encountered in the experimental data with different samples.

method, inflexion-point method and equal areas method. The inflexion-point method was chosen as this method will return the same value of T_g regardless of the user. The transition temperatures are the temperatures corresponding to the peaks in the derivative of heat flow versus temperature curve. Each composition exhibits two distinct glass transitions, and evidence of the presence of two separate phases. The lower glass transition temperature, at around ~ -100 °C is associated with the silicone, and the higher, at around ~ -43 °C is associated with acrylate. T_g (± 2 standard errors) for all of the cured compositions are illustrated on Figure 3.7. Both appear to be independent of the ratio of the components.

3.4.2 Uniaxial stress-strain response

The average uniaxial tensile stress-strain responses obtained from a minimum of three specimens per sample for all the silicone/acrylate systems explored in this study are illustrated in Figure 3.6, and the error bars represent ± 2 standard errors. The standard errors were obtained from the stress values obtained at fixed intervals; linear interpolation was used for this purpose. Figure 3.6 confirms that an excellent level of repeatability was achieved. The average curves are limited to the lowest failure strain recorded in each

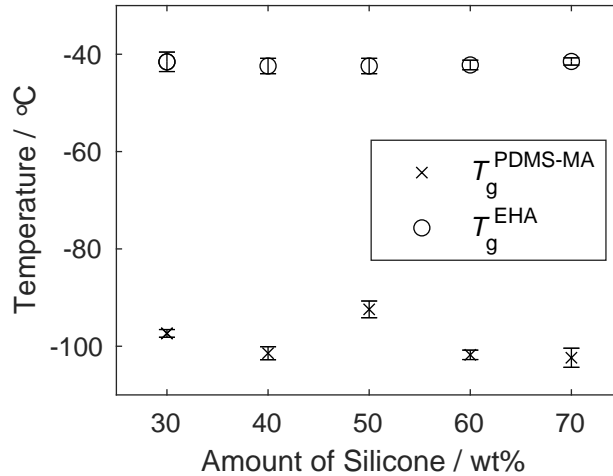


Figure 3.7: The glass transition temperatures T_g (± 2 standard errors) obtained for the various silicone/acrylate systems explored in the study.

batch of samples. It is apparent that increasing the proportion of silicone leads to a stiffer response, but at the expense of a reduction in the failure strain.

3.4.3 Modelling

To quantify the overserved changes in the mechanical response with composition, a rubber model was fitted to the data. The stress-strain response shown on Figure 3.6 has the characteristic features of rubber elastomers, and hence a simple Gaussian model is not sufficient. Although there are numerous applicable models in the literature that could model this response, an EV strain energy function W was selected due to the physical origin of its

parameters [80]. The EV strain energy function is defined as

$$W = W_C + W_S \quad (3.7)$$

$$W_S = \frac{1}{2} N_S kT \left\{ \sum_{i=1}^3 \left\{ \frac{\lambda_i^2 (1 - \alpha^2) (1 + \eta)}{(1 - \alpha^2 \sum \lambda_i^2) (1 + \eta \lambda_i^2)} + \log(1 + \eta \lambda_i^2) \right\} + \log(1 - \alpha^2 \sum_{i=1}^3 \lambda_i^2) \right\} \quad (3.8)$$

$$W_C = \frac{1}{2} N_C kT \left\{ \frac{\sum_{i=1}^3 \lambda_i^2 (1 - \alpha^2)}{1 - \alpha^2 \sum_{i=1}^3 \lambda_i^2} + \log(1 - \alpha^2 \sum_{i=1}^3 \lambda_i^2) \right\} \quad (3.9)$$

where W_C is the strain energy density due to cross-links, W_S is the strain energy density due to slip-links, N_C is the density of cross-links, N_S is the density of slip-links, α is a measure of inextensibility and η is a measure of slippage. To fit the EV model to the data, the model stress has to be determined.

Assuming incompressibility, i.e., that the volume remains unchanged, and symmetry, for a uniaxial tensile test the principal stretches λ_1 , λ_2 and λ_3 are

$$\lambda_1 = \lambda; \quad \lambda_2 = \lambda_3 = \lambda^{-1/2} \quad (3.10)$$

where λ is the stretch imposed on the specimen during the test [9]. The EV stress is obtained by differentiation of eq. A.1 with respect to λ , once the conditions on eq. A.4 have been applied. Readers are referred to Appendix A.4 for detailed calculations.

Prior to fitting the EV function to the data, the impact of the various EV parameters will be illustrated. Firstly, the impact of N_C will be considered. For this purpose, α and η are set to 0.1 and 0.2, respectively. The α and η values utilised here are typically observed values for elastomers [80]. N_S is set to be zero. N_C is varied from 1.24×10^{26} to 4.95×10^{26} , inclusive. This particular N_C range was chosen because it corresponds to elastic constant ($=N_C kT$) values between 0.5 and 2 MPa. This particular elastic constant is associated with the number of cross-links. The values of the elastic constant are typically of this order. The resulting response has been illustrated on Figure 3.8. It can be seen that increasing N_C results in an increase in the stress at any given λ value. Subsequently, the impact of N_S is considered, and therefore N_C is set to zero. N_S is also varied from 1.24×10^{26} to 4.95×10^{26} to ensure that the elastic constant corresponding to entanglements ($=N_C kT$)

is between 0.5 and 2 MPa. It can be seen that an increase in N_S results in an increase in stress and is illustrated on Figure 3.8. The stress-strain curve for when only considering N_C has a stress-strain response similar to those of typical elastomeric material. However, the stress-strain curve obtained for when only the entanglements are considered ($N_C = 0$) looks similar to the response of strain-hardening glassy polymers [127]. The key takeaway is that the stress response due to cross-link density is an order of magnitude greater than that of an equivalent value of slip-link density.

The parameters α and η also influence the stress-strain response. To probe the impact of α , four values between 0.05 to 0.2, inclusive, were trialled. N_C and N_S were set to 2.47×10^{26} , this corresponds to an elastic constant of 1 MPa. η was set to 0.2. The results have been highlighted on Figure 3.8. It can be seen that increasing α leads to a reduction in the maximum stretch λ_{\max} . This is expected as α is related to λ_{\max} *via* the relation $\lambda_{\max} = 1/\alpha$. As λ approaches λ_{\max} , the stress approached infinity, i.e., $\lambda = 1/\alpha$ is an asymptote to the stress-strain curve. To probe the impact of η , it is varied from 0.2 to 2. N_C and N_S were set to 0 and 2.47×10^{26} respectively. N_C was set to 0 to highlight the impact of η . The value of N_S corresponds to a 1 MPa elastic constant. α was set to 0.1. The results are illustrated on Figure 3.8. It can be seen that increasing η results in a reduction in stress for any given λ value. Largest reduction in stress values are seen for when η transitioned from 0.2 to 0.8, minimal reductions are seen subsequently.

The EV model is then fitted to the experimental data by minimising the RMS error between the experimental and model stress. MATLAB *lsqcurvefit* [128] function was used for the minimisation process. The model was fitted to all the experimental stress-strain responses, and in all cases the EV function provided an excellent fit to the experimental data with RMS errors not exceeding 1.8 kPa (error corresponds to the 50/50 composition and is $\sim 0.2\%$ of the maximum stress of that composition, see Figure 3.6).

3.4.4 Evolution of EV parameters

The EV parameters obtained from fitting the EV strain energy function to the experimental data sets were extracted and the averages (± 2 standard errors) of each parameter for a given composition is illustrated on Figure 3.9 as a function of composition. Figure 3.9a shows an increase in slip-link density with increasing silicone content. This is attributed to the presence of longer chains with increasing silicone content, and therefore an increase in the possi-

Table 3.2: The EV parameters used to illustrate the impact of each parameter on the resulting stress-strain response on Figure 3.8. Test IDs are used to identify the corresponding curve.

Test ID (TID)	N_C	α	N_S	η
1	1.24×10^{26}	0.1	0	0.2
2	2.47×10^{26}	0.1	0	0.2
3	3.71×10^{26}	0.1	0	0.2
4	4.94×10^{26}	0.1	0	0.2
5	0	0.1	1.24×10^{26}	0.2
6	0	0.1	2.47×10^{26}	0.2
7	0	0.1	3.71×10^{26}	0.2
8	0	0.1	4.94×10^{26}	0.2
9	2.47×10^{26}	0.05	2.47×10^{26}	0.2
10	2.47×10^{26}	0.1	2.47×10^{26}	0.2
11	2.47×10^{26}	0.15	2.47×10^{26}	0.2
12	2.47×10^{26}	0.2	2.47×10^{26}	0.2
13	0	0.1	2.47×10^{26}	0.8
14	0	0.1	2.47×10^{26}	1.4
15	0	0.1	2.47×10^{26}	2

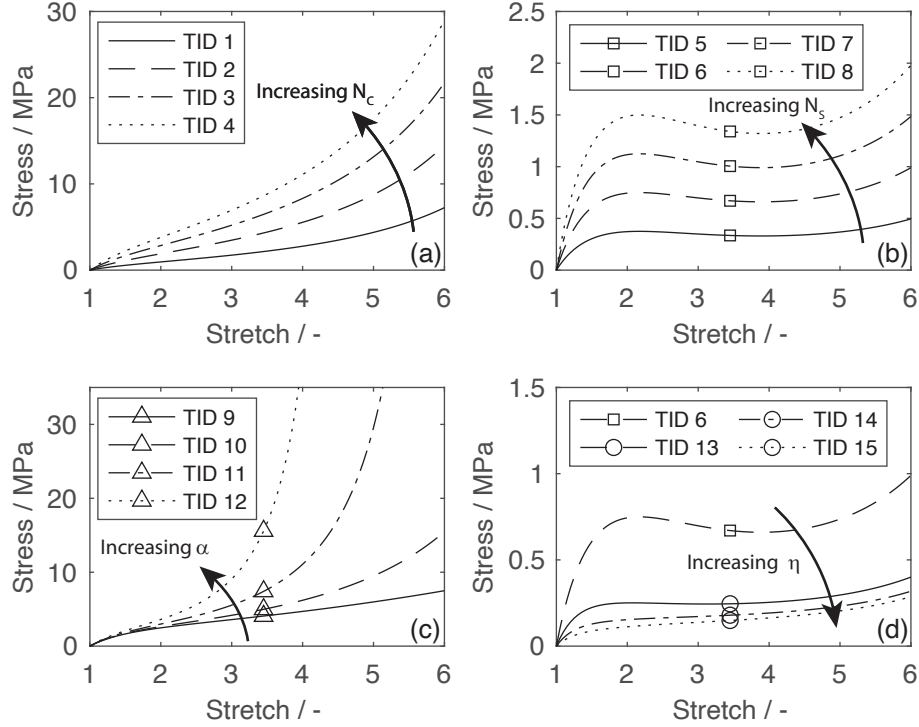


Figure 3.8: A plot illustrating the impact of the various Edwards-Vilgis (EV) parameters. The legend entries are used in parallel with Table 3.2 to identify the magnitude of the individual EV parameters used to obtain a given curve.

bility of becoming entangled. The cross-link density on the other hand is seen to increase, peak and then decrease with increasing silicone content as shown on Figure 3.9c. This is also attributed to the presence of longer chains with increasing silicone content; the likelihood of interactions between the two methacrylate end groups of the PDMS and the mono-acrylate chains are reduced. The figures also highlight the fact that slip-link density is typically an order of magnitude greater than the cross-link density in these compositions. The overall network constraints (sum of slip-link and cross-link densities) therefore increase with increasing silicone content.

Figure 3.9d shows the limiting extensibility of the network λ_{\max} , which is obtained from the inverse of the model parameter α . In line with the network density, the limiting extensibility decreases with increasing silicone content,

except for 60/40 ($f_{\text{PDMS}} = 0.6$) composition where the determination of the limiting extensibility was hampered by a more limited dataset due to failure of the specimens at reduced strains. Nevertheless, overall, as the density of the network constraints increases, the chain length between these constraints decreases, leading to a reduction in the limiting elongation. Lastly, Figure 3.9b shows that the slip-link mobility η increases with increasing silicone content, most likely attributed to the greater flexibility of the silicone chains relative to the acrylate chains.

3.4.5 Tuning mechanical properties

As illustrated above, the EV model parameters can shed a light on the underlying network and how it influences the properties of each composition. This data can be further leveraged to develop a predictive model; this model can then be utilised to enable the fine tuning of properties for various applications. To achieve this, the evolution of EV parameters (± 2 standard uncertainties) are expressed as function of f_{PDMS} as illustrated on Figure 3.9. The uncertainties refer to the confidence in the fitted parameters and are obtained directly from MATLABs *lsqcurvefit* tool [128]. This tool was used for both the fitting process and to determine the uncertainties in the parameters.

For all parameters, with the exception of α , the full data set was used in the fitting process. For α , the data point corresponding to the composition 60/40 ($f_{\text{PDMS}} = 0.6$) was not used due to deviations of the mean from the general trend and due to the presence of a large uncertainty. This is likely due to the failure of the 60/40 specimens prior to the upturn typically exhibited by elastomers; the α parameter is sensitive to this upturn.

The forms of the functions selected to describe the evolution of the parameters are

$$N_{\text{S}} = C_{1,N_{\text{S}}}f_{\text{PDMS}}^2 + C_{2,N_{\text{S}}}f_{\text{PDMS}} + C_{3,N_{\text{S}}} \quad (3.11)$$

$$\eta = C_{1,\eta}f_{\text{PDMS}}^2 + C_{2,\eta}f_{\text{PDMS}} + C_{3,\eta} \quad (3.12)$$

$$N_{\text{C}} = C_{1,N_{\text{C}}}f_{\text{PDMS}}^2 + C_{2,N_{\text{C}}}f_{\text{PDMS}} + C_{3,N_{\text{C}}} \quad (3.13)$$

$$\alpha = C_{1,\alpha}f_{\text{PDMS}} + C_{2,\alpha} \quad (3.14)$$

The estimates (± 1 standard uncertainty) of the coefficients for these functions have been reproduced in Table 3.3. The uncertainties refer to the con-

fidence in the fitted parameters and are obtained directly from MATLABs *lsqcurvefit* function.

Table 3.3: Estimate ± 1 standard uncertainty for the coefficients of equations 3.11 - 3.14 describing the evolutions of the EV parameters: slip-link density N_S , slip-link mobility η , cross-link density N_C and chain inextensibility α , as a function of silicone weight fraction f_{PDMS} .

Parameters	Coefficients	
N_S	C_{1,N_S}	$(2.589 \pm 1.441) \times 10^{27} \text{m}^{-3}$
	C_{2,N_S}	$(-1.582 \pm 1.451) \times 10^{27} \text{m}^{-3}$
	C_{3,N_S}	$(2.755 \pm 3.430) \times 10^{26} \text{m}^{-3}$
η	$C_{1,\eta}$	14.625 ± 9.016
	$C_{2,\eta}$	-9.687 ± 9.079
	$C_{3,\eta}$	2.959 ± 2.147
N_C	C_{1,N_C}	$(-1.023 \pm 0.480) \times 10^{26} \text{m}^{-3}$
	C_{2,N_C}	$(1.047 \pm 0.484) \times 10^{26} \text{m}^{-3}$
	C_{3,N_C}	$(-1.788 \pm 1.144) \times 10^{25} \text{m}^{-3}$
α	$C_{1,\alpha}$	0.132 ± 0.026
	$C_{2,\alpha}$	0.019 ± 0.013

For any given composition, the model uniaxial stress-strain (or stress-stretch) response can be calculated by:

1. Determining the EV parameters for the corresponding composition from the evolution laws as expressed by eq. 3.11 - 3.14
2. Substituting the obtained EV parameters and the conditions proposed in eq. A.4 into the EV strain energy function (eq. 2.8)
3. Differentiating the strain energy function with respect to λ

The procedure stated above has been utilised to predict the stress-strain response of the various compositions examined herein. The model responses were superimposed on the experimental stress-strain response as shown on Figure 3.10. Considering the fact that the models were generated based on the evolution functions, in all cases, the model provides an excellent fit to the experimental data with RMS error not exceeding 6.3kPa (error corresponds to the 60/40 composition and is $\sim 2.1\%$ of the maximum stress of that composition, see Figure 3.10).

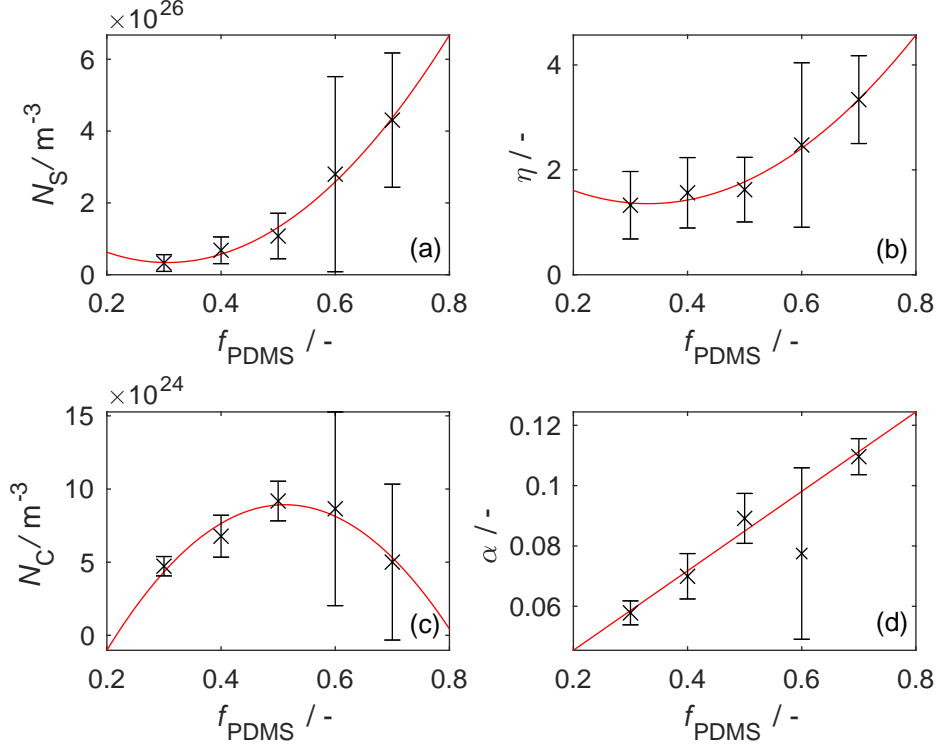


Figure 3.9: The evolution of (a) slip-link density N_S , (b) slip-link mobility η , (c) cross-link density N_C and (d) chain inextensibility α with silicone weight fraction f_{PDMS} . The EV parameters are represented as crosses with ± 2 standard uncertainties. To describe the evolution of these parameters, simple functions (lines) are fitted to the experimental data. Large crosses are used to highlight the data points utilised in the fitting process.

Various mechanical properties can be determined from the stress-strain response, for instance the secant modulus. The secant modulus is the slope on the line from the origin to a particular point in the stress-strain curve. The secant modulus at 100% strain ($E_{s,100\%}$) is a typically quoted value in material data sheets. To illustrate the capabilities of the model, the secant modulus E_s at 50%, 100%, 150% and 200% strains are determined for all compositions and are compared with the experimental data (± 3 standard errors) in Figure 3.11. For $E_{s,100\%}$, an increase in silicone content from 30 to 70 wt%, increases $E_{s,100\%}$ by a factor of ~ 3.6 . The model provides a good

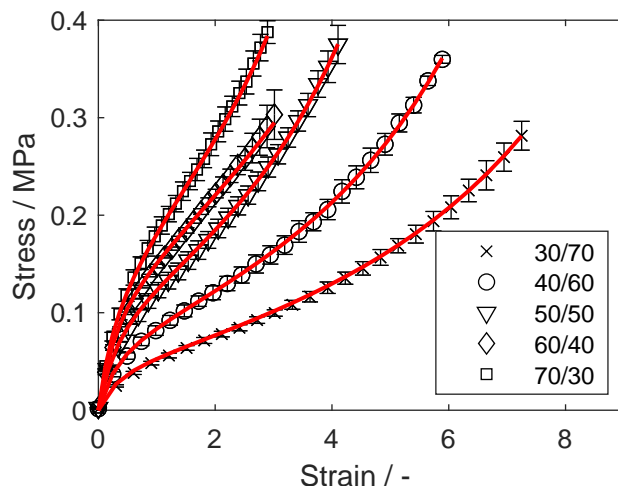


Figure 3.10: The stress-strain response of the various silicone/acrylate systems explored. The error bars (± 2 standard errors) show variations encountered in the experimental data (symbols) with different samples. Edward-Vilgis EV model fits represented using solid lines.

representation of experimental data.

3.4.6 Influence of UV light intensity

UV light is used in this study to cure the elastomers. The energy density is dependent on a number of factors, including UV light intensity, distance and exposure time. The distance from the lamp to the curing surface and exposure time were fixed for this work at values of 10 mm and 30 seconds, respectively. However, the UV light intensity was varied. Three different intensity levels, 5%, 50% and 100% were explored. A 50/50 composition was used for this purpose. The resulting mechanical responses are illustrated on Figure 3.12.

An increase in cross-linking and hence a stiffer response was expected with increasing intensity, however, the opposite is true as illustrated by Figure 3.12. Jiang and Drummer [129] have also illustrated the increase in cross-link density with increasing UV light intensity so the observed results are counter intuitive. The authors also show that increasing intensity reduced the cure time, therefore, a plausible explanation for the observed results is that the UV light penetration is hindered by the premature cure of the surface

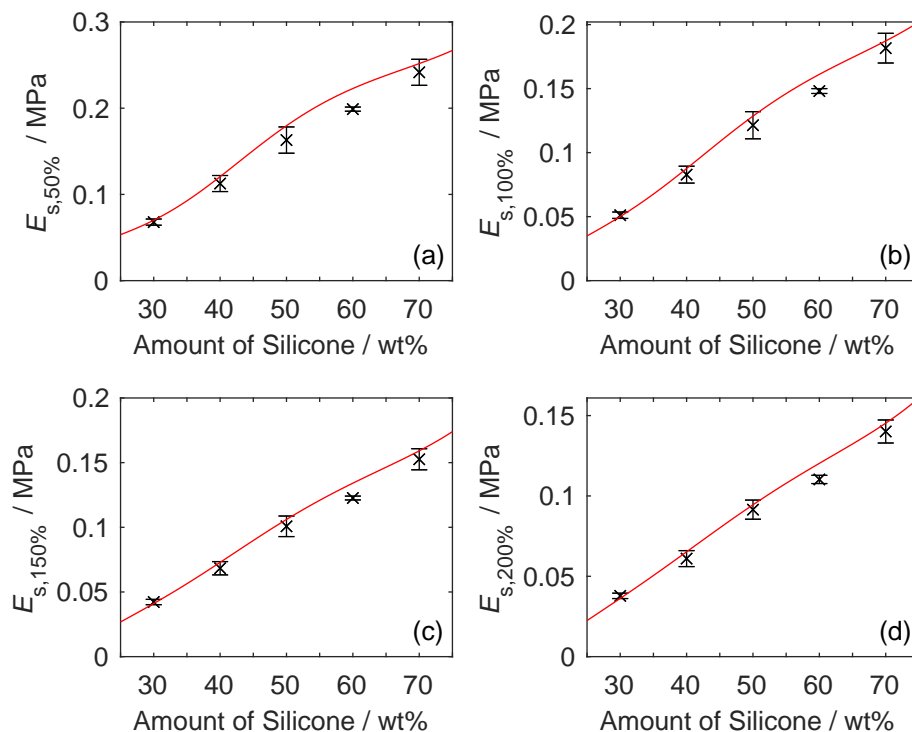


Figure 3.11: The experimentally measured (symbols) (± 3 standard error) and model (line) predicted secant modulus as a function of composition for strain level of a) 50%, b) 100%, c) 150% and d) 200%.

layer at high intensity, leading to a reduction in stiffness.

The observations made above indicate that intensity alongside composition can be utilised to fine tune the mechanical properties of elastomers. Further experiments are required to quantify the variation in stiffness and curing time with varying intensity. Mechanical tests as demonstrated earlier in this chapter are required to establish variations in stiffness. The cure time or duration can be established using a photo-DSC or even by monitoring variations in temperature during curing. By plotting the temperature variations with time, the duration of the curing reaction can be established.

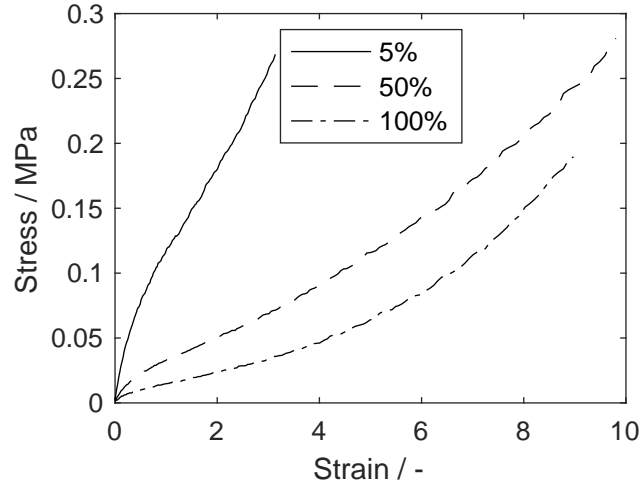


Figure 3.12: A comparison of the stress-strain response of cast specimen of the 50/50 composition exposed to various intensities.

3.4.7 Validation of 3D printing capabilities

The goal of this chapter was to develop a novel UV light curable silicone elastomer suitable for jetting application. As this particular material was intended for jetting, the materials jetting capabilities will be assessed herein. The custom setup utilised to fabricate the silicone material and a successfully printed silicone sample of 70/30 composition is shown on Figure 3.13. On closer inspection one can observe that the surface is not completely smooth and that a few air bubbles are present. Nonetheless, qualitatively, the print quality was satisfactory. The printed sample was then cut using parallel blades to dimensions equivalent to that of the cast samples. A mechanical test was then conducted using the same protocol employed for the cast samples, and the corresponding stress-strain response can be observed on Figure 3.14.

By comparing the response of 3D printed and the equivalent cast sample, one can see that the stress at a given strain level is ~ 3.5 times lower for the 3D printed sample. One reason is the different intensity of the UV light as discussed in the section above. Another is that the oxygen exposure during the 3D printing process is greater as a result of the thinner layers, and the oxygen inhibits the cross-linking reaction [130]. Although the individually 3D printed layers are more susceptible to oxygen exposure in comparison to case samples, it may be possible to control the printing environment to

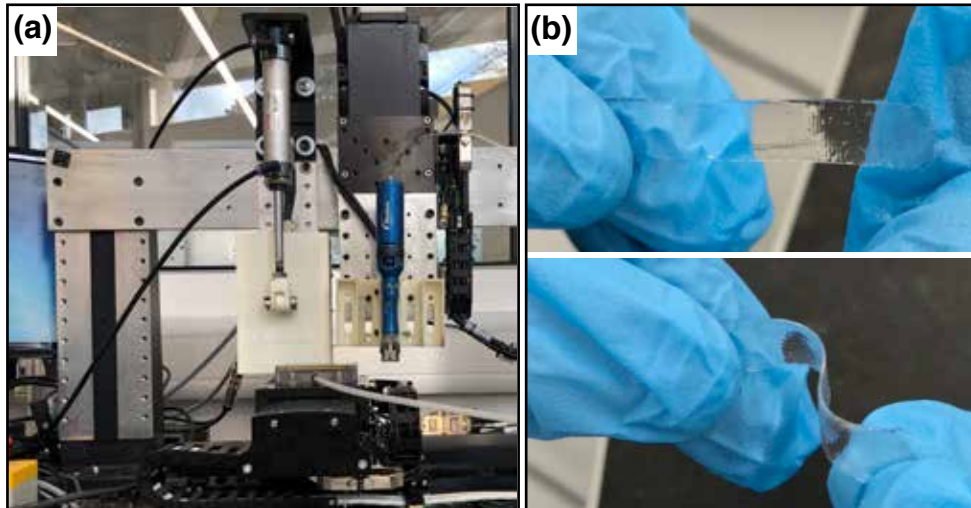


Figure 3.13: (a) The custom jetting setup used for 3D printing; and, (b) a printed 70/30 sample.

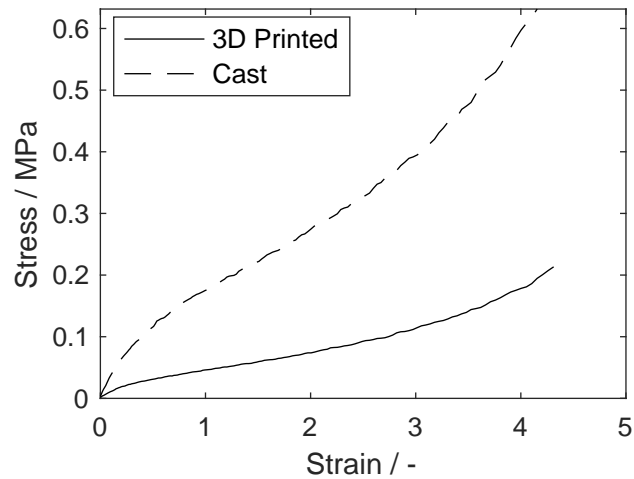


Figure 3.14: The stress-strain response of the 3D printed (solid line) and a cast (dashed line) 70/30 sample.

control this. There were insufficient opportunities to explore these factors. Subsequent work in the laboratory aims to optimise the jetting process to for these specific materials, these factors will be considered therein.

3.5 Summary

The preparation of five different compositions of novel, UV curable, silicone-based elastomer was presented in section 3.2. Following this the material was characterised in section 3.3, specifically the glass transition T_g and the mechanical response of the material under uniaxial tensile strain as determined. The softness of the specimen posed a challenge for the thickness measurement and tensile testing. The weight of the thickness gauge probe cause the specimen to deform during the measurements. This problem was overcome by applying the theory developed by Lebedev and Ufliand [122], allowing the actual thickness to be determined. To account for the softness, the uniaxial tensile tests were conducted on Anton Paar rheometer equipped with an SER3-P fixture as opposed to a typical universal tensile tester.

The results presented in section 3.4 show that the novel material exhibits two unique phases: a silicone and an acrylate phase. The results from the mechanical tests suggests that varying the silicone content results in a systematic variation in the stress-strain response. An EV model was fitted to the experimental data to study this variation. The network density is seen to increase with increasing silicone content due to the increase in availability of reaction sites. Correspondingly, the limiting extensibility is seen to decrease as the chain length decreases with increasing density of network constraints. The increase in slip-link mobility with silicone content is attributed to the greater flexibility of the silicone molecule. An empirical model was developed based on these observations to predict the mechanical properties of this particular group of materials. The predicted secant modulus was in good agreement with the experimental data. Lastly, an initial assessment was performed to study the impact of intensity and to validate the 3D printing capability of these materials. The results indicate that alongside the composition, the UV intensity could be another user defined variable that could be used to fine tune the mechanical properties, and that the material is printable.

4. The influence of deformation history on the mechanical response - part I

To study the impact of deformation history on the mechanical response of elastomer, EPDM specimen were subjected to uniaxial cyclic tensile tests to various maximum strain (or stretch) levels. The third unload-reload loops of the cyclic tests are decomposed into equilibrium and viscous contributions. The physically motivated Edwards-Vilgis (EV) function is leveraged to describe the evolution of the equilibrium contribution with pre-deformation. A constitutive model is derived from the observations made and is validated against the experimental third loop response and other complex deformation histories. Subsequently, the model's strengths and shortcomings are evaluated.

The material, material preparation and test method utilised in this chapter are presented on section 4.2. Section 4.3 outlines a method to decouple the experimental data into equilibrium and viscous contributions. Alongside this, the evolution of the equilibrium response with pre-deformation is also discussed in section. The viscous contribution is discussed in section 4.4. A constitutive model to describe the mechanical response of an EPDM materials subjected to uniaxial cyclic tensile deformations is developed in section 4.5. In section 4.6, the constitutive model is used to simulate a range of complex deformation histories. The strengths and weaknesses of this model are discussed in section 4.7. Lastly, the conclusions are provided on section 4.8.

This work has been presented at the 'Mechanics of Time-Dependent Materials Conference 2018' at Milan, Italy. This work has also been published in: Annarasa, V., Popov, A. A. & De Focatiis, D. S. A. A phenomenologi-

cal constitutive model for the viscoelastic deformation of elastomers. *Mech Time-Depend Mater* (2020). <https://doi.org/10.1007/s11043-020-09452-2>.

4.1 Introduction

Elastomers are essential to a wide range of industrial applications, including tyres, dampers and seals to name a few. Constitutive models are a critical element in the design process to enable simulation of the in-service behaviour of these products during their life cycle. Owing to stress softening, permanent set and viscoelasticity, amongst others, these materials exhibit a complex mechanical response. Furthermore, there is still much debate in the academic literature regarding the physical origins of several aspects of the underlying material behaviour. A combination of the two factors described above has resulted in numerous modelling approaches being suggested by the research community as presented within the literature review.

In the previous chapter, the modelling of a simple elastomeric system was explored. The aim of this section is to develop a constitutive model to predict the mechanical response of filled elastomer systems following pre-deformation. This model takes inspiration from the study conducted by De Focatiis *et al.* [131] involving cyclic tests. In their study, they decomposed the stress-strain response into equilibrium (or elastic) and viscous contributions. They showed that the elastic contribution is a function of the maximum stretch (pre-deformation) seen by the elastomer. The viscous contribution was shown to be independent of pre-deformation and a unique function of network stretch, once the permanent deformation (or permanent set) is accounted for. Although non-linear viscosities have been incorporated in previous constitutive models, to the authors' knowledge, none have been linked to strain in elastomers.

A one-dimensional (1D) constitutive model based on the ideas of an evolving hyperelastic component and a non-linear viscoelastic Maxwell element is formulated in this chapter. The evolving hyperelastic components concept was introduced in the previous chapter, the evolution was with respect to the composition. Here, the evolution is with respect to pre-deformation. The extent of which such a model can capture the observed cyclic response and the dissipated energy of an EPDM rubber deformed in a series of complex strain histories is also explored.

4.2 Materials and methods

The experimental data employed in this study have been described previously by De Focatiis *et al.* [131], and only a brief overview of the experimental procedure is given here.

4.2.1 Materials and manufacturing

EPDM rubber filled with 50 parts per hundred rubber (phr) of carbon black, provided by Dr. T. Alshuth of the German Institute of Rubber Technology (DIK), was compression moulded for 13 minutes at 160 °C into approximately 0.5 mm thick sheets. Uniaxial tensile test specimens were cut from the sheet using a hand operated Wallace specimen cutting press fitted with a dumbbell shaped cutter 1BA according to BS ISO 527-2.

4.2.2 Mechanical testing

Uniaxial tensile cyclic tests were performed on an Instron 4204 tensile testing machine fitted with a counterbalanced travelling extensometer to record the strain at a constant nominal strain rate of 0.03 s^{-1} at room temperature, $(24 \pm 1) \text{ }^\circ\text{C}$. The specimens were subjected to four load-unload cycles (displacement controlled, mixed mode) through to a specified pre-deformation λ_{max} , as illustrated in the inset of Figure 4.1, and ten separate λ_{max} increments between 1.5 and 6 inclusive were explored. To prevent buckling, the specimens were always unloaded to a stretch $\lambda_{0.1\text{N}}$ corresponding to a small tensile force of 0.1 N.

Representative stress-stretch responses to the cyclic loading are illustrated in Figure 4.1. Many of the characteristic features of the deformation of filled elastomers can be observed, including stress-softening, permanent set and hysteresis. The stress-softening and permanent set increase with increasing λ .

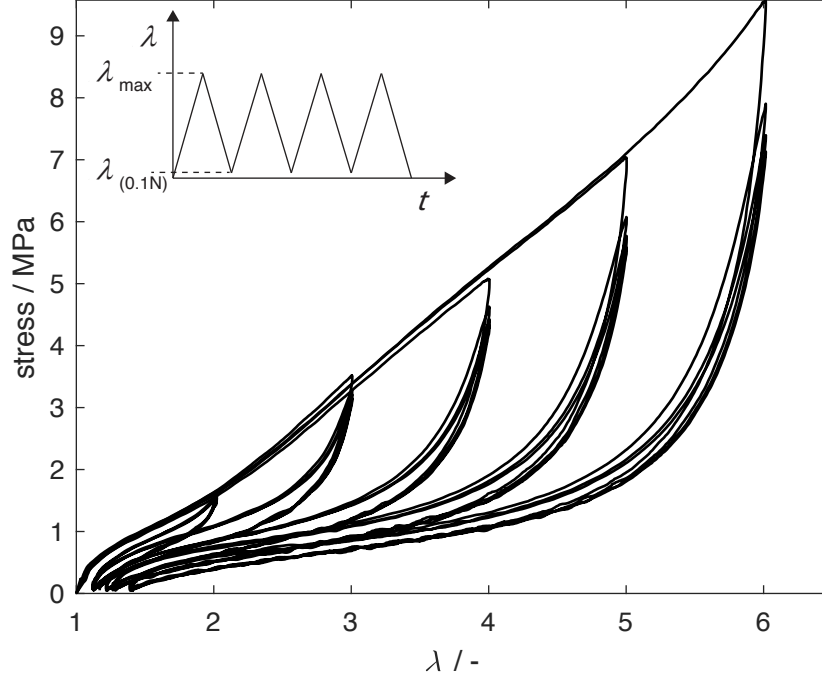


Figure 4.1: The stress-stretch response of selected EPDM specimens subjected to cyclic loading (displacement controlled, mixed mode) as shown in the inset to λ_{\max} of 2, 3, 4, 5 and 6. The specimens are unloaded to a stretch corresponding to a load of 0.1 N ($\lambda_{0.1\text{N}}$) to prevent buckling. A virgin specimen was used for each test.

4.3 Experimental analysis

4.3.1 Extraction of elastic and viscous Contributions

Decompositions into elastic and viscous contributions are commonly used in constitutive models describing elastomers and polymers, as first suggested by Haward and Thackray [132], and as implemented by Bergström and Boyce [133], and several others. In this study, it is assumed that the changes to the constitutive behaviour of the rubber due to the Mullins effect arise as a result of the maximum level of deformation experienced, and hence depend on λ_{\max} . As subsequent unloading-reloading loops are similar (see Figure 4.1), any unloading-reloading loops following λ_{\max} can be used in the decoupling

of the mechanical response. The third unload-reload loop has been chosen in this instance since the constitutive response shows the most dramatic change in the first few cycles.

The assumption is that the steady-state response at a given strain level can be decomposed as the sum of an elastic (equilibrium) σ_e and a dissipative, or viscous σ_v stress. σ_v changes sign depending on the sign of the strain rate, positive on loading and negative on unloading. Following the ideas proposed by De Focatiis *et al.* [131] and Prisacariu *et al.* [134], σ_e and σ_v are computed from the experimental measurements as the mean and as half of the difference between the loading and the unloading stress, respectively. Here, to ensure that the viscoelastic transients have saturated, the initial and final 0.33 strain of each cycle are discarded. The elastic and viscous contributions obtained in this way are highlighted in Figure 4.2.

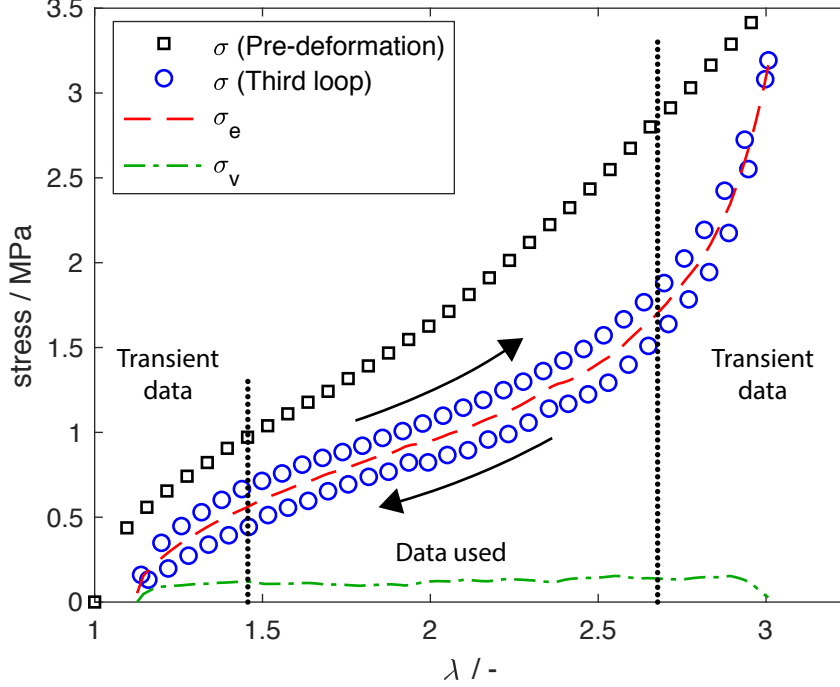


Figure 4.2: The experimental stress-stretch response (symbols) to cyclic tension to a λ_{\max} of 3, showing only the pre-deformation and the third unload-reload loop. σ_e (dashed line) and σ_v (dot-dash line) are obtained from the mean and from half of the difference between the third loop unloading and reloading stress, respectively. The transient portion of the data (here indicated as a strain of 0.33 at each end of the deformation) and the data used in the procedure are highlighted.

4.3.2 Equilibrium contribution

The evolution of σ_e as a function λ , with increasing λ_{\max} , is illustrated in Figure 4.3. The elastic response is strongly affected by the increase in historical maximum strain, and this implies that at least some of the Mullins effect arises from an evolution of the underlying elastic network, here simply dependent on λ_{\max} . Various hyperelastic models can be used to capture the elastomer's equilibrium response arising from the entropic nature of the network. In this instance, an EV hyperelastic function [80] is chosen due to the physically inspired model parameters. The EV strain energy density W function is given by eq. A.8.

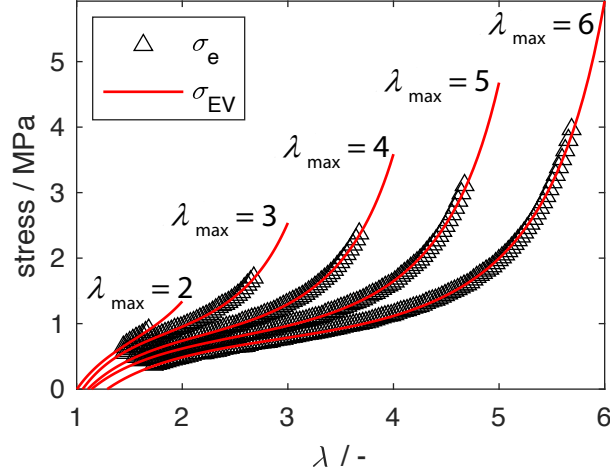


Figure 4.3: The experimental σ_e (symbols) and model σ_{EV} (lines) equilibrium contributions as a function of stretch for five λ_{\max} levels between 2 and 6. The model is an EV function accounting for λ_{set} .

The stress in the EV spring can be determined by differentiation of eq. A.8 with respect to the stretch direction, accounting for isochoric deformation. EV parameters were obtained by optimisation on each third loop elastic contribution, and the process was repeated for all values of λ_{\max} . The optimisation algorithm was coded in MATLAB using the *lsqcurvefit* tool [128] to obtain values of N_C , N_S , α and η by minimisation of the error, defined here as the RMS of the difference between experimental and numerical stress values within one unload-reload loop. It was found that an EV function on its own was unable to produce satisfactory fits to the data, and in order to achieve good agreement, it was necessary to incorporate a measure of λ_{set} , achieved *via* a multiplicative decomposition of λ into

$$\lambda = \lambda_{\text{set}} \lambda_{\text{eff}} \quad (4.1)$$

where λ_{eff} is the effective stretch, i.e. the stretch actually experienced by the network. In addition, N_C was always several orders of magnitude smaller than N_S , and hence insignificant as far as the total elastic stress is concerned. This is most likely due to the difficulty in separating the effects of cross-links and slip-links. Hence, for the purpose of modelling the elastic response, it

was sufficient to express the EV function as

$$W = \frac{1}{2}N_S kT \left\{ \sum_{i=1}^3 \left\{ \frac{\lambda_i^2(1-\alpha^2)(1+\eta)}{(1-\alpha^2\sum\lambda_i^2)(1+\eta\lambda_i^2)} + \log(1+\eta\lambda_i^2) \right\} + \log\left(1-\alpha^2\sum_{i=1}^3\lambda_i^2\right) \right\} \quad (4.2)$$

This combination produced excellent agreement between the elastic data and the EV functions, as shown in Figure 4.3, with RMS errors typically of the order of 0.01 MPa, and always less than 0.02 MPa. The RMS error is $\sim 0.3\%$ of the maximum third loop stress.

4.4 Viscous contributions

The viscous contribution to the stress σ_v is illustrated in Figure 4.4a for all values of λ_{\max} as a function of λ . The varying levels of λ_{\max} lead to different σ_v vs. λ curves. This viscous contribution is associated with flow of the network, and, as such, a viscosity η_v is defined as

$$\eta_v = \frac{\sigma_{v,\text{true}}}{\dot{\epsilon}_{\text{true}}} \quad (4.3)$$

where $\sigma_{v,\text{true}}$ is the true flow stress and $\dot{\epsilon}_{\text{true}}$ is the true strain rate. It was found that σ_v differed with varying levels of λ_{\max} , however once λ_{set} obtained from the elastic optimisation is accounted for, and η_v is plotted as a function of λ_{eff} , the curves overlap to form a single master curve as shown in Figure 4b. The implication of this is that η_v may be modelled as a Mullins-independent, but λ_{eff} -dependent quantity. A plausible explanation for this effect is that molecular alignment leads to an increasingly anisotropic flow process. Similar effects have been noted in polymer glasses [135, 136].

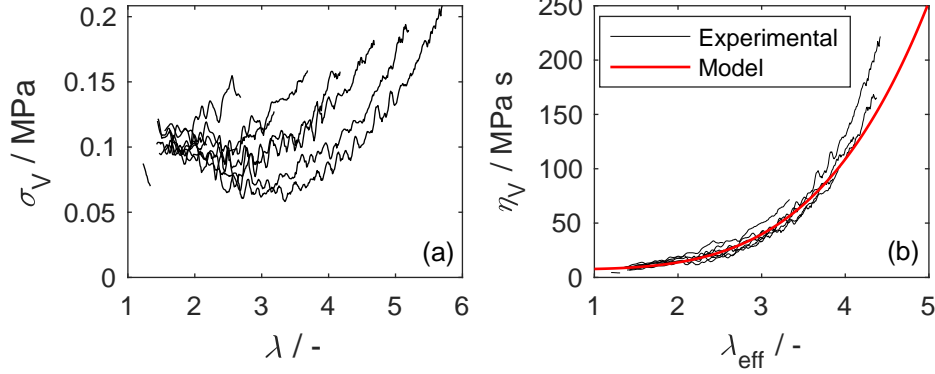


Figure 4.4: (a) Viscous stress σ_v as a function of λ , and (b) the viscosity η_v as a function of λ_{eff} . When expressed as a function of λ_{eff} , the viscosity data overlay to form a master curve. A simple function is fitted to describe the viscosity master curve.

Starting from the definition of true strain,

$$\epsilon_{\text{true}} = \ln(\lambda) = \ln(\lambda_{\text{eff}}) + \ln(\lambda_{\text{true}}) \quad (4.4)$$

The time derivative of eq. 4.4 is calculated to determine $\dot{\epsilon}_{\text{true}}$ and is expressed as,

$$\dot{\epsilon}_{\text{true}} = \frac{\dot{\lambda}}{\lambda} = \frac{\dot{\lambda}_{\text{eff}}}{\lambda_{\text{eff}}} + \frac{\dot{\lambda}_{\text{set}}}{\lambda_{\text{set}}} \quad (4.5)$$

where $\dot{\lambda}_{\text{eff}}$ is the effective stretch rate and $\dot{\lambda}_{\text{set}}$ is the rate of change of permanent set. The data used to determine the viscosity is obtained from the third loop. The evolution of λ_{set} predominantly takes place during the first loading, and it is assumed that $\dot{\lambda}_{\text{set}}=0$ for subsequent loadings. Eq. 4.5 is thus reduced to

$$\dot{\epsilon}_{\text{true}} = \frac{\dot{\lambda}}{\lambda} = \frac{\dot{\lambda}_{\text{eff}}}{\lambda_{\text{eff}}} \quad (4.6)$$

The relationship between true $\sigma_{v,\text{true}}$ and nominal σ_v flow stresses can be expressed as $\sigma_{v,\text{true}}=\lambda\sigma_v$, and hence, by substitution of eq. 4.6 into 4.3, η_v can be expressed as

$$\eta_v = \frac{\sigma_v \lambda \dot{\lambda}_{\text{eff}}}{\dot{\lambda}_{\text{eff}}} \quad (4.7)$$

4.5 Constitutive modelling

This section describes the implementation of a constitutive model incorporating the experimental observations stated above: (1) an additive decomposition of stress into elastic and viscous components; (2) the need for an effective stretch to account for permanent set; (3) network elasticity evolving with maximum stretch; and, (4) a stretch-dependent viscosity. In addition, the behaviour within viscoelastic transients will be considered to complete the model.

The proposed model, illustrated in Figure 4.5, is a modified viscoelastic standard linear solid (SLS) model in series with a custom ‘slider’ element representing the permanent set. The modified SLS model consists of an EV hyperelastic spring in parallel with a non-linear Maxwell element. The non-linearity of the Maxwell element arises from the non-linearity of the dashpot viscosity.

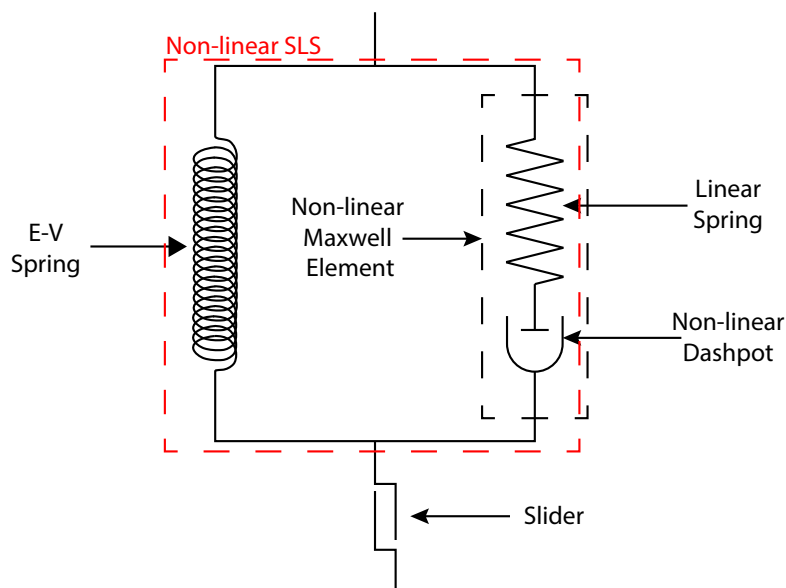


Figure 4.5: A modified viscoelastic standard linear solid (SLS) model in series with a slider intended to represent permanent set. The SLS part of the model consists of an Edwards-Vilgis hyperelastic spring in parallel with a linear spring and a non-linear dashpot.

4.5.1 Model elements

4.5.1.1 Slider

In the proposed model, λ is decomposed into λ_{eff} and λ_{set} *via* a multiplicative decomposition as described in (2). The significance of λ_{eff} in this model is that it refers to the stretch that the EV spring and the Maxwell element actually experience. The permanent set here represents the combined effects of irreversible deformation experienced by rubber and filler combined. It is modelled by a slider as shown on Figure 4.5 whose stretch is, for the case of simple uniaxial deformation dealt with here, dependent on a monotonic function of λ_{max} . To cover more general cases this may need to be a more complex tensorial function of time, temperature and deformation history.

4.5.1.2 Non-linear Maxwell element

The viscoelastic behaviour exhibited by the elastomer arises from local bond stiffness and viscous flow of monomer segments past each other and past the filler. Here it is modelled by a non-linear Maxwell element consisting of a linear elastic spring in series with a non-linear dashpot, as shown in Figure 4.5. The governing differential equation for this element is

$$\dot{\sigma}_M + \frac{\sigma_M}{\tau} = \dot{\lambda}_{\text{eff}}E \quad (4.8)$$

where σ_M is the stress in the Maxwell element, $\dot{\sigma}_M$ is the stress rate, τ is a relaxation time, and E is the stiffness of the linear spring. The relaxation time τ is given by $\eta_v/\lambda\lambda_{\text{eff}}E$, where $\eta_v(\lambda_{\text{eff}})$ is the viscosity of the dashpot, which itself is a function of the effective stretch λ_{eff} , i.e. the viscosity master curve.

4.5.2 Parameter evolution

The values and uncertainties (expressed as 95% confidence intervals) of N_S , η , α and λ_{set} obtained from the optimisations carried out on the equilibrium contributions are illustrated on Figure 4.6, for the full range of experiments carried out to different λ_{max} . At small values of λ_{max} , there is considerable uncertainty on these parameters due to the limited strain range of equilibrium data away from transients, i.e., a small data set. All parameters exhibit a dependence on λ_{max} , suggesting that the maximum level of deformation

influences all aspects of the elastic network. To describe this evolution, simple mathematical functions were fitted to the parameters as shown in Figure 4.6, for values of $\lambda_{\max} \geq 2.5$ only. Several forms of these functions were explored, and the functions selected are by no means unique, but provide simple and numerically stable representations of the parameter evolutions.

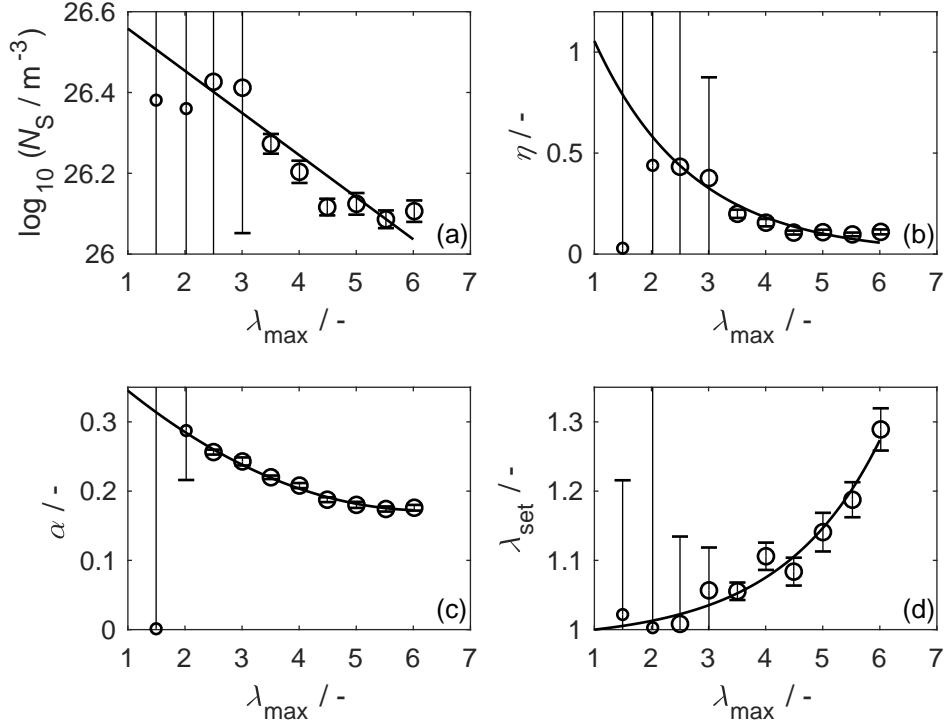


Figure 4.6: The evolution of (a) slip-link density N_S , (b) slip-link mobility η , (c) chain inextensibility α , and (d) permanent set λ_{set} with pre-deformation λ_{\max} . The parameters extracted from the elastic contributions are shown as circles. The corresponding uncertainties (95% confidence interval) are also shown. To describe the evolution of these parameters, simple functions (lines) are fitted to the extracted parameter values as functions of for $\lambda_{\max} \geq 2.5$ (larger circles).

The forms of the functions selected to describe the evolution of the EV

parameters and of λ_{set} are

$$\log_{10}(N_S) = C_{1,N_S} \lambda_{\text{max}} + C_{2,N_S} \quad (4.9)$$

$$\alpha = C_{1,\alpha} \lambda_{\text{max}}^2 + C_{2,\alpha} \lambda_{\text{max}} + C_{3,\alpha} \quad (4.10)$$

$$\eta = C_{1,\eta} \exp(-C_{2,\eta}(\lambda_{\text{max}} - 1)) \quad (4.11)$$

$$\lambda_{\text{set}} = 1 + C_{1,\text{set}}(\exp(C_{2,\text{set}} \lambda_{\text{max}}) - \exp(C_{2,\text{set}})) \quad (4.12)$$

To ensure that the permanent deformation is zero for virgin specimens, the condition $\lambda_{\text{set}} = 1$ at $\lambda_{\text{max}} = 1$ is applied to an exponential equation of the form $\lambda_{\text{set}} = C_{3,\text{set}} + C_{1,\text{set}} \exp(C_{2,\text{set}} \lambda_{\text{max}})$, resulting in eq. 4.12. The estimates and the standard uncertainties for the coefficients of the equations were obtained from the regression analysis conducted on MATLAB and are reproduced in Table 4.1.

Table 4.1: Estimate ± 1 standard uncertainty for the coefficients of equations 4.9 - 4.13 describing the evolutions of the elastic parameters: slip-link density N_S , chain inextensibility α , slip-link mobility η , and of the permanent set λ_{set} , and of the viscosity η_v , as a function of maximum stretch λ_{max} .

Parameters	Coefficients	
$\log_{10}(N_S)$	C_{1,N_S}	-0.104 ± 0.048
	C_{2,N_S}	26.662 ± 0.211
α	$C_{1,\alpha}$	0.006 ± 0.004
	$C_{2,\alpha}$	-0.079 ± 0.031
	$C_{3,\alpha}$	0.417 ± 0.063
η	$C_{1,\eta}$	1.055 ± 0.234
	$C_{2,\eta}$	0.586 ± 0.100
λ_{set}	$C_{1,\lambda_{\text{set}}}$	0.009 ± 0.006
	$C_{2,\lambda_{\text{set}}}$	0.577 ± 0.113
η_v	C_{1,η_v}	(0.411 ± 0.079) MPa s
	C_{2,η_v}	3.974 ± 0.148
	C_{3,η_v}	(7.379 ± 0.569) MPa s

4.5.3 Viscosity master curve

To describe the viscosity master curve as illustrated in Figure 4.4b, a function of the form

$$\eta_v = C_{1,\eta_v} \lambda_{\text{eff}}^{C_{2,\eta_v}} + C_{3,\eta_v} \quad (4.13)$$

is proposed, and parameters are obtained by minimising the error normalised with respect to the experimental data and provided in Table 4.1. The normalised error allows for a fair representation of η_v and is discussed in detail in Appendix A.5.

Different approaches have been proposed to describe viscosity within a rubber constitutive model. These approaches often modify the dashpot element within a generalised Maxwell framework to capture inelastic effects, for example see the work of Rendek and Lion [137], and Jalocha *et al.* [138]. Currently, to the authors' knowledge, despite the experimental evidence suggesting a Mullins-independent but stretch-dependent viscosity, such an implementation has not been previously attempted for elastomers.

4.5.4 Determination of the linear spring modulus

The non-linear Maxwell element includes a linear elastic spring that, together with the non-linear dashpot, describes the transient response of the viscoelastic arm of the model. In order to determine E , the response within the transient regions must be considered. One can determine E *via* the numerical evaluation of eq. 4.8 for the case of constant effective rate of deformation, where E is the only unknown.

The viscous contribution is obtained by subtracting the extrapolated elastic contribution predicted by the EV model from the experimental third loop response within the transient, i.e. $\sigma - \sigma_{EV}$. This is necessary because it is not possible to use the mean equilibrium experimental data within a transient. Figure 4.7a illustrates an example of the third loop experimental data and the model elastic response extrapolated into the transients. The stress resulting from the subtraction process is shown in Figure 4.7b.

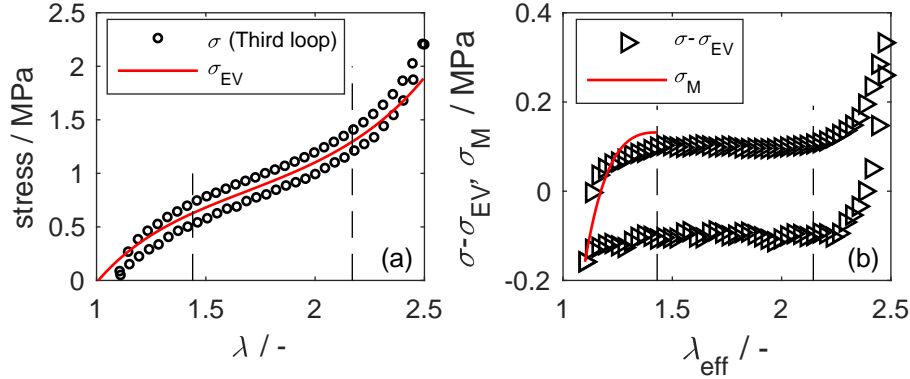


Figure 4.7: (a) The experimental third loop response (symbols) for a pre-deformation λ_{\max} of 2.5 and the model elastic contribution σ_{EV} (line). (b) Viscous contribution obtained by subtraction of the elastic stress obtained from the EV model (symbols) from the total experimental stress, as a function of the effective stretch. The Maxwell model response σ_M (line) is obtained by solving numerically the governing equation for the non-linear Maxwell element (eq. 4.8) and optimising for the spring stiffness E . The vertical dashed lines are used to identify the transition between transient and steady state portions of the data.

In order to obtain a suitable value of E , the loading portion of $\sigma - \sigma_{EV}$ is used in a least squares algorithm against a numerical solution for eq. 4.8. This procedure was implemented on all experimental data sets to obtain $E = 3.07 \pm 1.09$ MPa. Figure 4.7b shows an example of the experimental and model response transients for the case $\lambda_{\max} = 2.5$. Although the agreement between model and experiment is far from perfect, it should be noted that experimental data within the transients is noisy, and that for an accurate reproduction of the transients it is likely that a spectrum of relaxation times would be required. See Appendix A.6 for the corresponding fits and optimised E values for the full range of λ_{\max} explored.

4.6 Results

4.6.1 Simulation of the third loop response

Once all model parameters have been obtained, they can be employed in generic simulations of the response. A comparison between the experimental and model third loop responses is shown on Figure 4.8 for five λ_{\max} levels

ranging from 2 - 6. Using a single set of model parameters, some of which evolve with λ_{\max} , simulation and experimental data are generally in good agreement, with the shape of the curves and the degree of permanent set matching reasonably well for all levels of stretch.

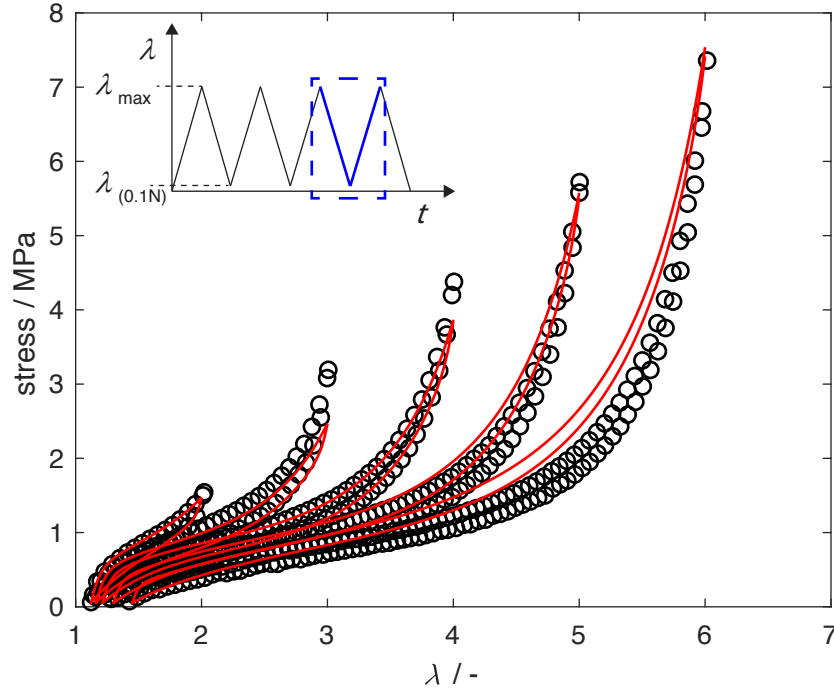


Figure 4.8: Comparison of experimental (symbols) and model (lines) third loop response for five pre-deformation λ_{\max} levels between 2 and 6. The inset shows the deformation history imposed on the specimens, the third unload-reload loop is shown in blue.

4.6.2 Simulation of more complex deformation histories

To probe the capability of the model, it was subjected to complex loading conditions probing cycles within a previously defined maximum stretch. Two protocols are employed, both of which condition the material by subjecting it to three cycles through to $\lambda = 4$. The first protocol (TP5) is followed by load/unload loops, where the specimen is loaded to increasing stretch levels

and always unloaded (to 0.1N). The second protocol (TP6) starts at the maximum of 4, and unloads to progressively smaller λ , always reloading to $\lambda = 4$. The two protocols are shown in the insets of Figure 4.9 and Figure 4.10. The protocols have been named TP5 and TP6 to keep consistent with work completed previously in our laboratory.

Comparisons between the experimental and the model responses for TP5 and TP6 are shown on Figure 4.9 and 4.10, respectively. The primary loading is also shown here, and it can be seen that the model underestimates the stress in the latter stages of the loading. Beyond the initial loading, during the cycles, the model reproduces the stress well during the remaining deformation histories, although the transient responses saturate somewhat faster in the simulations compared to the experiments.

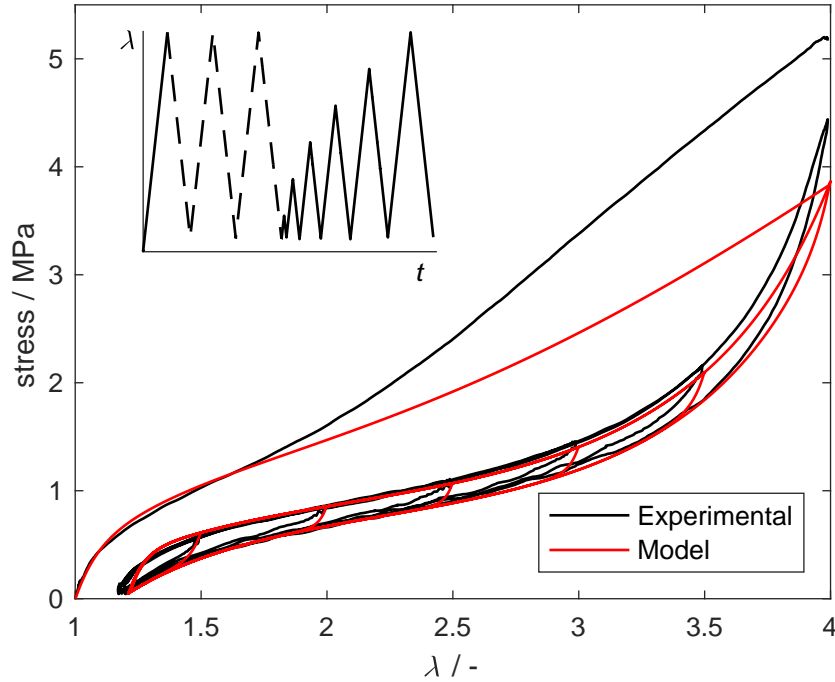


Figure 4.9: A comparison between the experimental and model responses for TP5. The protocol consists of three uniaxial load/unload cycles, followed by five reload/unload loops and a reload/unload cycle, as shown in the inset. The dashed line in the inset represents the data that has been omitted from the plot.

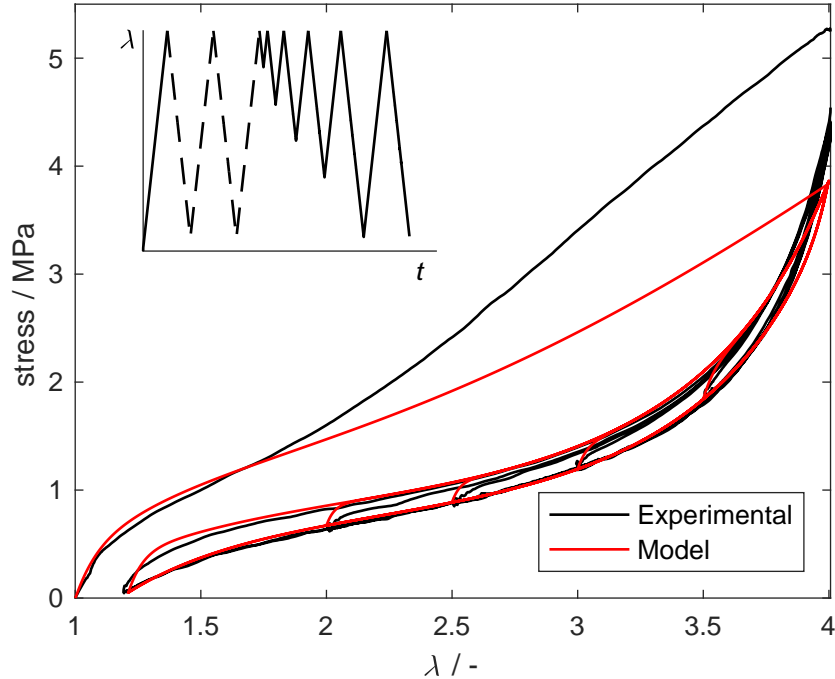


Figure 4.10: A comparison between the experimental and model responses for TP6. The protocol consists of two uniaxial load/unload cycles, a reload step, four unload/reload loops, and lastly an unload/reload cycles and an unload step, as shown in the inset. The dashed line in the inset represents the data that has been omitted from the plot.

4.7 Discussion

4.7.1 Post-Mullins response

The model parameters were obtained by the use of cyclic experimental data sets, each of which remains within a pre-defined value of λ_{\max} . Thus, it is perhaps not surprising that the third unload-reload loops are reproduced to a good degree of accuracy. It should be noted, however, that the model does overestimate the stress for large values of λ_{\max} . This overestimation is attributed primarily to the combined inaccuracies arising from the functions describing the evolution of the EV parameters. It is possible that selection of more complex functions may lead to a better overall fit, but at the expense

of an increase in the number of constants. What is particularly encouraging is the agreement in the energy dissipated per cycle between simulation E_C^{mod} and experiment E_C^{exp} , illustrated in Figure 4.11. This is of interest in damping applications, and it shows that the model can accurately account for changes to dissipation arising as a result of changes to the constitutive behaviour associated with the Mullins effect.

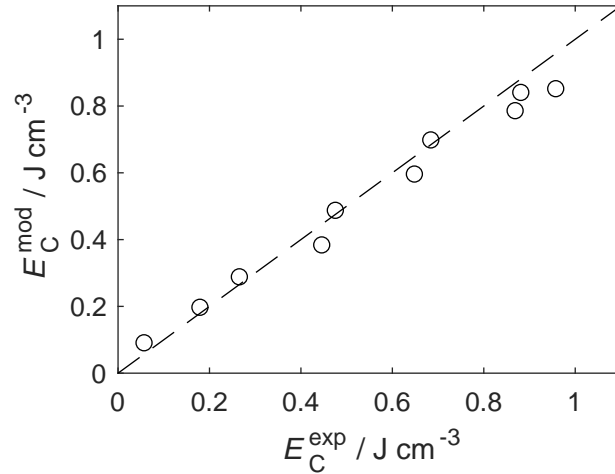


Figure 4.11: A comparison of the experimental E_C^{exp} and model E_C^{mod} energy dissipated by the third loop.

A further analysis of the dissipated energy can be obtained by considering the more complex deformation histories explored in Figure 4.9 and Figure 4.10. E_C^{exp} and E_C^{mod} are compared in Figure 4.12, and again show generally a good level of agreement. The model overpredicts the energy dissipated by a small fraction, and this is attributed to the discrepancy in the transient behaviour noted in Figure 4.9 and Figure 4.10.

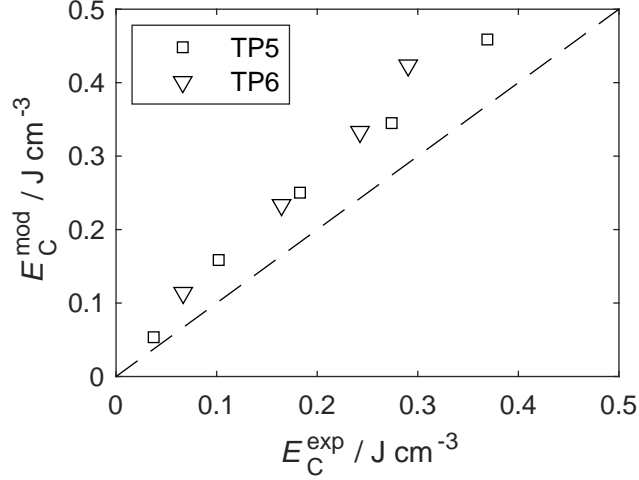


Figure 4.12: Comparison between the dissipated energy obtained from experimental E_C^{exp} and model E_C^{mod} loops in complex loading histories TP5 (square) and TP6 (triangle).

4.7.2 Pre-mullins response

Although the virgin loading response is never employed in obtaining the model parameters, it can be obtained from the model by extrapolation of the E-V parameters to zero strain. This allows for a comparison between the model and experimental first loading as highlighted on Figure 4.9 and Figure 4.10. It is apparent that there is an increasing discrepancy in the stress for $\lambda > 2$, and the model underpredicts the stress during the first loading. It is plausible that the changes occurring when the material is exceeding its previous λ_{max} (i.e. when $\lambda_{\text{set}} = 0$ and model parameters are evolving) might themselves be associated with a dissipative and time-dependent process. This would not be surprising since there is evidence in the literature of Mullins recovery [48].

In line with the above idea, one approach to achieving a larger stress during the first loading could be to include an additional viscosity dependent on $\dot{\lambda}_{\text{set}}$. A stress defined in this way would only be present during the initial loading stage, and hence not impact the rest of the simulations. This concept will be explored in detail below. Other approaches, such as the implementation of a strain amplification factor, can give rise to different first loadings, as proposed by Mullins and Tobin [3].

4.7.2.1 Set rate dependent viscosity

As stated previously, the discrepancy in the stress-stretch response during the initial loading case is a drawback of the model. This discrepancy could be time-dependent in nature, one approach to address this issues is to incorporate a flow stress $\sigma_{f,set}$ that is dependent on set rate $\dot{\lambda}_{set}$. λ_{set} , and thus $\dot{\lambda}_{set}$, only evolves when λ exceeds λ_{max} , therefore, all the previous results, except the initial loading case, remain unaffected.

To implement a flow stress, the viscosity associated with the stress must be determined. Firstly, the discrepancy between the experimental and model uniaxial monotonic stress-stretch response is calculated by interpolating the experimental and model data at small λ intervals, and then subtracting them. This discrepancy is assumed to be $\sigma_{f,set}$. $\dot{\lambda}_{set}$ is then determined by numerically differentiating λ_{set} with respect to time for uniaxial case. Linear interpolation is utilised again to determine $\dot{\lambda}_{set}$ at the same λ intervals as the stress discrepancy. The evolution of $\sigma_{f,set}$ and $\dot{\lambda}_{set}$ are shown of Figure 4.13. η_{set} can then be computed by dividing the true $\sigma_{f,set}$ by the true $\dot{\lambda}_{set}$. For the relationships between the nominal and true stresses and strain/stretch rates, the readers are referred to section 4.4. The evolution of η_{set} with λ is illustrated by Figure 4.14.

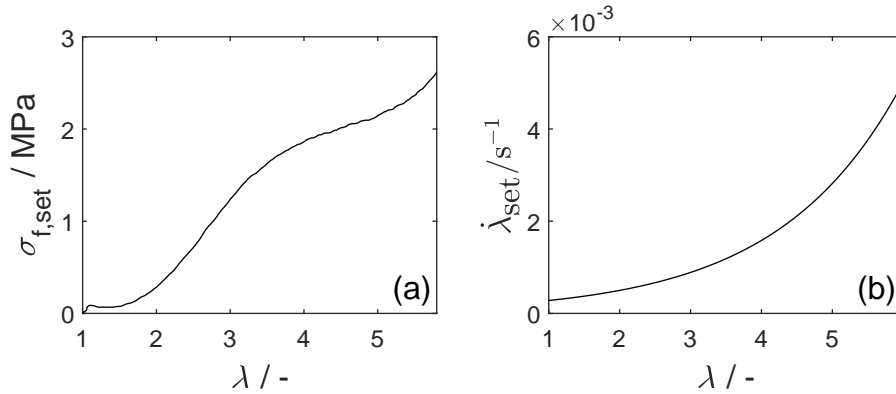


Figure 4.13: The evolution of (a) flow stress $\sigma_{f,set}$ and (b) set rate $\dot{\lambda}_{set}$ with stretch.

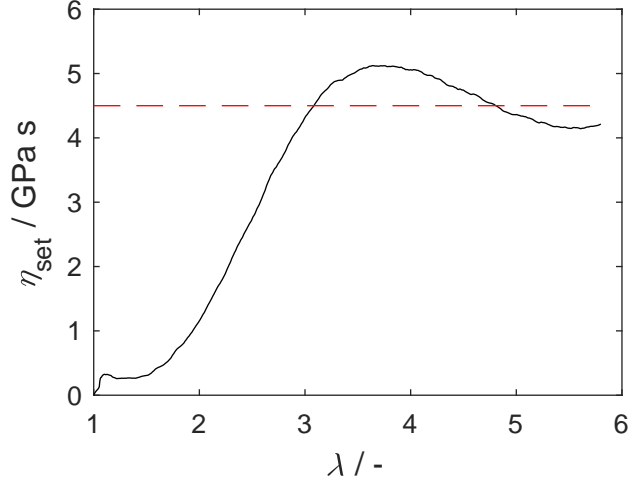


Figure 4.14: The evolution of viscosity associated with set with increasing stretch λ . A constant η_{set} is utilised within the constitutive model for simplicity and is represented as a dashed line on the plot.

For simplicity, η_{set} is modeled as a constant with a value of 4.5 GPa s. $\sigma_{\text{f,set}}$ can now be determined by multiplying the constant η_{set} by the true $\dot{\lambda}_{\text{set}}$ and the reciprocal of λ . The model is then determined by the summation of σ_{EV} , σ_{M} and $\sigma_{\text{f,set}}$. The initial loading response is recomputed and illustrated on Figure 4.15. A spike in the model stress levels is observed for λ values of up to 3, a good agreement is seen thereafter. The initial overshoot of stress can be avoided by modelling η_{set} as a more complex function of λ ; this approach is illustrated in Appendix. A.7.

The overshoot could also be partly attributed to deformation that results from the material preparation, i.e., compression moulding. Similar overshoots are observed when previous maximum strain histories are exceeded as demonstrated by Figure 2.10. For example, the process of peeling the compression moulded sheet from the mould, as illustrated on Figure 4.16, causes a deformation. This deformation can be approximated using theory from solid mechanics,

$$\epsilon = \frac{t_{\text{s}}}{2R_0} \quad (4.14)$$

where ϵ is the strain seen by the material, t_{s} is the thickness of the material and R_0 is the radius of curvature. If 0.5 mm and 1 mm are taken as representative values for t_{s} and R_0 , respectively, ϵ can reach values of 0.25 (or 25%).

It should be noted here that the bending theory is a linear theory, i.e., only applicable for very small strains. A prediction of 25% strain shows that this is beyond the remit of the linear bending theory. Nonetheless, this theory is still a good first consideration. Furthermore, the strains experience throughout the thickness of the specimen will vary due to the bending. Alongside peeling, the compression moulding process itself subjects the material to a complex strain and temperature history. The specimens prepared from these materials are therefore never in their theoretical state.

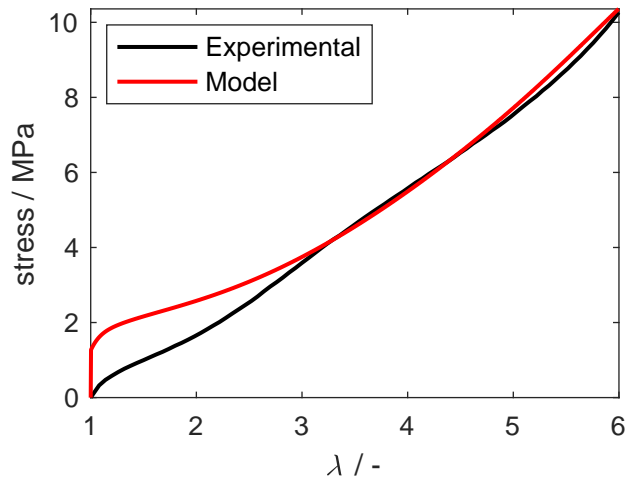


Figure 4.15: A comparison of the experimental and model initial (or virgin) loading behaviour. The model stress is obtained by the summation of σ_{EV} , σ_M and $\sigma_{f,set}$.

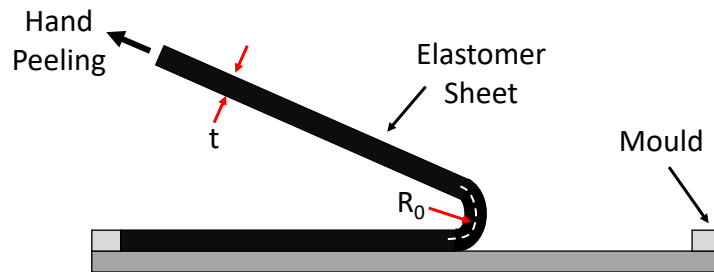


Figure 4.16: An illustration of a compression moulded specimen being peeled off. The key parameters required to calculate the deformation are highlighted on the diagram.

4.8 Summary

In this chapter, the impact of pre-deformation on the stress-strain response of EPDM was studied using uniaxial cyclic tensile tests. Following initial loading, a significant difference in the stress-strain response of the subsequent cycles is noted. This effect is known as the Mullins phenomena. By decomposing the third unload-reload loops of each uniaxial tensile cyclic test into equilibrium and viscous contributions, a constitutive model is formed to describe the impact of deformation history on the mechanical response. The equilibrium contribution evolves with pre-deformation. This evolution is captured by evolving Edwards-Vilgis model parameters and permanent set. The viscous contribution forms a master curve once the permanent set is accounted for; it is described by a non-linear Mullins-independent but strain dependent flow stress. The novelty of the model arises from the use of the viscosity master curve. The approach described also presents a straightforward route to obtaining the relevant parameters from cyclic experimental data.

The model reproduces the cyclic response of the deformation histories explored in this study to a good level of accuracy. The model is also able to accurately predict the dissipated energy per cycle and its change with increasing levels of pre-deformation. Where cycles are smaller in amplitude, and dissipated energy is more influenced by transients, accuracy of predictions is reduced since the model employs a single relaxation time.

When the prediction of the initial loading is compared to experimental data, the model underestimates the stress at larger strain levels. In practical applications, where elastomeric products are often scragged (i.e., subjected to pre-deformation), this limitation is less relevant, and the focus is always on the cyclic response, and how it changes with different scragging level, something which the model predicts well.

5. The influence of deformation history on the mechanical response - part II

In the previous chapter, a constitutive model was developed to study the impact of deformation history on the mechanical response. In this chapter, the modelling framework is applied to three more materials. Alongside this, further steps are taken to optimise the model and reduce the experimental effort required to fit the model to data.

The materials, materials preparation and the experimental methods used in this chapter are presented on section 5.2. In section 5.3, the experimental data is decomposed into elastic and viscous components. The evolution of the elastic and viscous components with stretch and maximum pre-deformation are then considered. The constitutive models are developed in section 5.4, and their responses are examined in section 5.5. The discussion is presented on section 5.6, key themes include: 1) the post-Mullins response, i.e., the response following deformation, 2) the pre-Mullins response (or virgin loading) response, 3) the impact of varying the amount of transient data discarded on the resulting model, and 4) the feasibility of using pseudo-cyclic tests instead of cyclic tests in the model development process. Lastly, conclusions are provided in section 5.7.

5.1 Introduction

As stated previously, elastomers are used in a wide range of applications, for example seals, gaskets and cable jackets, to name a few. The operating conditions, such as temperature, pressure and media, determine the elas-

tomers to be used in particular applications. Typically, elastomer products are scragged, i.e., pre-conditioned to a large strain to avoid changes in the mechanical response due to the Mullins phenomenon. It is therefore advantageous if models are capable of capturing the mechanical response following pre-conditioning (or pre-deformation) of various elastomers.

In the previous chapter, a constitutive model was developed by decomposing uniaxial cyclic tensile data from compressions moulded EPDM specimen into equilibrium (or elastic) and viscous contributions. The elastic contribution was shown to evolve with increasing λ_{\max} , and the viscous contribution was shown to form a master curve once λ_{set} is accounted for. The model was shown to be able to reasonably reproduce the mechanical response of elastomers following the scragging process. The model also provided an excellent prediction of the energy dissipated following the scragging process.

This chapter extends the work carried out in chapter 4 and explores the applicability of modelling approach to various other materials including sheet rolled CR, EPDM and NBR. To differentiate from the compression moulded EPDM, the sheet rolled EPDM material will be referred to as EPDM2 henceforth. Alongside this, the impact of the amount of transient data discarded is also investigated. Another question that is raised in this chapter is whether if the experimental effort required to fit the model to data can be reduced by the means of pseudocyclic tests.

5.2 Materials and methods

5.2.1 Materials and specimen preparation

Three different sheet rolled rubber materials, CR, EPDM2 and NBR, obtained from J-Flex Rubber Products were used in this study. These materials were reinforced with carbon black, and $\sim 31\%$, 35% and 23% of the CR, EPDM2 and NBR compound, respectively, is carbon black (mass%), as revealed by the thermogravimetric study conducted by Fernandes [35]. The sheets were ~ 0.5 mm in thickness. Uniaxial tensile test specimens were cut from the sheet using a hand operated Wallace specimen cutting press fitted with a dumbbell shaped cutter 1BA according to BS ISO 527-2. The thickness of the specimens were measured using the rubber thickness gauge and a calibrated scanner was used for the width measurement. The reader is referred to chapter 3 for details on specimen measurement.

5.2.2 Mechanical testing

The mechanical tests were performed on an Instron 5969 tensile testing machine equipped with a 5kN load cell and an Instron counterbalanced travelling extensometer. The clamps of the extensometer, 20 mm apart, were attached to the specimen gauge length. Care was taken to ensure that the clamps were central to the specimen. The extensometer was used to accurately determine the actual deformation experienced by the specimen. Two different mechanical tests were performed: cyclic and pseudocyclic. In all cases the tests were performed at a strain rate of 0.03 s^{-1} , at room temperature (24 ± 1) °C and the specimen were always unloaded to a stretch corresponding to a load of 0.1 N ($\lambda_{0.1\text{N}}$) to prevent buckling.

The cyclic tests were performed on all compounds, the procedure utilised is identical to that specified on the previous chapter. However, λ_{max} values explored for each compound differ. For CR, ten different λ_{max} increments between 1.25 and 3.5 inclusive were used. For EPDM2, the increments used were identical to that of the EPDM1 material in the previous chapter, and ten different λ_{max} increments between 1.5 and 6 inclusive were used. For NBR, ten different λ_{max} increments between 1.4 and 2.3 inclusive were used. The deformation history, and the representative stress-stretch response to cyclic loading for CR, EPDM2 and NBR are presented on Figure 5.1a-d.

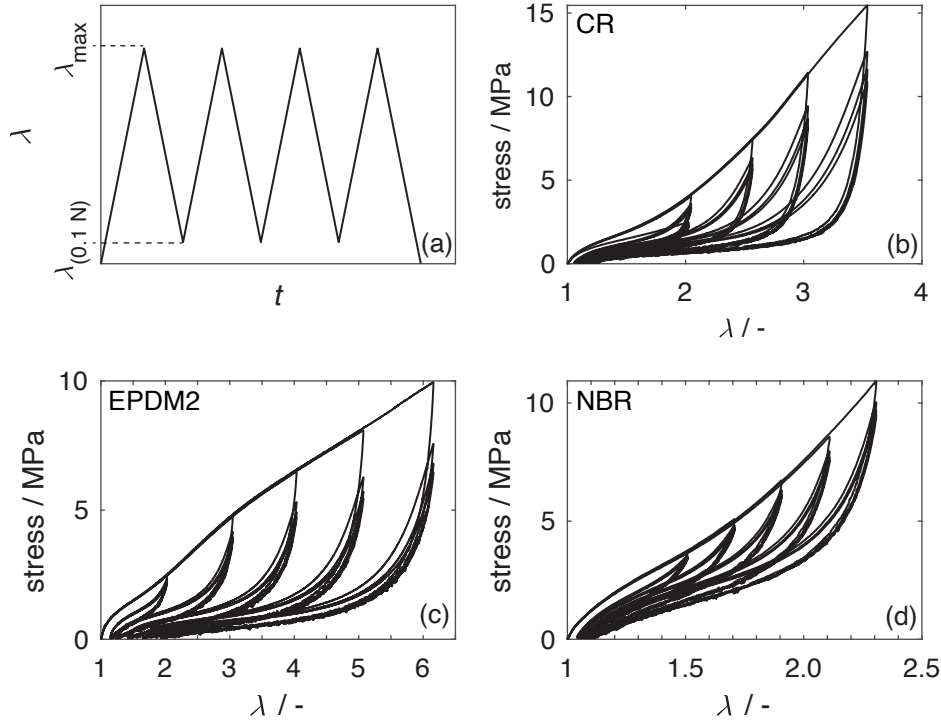


Figure 5.1: (a) The deformation history used for the cyclic tests consisting of four load-unload cycles. The specimen are unloaded to a stretch corresponding to a load of 0.1 N ($\lambda_{0.1N}$) to prevent buckling. A virgin specimen was used for each test. The stress-stretch response of selected (b) CR, (c) EPDM2, and (d) NBR specimens subjected to cyclic loading.

The pseudocyclic test were only performed on EPDM2 specimens. In a pseudocyclic test, a single specimen is used to explore all λ_{\max} increments. The increments used are the same as those explored for the cyclic tests. To account for the Mullins phenomenon, the deformation scales from the smallest to the largest value and at each increment the specimen is subjected to four load-unload cycles. Two different pseudocyclic tests were conducted, one with a ten minute pause prior to transitioning onto a larger λ_{\max} increment and one without the pause. During the pause the stretch was maintained at $\lambda_{0.1N}$. The pseudocyclic tests take a significantly longer time period to complete versus a cyclic test. This means that there is an opportunity for a gradual build-up of heat during a pseudocyclic test. By comparing the

results from the pseudocyclic tests with and without a pause, the impact of any gradual build-up of heat can be assessed. The deformation histories and the resulting stress-stretch responses are illustrated on Figure 5.2 and 5.3.

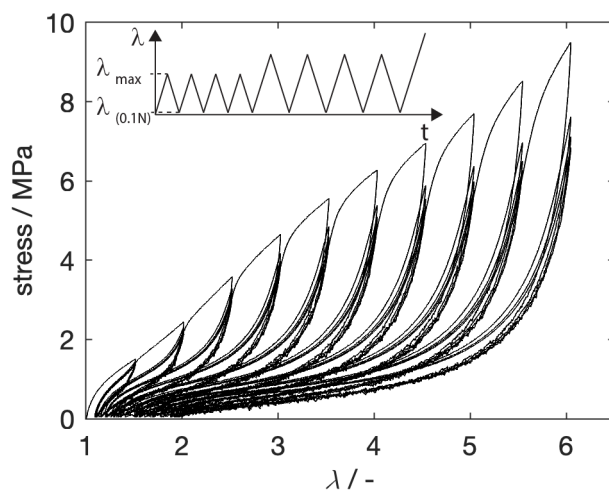


Figure 5.2: The stress-stretch response of a EPDM2 specimen subjected to pseudocyclic loading, as shown in the inset, to ten linearly spaced λ_{\max} values between 1.5 and 6 inclusive. At each λ_{\max} increment the specimen is subjected to four load-unload cycles. To prevent buckling the specimens are unloaded to a stretch corresponding to a load of 0.1 N ($\lambda_{0.1N}$).

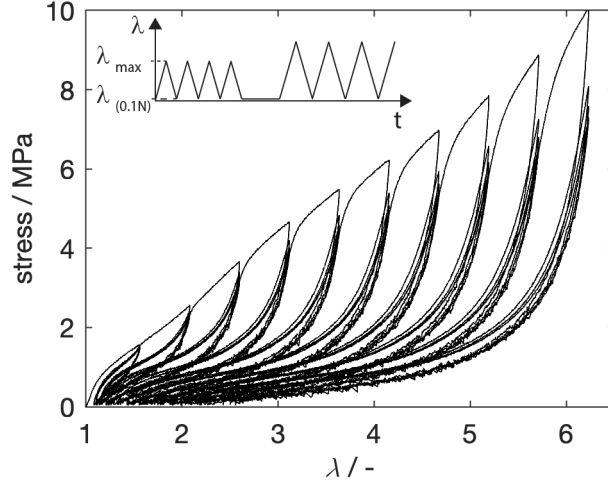


Figure 5.3: The stress-stretch response of a EPDM2 specimen subjected to pseudocyclic loading, as shown in the inset, to ten linearly spaced λ_{\max} values between 1.5 and 6 inclusive. At each λ_{\max} increment the specimen is subjected to four load-unload cycles. A ten minute pause is implemented prior to transitioning onto the next λ_{\max} increment. To prevent buckling the specimen is unloaded to a stretch corresponding to a load of 0.1 N ($\lambda_{0.1N}$).

The characteristic behaviours observed for filled elastomers, such as stress-softening, permanent set and hysteresis, are present in both the cyclic and pseudocyclic tests.

5.3 Analysis of experimental data

The procedure utilised to decompose the experimental data into equilibrium σ_e and viscous contributions σ_v , for the most part, remains identical to that of the previous chapter. The decomposed data for CR, EPDM2 and NBR are shown on Figs. 5.4 and 5.5. An EV function (Eq. 4.2), accounting for λ_{set} *via* a multiplicative decomposition of λ (Eq. 4.1), was fitted to σ_e for all values of λ_{\max} . Prior to fitting, 0.33 strain were discarded from the lower and upper stretch limits of the equilibrium contributions to account for transients. Due to the limited data available for NBR as a consequence of the maximum stretch to failure being small, the amount discarded in this instance has been reduced to a strain of 0.20 (either side). A good fit was achieved in all cases.

For CR, EPDM2 and NBR the RMS errors were typically of the order of 0.02, 0.01 and 0.01 MPa, and always less than 0.04, 0.02 and 0.03 MPa, respectively. In all cases, the RMS errors were $\sim 0.3\%$ of the maximum stress observed during the third loop.

In most instances, once λ_{set} is accounted for, σ_v is shown to form a master curve, the only exception being CR, as illustrated on Figure 5.5b. The absence of a master curve is attributed to the fact that λ_{set} was not accurately captured by the EV model. The model predicts zero permanent set as shown on Figure 5.1b. A similar observation can be made for NBR. However, the formation of a master curve is not impacted here due to the small permanent deformation experienced by the material. For EPDM2, in the pseudocyclic case with a pause, more scatter in the viscous contribution is observed at large values of λ_{eff} , as shown in Figure 5.4f.

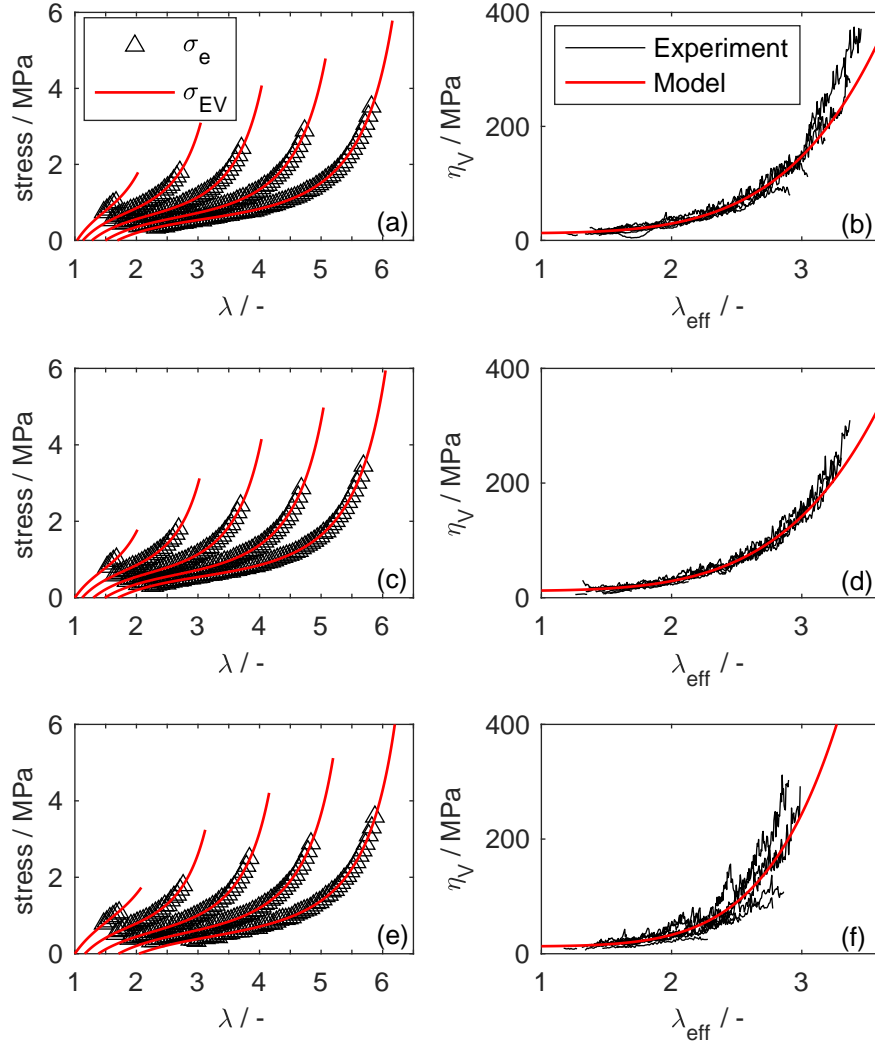


Figure 5.4: The experimental σ_e (symbols) and model σ_{EV} (lines) equilibrium contributions as a function of stretch for EPDM2 subjected to (a) cyclic tests, (c) a pseudocyclic test, and (e) a pseudocyclic test with pauses. The model is an EV function accounting for λ_{set} . The viscosity η_v as a function of λ_{eff} for EPDM2 subjected to (b) cyclic tests, (d) a pseudocyclic test, and (f) a pseudocyclic test with pauses. When expressed as a function of λ_{eff} , the viscosity data overlay to form a master curve. A simple function is fitted to describe the viscosity master curve.

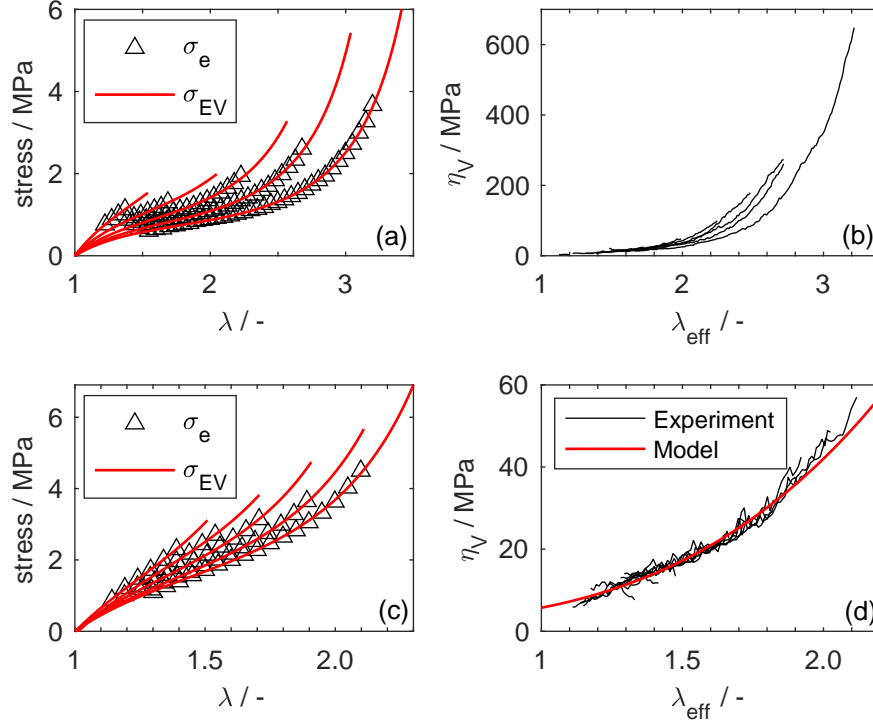


Figure 5.5: The experimental σ_e (symbols) and model σ_{EV} (lines) equilibrium contributions as a function of stretch for (a) CR and (c) NBR. The model is an EV function accounting for λ_{set} . The viscosity η_V as a function of λ_{eff} for (b) CR and (d) NBR. When expressed as a function of λ_{eff} , the viscosity data overlay to form a master curve. A simple function is fitted to describe the viscosity master curve.

5.4 Constitutive modelling

The constitutive modelling methodology developed in chapter 4 has been applied to develop the models for EPDM2 and NBR. As a viscoelastic master curve could not be realised for CR, a model was not developed.

5.4.1 EV parameter evolution

The parameters and corresponding uncertainties extracted from fitting the EV model, for EPDM2 cyclic and pseudocyclic cases, are comparable with that of the compression moulded EPDM1 on the previous chapter. These plots will therefore not be reported in the main text but can be found on Appendix A.8. For the pseudocyclic case with a pause, the evolution of α , η and N_S were not as smooth as the other cases involving EPDM and can be observed on Figure 5.6.

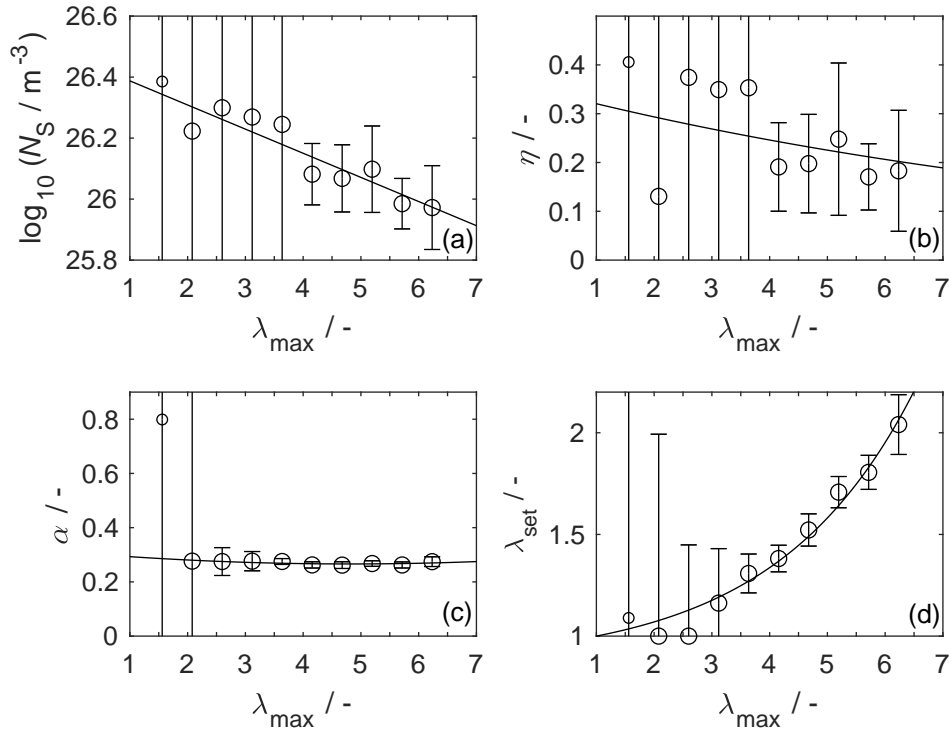


Figure 5.6: The evolution of (a) slip-link density N_S , (b) slip-link mobility η , (c) chain inextensibility α , and (d) permanent set λ_{set} with pre-deformation λ_{\max} for an EPDM2 specimen subjected to a pseudocyclic test with a pause. The parameters extracted from the elastic contributions are shown as circles. The corresponding uncertainties (95% confidence interval) are also shown. To describe the evolution of these parameters, simple functions (lines) are fitted to the extracted parameter values as functions of λ_{\max} for $\lambda_{\max} \geq 2$ (larger circles).

The evolution of the EV parameters for NBR have been illustrated on Figure 5.7 and are observed to be smooth. However, the observed uncertainties are significant. This is to be expected as the extension stretch for NBR is small ($\sim 130\%$) and therefore only a small number of data points were be available for the fitting procedure. For perspective, it should be noted that large uncertainties were also present in EPDM1 specimen for λ_{\max} values of up to 2.5. λ_{set} has been omitted from Figure 5.7 as model fitting suggested that permanent deformation does not occur, see Figure 5.5c, and therefore no evolution is required.

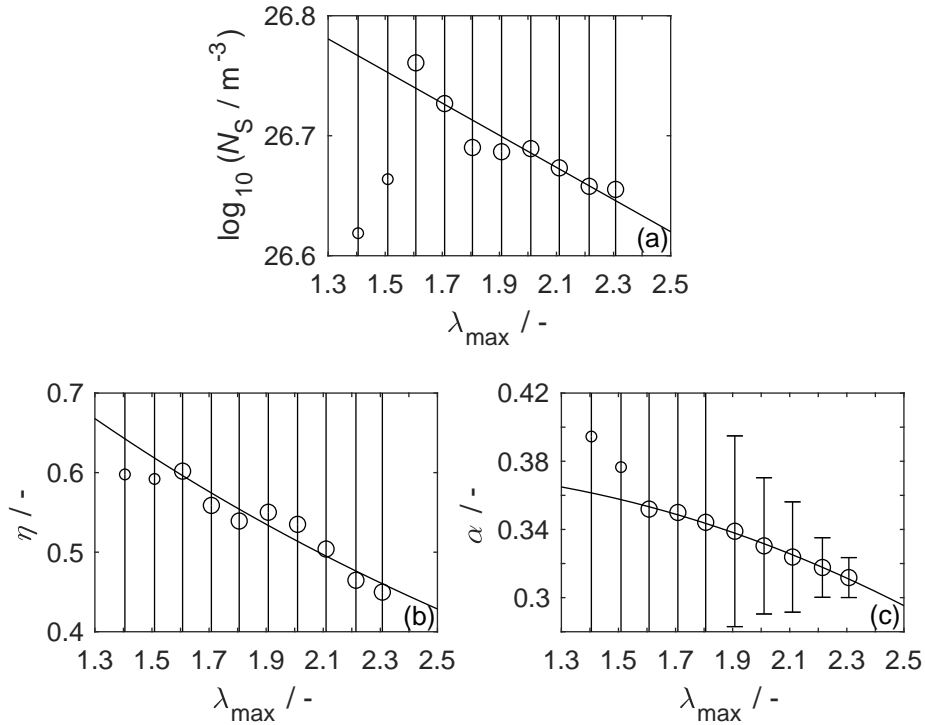


Figure 5.7: The evolution of (a) slip-link density N_S , (b) slip-link mobility η and (c) chain inextensibility α with pre-deformation λ_{\max} for NBR specimens. The parameters extracted from the elastic contributions are shown as circles. The corresponding uncertainties (95% confidence interval) are also shown. To describe the evolution of these parameters, simple functions (lines) are fitted to the extracted parameter values as functions of λ_{\max} for $\lambda_{\max} \geq 1.6$ (larger circles).

Table 5.1: Modulus (± 2 standard uncertainty) of the linear spring in the modified SLS model.

Materials	E / MPa
EPDM (Cyclic)	3.05 ± 0.48
EPDM (Pseudocyclic)	3.08 ± 0.43
EPDM (Pseudocyclic + Pause)	3.81 ± 1.35
NBR	4.76 ± 0.72

To describe parameter evolution, eqs. 4.9-4.12 were fitted. Using the same functions suggested in the previous chapter allows the generality of the evolution behaviour to be examined. A reasonable fit is achieved in all cases. The models describing the parameter evolutions for EPDM2 (pseudocyclic-pause) and NBR are shown on Figure 5.6 and 5.7, respectively. In some instances, it is evident that a better fit could be achieved by using an alternative function, i.e., a linear function for Figure 5.6c. The model fits corresponding the parameter evolution for the cases omitted here, alongside all the resulting coefficients (± 1 standard uncertainty) for all cases considered have been reported in Appendix A.8.

5.4.2 Viscosity master curve

A viscous master curve was observed for all EPDM and NBR cases as shown on Figure 5.4 and 5.5, respectively. Eq. 4.13 was fitted to describe this evolution. To ensure a fair representation the error was normalised with respect to the experimental data as stated in the previous chapter. The resulting coefficients (± 1 standard uncertainty) have been reported in Appendix A.8.

5.4.3 Linear spring modulus

By fitting eq. 4.8 to the transient portions of all the all EPDM and NBR cases, the linear spring modulus E could be determined. For EPDM, the initial 0.33 strain and for NBR the initial 0.20 strain. The resulting values can be seen on Table 5.1.

5.5 Results

5.5.1 Simulation of the third loop response

The developed models were used to probe the third loop response of the various materials, the comparisons are given on Figure 5.8. For EPDM2 and NBR, λ_{\max} increments between 2 and 6, and 1.5 and 2.1, respectively, were explored. Reasonable responses were achieved in most instances, with the exception of the pseudocyclic case with the pause for EPDM2 as illustrated on Figure 5.8c.

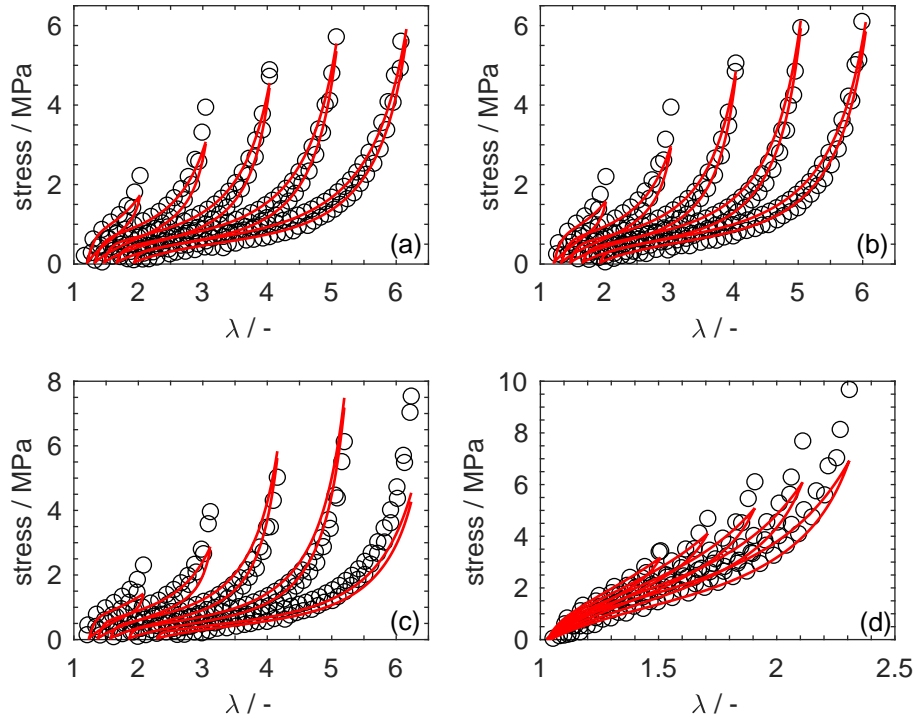


Figure 5.8: Comparison of the experimental (symbols) and model (lines) third loop response for EPDM2 ((a) cyclic, (b) pseudocyclic and (c) pseudocyclic with pause) and (d) NBR. In each instance, five different pre-deformation levels λ_{\max} out of ten have been highlighted.

5.6 Discussion

5.6.1 Post Mullins response

As previously stated in the results section, the model captures, to a reasonable degree, the third loop response for EPDM2, cyclic and pseudocyclic cases, and NBR. This is to be expected as experimental cyclic data were used to define the models. It should however be noted that at small levels of λ_{\max} , the EPDM2 cyclic and pseudocyclic models underestimate the stress as shown on Fig 5.8a & b. For the instance where a pause was introduced to the pseudocyclic test, the stress was underestimated at both small and large λ_{\max} values. At intermediate values of λ_{\max} , the stress is overestimated as illustrated by Figure 5.8c. The underestimation was present at all λ_{\max} levels for NBR as shown on Figure 5.8d. The underestimation or overestimation of the stresses are primarily associated with combined inaccuracies arising from the function describing the EV parameter evolution. While this problem can be addressed by the introduction of more complex functions to describe EV parameter evolution, the number of constants utilised in the model will also increase.

For EPDM2, notable difference can be observed in the evolution of the EV parameters and the viscosity master curve for the pseudocyclic case with the pauses when compared with the other two cases. The EV parameter evolution are less smooth and at large values of λ_{eff} , the experimental viscosities are seen to deviate from the master curve as shown on Figure 5.4f. These differences could be attributed to the changes occurring in the material during the pauses. To prevent buckling, the load is maintained at 0.1 N during the pauses, causing the sample to creep. While the stress observed for all EPDM2 cases is comparable, notable differences are observed in λ_{set} ; it is larger for the pseudocyclic case with the pauses. This is expected as the load applied to the sample during the pause stage is not fully removed until the completion of the test, therefore there is insufficient time for creep recovery to occur. In an ideal world, where the load can be held perfectly at 0 N, creep would not be an issue. In this scenario, the λ_{set} for the EPDM2 material subjected to a pseudocyclic case with a pause is expected to be similar to those observed for the cyclic case and the pseudocyclic case without the pauses. By using the λ_{set} associated with either the cyclic case or the pseudocyclic case without the pauses, it can be shown that the viscosities corresponding to the pseudocyclic case with pauses forms a master curve.

Thus, it is likely that creep is mainly responsible for the observed scatter in viscosities at large values of λ_{eff} as shown of Figure 5.9. It is likely that the lack of smoothness in the evolution of the EV parameters is also caused by creep. Both of these contribute to the discrepancies observed between the experimental and model third loop response.

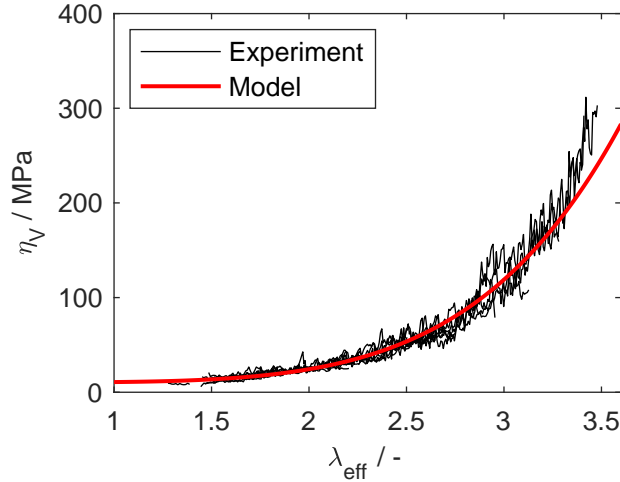


Figure 5.9: Viscosities obtained for the EPDM2 sample subjected to a pseudocyclic test with pauses. The λ_{set} utilised here corresponds to the λ_{set} obtained from fitting to the pseudocyclic EPDM2 case. In this instance the viscosities are seen to form a master curve.

The comparison of the energy dissipated in the third-loop response is more encouraging for both EPDM2 and NBR, as shown on Figure 5.10. For EPDM2, an excellent agreement between experimental and model energies exists for λ_{max} values of up to 5. Thereafter the model underestimates the dissipated energy. This is expected as the model viscosity master curve underestimates the observed experimental viscosity master curve. For NBR, the predicted energy dissipated is marginally underestimated by the model. By using a more complex function this could be addressed, however this will be done so at the expense of simplicity. The accurate estimation of energy dissipation following scragging, i.e., once the Mullins effect is accounted for, is useful for various damping applications.

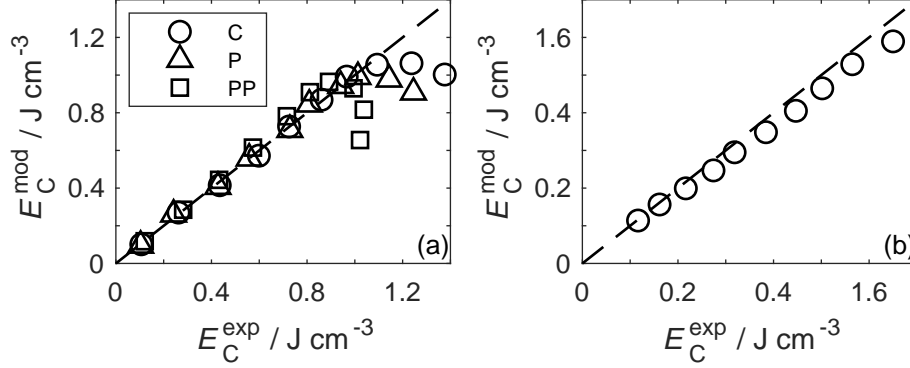


Figure 5.10: Comparison of the energy dissipated in the experimental and model third loop response for (a) EPDM2 (cyclic (circles), pseudocyclic (triangles), and pseudocyclic with pause (squares)) and (b) NBR.

5.6.2 Pre Mullins response

The initial loading response was not utilised in the development of the model; however, the initial loading response can be obtained by extrapolation of the EV parameter evolution models to a λ_{\max} value of 1, i.e., the virgin state. The experimental and model initial loading response for all EPDM2 cases and NBR are shown on Figure 5.11. A spike in the initial loading response is observed for the pseudocyclic cause with pauses as shown on Figure 5.11a. This spike is likely caused by a combination of creep and the combined inaccuracies in the functions describing EV model parameters. Besides this, the model stress is generally much lower than the experimental stress for both materials. It is plausible that the EV parameter evolution itself is dissipative and time-dependent in nature as evidenced in literature [48]. Another way to address, this issues is to implement a viscosity that is dependent of $\dot{\lambda}_{\text{set}}$ as suggested in the previous chapter.

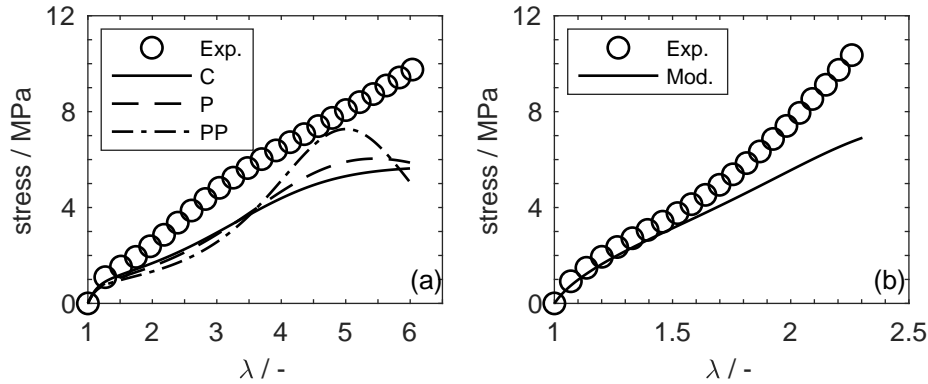


Figure 5.11: Comparison of the experimental (symbols) and model (lines) initial loading response for (a) EPDM2 and (b) NBR. For EPDM2, the models corresponding to cyclic, pseudocyclic and pseudocyclic case with a pause correspond to the solid, dashed and dash-dot lines, respectively.

5.6.3 Transient portion

The primary reason for discarding experimental data at the extremes is to ensure that the transient portions are removed. The main criterion is to ensure that sufficient data is removed to account for the transients, but not significantly more as this will hinder the fitting process and the quality of fit. The quality of fit is defined by the RMS error and uncertainties of the EV parameters. The impact of removing more data than necessary will reduce the RMS error as there are less points to compare, however it will increase the uncertainty in the EV parameter as illustrated on Figure 5.12a and b, respectively. The half width of the confidence interval (CI) for λ_{set} , as shown on Figure 5.12b, is used as a representative example to illustrate that the CI reduces when the amount of data available is increased, i.e., more confidence in the model parameters. The significance is less pronounced at larger values of λ_{max} , as regardless of whether 0.1, 0.2 or 0.33 of the initial and final strain are removed, sufficient data is still available to carry out the fitting process.

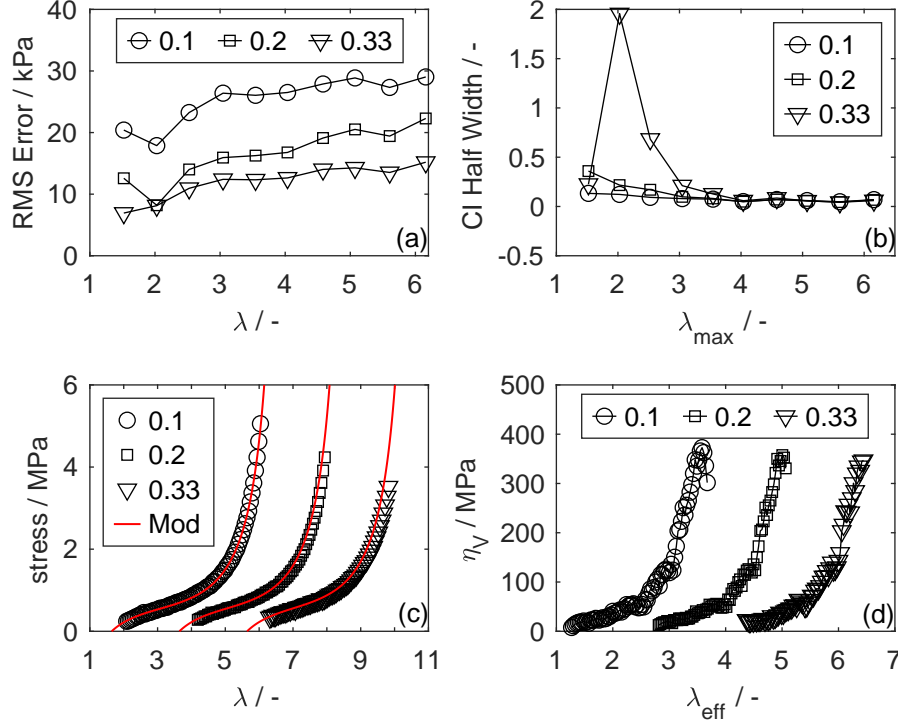


Figure 5.12: Comparison of the change in (a) RMS error, (b) confidence interval for λ_{set} , (c) elastic contribution (at $\lambda_{\text{max}} = 6$) and (d) viscosity η_v (at $\lambda_{\text{max}} = 6$) with varying amounts of strain discarded to account for transients. This data corresponds to the cyclic EPDM2 test.

The impact of the amount of data discarded to account for transients in σ_e and σ_v is illustrated on Figure 5.12c and d, respectively. Only the data corresponding to λ_{max} of 6 is presented. Each curve has been shifted by a λ of 2 and a λ_{eff} of 1.5 from each other, for σ_e and η_v , respectively. This allows for the comparison to be made on a single plot. The impact on σ_e is not obvious, unless the corresponding RMS errors and CI are studied as shown above. However, the impact on σ_v is evident, η_v is seen to drop at large λ_{eff} values when the amount of data discarded is decreased. This drop is associated with the transients and acts as a visual cue in to determine the amount of data that must be discarded. The data presented on Figure 5.12 is associated with the EPDM2 material, but a similar behaviour is also observed for NBR.

For EPDM, data corresponding to the initial and final 0.33 strain were discarded. To maintain consistency, initially, the same 0.33 strain either side were discarded for NBR. However, unlike for EPDM, no trends were observed in the evolution of the EV parameters with pre-deformation for NBR. This is to be expected, a combination of small strain levels explored for NBR and a large amount of data discarded to account for transients results in insufficient data available for the fitting process. To address this, only data corresponding to initial and final 0.2 strain were discarded for NBR.

Beyond the visual cues from η_v , how can one determine when transients are over? The transient response can be assumed to last for a time equivalent to three relaxation times 3τ ($= \eta_v/\lambda\lambda_{\text{eff}}E$). 3τ is chosen as the transient response reaches 99% saturation over this time period. Figure 5.13a and b illustrates the evolution of 3τ with λ for EPDM2 and NBR. The relaxation time is not a constant due to variations in the true strain rate and the viscosity. Alike η_v , τ is also a function of λ and can be seen to evolve with the cycles. NBR also evolves with the cycles but a combination of small λ and λ_{set} cause it to appear as a single line.

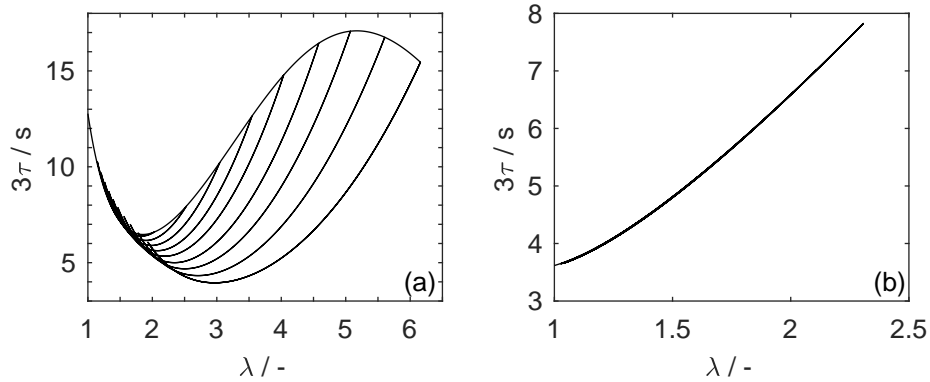


Figure 5.13: The change in relaxation time τ against stretch λ for (a) EPDM2 and (b) NBR. It is assumed that the transients are over in a time equivalent to three relaxation times, hence 3τ is used here.

The corresponding strain can then be determined by multiplying 3τ by $\dot{\lambda}$. The amount of data that is required to be discarded, for EPDM2 and NBR for a given λ_{max} value, to account for transients has been tabulated on Table 5.2. For EPDM2, at a λ_{max} of 1.5, the data suggests that transients can only be fully eliminated by discarding the entire dataset. Beyond λ_{max}

of 2, discarding the initial 0.33 strain was sufficient to capture the transients during the loading portion. For unloading, beyond λ_{\max} of 3.5, it is necessary to discard larger strains to ensure the transients is fully captured. Discarding the initial 0.20 strain is sufficient to capture the transients during the loading portion for NBR. For unloading, discarding the final 0.2 strain is sufficient for most λ_{\max} cases.

For EPDM2, discarding the final 0.33 strain was not sufficient to capture the transients during the unloading portion. A qualitative assessment of the EV parameter evolution and viscoelastic master curve for EPDM2 revealed that the impact of increasing the amount of final strain discarded is negligible. The data discarded for the loading portion was used to identify the linear spring stiffness E , since sufficient data was discarded for the loading section this value does not need to be recalculated for EPDM2 and NBR. This assessment of the transients reveals that there are opportunities for optimisation. For example, the amount discarded can be tuned for both the loading and unloading cases. One should note the process of guessing the amount of data to discard, defining the model, calculating E and determining τ is an iterative process. In both instances, we were able to identify a reasonable amount to discard initially so no further iterations were required in this instance.

5.6.4 CR

A model was not realised for CR. The fitting process utilised for the rubbery contribution revealed that the best fit, for all values of λ_{\max} explored, was achieved when the residual stretch equated to zero. As a result the viscoelastic master curve could not be formed. To address this issues the amount of data discarded to account for transients was reduced from an initial and final strain of 0.33 to 0.20 and then to 0.1. For the latter case, in a similar fashion to the data on Figure 5.12d, η_v was seen to fall at large values of λ_{eff} , indicating the presence of transient data. Even in this instance, the residual strain remained at zero.

A master curve for η_v is shown on Figure 5.14, the λ_{set} values utilised here were qualitative approximations obtained from the CR cyclic response. It is therefore evident that a master curve could be formed if λ_{set} can be predicted. The factors which hinder this include the small residual strain exhibited by CR and the model's inability to capture the sharp downturn observed when unloaded. One approach to address the latter issue is to trial different and

Table 5.2: A summary of the amount of data that must be discarded from the initial $\epsilon_{\text{discard,initial}}$ and final $\epsilon_{\text{discard,final}}$ portion of the strain range explored to account for transients, and the amount of data available $\epsilon_{\text{available}}$ for the fitting process once the transients is accounted for, for a given λ_{max} value. The data provided below corresponds to EPDM2 and NBR.

EPDM2			
λ_{max}	$\epsilon_{\text{discard,initial}}$	$\epsilon_{\text{discard,final}}$	$\epsilon_{\text{available}}$
1.5	0.38	0.21	0.00
2.0	0.31	0.20	0.32
2.5	0.29	0.24	0.74
3.0	0.28	0.30	1.14
3.5	0.26	0.38	1.51
4.0	0.25	0.44	1.89
4.5	0.24	0.49	2.29
5.0	0.22	0.51	2.68
5.5	0.21	0.50	3.12
6.0	0.20	0.46	3.57

NBR			
λ_{max}	$\epsilon_{\text{discard,initial}}$	$\epsilon_{\text{discard,initial}}$	$\epsilon_{\text{available}}$
1.4	0.11	0.14	0.13
1.5	0.11	0.14	0.23
1.6	0.11	0.15	0.31
1.7	0.11	0.17	0.40
1.8	0.11	0.18	0.48
1.9	0.11	0.19	0.57
2.0	0.11	0.20	0.66
2.1	0.11	0.21	0.75
2.2	0.11	0.22	0.84
2.3	0.11	0.23	0.91

more complex strain energy functions. However, this may prove futile as once transients is accounted for even the most complex of models will be unable to capture the downturn. Only a model whose behaviour naturally predicts a downturns at small strains will achieve an accurate prediction of λ_{set} . To the authors knowledge, no such model exists in the literature.

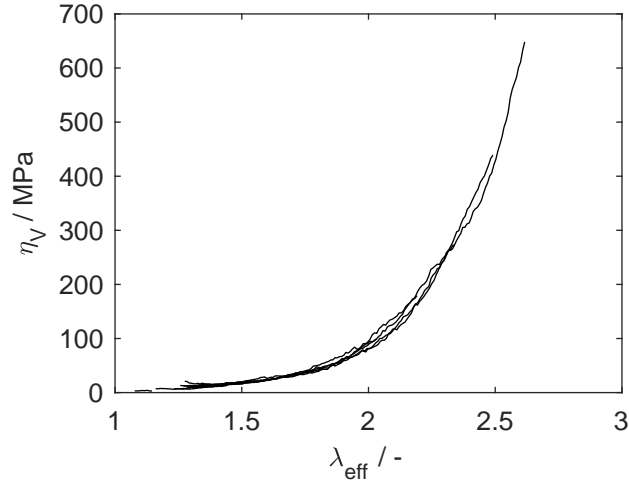


Figure 5.14: η_v as a function of λ_{eff} . A qualitative approximation for the λ_{set} was used to obtain the corresponding λ_{eff} . A formation of a master curve can be observed.

An alternative approach is to obtain the equilibrium contribution *via* experimental means. One method that has been employed extensively in literature for this purpose is the interrupted constant rate of strain uniaxial test [133, 139, 140, 141]. The primary focus of these tests is to understand the equilibrium and viscous behaviour of the material, hence the scragging process is applied to eliminate all other effects. During the interruptions, the strains are maintained for a given time period, i.e., a stress-relaxation experiment. The stress relaxes towards the equilibrium, and by joining the equilibrium points for the various strain levels tested, one can arrive at the curve corresponding to the equilibrium contribution without the need to discard data. However, experiments of this type are time consuming, Laurent *et al.* [140] show that only small changes in the relaxation are noticed when comparing a time period of 900 seconds to 4500 seconds. Nonetheless, an experiment of this sort is a powerful addition, the ambiguity in the α parameter

can be eliminated as no data is required to be discarded.

Another aspect of CR which may impact the model development is the differing hysteresis behaviour. From Figure 5.1 it is evident that the shape of the unload-reload loops differ from those of EPDM and NBR, for CR the loops get broader with increasing stretch. To fully understand the consequences of this, further work must be conducted on materials that displays a similar hysteretic behaviour but has significant amounts of permanent deformation.

5.6.5 Cyclic or pseudocyclic?

The experimental data required to develop this constitutive model consists of approximately ten different uniaxial tensile tests. In this chapter, the idea of using a single pseudocyclic test instead of numerous cyclic tests was explored. Using EPDM2, it was shown that a single pseudocyclic test is sufficient. The model developed on the basis of the pseudocyclic test was shown to be reasonable at capturing the third loop response, and excellent at capturing the energy dissipated. A pseudocyclic tests with pauses was also trialled as shown on Figure 5.3, the intention of this test was to study the impact of heating (if any) on the standard pseudocyclic test as a result of the extended duration of the test (~ 2 hours). However, as identified above, creep plays a significant role on the results of the pseudocyclic test with the pauses and therefore a direct comparison cannot be made. Thus, a theoretical approach is necessary.

One approach is to show that the sample remains in the uniform isothermal region, i.e., the specimen temperature remains constant. Buckley [10] and De Focatiis [142] have provided a detailed account of the theory in their works, therefore only the essential insights will be provided. Firstly, it is assumed that radiative heat transfer is negligible. The heat generated in the sample is transferred to the surface of the sample *via* conduction, subsequently the heat is transferred to the environment *via* convection with air being the working fluid. To ensure isothermal conditions, a strain rate $\dot{\epsilon}$ slower than the slowest of the two heat transfer processes must be utilised, otherwise the sample temperature would rise.

The time requirement for conduction and convection are defined by char-

acteristic time-constants τ_{cond} and τ_{conv} [10, 142], respectively,

$$\tau_{\text{cond}} = \frac{t_s^2}{4\alpha_{\text{diff}}} \quad (5.1)$$

$$\tau_{\text{conv}} = \frac{t_s \rho c}{2h} \quad (5.2)$$

where α_{diff} is the thermal diffusivity of the rubber, c is the specific heat and h is the heat transfer coefficient for convection on the surface of the specimen. The typical values for EPDM samples were specimen thickness $t_s = 0.5$ mm, material density $\rho = 1139$ kgm⁻³ [35], $\alpha_{\text{diff}} = 10^{-7}$ m²s⁻¹ [143] and $c = 2167$ Jkg⁻¹K⁻¹ [143]. For air, a typical value for h is 10 Wm⁻²K⁻¹ [10, 142]. Based on these values, τ_{cond} and τ_{conv} are calculated as 0.63 s and 61.71 s, respectively. The experiment must therefore be conducted such that ~ 62 seconds are allowed for the sample to be in equilibrium and to ensure that there are no temperature gradients.

To ensure isothermal conditions, the maximum power input s from the tensile testing machine must be less than the amount that can be diffused *via* convection,

$$s < \frac{c\Delta T_{\text{tol}}}{\tau_{\text{conv}}} \quad (5.3)$$

where ΔT_{tol} is the tolerance for allowable temperature change, typically ± 2 K in value. The maximum power input (per unit mass) s *via* the testing machine is equivalent to $\sigma_{\text{n,max}}\dot{\epsilon}/\rho$. Hence, to ensure isothermal conditions

$$\dot{\epsilon} < \frac{\rho c \Delta T_{\text{tol}}}{\sigma_{\text{n,max}} \tau_{\text{conv}}} \quad (5.4)$$

where $\sigma_{\text{n,max}}$ is the maximum stress values seen by the material. The maximum nominal stress seen by EPDM is of the order of 10 MPa, therefore $\dot{\epsilon} < 0.008$ s⁻¹ for EPDM specimen. The strain rate required for isothermal conditions are ~ 3.8 times smaller than that of the rate utilised. However, it should be noted that the calculation stated above is conservative as it does not account for the large increase in the surface due to stretching. Thus, the test will remain isothermal at larger $\dot{\epsilon}$ than that calculated.

It is possible that $\dot{\epsilon}$ of 0.03 s⁻¹ puts the specimen in the “nonisothermal/nonadiabatic” regime, i.e., not slow enough to allow heat to dissipate and not fast enough to prevent any heat from entering or leaving. The reader should note that $\dot{\epsilon}$ has to be significantly larger than 7.94 s⁻¹ to be in the

adiabatic regime. The corresponding calculations can be found on Appendix. A.9. A small temperature rise is therefore expected. The maximum temperature rise due to the mechanical work can be determined by considering the strain energy,

$$W = \int_0^\lambda \sigma(\lambda) d\lambda \quad (5.5)$$

The integration procedure was carried out using the EPDM2 pseudocyclic data, the temperature rise can then be determined by dividing W by the multiple of ρ and c [10, 142]. The evolution of W and temperature rise with λ are highlighted on Figure 5.15.

The specimen temperature is seen to rise by ~ 22 °C, thus the sample would reach a maximum temperature of 46 °C. This approximation assumes that the entirety of the strain energy is utilised to increase the temperature of the specimen, and it does not account for the heat transferred *via* convection to and from the room or conduction to and from the instrument or the travelling extensometer grips. To consider these contributions, an iterative approach implemented on MATLAB. The key outcomes of incorporating these contributions include:

- By accounting for convection alone, the temperature change experienced by the specimen is reduced to a minimum and maximum of -0.5 °C and 3°C, respectively.
- By accounting for conduction *via* grips, the temperature change in the specimen is reduced to ± 0.06 °C.

The process used to determine the energy dissipated *via* conduction and convection, alongside the assumptions and equations, is discussed in detail in Appendix. A.10. It is evident that these processes significantly reduce the change in the specimen temperature. A good agreement exists between the cyclic and pseudocyclic cases, for the elastic and viscous contributions, reinforcing the fact that the temperature change was not significant.

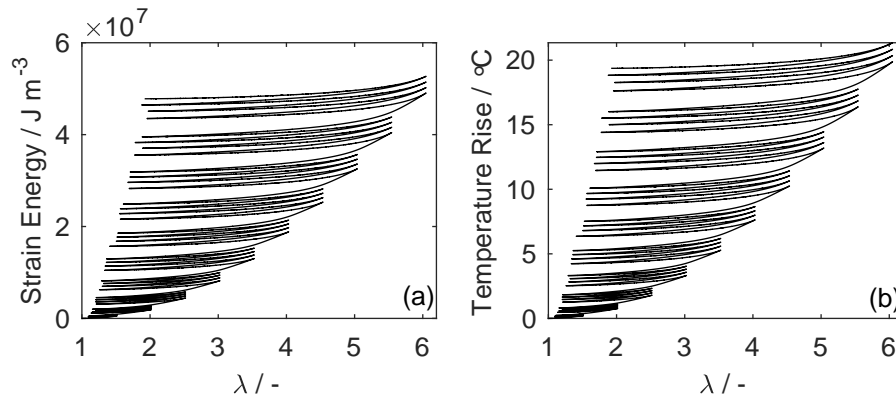


Figure 5.15: The evolution of (a) strain energy W and (b) temperature rise as a function of stretch for an EPDM2 specimen subjected to a pseudocyclic test.

Even if conduction and convection were not significant in minimising the temperature rise, the sample reaching an excess of $40\text{ }^{\circ}\text{C}$ is not a problem as the T_g of EPDM2 is $\sim -47\text{ }^{\circ}\text{C}$ [35]. Since the sample is always at a temperature that is significantly greater than the T_g , the impact on the elastic and viscous contributions are minimal. Dynamic mechanical analysis (DMA) conducted by Komalan *et al.* [144] and Jaunich *et al.* [145] illustrate this, only small changes in the storage and loss moduli are observed at temperatures significantly greater than the T_g . Although the EPDM utilised in their study differs to that of the EPDM systems used herein, the results should be comparable.

It was shown that a pseudocyclic tests can be used instead of a number of cyclic tests for EPDM, significantly reducing the material requirement and experimental effort. Pseudocyclic tests could be used, instead of numerous cyclic tests, for other materials but prior work is necessary to determine appropriate strain rates to ensure the test is isothermal. In the instance the test falls in the “nonisothermal/nonadiabatic” region, one must confirm that the resultant temperature rise does not impact the material behaviour *via* DSC and DMA.

5.7 Summary

This applicability of the modelling formulation developed in the previous chapter on three other materials. It was shown that the modelling processes

was applicable to both sheet rolled EPDM and NBR. However, a model could not be implemented for CR due to the inability of the EV model to capture the downturn at small strain values, coupled with the small residual strain observed. This meant that a viscoelastic master curve could not be formed and hence a model could not be realised.

For EPDM2 and NBR it was shown that the prediction of the third loop response was reasonable. The prediction of the energy dissipated for these two material were excellent. This reinforces the conclusions from the previous chapter that a model of this type can be leveraged for applications where the prediction of energy dissipation is vital, such as dampers.

An in-depth analysis of the amount of data to discard to account for transients was carried out. The amount of data discarded influences the quality of the EV fit to the elastic contribution and the viscoelastic master curve. A method to scrutinise the validity of the chosen amount of data to discard was also developed. This method revealed that the amount discarded was apt, however there is room for optimisation.

Lastly, it was shown that it is possible to further eliminate the amount of work required experimentally by leveraging pseudocyclic tests. The results obtained from the models generated on this basis were comparable to those of the models generated *via* numerous cyclic tests.

6. The influence of filler choice on the mechanical response

Thus far, the focus has predominantly been on the underlying elastomer network. In chapter 3, the impact on the mechanical response due to varying the ratio of PDMS-MA to EHA was studied. In chapters 4 and 5, the impact of varying the underlying elastomer matrix, namely CR, EPDM and NBR, on the mechanical response and the model development of filled elastomers was explored. Although reinforcing agents were present in the latter chapters, the impact of these agents were coupled in with the elastic contribution. Fillers play a crucial role in industrial elastomers, it is therefore vital to explore their contribution in a systematic manner.

To study the impact of filler on the mechanical response of elastomers, SBR compounds with three different types and amount of carbon black fillers were subjected to dynamic tests. Small strain torsional oscillations were utilised for the dynamic tests. Subsequently, to explore the impact of pre-deformation on the dynamic response, the amplitude sweep was repeated following a uniaxial cyclic tensile test. The tensile test consisted of four load/unload loops. Several iterations of uniaxial cyclic tensile tests followed by dynamic tests were conducted, the pre-deformation levels increased in magnitude during each tensile test. Another similar protocol was also implemented, in this instance a further loading stage was added to the tensile test, the torsional oscillations were then superimposed on it. It is well known that at small dynamic strains elastomers exhibit the Payne effect, i.e., amplitude dependence. A popular model used to describe this amplitude dependence is the Kraus model. In this chapter, the Kraus model is used to understand the impact of fillers and pre-deformation on the dynamic response of the SBR compounds studied.

The materials and experimental methods utilised in this study are high-

lighted in section 6.2. The results and discussion are presented in section 6.3. Particularly, the impact of filler amount, filler type and pre-deformation are discussed in sections 6.3.4 and 6.3.5. The observations made from the experiments were used to suggest a modified Kraus model to account for the filler and pre-deformation. The quality of the fit was validated against the experimental data of one particular elastomer compound. Lastly, a summary of the findings are provided in section 6.4.

Aspects of this chapter were presented as an oral presentation and as a conference paper in the International Rubber Conference held in London in 2019. A journal paper is being prepared to be submitted in the peer-reviewed Rubber Chemistry and Technology journal.

6.1 Introduction

A phenomenon that is associated with fillers, more specifically to the filler-filler interactions, is the Payne or Fletcher-Gent effect [60, 64]. The Payne effect is characterised by the reversible amplitude dependence of the elastic modulus when deformed dynamically to small strain levels. At sufficiently small strains, the storage modulus is amplitude independent and a plateau is observed. With increasing strains and beyond a critical strain value, typically around 0.1%, the storage modulus falls to another plateau. Several studies [60, 64, 69] have shown that increasing the filler fraction and surface area leads to an increase in the shear modulus.

Previous chapters have highlighted the importance of deformation histories in the mechanical response of elastomers. In most Payne effect studies, test specimen are pre-conditioned prior to tests to circumvent the impact of deformation history, i.e. of the Mullins effect. Although for the purpose of selected applications this may suffice, a complete understanding of how deformation history influences the Payne effect in different filler types and amounts is currently lacking. This study examines the experimentally the impact of deformation history, i.e. the Mullins effect, on the amplitude dependence, i.e. the Payne effect, of a carefully selected range of carbon black-filled styrene butadiene rubber (SBR) tyre compounds with varying filler content and surface area. Uniaxial tensile strains were used to apply deformation histories and dynamic torsional oscillations to study the amplitude dependence. To prevent discontinuities in the experiment, the same instrument was used for both modes of deformations.

6.2 Materials and methods

6.2.1 Materials

Carbon-black filled SBR with varying types and amounts of carbon black fillers were used in this study. These materials were kindly provided by Dr Lewis Tunnicliffe of Birla Carbon. The SBR compounds used in this study were produced as per ASTM D3191 [146] standard and consist of 3 parts of zinc oxide, 1 part of steric acid, 1.75 parts of sulfur and 1 part of TBBS for every 100 part of SBR 1500. Standard N234, N330 and N660 fillers were compounded into the SBR matrix at 40, 50 and 60 parts per hundred rubber (phr). The fillers have a surface area of 112, 75, and 34 m^2g^{-1} , respectively. Transmission electron microscopy (TEM) images of N234, N330 and N660 are given in Figure 6.1.

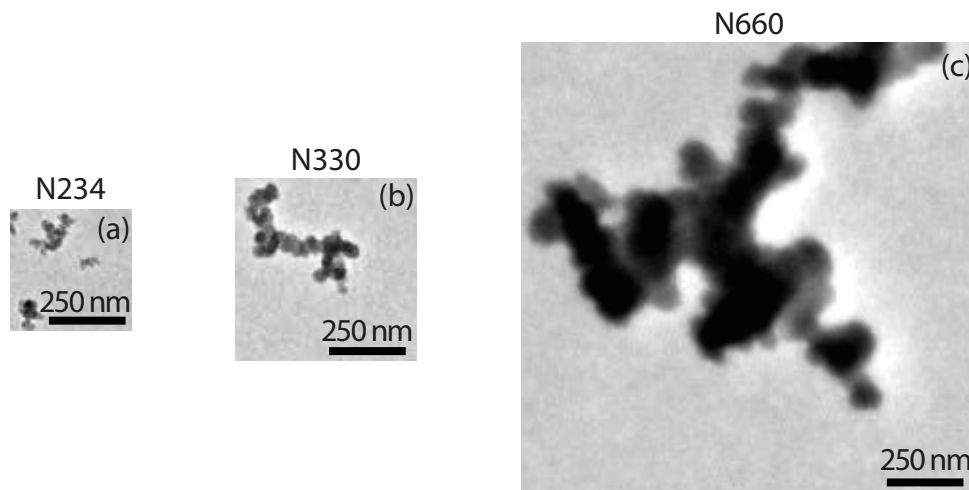


Figure 6.1: TEM images of (a) N234, (b) N330 and (c) N660 carbon black filler particles. These images were provided by Dr Lewis Tunnicliffe of Birla Carbon. As the magnification was different for each micrograph, the images have been resized to allow for the same size scale bar and scale for comparative purposes.

6.2.2 Compression moulding

The materials were provided as unvulcanised sheets, ~ 2 mm in thickness. Prior to the compression moulding, the sheets were hand rolled to a thickness closer to the intended specimen thickness using a Durston DRM F130 mill.

This is essential as filled SBR compounds offer a lot of resistance to flow and to achieve the intended thickness the specimen must be rolled to a thickness close to that value. The rolled sheets were placed in a mould of dimension $120 \times 120 \times 0.6 \text{ mm}^3$. The best results were achieved when the rolled sheet covered the entire mould, as shown of Figure 6.2 and the mould cavity is overfilled, i.e., material volume exceeding the mould volume. An overfill of approximately 20% was used in this study.

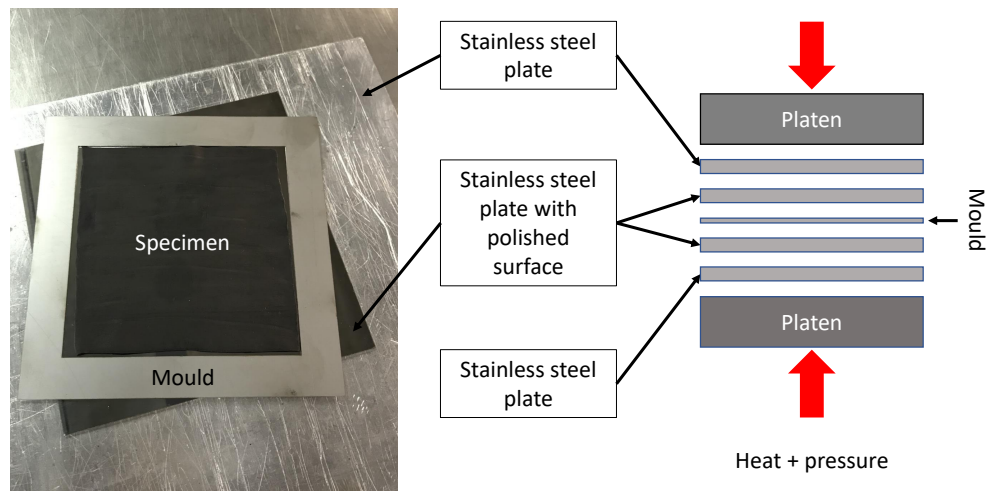


Figure 6.2: Compression moulding setup. An image of a rolled sheet of rubber of dimensions similar to that of the mould cavity, above two stainless steel layers is also illustrated here. The stainless steel surface in contact with the rubber is polished.

The mould is then sandwiched between two stainless steel plates; one surface on each plate is polished and the polished surface is in contact with the rubber. An additional two stainless steel layers are placed on either side to aid the insertion into and removal from the press platens. A schematic of this setup is shown on Figure 6.2. A hand operated hydraulic Daniels heated press was utilised for this purpose. The material was compression moulded at $150 \text{ }^\circ\text{C}$ for a time corresponding to the time required to reach 90% cure plus five minutes. The time required to reach 90 % cure for each material was determined *via* a moving die rheometer by Dr Lewis Tunnicliffe of Birla Carbon. The time requirement t_v for each compound has been given on Table 6.1 and were provided. Once the platens have heated to the required temperature and the mould sandwich has been placed on the

Table 6.1: Vulcanisation time t_v required for the various SBR compounds explored in this study. The vulcanization time corresponds to the time required to reach 90% cure plus five minutes. The cure time was determined *via* a moving die rheometer by Dr Lewis Tunnicliffe of Birla Carbon.

Compound	Vulcanisation Time t_v / min
N234 40 phr	33.38
N234 50 phr	31.21
N234 60 phr	29.60
N330 40 phr	34.62
N330 50 phr	34.15
N330 60 phr	30.11
N660 40 phr	41.31
N660 50 phr	40.89
N660 60 phr	34.94

lower platen, the top platen is lowered by a hydraulic ram of diameter [x]. Subsequently, the ram pressure was increased to 150 bars. The pressure was released after 60 seconds to remove any trapped air in the cavity. This process was repeated several times prior to maintaining a constant pressure of 150 bars. The stainless steel plates, the mould and the moulded sheet were removed immediately from the press following a time duration of t_v , and were transferred to a bench. The moulded sheets were carefully removed from the mould immediately afterwards.

6.2.3 Physical characterisation

6.2.3.1 Density measurement

The densities ρ of the materials were measured prior to and post the vulcanisation process using a Mettler Toledo XS105DU analytical balance fitted with a density kit. This instrument uses the Archimedes' principle to determine the density of the material. From the unvulcanised and vulcanised sheets, square specimens of dimensions $20 \times 20 \times 0.5 \text{ mm}^3$ were cut. By measuring the specimen weight in air and then in de-ionised water, ρ could be calculated. Three measurements were made in each case. For measurements in the liquid, care was taken to ensure that no large air bubbles were present. The obtained values (± 1 standard error) have been tabulated on

Table 6.2: The density ρ (± 1 standard error) in $\text{g}\cdot\text{cm}^{-3}$ of the cured and uncured styrene-butadiene rubber (SBR) systems. The data provided below is based on three repeats. The theoretical density is also provided.

Filler Type	Filler content / phr		
	40	50	60
N234 - Uncured	1.111 ± 0.002	1.138 ± 0.003	1.160 ± 0.001
N234 - Cured	1.109 ± 0.000	1.139 ± 0.003	1.165 ± 0.000
N330 - Uncured	1.109 ± 0.001	1.135 ± 0.001	1.164 ± 0.001
N330 - Cured	1.108 ± 0.001	1.141 ± 0.001	1.169 ± 0.001
N660 - Uncured	1.110 ± 0.003	1.131 ± 0.002	1.169 ± 0.002
N660 - Cured	1.110 ± 0.000	1.145 ± 0.001	1.161 ± 0.001
Theory	1.108	1.136	1.161

Table. 6.2.

The theoretical values for the density of the various specimen can be determined by the summation of the multiple of the volume fraction ϕ_{comp} of the components in the compound by the density of the corresponding component. The details corresponding to the components of the various SBR compound used in the study can be found on section 6.2.1. The theoretical values were determined to be 1.108, 1.136 and $1.161 \text{ g}\cdot\text{cm}^{-3}$ for compounds containing 40, 50 and 60 phr of carbon black, respectively. The details of the calculations are provided in Appendix. A.11. These values have been reported on Table. 6.2, and can be observed to compare well with the experimental density values.

6.2.3.2 Glass transition temperature

To determine T_g , a TA Instruments Discovery DSC2500 was used. Only the T_g of cured specimens are reported herein.

A punch cutter was used to cut disk samples of ~ 6 mg from vulcanised sheets, these specimens were then sealed in hermetic aluminium pans. The specimens were heated from room temperature to $140 \text{ }^\circ\text{C}$ to remove any thermal histories. Following this the samples were cooled to $-90 \text{ }^\circ\text{C}$ and then reheated to $20 \text{ }^\circ\text{C}$. The thermal cycling was conducted in a nitrogen rich atmosphere to be prevent oxidation and any air contamination, the nitrogen purge gas was set at a flow rate of $100 \text{ ml}\cdot\text{min}^{-1}$. A rate of $5 \text{ }^\circ\text{C}\cdot\text{min}^{-1}$ was used for both heating and cooling. Three specimen per SBR

Table 6.3: The glass transition temperature T_g (± 1 standard error) in $^{\circ}\text{C}$ of the cured SBR compositions calculated using the inflection-point method.

Filler Type	Filler content / phr		
	40	50	60
N234	-48.12 ± 0.27	-47.37 ± 0.63	-48.76 ± 0.57
N330	-47.69 ± 0.19	-47.54 ± 0.82	-48.27 ± 0.30
N660	-48.51 ± 0.26	-47.36 ± 0.24	-48.15 ± 1.11

composition were tested under these conditions.

SBR is a copolymer and thus has two T_g values, one corresponding to the styrene and the other to the butadiene. The glass transition temperature of styrene is significantly larger than the test temperatures. Nonetheless, a DSC test was carried out to obtain a reference. This DSC test was identical to that of the test proposed in the paragraph above with one exception, the reheating process is conducted to 300°C . Only one specimen per composition was tested in this instance.

The inflection-point method was chosen to analyse that data. The analysis was carried out in MATLAB. Firstly, the smoothing function *smooth* was applied to the data. The derivative of the heat flow data with respect to temperature was calculated; the T_g corresponds to the peak observed in the derivative data. The results have been tabulated on Table 6.3. The transitions are observed to occur at $\sim -48^{\circ}\text{C}$ and 89°C . In both cases, the transition temperatures are independent of the filler type and amount.

6.2.4 Specimen preparation

Specimens were cut from the moulded sheets using a hand operated Wallace specimen cutting press fitted with a dumbbell shaped cutter 1BA according to BS ISO 527-2. A rectangular sample of dimensions $46 \times 5 \times 0.6 \text{ mm}^3$ was then prepared by removing the ends of some of the dumbbell specimen as shown on Figure 6.3. Both dumbbell shaped specimens and rectangular specimens are used for the mechanical tests.

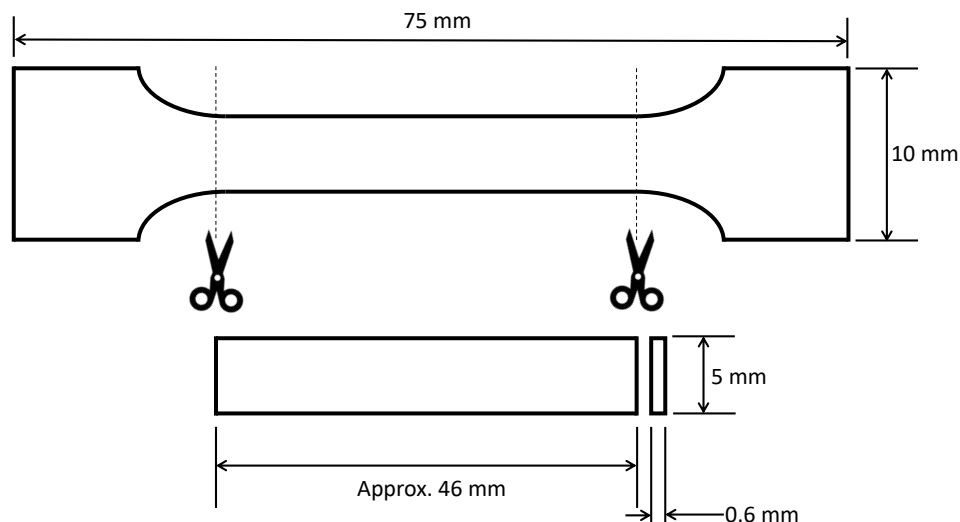


Figure 6.3: Rectangular specimen preparation.

6.2.5 Mechanical testing

6.2.5.1 Uniaxial tensile test

The dumbbell specimen were used in this instance. A uniaxial tensile test to failure was carried out on an Instron 5696 tensile testing machine equipped with a 5kN load cell. As this test was carried out to failure, a travelling extensometer was not utilised in this instance to prevent damage to the instrument. The strain was simply determined from the cross-head displacement of the instrument. At the beginning of the tensile test, the cross-heads were set to be 50 mm apart. The tests were conducted at a strain rate of 0.03 s^{-1} at room temperature (24 ± 1) ° C. These tests were only conducted on the SBR compounds containing 50 phr of N234, N330 and N660 type filler, and only one specimen was tested per compound.

6.2.5.2 Frequency sweep

A frequency sweep experiment was carried out on the various compositions (+ unfilled SBR) explored in this study to determine the frequency to be used for the amplitude sweep experiments. For this purpose, an Anton Paar Rheometer MCR 302 equipped with a solid rectangular bar fixture (SRF) was used. The rectangular specimen were fixed to the SRF using cyanoacrylate

adhesive to prevent slippage from the grips. A dynamic strain amplitude γ of 0.01% was used for the frequency sweep, and frequencies of 0.1 Hz to 10 Hz were explored. These tests were conducted at room temperature (24 ± 1) ° C.

6.2.5.3 Amplitude sweep

Amplitude sweep experiments are typically used to highlight the Payne effect. These experiments were carried out on the various compositions explored in this study. For this purpose, an Anton Paar Rheometer MCR 302 equipped a SRF was used. The rectangular specimens were fixed to the SRF using a cyanoacrylate adhesive to prevent slippage from the grips. Subsequently, a small tensile load of 0.1 N was applied to ensure that the specimens do not buckle. The specimens were then subjected to dynamic torsional strains γ at logarithmically increasing amplitudes between 0.01% and 1% at a fixed frequency ω of 0.3 Hz. These tests were conducted at room temperature (24 ± 1) ° C.

6.2.5.4 Combined tension torsion - TP3

To study the impact of deformation history on the small strain dynamic properties, i.e., the impact of Mullins effect on the Payne effect, a series of experiments were conducted on the rheometer equipped with the SRF. The rectangular specimens were used for this purpose and were secured to the SRF using cyanoacrylate adhesive. Specimens were then subjected to an amplitude sweep as detailed in section 6.2.5.3. Following a 10 minute rest time to allow for viscoelastic transients, each specimen was subsequently subjected to four cycles of tensile strain at a strain rate of 0.03 s^{-1} , through to a maximum strain level of 25%, and unloading to 0.1N to prevent buckling, still clamped to the same instrument. Again after a 10 minute rest time, the same amplitude sweep was then repeated. Following another relaxation period, the same test sequence was employed with uniaxial strains of 50%, 75% and 100%, each time followed by a relaxation period and an amplitude sweep. This procedure is illustrated schematically in Figure 6.4. Moving forward, this test protocol will be addressed as TP3. The protocol naming convention has been adopted from work done previously in the laboratory by Fernandes *et al.* [147]. Their focus was on the impact of pre-deformation on stress-relaxation, whereas here the focus is on the impact of pre-deformation

on the Payne effect.

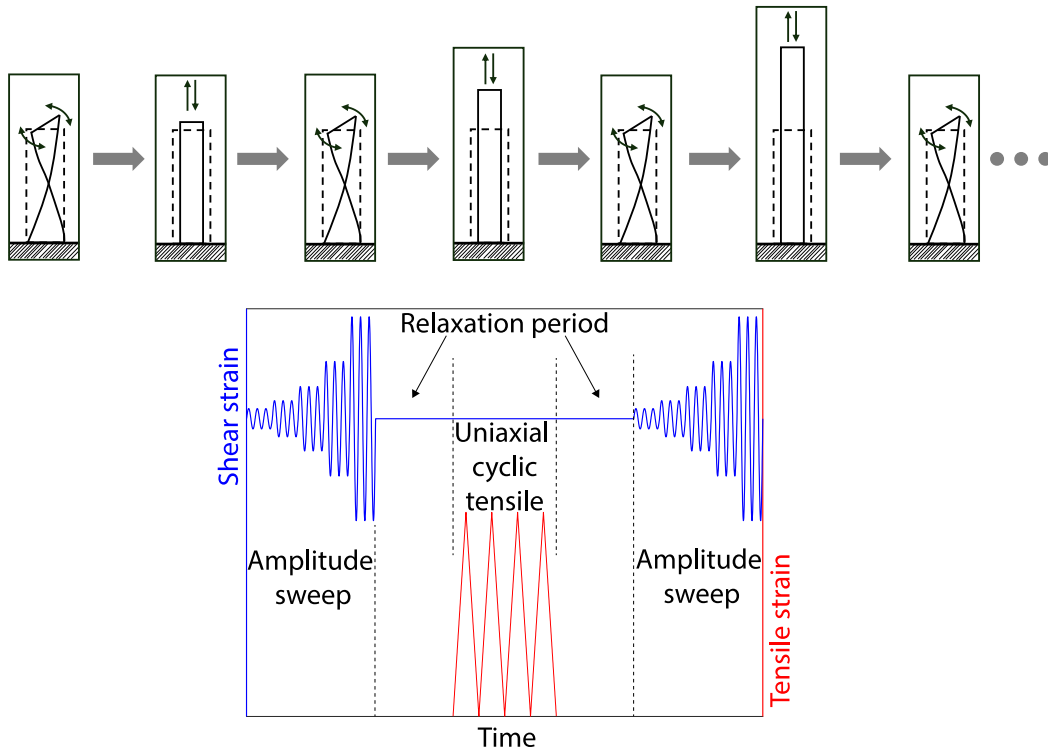


Figure 6.4: A schematic of the test procedure.

The maximum dynamic amplitude that could be explored was limited to 1% as beyond this range, the specimen will twist onto itself leading to difficulties in interpreting the results. Similarly, the uniaxial tests were limited to a maximum strain of 100% on a 35 mm specimen due to the limited axial displacement of the instrument cross-head. While other methods could be utilised to achieve larger pre-deformations, difficulties would arise during the subsequent test sequences. For example, larger deformation histories can be explored using an Instron tensile tester. The sample then needs to be cut to cater for a small strain dynamic test as instruments such as the Rheometer and the DMA utilise smaller specimens. The smaller specimen cannot then be used for the following tensile test. Although a virgin specimen can be utilised for each combination of deformation history and amplitude sweep, there will be discontinuities in the test and an increase in material requirements.

6.2.5.5 Combined tension torsion - TP1

A slight variation was introduced to TP3 to address the impact of deformation and static pre-deformation on the small strain dynamic properties. An additional loading step to the same maximum strain level was added to the “uniaxial cyclic tensile” portion of the previous protocol, i.e., five loading and four unloading steps. Following a 10 minute relaxation period at the maximum strain, in which more substantial stress-relaxation occurs, an amplitude sweep is performed at that strain level. This is equivalent to superimposing an amplitude sweep on a static pre-deformation. Subsequently the sample is unloaded to a strain corresponding to a load of 0.1 N. This process is repeated with uniaxial strains of 50%, 75% and 100%. Moving forward, this test protocol will be addressed as TP1. The protocol naming convention has been adopted from work done previously in our laboratory by Fernandes *et al.* [147]. In their work, TP1 investigated the impact of a static pre-deformation on stress-relaxation, whereas herein the focus is on the impact of a static pre-deformation on the Payne effect.

6.3 Results and discussion

6.3.1 Frequency Sweep

The frequency sweep results are shown on Figure 6.5. It can be observed that the storage modulus $G'(\gamma)$ starts to rise significantly at a frequency of ~ 1 Hz for all materials considered, including unfilled SBR. The peak of the overshoot was not determined as the frequency sweep could not be conducted beyond 10 Hz. It was thought that the overshoot could be a result of resonance. In order to confirm this, theoretical calculations were carried out to identify the natural frequencies ω_n of this geometry. A rectangular beam of dimensions and conditions equivalent to the experiment was modelled. The length of the specimen between clamps in the SRF is 35 mm. The ends of the specimen are constrained such that both ends are fixed. The theoretical

solution [148] is obtained *via*

$$\omega_{n,i} = \frac{i}{2L} \left(\frac{CG'}{\rho I_p} \right)^{1/2} \quad (6.1)$$

$$C = \frac{at_s^3 w^3}{t_s^2 + w^2} \quad (6.2)$$

$$I_p = \frac{wt_s^3}{12} + \frac{w^3 t_s}{12} \quad (6.3)$$

where i refers to the mode shape of interest, C is the torsional constant of a rectangular cross-section, I_p is the polar area moment of inertia of cross-section about axis of torsion and a is a constant that is associated with the ratio of t_s to w .

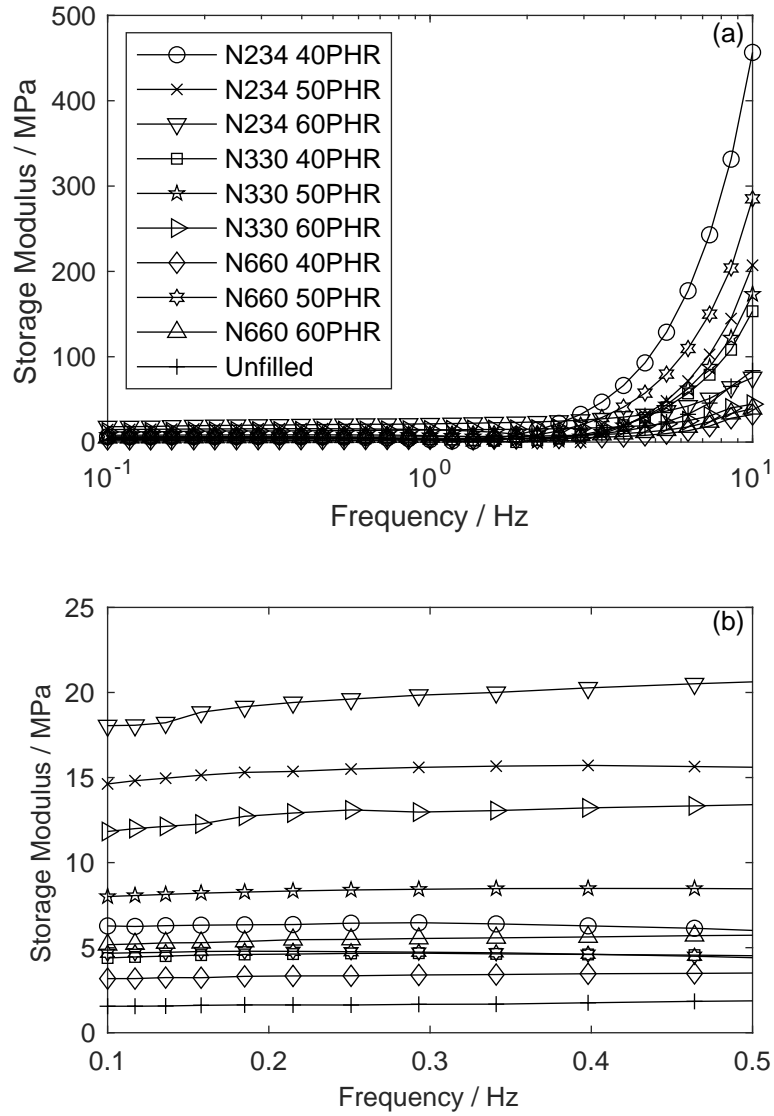


Figure 6.5: A plot of the storage modulus $G'(\gamma)$ against frequency for (a) the full frequency range explored and (b) for frequencies between 0.1 and 0.5 Hz.

For the cross-section used in this work, a is $1/3$ [148], ρ is obtained from Table. 6.2 and G' is obtained from the experimental data at a γ of 0.01% and

at a frequency of 0.3 Hz. The only criterion is to ensure that γ is in the linear region, i.e., the plateau observed at small dynamic strains. While elastomers are frequency dependent [149], the variations in G' with frequency prior to the onset of the overshoot were not significant as shown on Figure 6.5b. This weak frequency dependence is typical of carbon black reinforced rubbers [150]. Any frequency value sufficiently far away from the overshoot can be chosen, 0.3 Hz was considered here. The storage modulus $G'(\gamma)$ ranges from ~ 1.7 MPa to 20 MPa as shown on Figure 6.5b. In this study, only the first mode shape is of interest, i.e., $i = 1$. The resonance therefore occurs at frequencies between 141 and 443 Hz.

The resonance frequency determined *via* the theoretical calculation is large compared with the peak suggested by the experimental data. However, the theory only provides an elastic solution and does not take into account the inelastic nature of the material. To account for this an FE simulation was conducted on Abaqus. Prior to performing an inelastic simulation, an elastic simulation was conducted to ensure that a correct setup was used on Abaqus. For this simulation, the material was first assumed to be elastic and incompressible. The Young's modulus is the requested input for an elastic material and it is simply obtained *via* the relation $E = 3G'$. This relation takes advantage of the incompressibility condition. In Abaqus, 0.49995 is the maximum value that can be set as the Poisson's ratio. The elastic simulation resulted in resonant frequencies ranging between 147 and 468 Hz. These results compare well with the values obtained through the theory and therefore a similar Abaqus setup is to be used for an inelastic simulation.

For the inelastic simulation, the material was assumed to be hyperelastic and incompressible. A neo-Hookean (or Gaussian) material model was used to capture the inelasticity of the material. This model is sufficient to describe the stress-stretch response for the strain value explored in this experiment. The stress-stretch data obtained from the uniaxial tensile test was used to obtain the model parameters. The simulation concluded that resonance occurs between 89 and 200 Hz for the materials considered. This is somewhat lower than the values obtained for the elastic case.

The analytical and the FE analysis above assume that the material is either elastic or hyperelastic. However, elastomers are viscoelastic and so it is the damped natural frequency ω_d that is of interest and it can be determined *via* [124]

$$\omega_d = \omega_n \sqrt{1 - \zeta^2} \quad (6.4)$$

where ζ is the damping ratio. ζ can be obtained from the loss factor η_{loss} *via* the relation $\eta_{\text{loss}} = 2\zeta$. In literature, values of ≈ 0.2 were quoted for η_{loss} [151, 152]. The frequency sweep experiments conducted in this study were utilised to determine η_{loss} by dividing the loss modulus by the storage modulus to obtain the loss tangent. The values of η_{loss} obtained *via* the experiments were smaller than those quoted in literature, especially for the unfilled SBR where η_{loss} was observed to be 0.01. For other compositions, η_{loss} reached as high as 0.1. Assuming a η_{loss} value of 0.1, one can determine the ζ to be 0.05. Using the frequency values obtained *via* the FE simulations for the inelastic case as ω_n , ω_d can then be calculated to fall in the 88.9 to 199.7 Hz range. As shown, the damping is not significant due to the fact $\sqrt{1 - \zeta^2}$ is small, this remains the case even when a η_{loss} value of 0.2 is used.

The damped natural frequency ω_d is calculated to be between 88.9 and 199.7 Hz for all materials studied in this chapter. These values are significantly higher than the frequencies explored experimentally, however, it is plausible that the experiments may also exhibit a peak this range. It should also be noted that frequency sweep experiments performed on CR, EPDM2 and NBR also revealed that similar effects begin to occur at around 1 Hz, indicating that this phenomenon could have occurred due to instrument resonance. Further experiments are necessary to identify the root cause. Based on the results obtained from the frequency sweep and the analysis performed thereafter, a frequency of 0.3 Hz was chosen to be utilised for amplitude sweeps as it is sufficiently distanced away from the resonance.

6.3.2 Monotonic and cyclic uniaxial tensile tests

6.3.2.1 Tensile tester vs. rheometer - validation Study

A validation study was conducted to ensure that the results obtained for uniaxial tensile tests *via* Anton Paar Rheometer MCR 302 and the Instron 4204 are comparable. For this purpose, CR specimen were used. The results can be observed on Figure 6.6. It can be seen that there is a good agreement between the data obtained using both instruments. At a strain of 25%, a stress (± 2 standard errors) of 1.20 ± 0.04 MPa was obtained *via* the tensile tester and a the stress (± 2 standard errors) of 1.16 ± 0.05 MPa was obtained *via* the rheometer.

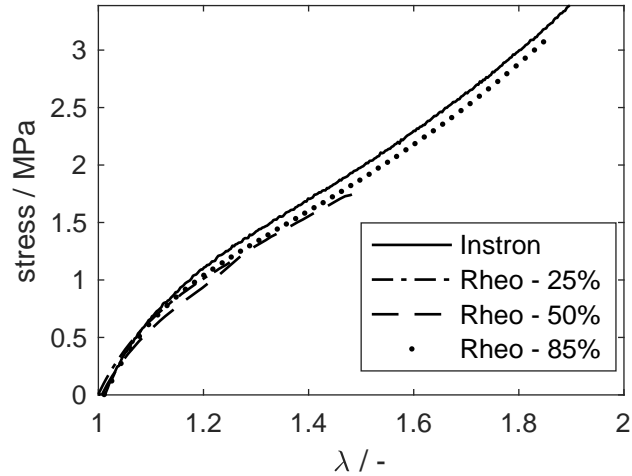


Figure 6.6: A comparison between the uniaxial tensile tests conducted on CR specimen using an Instron tensile tester and an Anton Paar Rheometer.

6.3.2.2 Monotonic uniaxial tensile test

A uniaxial tensile test was conducted on the Instron tensile tester for the SBR compounds containing 50 phr of N234, N330 and N660 fillers. This test was carried out to gain an appreciation for the stress-strain behaviour of the various compounds and their failure strains. The results are shown on Figure 6.7. The stress corresponding to a given value of stretch is greatest for N234, followed by N330 and N660. This is to be expected as N234 filler has the largest specific surface area and therefore the greatest interaction with the fillers and the polymer, resulting in a greater reinforcement [33, 153]. Similarly, the reinforcement observed for the SBR compound consisting of N330 filler is larger than that of the compound containing N660 filler, owing to the larger specific surface area of N330.

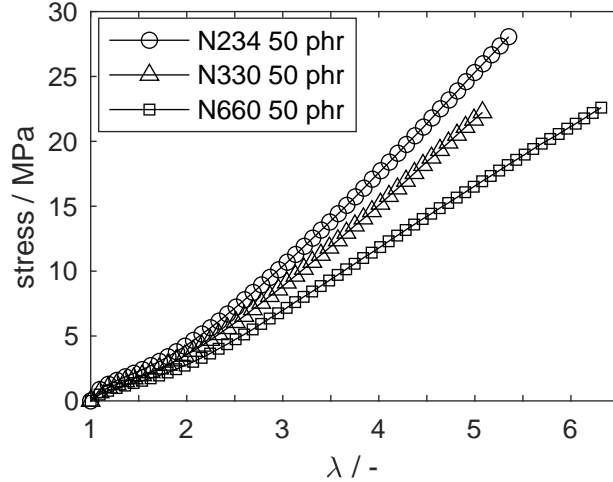


Figure 6.7: A comparison of stress-stretch response obtained by conducting uniaxial tensile tests on SBR compounds containing 50 phr of N234, N330 and N660.

6.3.2.3 Cyclic uniaxial tensile test

The SBR specimens are subjected to cyclic loading during TP3 and TP1, so that the stress-softening phenomenon can be examined. The stress-stretch response for selected SBR compounds utilised in this study have been illustrated on Figure 6.8 and 6.9, the remaining compounds have been presented in Appendix. A.12. Stress-softening is observed for all compounds studied.

As demonstrated with the monotonic loading case, the stress corresponding to a given stretch is seen to increase with increasing surface area. Similarly, in the majority of cases, the stress at a given stretch is seen to increase with increasing filler content. This is expected as both increasing the surface area of the filler and the filler content are known to increase the reinforcement [33, 153]. However, the stress for a given stretch is seen to reduce when the filler amount is increased from 50 to 60 phr, for SBR compound with N234 type filler. This can be observed by comparing Figure 6.9a and b. Stress values of 5.27 and 5.10 MPa are observed at a stretch of 2 for SBR with 50 and 60 phr, respectively, of N234 type filler. This is also a known phenomenon, there is a threshold beyond which increasing the filler amount leads to a reduction in the tensile strength [154].

The permanent set is also observed to increase with increasing filler amount and surface area. Note that this permanent set mentioned herein

is measured directly from the experimental results and is not extracted from a model as in Chapters 4 and 5. The permanent set is obtained from the cyclic stress-strain curves and is the stretch value corresponding to \sim zero stress upon unloading. For SBR N330 compounds, following a pre-deformation to a stretch value of 2, the permanent set increases from 1.066 to 1.072, when the filler content is increased from 40 to 60 phr. Similarly, following a pre-deformation to a stretch value of 2, permanent set increases from 1.065 to 1.075 when the filler surface area is increased from 34 to 112 m^2g^{-1} , i.e., N660 50 phr to N234 50 phr. From literature [154, 155], it is evident that both filler content and surface area lead to an increase in permanent deformation, consistent with the findings herein.

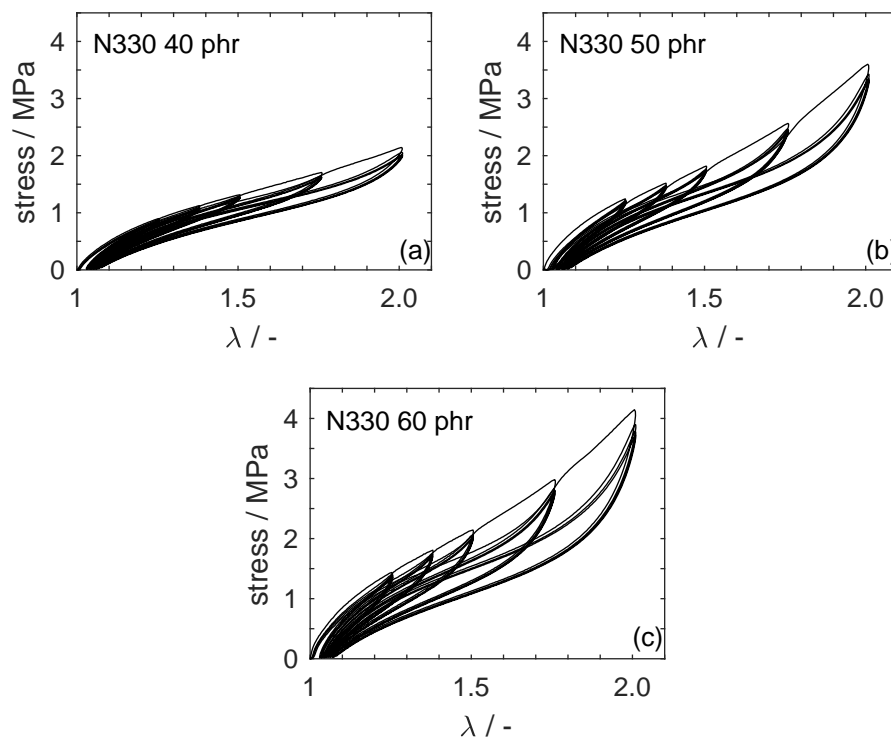


Figure 6.8: The stress-stretch response of uniaxial cyclic tensile test of selected SBR compounds utilised in this study.

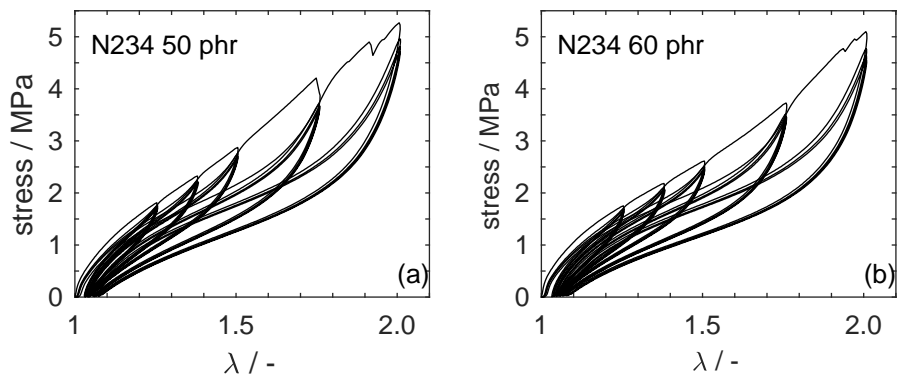


Figure 6.9: The stress-stretch response of uniaxial cyclic tensile test of SBR N234 (a) 50 phr and (b) 60 phr compounds. For these compounds, the stress value is seen to reduce when the filler amount is increased from 50 to 60 phr.

6.3.3 Reversible amplitude dependence

Experiments were conducted to demonstrate the reversibility of the amplitude dependence of the Payne effect. This experiment consists of an amplitude sweep with increasing amplitude, as detailed in TP3 and TP1, followed by an amplitude sweep exploring the same dynamic shear strains in reverse, i.e., decreasing amplitude. The result for SBR N330 50 phr compound is presented in Figure 6.10. The results corresponding to the remaining compounds are provided in Appendix. A.13. It can be observed that the storage modulus is slightly lower for the reverse direction; this difference can be attributed to a small amount of irreversible damage occurring to the elastomer and/or filler network due to exposure to larger strains during the amplitude sweep. Rendek and Lion [137] support this argument. They also show *via* cyclic amplitude sweeps that there is an additional temporal element in the recovery of the broken bonds that leads to lower storage modulus for the reverse direction.

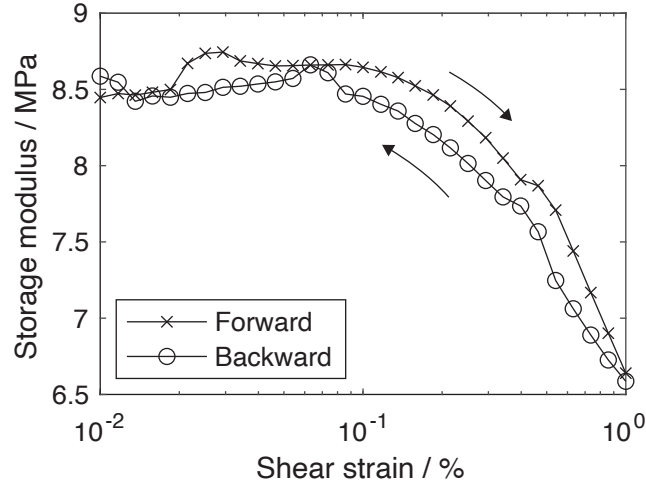


Figure 6.10: A plot of storage modulus against dynamic shear strain demonstrating the reversibility of the Payne effect.

6.3.4 TP3

A representative example for the evolution of the Payne effect with pre-deformation is provided in Figure 6.11 for data from SBR N330 50 phr. It is immediately apparent that a tensile strain history results in a reduction of the modulus during the subsequent amplitude sweep. Diercks *et al.* [149] implemented a similar protocol on a natural rubber specimen with 60 phr of carbon black and reported similar results. In their work, shear deformation was used for both the large quasi-static and small strain dynamic tests. Besides Diercks and co-workers, to the author knowledge, no others implemented a similar protocol in the literature.

In order to quantify the impact of deformation history on the Payne effect, the Kraus model is fitted to the storage modulus data. The Kraus model [100] is a phenomenological model based on the breakdown and reformation of filler aggregates used to describe the evolution of $G'(\gamma)$ with change in γ , and was described earlier by Eq. 2.12. As stated previously, to prevent the sample from twisting in on itself, large torsional strains were avoided, hence G'_∞ was not reached. To account for this, a simplified form of the Kraus model was used by letting $G'_\infty=0$, leading to

$$G'(\gamma) = \frac{G'_0}{1 + \left(\frac{\gamma}{\gamma_c}\right)^{2m}} \quad (6.5)$$

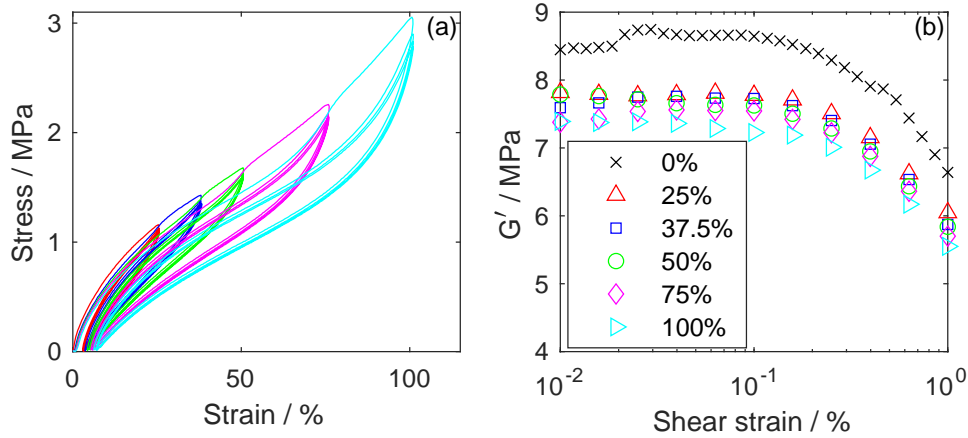


Figure 6.11: a) Typical cyclic tensile response and b) amplitude sweep following the cyclic history of SBR compound filled with 50 phr of N330 carbon black. The different strain histories explored in the experimental protocol are marked in the same colour.

The modified Kraus model is fitted to the experimental data set using the MATLAB function *lsqcurvefit* to obtain a set of parameters G'_0 , γ_c , m for each amplitude sweep. An example of such a fit is shown in Figure 6.12a for an SBR N330 50 phr system, illustrating the quality of fit of such a model. Although G'_0 changes significantly across the datasets with differing tensile histories, only small changes can be observed in γ_c and m for a given compound, as shown in Figure 6.13. A hypothesis is that, for a given system, γ_c and m may be approximately constant is formed. Subsequently, a simultaneous optimisation is performed on all amplitude sweeps for a given compound allowing only G'_0 to vary with tensile history, using MATLAB's *fminunc* function. The model fits shown in Figure 6.12b are virtually indistinguishable from those performed individually, and the RMS errors are comparable, 0.34 MPa with individual fits and 0.41 MPa with the simultaneous fits. The values of the parameters γ_c and m obtained are shown as horizontal dashed lines on Figure 6.13. A value of 2.3 and 0.7 were obtained

for γ_c and m , respectively. This suggests that the Mullins effect influences primarily the value of G'_0 as far as the Payne effect is concerned, and does not significantly alter the onset or the rate at which it occurs.

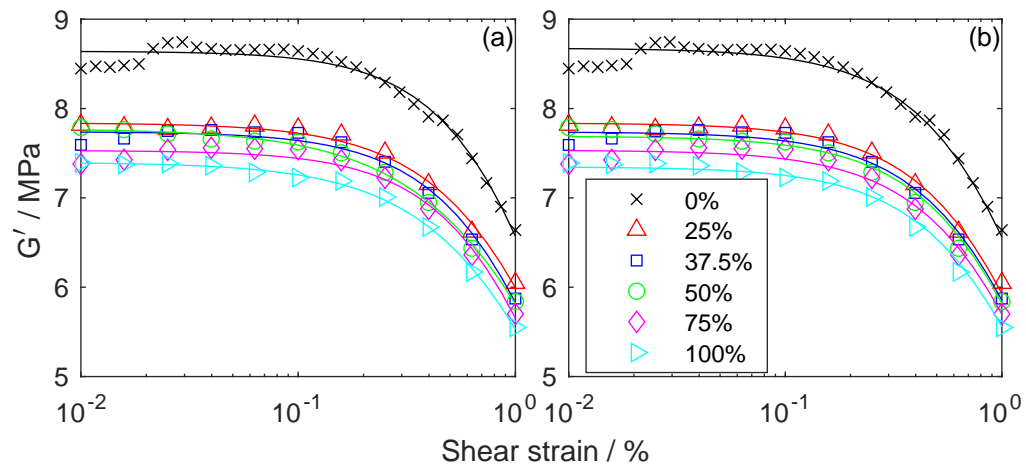


Figure 6.12: A comparison of the model fits (lines) obtained by a) individually fitting modified Kraus models to amplitude sweeps for SBR filled with 50 phr of N330 filler for each tensile strain history, and b) simultaneously fitting modified Kraus models with a single value of γ_c and m for all datasets. Colours are used to highlight the different strain histories explored and the experimental data is represented by symbols. The RMS errors for the individual and simultaneous fits are 0.34 and 0.41 MPa, respectively.

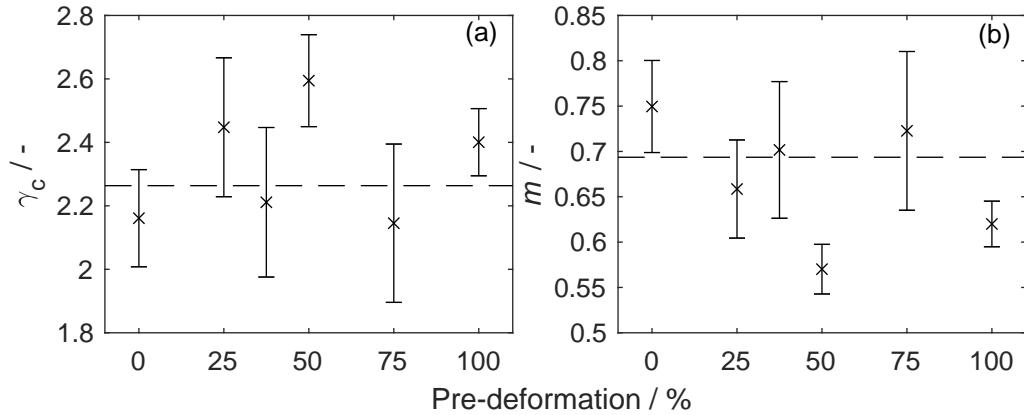


Figure 6.13: Values of a) γ_c and b) m obtained *via* fitting modified Kraus models to experimental amplitude sweep data (± 1 standard uncertainty) for the SBR with 50 phr of N330 carbon black filler. Also shown as horizontal dashed lines are values of a) γ_c and b) m obtained by simultaneous fitting of all amplitude sweeps.

The evolution of G'_0 with increasing pre-deformation for all filled systems is shown on Figure 6.14. The corresponding uncertainties are also displayed on the plot, but are in general very small. The evolution of γ_c and m obtained by simultaneous fits are illustrated on Figure 6.15.

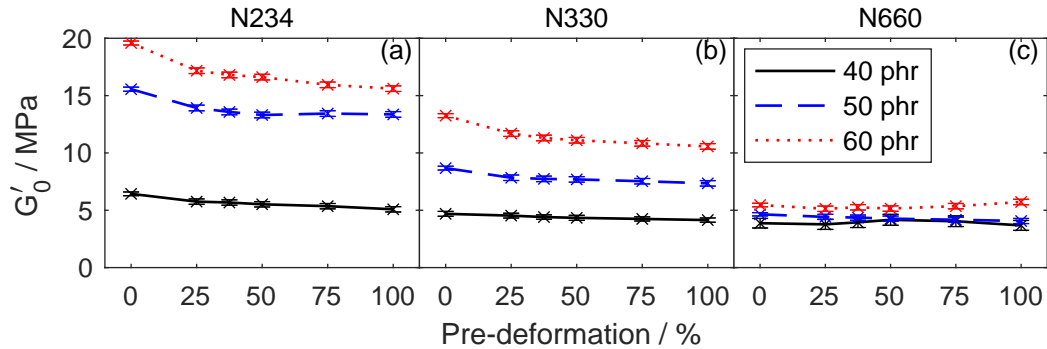


Figure 6.14: The evolution of G'_0 obtained by fitting Kraus models to amplitude sweep data for TP3 as a function of tensile pre-deformation for SBR systems filled with a) N234, b) N330 and c) N660 type carbon black. For each system three different filler contents are explored, 40, 50 and 60 phr, and are indicated by red, blue and black colours, respectively. The uncertainties (± 1 standard uncertainty) associated with each plot are also shown. The lines are for guidance only.

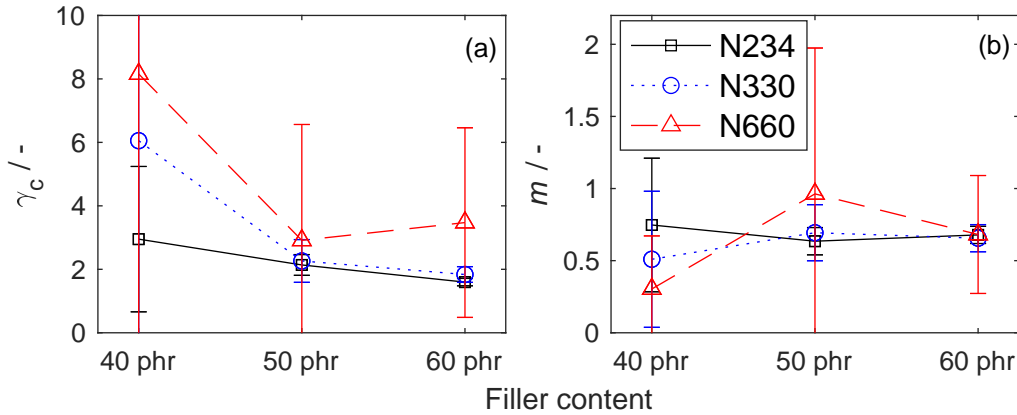


Figure 6.15: The evolution of γ_c and b) m with increasing filler content for SBR systems filled with N234, N330 and N660 type carbon black, represented by square, circle and triangle symbols, respectively. The uncertainty (± 1 standard uncertainty) associated with each plot are also shown.

The experiments performed and the subsequent Kraus model fits help to identify the impact of pre-deformation on the Payne effect; there is dependence on both the filler content and the filler morphology. An increase in filler content and in filler surface area increases the plateau value G'_0 as shown on Figure 6.14. This is expected as both are known to lead to a stiffening of the rubber. To demonstrate this, G'_0 is plotted as a function of filler volume fraction, Figure 6.16a, and of effective surface area, Figure 6.16b. For details on determining the filler volume fraction and effective surface area, the readers are referred to Appendix. A.14. In Figure 6.16a, the increase in filler amount and area are captured by the increasing filler volume fraction, and the apparent increase in slope steepness as the filler type is varied from N660 to N234, respectively. Similar observations can be made for Figure 6.16b. However, in this instance, alongside the sub-trends, an overarching trend seems to exist. Figure 6.14 also illustrated the decrease in G'_0 values with increasing levels of pre-deformation. This was less apparent for SBR filled with N660 carbon black, and a clear trend was not observed in this case despite repeated attempts. This decrease is attributed to the stress-softening phenomenon.

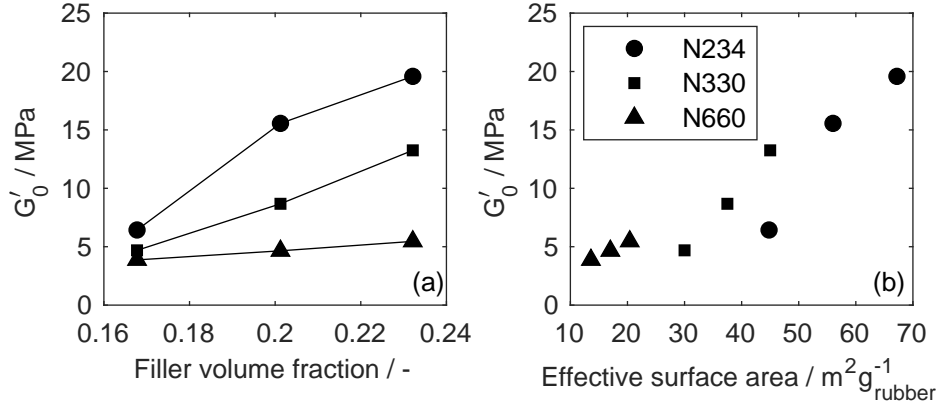


Figure 6.16: The evolution of G'_0 with (a) filler volume fraction, and (b) effective surface area. The lines are a guide to the eye.

Literature suggests that an increase in filler content of a system should reduce the strain at the onset of nonlinearity, i.e. γ_c [69]. This effect can be seen to some extent in Figure 6.15a, although there is significant uncertainty and the reduction is not large. Similarly, large uncertainties are observed for the parameter m as shown in Figure 6.15b, and it is difficult to say whether m is dependent on filler type and content – the variation is limited across the datasets studied here.

The data shown suggests that it might be possible to control the stiffness, and to some extent the onset of the Payne effect by a careful combination of filler selection and mechanical preconditioning. The ability to control the Payne effect can have benefits in several applications, for example in vehicle tyres where it affects rolling resistance, and hence fuel consumption.

For the purpose of modelling, the evolution of G'_0 with strain history is the dominant effect, and may be integrated into a Kraus model by a functional form of G'_0 , such as

$$G'_0(\epsilon_{\max}) = G'_{0,0\%} \left(1 - b \left(1 - \exp\left(-\frac{\epsilon_{\max}}{\epsilon_0}\right) \right) \right) \quad (6.6)$$

where $G'_0(\epsilon_{\max})$ is the plateau storage modulus value at a given tensile strain history ϵ_{\max} , $G'_{0,0\%}$ is the plateau storage modulus value of the virgin specimen, and b and ϵ_0 are constants. For the range of filler types and content explored in this study, b ranges from 0.14 to 0.23 and ϵ_0 ranges between 0.17% and 1.1%. For a more complete model the trends in the γ_c and possi-

bly m parameters need to be included, but to do so with confidence requires a reduction of the uncertainties currently present in these parameters.

In order demonstrate the quality of fit, Eq. 6.6 was employed alongside Eq. 6.5 to predict the amplitude sweep response of SBR N330 50 phr and is illustrated on Figure 6.17. For SBR N330 50 phr, the constants γ_c , m , $G'_{0,0\%}$, b and ϵ_0 are 2.26, 0.69, 8.68 MPa, 0.15 and 0.28%, respectively. A reasonable agreement between the experimental data and the model can be observed. In this instance, RMS error of 0.55 MPa was obtained.

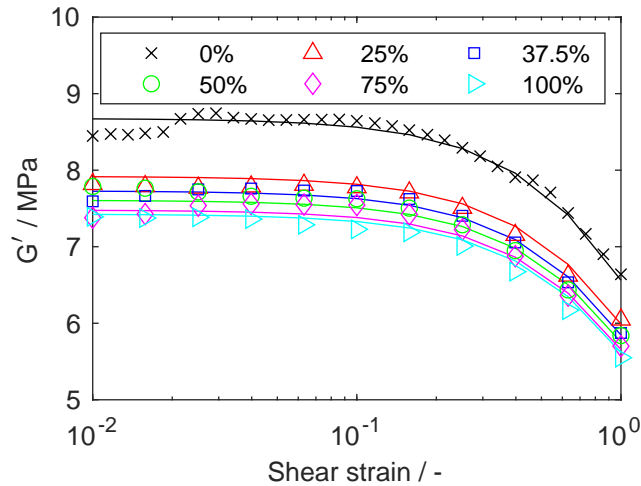


Figure 6.17: A comparison of the model fits (lines) obtained from employing Eq. 6.6 alongside Eq. 6.5, and the experimental data (symbols) for the SBR N330 50 phr compound for all the strain histories explored. RMS error of 0.55 MPa was obtained.

6.3.5 TP1

For a range of real world applications, dynamic strains are superimposed on static strains (or loads). Vibration isolators are one such application [150], the static strain arises due to self-weight of target structures. Due to this, several researchers have investigated the impact of dynamic strains superimposed on static strains on both unfilled [156, 157] and filled [150, 137, 158, 159, 138, 157] rubbers. In these works, the dynamic behaviours were achieved *via* either free or forced vibrations. Various combinations of deformation modes were also utilised, including uniaxial tensile static strain

with tensile oscillations [156, 137, 159, 157, 138], uniaxial tensile static strain with torsional oscillations [160, 156, 159, 157] and pure shear static strain with simple shear oscillations [158].

The experimental work herein investigates the impact of a tensile static strain on torsional oscillations and therefore the works of Suphadon *et al.* [156, 159], and Kuhn and Künzle [160] are of relevance. In their work, Suphadon and co-workers used SBR 1500 compounds with 0, 25 and 50 phr of N330 filler. These materials are similar to the materials used in this study. However, unlike in this study, their study utilised a rod shaped specimen that was subjected to free vibrations. Suphadon and co-workers also only report the loss modulus and the loss factor ($\tan\delta$), the storage modulus was therefore obtained by using the relation $\tan\delta = \frac{G''}{G'}$. Kuhn and Künzle studied the complex viscosity using rectangular specimens, and the relationship between the complex viscosity and dynamic modulus [161] can be leveraged to determine the storage modulus.

In this work, rectangular SBR specimens with varying filler type and amount were subject to TP1 as described in section 6.2.5.5. A representative example of the impact on the amplitude sweep due to a static strain is provided on 6.18, data from SBR N330 50 phr is used. It can be observed that the characteristic plateau modulus of the Payne effect is maintained even at larger dynamic shear strains. The onset of the non-linearity is shifted to larger dynamic strains. A similar result is observed for all the compounds tested. The storage modulus appears independent of the dynamic strain values in the strain range explored. For this reason, only G'_0 parameter will be studied for TP1.

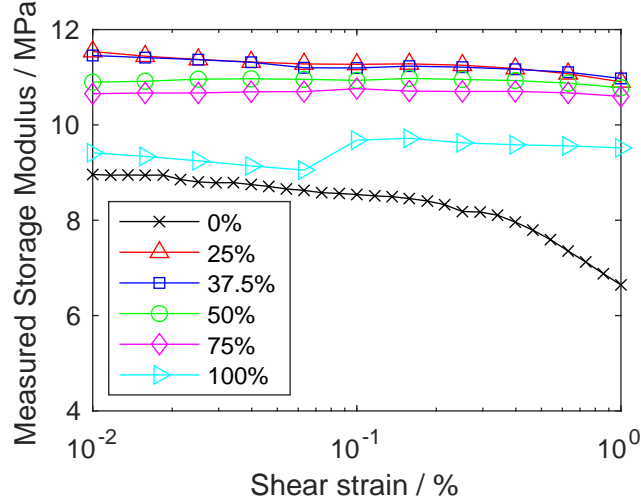


Figure 6.18: The impact of varying the static strain on the resulting dynamic response for a SBR N330 50 phr compound. The dynamic strains are superimposed on the static strain, refer to TP1.

Figure 6.18 illustrates that as the static-strain increases, G'_0 increases and then reduces in magnitude. The increase is observed when transitioning from a pre-deformation of 0% to a pre-deformation of 25%, thereafter the magnitude of G'_0 decreases with increasing pre-deformation. This is in line with the observation made by Kuhn and Künzel [160]. However, Suphadon and co-workers [156, 159, 157] found that as static-strain increases, G'_0 increases in magnitude. This is due to the fact that Suphadon and co-workers account for the geometric effects, i.e., the storage modulus is calculated with respect to the dimensions of the specimen following the application of the static-strain. Similarly, the results shown on Figure 6.18 do not account for the geometric effects.

To study the impact of static strain on the dynamic shear modulus G , and by extension the storage and loss modulus, one must consider the torsion equation for a uniform rectangular bar [162]

$$G = \frac{ML}{\beta w t_s^3 \theta_1} \quad (6.7)$$

$$\theta_1 = \frac{\alpha_1 \gamma L}{\beta t_s} \quad (6.8)$$

where α_1 and β are constants associated with the thickness to width ratio of

the rectangular beam, and θ_1 is the angle of twist. Eq. 6.7 refers to G prior to the application of static strain. The dynamic modulus \bar{G} post application of static strain can be determined by accounting for the change in L , t_s and w with static strain. For a uniaxial tensile deformation, L scales by λ , and t_s and w scale by $\lambda^{-1/2}$. This relationship was also highlighted earlier by Eq. A.4. The dependence of θ_1 on L and t_s is highlighted in Eq. 6.8. By combining Eqs. 6.7 and 6.8, it can be shown that G is only a function of w and t_s ,

$$G = \frac{T}{wt_s^2\gamma\alpha} \quad (6.9)$$

\bar{G} can then be obtained by replacing w and t_s by $\lambda^{-1/2}w$ and $\lambda^{-1/2}t_s$ respectively,

$$\bar{G} = \frac{T}{wt_s^2\gamma\alpha}\lambda^{3/2} = G\lambda^{3/2} \quad (6.10)$$

Eq. 6.10 highlights the relationship between the dynamic modulus of the specimen subjected to static strain and the dynamic modulus of a specimen without an imposed static strain.

To account for the static strain, all $G'(\gamma)$ values are scaled by a factor of $\lambda^{3/2}$. Subsequently, the modified Kraus model is fitted to the data. The evolution of G'_0 with imposed static strain for the various filler types and content considered can be observed on Figure 6.19. G'_0 is seen to increase with increasing static strain. This is in agreement with the observations made by Kuhn and Künzel, and Suphadon and co-workers, once the geometric effects are accounted for. The combined torsion and extension theory proposed by Rivlin [9] also supports these findings. In Rivlin's theory, the shear modulus G is defined as

$$\frac{d\tau}{d\gamma} = G = 2\lambda^{3/2}(C_1 + C_2/\lambda) \quad (6.11)$$

where C_1 and C_2 are constants corresponding to the Mooney-Rivlin strain energy function. For simplicity, the Gaussian (or neo-Hookean) case will be considered here, achieved by letting C_2 in Eq. 6.11 be zero. C_1 is then determined by fitting to a set of stress-strain data. For a fixed value of C_1 , G will increase with increasing static stretch λ . Rivlin's theory refers specifically to G . However, as stated previously $G''(\gamma)$ is $\approx 10\%$ of $G'(\gamma)$ for the materials considered in this study. Using this fact and $G = \sqrt{(G'(\gamma))^2 + (G''(\gamma))^2}$, G can be determined to be $1.004G'(\gamma)$. $G'(\gamma)$ can be therefore be approximated by G .

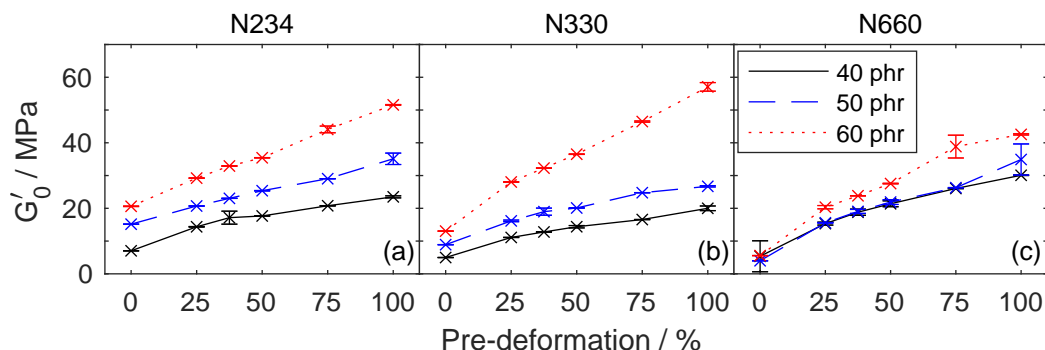


Figure 6.19: The evolution of G'_0 obtained by fitting Kraus models to amplitude sweep data obtained for TP1 as a function of tensile static strain for SBR systems filled with a) N234, b) N330 and c) N660 type carbon black. For each system three different filler contents are explored, 40, 50 and 60 phr, and are indicated by red, blue and black colours, respectively. The uncertainty (± 1 standard uncertainty) associated with each plot are also shown. The lines are a guide to the eye

Figure 6.19 also demonstrates that alongside static strain, increasing the filler amount also leads to an increase in G'_0 . The only exception to this rule is with the N660 filler, where G'_0 is observed to be the same for 40 and 50 phr. To understand the complex data set, the data observed in Figure 6.19 was normalised with respect to the corresponding G'_0 value at zero static strain and is illustrated on Figure 6.20. This plot reveals that the largest relative change in G'_0 is observed for N660 system, followed by N330 and N234. These results contradict those of TP3, where the largest change in G'_0 was observed for N234, followed by N330 and N660, for any given filler amount. The complexity of this response is somewhat expected since the material is still evolving while under strain due to the Mullins phenomenon. An alternative experiment is to subject the material to a significantly larger tensile strain history in order to limit the evolution of the Mullins phenomenon and then repeat TP1 at a reduced tensile strain.

Rivlin's theory was used to predict the response of TP1 as illustrated on Figure 6.19 but the theory falls short of the experimental data in most instances. In Rivlin's theory, the Mooney-Rivlin strain energy function was used. However, in this study the Gaussian function was considered by letting $C_2 = 0$. This is the reason why the theoretical response is the same for all systems considered, as normalisation removes the dependence of the C_1 parameter. Even if the Mooney-Rivlin strain energy function was utilised,

the discrepancy will still exist as the Mooney-Rivlin function is inadequate to describe the uniaxial tensile stress-strain data in the stretch ranges considered.

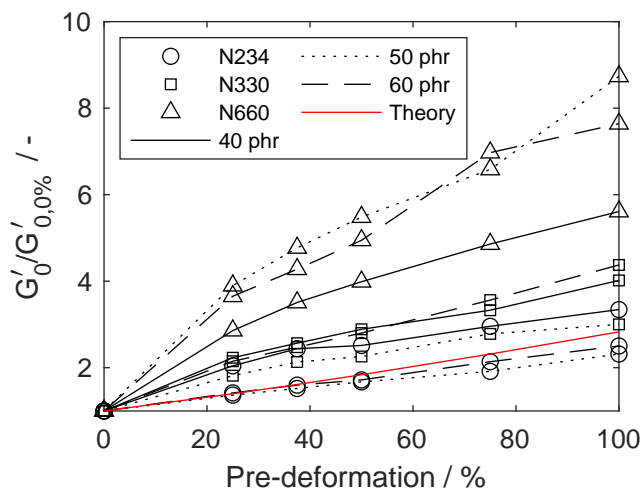


Figure 6.20: Evolution of the normalised G'_0 for TP1 as a function of tensile static strain for SBR systems with N234 (circles), N330 (squares) and N660 (triangles) type of carbon black. For each system three different filler contents are explored, 40 (solid line), 50 (dotted lines) and 60 (dashed lines) phr. For any given system, the normalisation was carried out with respect to the corresponding G'_0 value at zero% static strain. A theoretical value (red line) was obtained *via* Rivlin's [9] theory.

Although the TP1 response is complex, for a given filler type and filler amount, evolution of G and G'_0 with static strain, as shown on Figure 6.19, can be described by linear functions with gradients and y-intercepts ranging between 14.0 to 42.3 MPa, and -3.7 to -27.9 MPa, respectively. The coefficient of determination for all the models is above 0.92, indicating that the fits obtained are reasonable.

6.4 Summary

The impact of a tensile deformation history on the small shear strain amplitude response on a set of SBR compounds filled with varying amounts and types of carbon black in an effort to understand the influence of the Mullins

effect on the Payne effect. For this purpose, two test protocols were employed, TP3 and TP1. The former subjected the specimen to four uniaxial tensile load/unload cycles to a given pre-deformation level, followed by an amplitude sweep. This sequence was repeated for various pre-deformation. In the latter protocol, a further loading stage is added to the tensile cycles and the amplitude sweep is performed under a static strain. It was found that all rubbers manifest the Mullins effect, and at any fixed pre-deformation level also the Payne effect.

TP3 revealed that increasing the filler amount and surface area resulted in an increase in the storage modulus. The role of filler at any level of uniaxial pre-deformation is broadly inline with literature observations. The imposed pre-deformation resulted in a non-linear decrease of the storage modulus. In order to further understand the material behaviour, a modified Kraus model was fitted. The model revealed that for a given filler type and amount, γ_c and m remained constant with respect to different levels of pre-deformation, i.e., independent of pre-deformation. However, the variation of filler type and amount impacts γ_c . This suggests that it might be possible to control the stiffness and to some extent the onset of the Payne effect by a careful combination of filler selection and pre-conditioning. A simple function is suggested to incorporate pre-conditioning effects in the Kraus model.

The observations made from TP1 were more complex. The imposition of a static strain seems to result in a delay in the onset of Payne effect as the $G'(\gamma)$ was approximately constant in the dynamic strain range considered, for all compositions in this study. $G'(\gamma)$ and G'_0 increased with increasing static strain. For any given filler type and at any values of static strain, G'_0 was larger when the filler amount was larger. However, unlike TP3, a larger filler surface area did not result in a larger $G'(\gamma)$ for TP1. The complexity of response obtained for TP1 could be attributed to the evolution of the Mullins phenomenon. To overcome this, an additional experiment was proposed, but not carried out, due to limitations in the equipments, where the specimen is deformed to a significantly larger strain than those exposed in TP1, prior to performing TP1. By coupling the new experiment with TP1, the impact of the Mullins phenomenon can be probed in more detail.

7. Conclusions

The focus of this thesis has been to develop modelling frameworks and models to capture the impact of the elastomer network, deformation history and fillers on the mechanical response of elastomers. For this purpose, a range of materials and various experimental protocols were employed. This chapter summarises the key findings of this thesis. The key conclusions are presented in section 7.1 and recommendations for future work are highlighted in section 7.2.

7.1 Conclusions

7.1.1 The influence of the network structure on the mechanical response

- A set of novel, UV curable, silicone-acrylate elastomers were developed to study the impact of elastomer network on the mechanical response. A systematic variation in the stress-strain response was observed when the ratio of silicone to acrylate was varied. This variation was attributed to changes in the elastomer network and by fitting the physically motivated EV model to the data it was shown that the network density and the slip-link mobility are seen to increase, and the limiting extensibility is seen to decrease with increasing silicone content.
- By fitting functions to the evolution of EV parameters with silicone content, a model was developed to predict the secant modulus for any given ratio of silicone to acrylate. A model of this sort can be used to fine-tune the elastomer composition, i.e., select the silicone to acrylate ratio, for a given application, such as 3D printing.

7.1.2 The influence of deformation history on the mechanical response

- A new model was developed to study the impact of deformation history on the mechanical response of compression moulded EPDM. A set of cyclic stress-strain tests were used for this purpose. The model utilises elastic contributions that evolve with pre-deformation and a pre-deformation independent, effective stretch dependent viscosity master curve. The novelty of this model arises from the use of the viscosity master curve. The model captures the impact of pre-deformation on the stress-strain response to a good degree of accuracy. The model also provides an excellent prediction of the energy dissipated following pre-deformation. In industry, elastomeric products are typically scragged prior to their use, the model presented here is therefore suitable for industrial applications. Particularly, this model is most suited for applications such as vibration isolations where prediction of energy dissipation is the main interest.
- The applicability of the modelling framework was examined for other materials including sheet rolled CR, EPDM and NBR. It was shown in all instances that the elastic contribution varies with pre-deformation and the viscous contribution forms a pre-deformation independent master curve. Full models were developed for EPDM and NBR. Alike the compression moulded EPDM, the models developed for the sheet rolled materials (EPDM and NBR) captured the impact of pre-deformation on the stress-strain response to a good accuracy and provided an excellent prediction of the energy dissipated following pre-deformation, reinforcing the model's suitability for applications such as vibration isolation.
- The model was unable to capture the initial loading (or pre-deformation stage) stress-strain response. This indicates the possibility that the changes taking place during the initial loading phase and when the material exceeds the previous maximum pre-deformation level are themselves dissipative and time-dependent. To address the discrepancy observed during the initial loading stage, an additional viscosity term that is dependent on the permanent set rate was proposed and was shown to reproduce the bulk of the initial loading response to a good degree of accuracy.

- The model development activity was also trialled using pseudocyclic EPDM2 stress-strain data. It was shown that the model derived using a single pseudo-cyclic test (one specimen) was comparable to that of the model derived using ten cyclic tests (ten specimens). This is significant as this allows for the development of models of this kind with one set of experiments, ideal for scenarios where material is limited.

7.1.3 The influence of filler choice on the mechanical response

- SBR compounds with three different types and amounts of carbon black fillers were used to examine the impact of fillers on the mechanical response. The small strain dynamic response was examined in these materials *via* torsional oscillations. As expected, the characteristic Payne effect was observed. The focus was on the storage modulus G' . It was shown that increasing the filler amount and surface area resulted in an increase in G' . This was in line with the literature.
- The test protocol, TP3, was implemented to understand the impact of large deformation on the small strain dynamic response, i.e., impact of deformation history (or Mullins phenomenon) on the small strain dynamic response (or Payne effect). The well-known Kraus model was fitted to understand the response. It was shown that pre-deformation results in a non-linear decrease in the plateau storage modulus G'_0 . The other Kraus model parameters remained independent of the pre-deformation but were dependent on the filler type and amount. Based on these observations, it was shown that it might be possible to control the stiffness and to some extent the onset of the Payne effect by a careful combination of filler selection and pre-conditioning. The ability to control Payne effect can lead to benefits in application such as vehicle tyres, where it controls the rolling resistance and hence the fuel economy. A simple function was suggested to incorporate the impact of pre-conditioning in the Kraus model.
- A further test protocol, TP1, where the dynamic tests were imposed atop of a static strain, was also implemented. G' was shown to be constant in the dynamic strain range explored. Increasing the static strain resulted in an increase in G' .

7.2 Recommendations for future work

This section aims to provide details of work to be conducted in the future either by the author or by the research community.

7.2.1 UV curing and 3D printing

In chapter 3, a set of novel soft ultraviolet light curable silicone-acrylate elastomers were studied. It was observed that alongside varying the composition, the intensity of the UV light could be leveraged to fine-tune the mechanical properties of the silicone-acrylate elastomers. In this work, Phiseon's FireEdge FE400 UV LED is used, allowing for intensity to be varied from 0.5% to 100%. At 100%, this UV light has a nominal flux density of 8 Wcm^{-2} . The intensity is also dependent on the distance of the light source from the illuminated area. Further experimental work is necessary to quantify the impact of the two factors on the resulting stress-strain response.

Furthermore, a significant amount of work has been conducted on the cast silicone-acrylate elastomers presented in this thesis. These elastomers were however intended to be used for 3D printing applications, therefore further work is necessary to optimise the 3D printing process. In chapter 3, it was shown that the 3D printed samples could not reproduce the mechanical behaviour observed in the cast samples. This was attributed to the intensity and increased oxygen exposure between the 3D printed layers. The 3D printed samples were exposed to 100% UV light intensity, whereas the cast samples were exposed to 5% intensity. By 3D printing at 5% intensity, one could verify the true discrepancy between the 3D printed and cast samples. The presence of oxygen inhibits the cross-linking process, this can be overcome by controlling the printing environment. Alongside this, it should be noted that the compounds were pre-mixed prior to printing, i.e., the silicone, acrylate and the photoinitiator were not mixed *via* the 3D printer. More work needs to be carried out to mix the compound on the go using the various nozzles available on the 3D printer. This leads to other issues such as the interfaceability between the different materials. Another avenue that should be explored is the impact of varying the photoinitiator.

7.2.2 Extension to a fully three-dimensional model

A model to predict the mechanical response of elastomers following pre-deformation is presented in chapter 4 and 5. A fully 3D model is essential to enable these models to be implemented in finite element software such as Abaqus. In principle, the only major obstacle to a fully 3D implementation of the proposed models concerns the description of the permanent set, of the elastic parameter evolution, and of a suitable effective stretch scalar, all of which are possible. It is well known, however, that both processing and deformation of elastomers can lead to anisotropic behaviour [32, 163, 34]. Constitutive models ought to accommodate this induced anisotropy, which undoubtedly affect not only the elastic part but also the viscosity and the permanent set. This would require a much more extensive experimental data set involving sequential straining in different directions to identify where simplifications might be made in order to reduce the number of material constants. Typically, the notion of material directions is used to tackle anisotropy, for example see work by Göktepe and Miehe [93], Diani *et al.* [91], Itskov *et al.* [164], Merckel *et al.* [165] and Rebouah *et al.* [166].

It is worth noting that in an early study by Mullins [34], when sheets of elastomers were subjected to sequential deformation in two perpendicular directions it was found that: (1) the ratio between the permanent sets in the alternating directions remained constant, largest in the direction of stretch; and, (2) the permanent deformation remained isochoric. It is therefore plausible that a significant part of the observed anisotropy could be attributed to permanent deformation alone, and that an isotropic (but evolving) hyperelastic formulation coupled with a simple 3D representation of permanent set might suffice in a generic 3D implementation.

7.2.3 The role of deformation history and choice of filler on the mechanical response of elastomers

In chapter 6, the impact of fillers on the mechanical response of elastomer is explored. To prevent discontinuities in the experiment an Anton Paar Rheometer MCR 302 with a SRF was used. This setup limited the torsional strain range for the dynamic tests. The large strain plateau G'_{∞} typically observed during amplitude sweeps was therefore not observed. This is also a reason as to why only G' was studied as the dynamic strains were not sufficient enough to observe the peak typically seen in the loss modulus G'' .

This issue could be addressed by developing a series of experiments using the new Anton Paar Rheometer MCR 702 MultiDrive. This rheometer allows for uniaxial tensile quasistatic and dynamic tests. It would be interesting to do a side-by-side comparison of the results. Would we expect the same behaviour? What would the outcome mean for model development?

It was also mentioned that the onset of non-linearity (or Payne effect), i.e., the strain where the amplitude dependence is initially observed, could be controlled to some extent by a careful combination of filler selection and mechanical pre-conditioning. More robust experiments are necessary to validate this. The onset of non-linearity is difficult to determine, and a set standard does not yet exist, however, a few approaches have been suggested in the literature. Leblanc [167] and Hyun *et al.* [168] have provided methods to establish the strain at the onset of non-linearity. Leblanc's [167] suggestion cannot be used in this work as it requires G'_∞ . The method suggested by Hyun *et al.* [168] can be applied, it utilises fast Fourier transform (FT) rheology to quantify the onset of non-linearity. To utilise FT rheology, the experimental setup must be capable of capturing and recording the waveform corresponding to the response of any oscillatory input. Conveniently, most modern commercial rheometers are equipped to handle this. By applying Fourier transform, the periodic contributions of the signals in the time domain can be represented as amplitude and phase difference in the frequency domain. The amplitudes, phase differences and frequencies enable the signals to be represented as a sum of sine and cosine functions. By studying these, more specifically the first and third harmonic difference of the signals, the onset of non-linearity could be determined. This process is automated in most modern commercial rheometers. Readers are directed to the works by Hyun *et al.* [168] for a detailed account on how to determine the strain at the onset of non-linearity.

Lastly, in chapter 6, it was shown that TP1 resulted in a complex response and therefore difficulties arose in making direct comparisons with other filler types. This is due to the Mullins phenomenon. A complementary study would be to pre-condition the specimen to strain levels that are significantly higher than that of the maximum uniaxial tensile static strains to be explored in the tensile test protocols and then repeat TP1. A correlations might then be observed between the different filler types.

Bibliography

- [1] L. Mullins. “Effect of Stretching on the Properties of Rubber”. In: *Rubber Chemistry and Technology* 21.2 (1948), pp. 281–300.
- [2] L. Mullins and N. R. Tobin. “Theoretical Model for the Elastic Behavior of Filler-Reinforced Vulcanized Rubbers”. In: *Rubber Chemistry and Technology* 30.2 (1957), pp. 555–571.
- [3] L. Mullins and N. R. Tobin. “Stress softening in rubber vulcanizates. Part I. Use of a strain amplification factor to describe the elastic behavior of filler-reinforced vulcanized rubber”. In: *Journal of Applied Polymer Science* 9.9 (1965), pp. 2993–3009.
- [4] J. A. C. Harwood, L. Mullins, and A. R. Payne. “Stress softening in natural rubber vulcanizates. Part II. Stress softening effects in pure gum and filler loaded rubbers”. In: *Journal of Applied Polymer Science* 9.9 (1965), pp. 3011–3021.
- [5] G. Heinrich, M. Klüppel, and T. A. Vilgis. “Reinforcement of elastomers”. In: *Current Opinion in Solid State and Materials Science* 6.3 (2002), pp. 195–203.
- [6] A. Y. Coran. “Vulcanization”. In: *The Science and Technology of Rubber*. Ed. by J. E. Mark, E. Burak, and C. M. Roland. 4th ed. Boston: Academic Press, 2013, pp. 337–381.
- [7] P. J. Flory. *Principles of polymer chemistry*. Ithaca: Cornell University Press, 1953.
- [8] B. Erman. “Molecular Aspects of Rubber Elasticity”. In: *Mechanics and Thermomechanics of Rubberlike Solids*. Ed. by G. Saccomandi and R. W. Ogden. 1st ed. CISM International Centre for Mechanical Sciences. Vienna: Springer-Verlag Wien, 2004, pp. 63–89.

- [9] L. R. G. Treloar. *The Physics of Rubber Elasticity*. 3rd ed. Oxford: Oxford University Press, 2009.
- [10] P. Buckley. “Experimental Methods for Rubberlike Solids”. In: *Mechanics and Thermomechanics of Rubberlike Solids*. Ed. by G. Saccomandi and R. W. Ogden. 1st ed. CISM International Centre for Mechanical Sciences. Vienna: Springer-Verlag Wien, 2004, pp. 1–62.
- [11] J. P. Queslel and J. E. Mark. *Elasticity, Rubber-like*. Ed. by H. F. Mark. Hoboken, 2001.
- [12] J. E. Mark and B. Erman. *Rubberlike elasticity: A molecular primer*. 2nd ed. Cambridge: Cambridge University Press, 2007.
- [13] A. Pegoretti and A. Dorigato. *Polymer Composites: Reinforcing Fillers*. Ed. by H. F. Mark. Hoboken, 2019.
- [14] C. M. Roland. “Reinforcement of Elastomers”. In: *Reference Module in Materials Science and Materials Engineering*. Elsevier, 2016.
- [15] M. E. Spahr and R. Rethon. *Carbon Black as a Polymer Filler*. Ed. by S. Palsule. Berlin, Heidelberg, 2014.
- [16] M. J. Wang. “Effect of polymer-filler and filler-filler interactions on dynamic properties of filled vulcanizates”. In: *Rubber Chemistry and Technology* 71.3 (1998), pp. 520–589.
- [17] H. M. Smallwood. “Limiting law of the reinforcement of rubber”. In: *Journal of Applied Physics* 15.11 (1944), pp. 758–766.
- [18] E. Guth. “Theory of filler reinforcement”. In: *Journal of Applied Physics* 16.1 (1945), pp. 20–25.
- [19] E. Guth. “Theory of Filler Reënforcement. II”. In: *Rubber Chemistry and Technology* 23.3 (1950), pp. 635–643.
- [20] G. K. Batchelor and J. T. Green. “The determination of the bulk stress in a suspension of spherical particles to order c^2 ”. In: *Journal of Fluid Mechanics* 56.3 (1972), pp. 401–427.
- [21] C. Hsiao-Sheng and A. Acrivos. “The solution of the equations of linear elasticity for an infinite region containing two spherical inclusions”. In: *International Journal of Solids and Structures* 14.5 (1978), pp. 331–348.

- [22] C. Hsiao-Sheng and A. Acrivos. “The effective elastic moduli of composite materials containing spherical inclusions at non-dilute concentrations”. In: *International Journal of Solids and Structures* 14.5 (1978), pp. 349–364.
- [23] A. I. Medalia. “Effective degree of immobilization of rubber occluded within carbon black aggregates”. In: *Rubber Chemistry and Technology* 45.5 (1972), pp. 1171–1194.
- [24] Y. Song and Q. Zheng. “Concepts and conflicts in nanoparticles reinforcement to polymers beyond hydrodynamics”. In: *Progress in Materials Science* 84 (2016), pp. 1–58.
- [25] *Elastomer Engineering Guide*. Tech. rep. James Walker, 2017.
- [26] S. S. Mahmood, H. Husin, M. S. Mat-Shayuti, and Z. Hassan. “A review on the cords & plies reinforcement of elastomeric polymer matrix”. In: *IOP Conference Series: Earth and Environmental Science*. Vol. 36. 2016, p. 012034.
- [27] C. Racles, M. Dascalu, A. Bele, V. Tiron, M. Asandulesa, C. Tugui, A. L. Vasiliu, and M. Cazacu. “All-silicone elastic composites with counter-intuitive piezoelectric response, designed for electromechanical applications”. In: *Journal of Materials Chemistry C* 5.28 (2017), pp. 6997–7010.
- [28] A. Bele, C. Tugui, M. Asandulesa, D. Ionita, L. Vasiliu, G. Stiubianu, M. Iacob, C. Racles, and M. Cazacu. “Conductive stretchable composites properly engineered to develop highly compliant electrodes for dielectric elastomer actuators”. In: *Smart Materials and Structures* 27.10 (2018), p. 105005.
- [29] F. Schmitt, O. Piccin, L. Barbé, and B. Bayle. “Soft robots manufacturing: A review”. In: *Frontiers Robotics AI* 5 (2018), p. 84.
- [30] Y. Poojari. “Silicones for Encapsulation of Medical Device Implants”. In: *Silicon* 9.5 (2017), pp. 645–649.
- [31] H. Bouasse and Z. Carrière. “Sur les courbes de traction du caoutchouc vulcanisé”. In: *Annales de la Faculté des sciences de Toulouse : Mathématiques* 5.3 (1903), pp. 257–283.
- [32] J. Diani, B. Fayolle, and P. Gilormini. “A review on the Mullins effect”. In: *European Polymer Journal* 45.3 (2009), pp. 601–612.

- [33] J. A. C. Harwood and A. R. Payne. “Stress softening in natural rubber vulcanizates. Part III. Carbon black-filled vulcanizates”. In: *Journal of Applied Polymer Science* 10.2 (1966), pp. 315–324.
- [34] L. Mullins. “Permanent Set in Vulcanized Rubber”. In: *Rubber Chemistry and Technology* 22.4 (1949), pp. 1036–1044.
- [35] V. A. Fernandes. “Manifestations of the Mullins effect in filled elastomers”. PhD thesis. Nottingham: University of Nottingham, 2016.
- [36] A. Dorfmann and R. W. Ogden. “A constitutive model for the Mullins effect with permanent set in particle-reinforced rubber”. In: *International Journal of Solids and Structures* 41.7 (2004), pp. 1855–1878.
- [37] G. Machado, G. Chagnon, and D. Favier. “Induced anisotropy by the Mullins effect in filled silicone rubber”. In: *Mechanics of Materials* 50 (2012), pp. 70–80.
- [38] T. T. Mai, Y. Morishita, and K. Urayama. “Induced anisotropy by Mullins effect in filled elastomers subjected to stretching with various geometries”. In: *Polymer* 126 (2017), pp. 29–39.
- [39] A. F. Blanchard and D. Parkinson. “Breakage of Carbon-Rubber Networks by Applied Stress”. In: *Industrial & Engineering Chemistry* 44.4 (1952), pp. 799–812.
- [40] F. Bueche. “Molecular basis for the mullins effect”. In: *Journal of Applied Polymer Science* 4.10 (1960), pp. 107–114.
- [41] R. Houwink. “Slipping of Molecules during the Deformation of Reinforced Rubber”. In: *Rubber Chemistry and Technology* 29.3 (1956), pp. 888–893.
- [42] G. Kraus, C. W. Childers, and K. W. Rollmann. “Stress softening in carbon black-reinforced vulcanizates. Strain rate and temperature effects”. In: *Journal of Applied Polymer Science* 10.2 (1966), pp. 229–244.
- [43] D. E. Hanson, M. Hawley, R. Houlton, K. Chitanvis, P. Rae, E. B. Orlor, and D. A. Wroblewski. “Stress softening experiments in silica-filled polydimethylsiloxane provide insight into a mechanism for the Mullins effect”. In: *Polymer* 46.24 (2005), pp. 10989–10995.

- [44] Y. Fukahori. “New progress in the theory and model of carbon black reinforcement of elastomers”. In: *Journal of Applied Polymer Science* 95.1 (2005), pp. 60–67.
- [45] S. Govindjee and J. Simo. “A micro-mechanically based continuum damage model for carbon black-filled rubbers incorporating Mullins’ effect”. In: *Journal of the Mechanics and Physics of Solids* 39.1 (Jan. 1991), pp. 87–112.
- [46] J. M. Clough, C. Creton, S. L. Craig, and R. P. Sijbesma. “Covalent Bond Scission in the Mullins Effect of a Filled Elastomer: Real-Time Visualization with Mechanoluminescence”. In: *Advanced Functional Materials* 26.48 (2016), pp. 9063–9074.
- [47] H. Wan, K. Gao, S. Li, L. Zhang, X. Wu, X. Wang, and J. Liu. “Chemical Bond Scission and Physical Slippage in the Mullins Effect and Fatigue Behavior of Elastomers”. In: *Macromolecules* 52.11 (2019), pp. 4209–4221.
- [48] M. Corby and D. S. A. De Focatiis. “Reversibility of the Mullins effect for extending the life of rubber components”. In: *Plastics, Rubber and Composites* 48.1 (2019), pp. 24–31.
- [49] E. M. Dannenberg and J. J. Brennan. “Strain Energy as a Criterion for Stress Softening in Carbon-Black-Filled Vulcanizates”. In: *Rubber Chemistry and Technology* 39.3 (1966), pp. 597–608.
- [50] J. Plagge and M. Klüppel. “Mullins effect revisited: Relaxation, recovery and high-strain damage”. In: *Materials Today Communications* (2019).
- [51] H. Luo, M. Klüppel, and H. Schneider. “Study of filled SBR elastomers using NMR and mechanical measurements”. In: *Macromolecules* 37.21 (2004), pp. 8000–8009.
- [52] T. Tsujimoto, A. Moriwaki, M. Fujii, M. Okano, and S. Watanabe. “Optical Response Change of Black Rubbers under Cyclic Deformation Investigated by Terahertz Polarization Spectroscopy”. In: *43rd International Conference on Infrared, Millimeter, and Terahertz Waves (IRMMW-THz)*. Nagoya, Japan, 2018, pp. 1–2.
- [53] R. Diaz, J. Diani, and P. Gilormini. “Physical interpretation of the Mullins softening in a carbon-black filled SBR”. In: *Polymer* 55.19 (2014), pp. 4942–4947.

- [54] K. Yamaguchi, J. J. Busfield, and A. G. Thomas. “Electrical and mechanical behavior of filled elastome. I. The effect of strain”. In: *Journal of Polymer Science, Part B: Polymer Physics* 41.17 (2003), pp. 2079–2089.
- [55] L. Mullins. “Softening of Rubber by Deformation”. In: *Rubber Chemistry and Technology* 42 (1969), pp. 339–362.
- [56] C. Ma, T. Ji, C. G. Robertson, R. Rajeshbabu, J. Zhu, and Y. Dong. “Molecular insight into the Mullins effect: Irreversible disentanglement of polymer chains revealed by molecular dynamics simulations”. In: *Physical Chemistry Chemical Physics* 19.29 (2017), pp. 19468–19477.
- [57] Y. Song, R. Yang, M. Du, X. Shi, and Q. Zheng. “Rigid nanoparticles promote the softening of rubber phase in filled vulcanizates”. In: *Polymer* 177 (2019), pp. 131–138.
- [58] M. Klüppel and J. Schramm. “A generalized tube model of rubber elasticity and stress softening of filler reinforced elastomer systems”. In: *Macromolecular Theory and Simulations* 9.9 (2000), pp. 742–754.
- [59] H. Zhang, A. K. Scholz, F. Vion-Loisel, Y. Merckel, M. Brieu, H. Brown, S. Roux, E. J. Kramer, and C. Creton. “Opening and closing of nanocavities under cyclic loading in a soft nanocomposite probed by real-time small-angle X-ray scattering”. In: *Macromolecules* 46.3 (2013), pp. 900–913.
- [60] A. R. Payne. *The dynamic properties of carbon black-loaded natural rubber vulcanizates. Part I.* 1962.
- [61] A. R. Payne. “The dynamic properties of carbon black loaded natural rubber vulcanizates. Part II”. In: *Journal of Applied Polymer Science* 6.21 (1962), pp. 368–372.
- [62] A. R. Payne. “Dynamic properties of heat-treated butyl vulcanizates”. In: *Journal of Applied Polymer Science* 7 (1963), pp. 873–885.
- [63] A. R. Payne and R. E. Whittaker. “Low Strain Dynamic Properties of Filled Rubbers”. In: *Rubber Chemistry and Technology* 44.2 (1971), pp. 440–478.
- [64] W. P. Fletcher and A. N. Gent. “Nonlinearity in the Dynamic Properties of Vulcanized Rubber Compounds”. In: *Rubber Chemistry and Technology* 27.1 (1954), pp. 209–222.

- [65] G. Heinrich and M. Klüppel. “Recent Advances in the Theory of Filler Networking in Elastomers”. In: *Filled Elastomers Drug Delivery Systems*. 1st ed. Advances in Polymer Science. Berlin, Heidelberg: Springer-Verlag Berlin Heidelberg, 2002, pp. 1–44.
- [66] G. Huber, T. A. Vilgis, and G. Heinrich. “Universal properties in the dynamical deformation of filled rubbers”. In: *Journal of Physics Condensed Matter* 8.29 (1996), p. 409.
- [67] P. G. Maier and D. Goeritz. “Molecular interpretation of the Payne effect”. In: *KGK-Kautschuk und Gummi Kunststoffe* 49.1 (1996), pp. 18–21.
- [68] L. Chazeau, J. D. Brown, and L. C. Yany. “Modulus Recovery Kinetics and Other Insights Into”. In: *Polymer Composites* 21.2 (2000), pp. 202–222.
- [69] R. Yang, Y. Song, and Q. Zheng. “Payne effect of silica-filled styrene-butadiene rubber”. In: *Polymer* 116 (2017), pp. 304–313.
- [70] J. L. Andrea and R. N. Sidney. “Nonlinear dynamics: Jamming is not just cool any more”. In: *Nature* 396.6706 (1998), pp. 21–22.
- [71] V. Trappe, V. Prasad, L. Cipelletti, P. N. Segre, and D. A. Weitz. “Jamming phase diagram for attractive particles”. In: *Nature* 411 (2001), pp. 772–775.
- [72] G. Holzapfel. *Nonlinear solid mechanics: A continuum approach for engineering*. 1st ed. Chichester: John Wiley & Sons Ltd., 2000.
- [73] R. W. Ogden. “Large Deformation Isotropic Elasticity - On the Correlation of Theory and Experiment for Incompressible Rubberlike Solids”. In: *Proceedings of the Royal Society A: Mathematical, Physical and Engineering Sciences*. Vol. 326. 1567. London: Royal Society, 1972, pp. 565–584.
- [74] Abaqus 6.13. *Abaqus 6.13*. Tech. rep. Dassault Systems, 2013.
- [75] G. Saccomandi. “Phenomenology of Rubber-Like Materials”. In: *Mechanics and Thermomechanics of Rubberlike Solids*. Ed. by G. Saccomandi and R. W. Ogden. 1st ed. CISM International Centre for Mechanical Sciences. Vienna: Springer-Verlag Wien, 2004, pp. 91–134.
- [76] M. Mooney. “A theory of large elastic deformation”. In: *Journal of Applied Physics* 11.9 (1940), pp. 582–592.

- [77] R. S. Rivlin. “Large Elastic Deformations of Isotropic Materials. I. Fundamental Concepts”. In: *Philosophical Transactions of the Royal Society A: Mathematical, Physical and Engineering Sciences* 240.822 (1948), pp. 459–490.
- [78] O. H. Yeoh. “Some Forms of the Strain Energy Function for Rubber”. In: *Rubber Chemistry and Technology* 66.5 (1993), pp. 754–771.
- [79] E. M. Arruda and M. C. Boyce. “A three-dimensional constitutive model for the large stretch behavior of rubber elastic materials”. In: *Journal of the Mechanics and Physics of Solids* 41.2 (1993), pp. 389–412.
- [80] S. F. Edwards and T. Vilgis. “The effect of entanglements in rubber elasticity”. In: *Polymer* 27.4 (1986), pp. 483–492.
- [81] J. C. Simo. “On a fully three-dimensional finite-strain viscoelastic damage model: Formulation and computational aspects”. In: *Computer Methods in Applied Mechanics and Engineering* 60.2 (1987), pp. 153–173.
- [82] L. Kachanov. “Time of the rupture process under creep conditions”. In: *Nank SSR Otd Tech Nauk* 8 (1958), pp. 26–31.
- [83] R. W. Ogden and D. G. Roxburgh. “A pseudo-elastic model for the Mullins effect in filled rubber”. In: *Proceedings of the Royal Society A: Mathematical, Physical and Engineering Sciences* 455.1988 (1999), pp. 2861–2877.
- [84] H. J. Qi and M. C. Boyce. “Constitutive model for stretch-induced softening of the stress-stretch behavior of elastomeric materials”. In: *Journal of the Mechanics and Physics of Solids* 52.10 (2004), pp. 2187–2205.
- [85] D. S. A. De Focatiis and M. Rahmeh. “A simple physically-inspired n-chain model for the elastic deformation of elastomers exhibiting anisotropic Mullins softening”. In: *International Rubber Conference*. London, 2019.
- [86] M. C. Wang and E. Guth. “Statistical theory of networks of non-gaussian flexible chains”. In: *The Journal of Chemical Physics* 20.7 (1952), pp. 1144–1157.

- [87] P. J. Flory and J. Rehner. “Statistical mechanics of cross-linked polymer networks I. Rubberlike elasticity”. In: *The Journal of Chemical Physics* 11.11 (1943), p. 512.
- [88] C. Miehe and J. Keck. “Superimposed finite elastic-viscoelastic-plastoelastic stress response with damage in filled rubbery polymers. Experiments, modelling and algorithmic implementation”. In: *Journal of the Mechanics and Physics of Solids* 48.2 (2000), pp. 323–365.
- [89] M. Kaliske, L. Nasdala, and H. Rothert. “On damage modelling for elastic and viscoelastic materials at large strain”. In: *Computers and Structures* 79.22 (2001), pp. 2133–2141.
- [90] R. C. Lin and U. Schomburg. “A finite elastic-viscoelastic-elastoplastic material law with damage: Theoretical and numerical aspects”. In: *Computer Methods in Applied Mechanics and Engineering* 192.13 (2003), pp. 1591–1627.
- [91] J. Diani, M. Brieu, and P. Gilormini. “Observation and modeling of the anisotropic visco-hyperelastic behavior of a rubberlike material”. In: *International Journal of Solids and Structures* 43.10 (2006), pp. 3044–3056.
- [92] D. Besdo and J. Ihlemann. “A phenomenological constitutive model for rubberlike materials and its numerical applications”. In: *International Journal of Plasticity* 19.7 (2003), pp. 1019–1036.
- [93] S. Göktepe and C. Miehe. “A micro-macro approach to rubber-like materials. Part III: The micro-sphere model of anisotropic Mullins-type damage”. In: *Journal of the Mechanics and Physics of Solids* 53.10 (2005), pp. 2259–2283.
- [94] L. Gornet, G. Marckmann, P. Fort, E. Verron, P. Charrier, and G. Chagnon. “A theory of network alteration for the Mullins effect”. In: *Journal of the Mechanics and Physics of Solids* 50.9 (2003), pp. 2011–2028.
- [95] G. Heinrich, E. Straube, and G. Helmis. “Rubber elasticity of polymer networks: Theories”. In: *Polymer Physics*. 1st ed. Advances in Polymer Science. Berlin, Heidelberg: Springer-Verlag Berlin Heidelberg, 1988, pp. 33–87.

- [96] H. Kilian, M. Strauss, and W. Hamm. “Universal properties in filler-loaded rubbers”. In: *Rubber Chemistry and Technology* 67.1 (1994), pp. 1–16.
- [97] E. Peña. “Computational aspects of the numerical modelling of softening, damage and permanent set in soft biological tissues”. In: *Computers and Structures* 130 (2014), pp. 57–72.
- [98] E. Maher, A. Creane, C. Lally, and D. J. Kelly. “An anisotropic inelastic constitutive model to describe stress softening and permanent deformation in arterial tissue”. In: *Journal of the Mechanical Behavior of Biomedical Materials* 12 (2012), pp. 9–19.
- [99] D. Zhong, Y. Xiang, T. Yin, H. Yu, S. Qu, and W. Yang. “A physically-based damage model for soft elastomeric materials with anisotropic Mullins effect”. In: *International Journal of Solids and Structures* 176–177 (2019), pp. 121–134.
- [100] G. Kraus. “Mechanical losses in carbon-black-filled rubbers”. In: *Journal of Applied Polymer Science: Applied Polymer Symposia* 39 (1984), pp. 75–92.
- [101] F. Clément, L. Bokobza, and L. Monnerie. “Investigation of the Payne Effect and its Temperature Dependence on Silica-Filled Polydimethylsiloxane Networks. Part II: Test of Quantitative Models”. In: *Rubber Chemistry and Technology* 78.2 (2005), pp. 232–244.
- [102] K. W. Stöckelhuber, S. Wießner, A. Das, and G. Heinrich. “Filler flocculation in polymers—a simplified model derived from thermodynamics and game theory”. In: *Soft Matter* 13.20 (2017), pp. 3701–3709.
- [103] C. Hopmann, A. Funk, and C. Windeck. “Investigations on the processing of solid silicon rubber in blow moulding”. In: *AIP Conference Proceedings*. Ed. by S. C. Jana. Vol. 1664. Cleveland, Ohio, USA: American Institute of Physics, 2015, p. 120001.
- [104] F. Y. Su and X. Q. Wu. “Experimental study on silicone rubber mold design for thermal expansion RTM”. In: *Journal of Reinforced Plastics and Composites* 29.17 (2010), pp. 2698–2704.
- [105] C. Hopmann and M. Röbig. “High precision optics for LED applications made of liquid silicone rubber (LSR)”. In: *Progress in Rubber, Plastics and Recycling Technology* 33.2 (2017), pp. 63–74.

- [106] Y. Wang, C. Gregory, and M. A. Minor. “Improving mechanical properties of molded silicone rubber for soft robotics through fabric compositing”. In: *Soft Robotics* 5.3 (2018), pp. 272–290.
- [107] M. Schaffner, J. A. Faber, L. Pianegonda, P. A. Rühs, F. Coulter, and A. R. Studart. “3D printing of robotic soft actuators with programmable bioinspired architectures”. In: *Nature Communications* 9.1 (2018), p. 878.
- [108] S. Abdollahi, A. Davis, J. H. Miller, and A. W. Feinberg. “Expert-guided optimization for 3D printing of soft and liquid materials”. In: *PLOS ONE* 13.4 (2018), e0194890.
- [109] A. Debelle, L. Hermans, M. Bosquet, S. Dehaeck, L. Lonys, B. Scheid, A. Nonclercq, and A. Vanhoestenbergh. “Soft Encapsulation of Flexible Electrical Stimulation Implant: Challenges and Innovations”. In: *European Journal of Translational Myology* 26.4 (2016), p. 6298.
- [110] A. Abbad, K. Jaboviste, M. Ouisse, and N. Dauchez. “Acoustic performances of silicone foams for sound absorption”. In: *Journal of Cellular Plastics* 54.3 (2018), pp. 651–670.
- [111] H. Khan, M. Amin, and A. Ahmad. “Characteristics of silicone composites for high voltage insulations”. In: *Reviews on Advanced Materials Science* 56.1 (2018), pp. 91–123.
- [112] M. Cai, S. Nie, Y. Du, C. Wang, and J. Song. “Soft Elastomers with Programmable Stiffness as Strain-Isolating Substrates for Stretchable Electronics”. In: *ACS Applied Materials and Interfaces* 11.15 (2019), pp. 14340–14346.
- [113] C. Sturgess, C. J. Tuck, I. A. Ashcroft, and R. D. Wildman. “3D reactive inkjet printing of polydimethylsiloxane”. In: *Journal of Materials Chemistry C* 5.37 (2017), pp. 9733–9743.
- [114] D. B. Kolesky, R. L. Truby, A. S. Gladman, T. A. Busbee, K. A. Homan, and J. A. Lewis. “3D bioprinting of vascularized, heterogeneous cell-laden tissue constructs”. In: *Advanced Materials* 26.19 (2014), pp. 3124–3130.

- [115] E. B. Duoss, T. H. Weisgraber, K. Hearon, C. Zhu, W. Small IV, T. R. Metz, J. J. Vericella, H. D. Barth, J. D. Kuntz, R. S. Maxwell, C. M. Spadaccini, and T. S. Wilson. “Three-dimensional printing of elastomeric, cellular architectures with negative stiffness”. In: *Advanced Functional Materials* 24.31 (2014), pp. 4905–4913.
- [116] F. Liravi, R. Darleux, and E. Toyserkani. “Additive manufacturing of 3D structures with non-Newtonian highly viscous fluids: Finite element modeling and experimental validation”. In: *Additive Manufacturing* 13 (2017), pp. 113–123.
- [117] T. J. Hinton, A. Hudson, K. Pusch, A. Lee, and A. W. Feinberg. “3D Printing PDMS Elastomer in a Hydrophilic Support Bath via Freeform Reversible Embedding”. In: *ACS Biomaterials Science and Engineering* (2016).
- [118] D. S. Kim, Y. T. Kao, and B. L. Tai. “Hydrostatic 3D-printing for soft material structures using low one-photon polymerization”. In: *Manufacturing Letters* 10.2 (2016), pp. 6–9.
- [119] C. S. O’Bryan, T. Bhattacharjee, S. Hart, C. P. Kabb, K. D. Schulze, I. Chilakala, B. S. Sumerlin, W. G. Sawyer, and T. E. Angelini. “Self-assembled micro-organogels for 3D printing silicone structures”. In: *Science Advances* 3.5 (2017).
- [120] D. S. Kim and B. L. Tai. “Hydrostatic support-free fabrication of three-dimensional soft structures”. In: *Journal of Manufacturing Processes* (2016).
- [121] N. R. Choudhury, P. P. De, and N. K. Dutta, eds. *Thermal analysis of rubbers and rubbery materials*. Shrewsbury: Smithers Rapra Technology, 2010.
- [122] N. N. Lebedev and I. Ufliand. “Axisymmetric contact problem for an elastic layer”. In: *Journal of Applied Mathematics and Mechanics* 22.3 (1958), pp. 442–450.
- [123] MATLAB. *version 9.7.0.1296695 (R2019b)*. Natick, Massachusetts, United State: The MathWorks Inc., 2019.
- [124] R. Brooks, A. Howe, A. Kennedy, S. McWilliam, P. Shayler, and P. Shipway. *An Introduction to Mechanical Engineering: Part 1*. Ed. by M. Clifford. 1st ed. Boca Raton, Florida: CRC Press, 2009.

- [125] M. L. Sentmanat. “Miniature universal testing platform: from extensional melt rheology to solid-state deformation behavior”. In: *Rheologica Acta* 43.6 (2004), pp. 657–669.
- [126] *BS EN ISO 11357-2:2014. Plastics — Differential scanning calorimetry (DSC) Part 2 : Determination of glass transition temperature and glass transition step height*. Tech. rep. British Standards Institution (BSI), 2014.
- [127] M. Wendlandt, T. A. Tervoort, and U. W. Suter. “Strain-hardening modulus of cross-linked glassy poly(methyl methacrylate)”. In: *Journal of Polymer Science, Part B: Polymer Physics* 48.13 (2010), pp. 1464–1472.
- [128] *MATLAB and Optimization Toolbox Release 2019b*. Natick, Massachusetts, United States.
- [129] F. Jiang and D. Drummer. “Curing kinetic analysis of acrylate photopolymer for additive manufacturing by photo-DSC”. In: *Polymers* 12.5 (2020), p. 1080.
- [130] M. K. Aromaa and P. K. Vallittu. “Delayed post-curing stage and oxygen inhibition of free-radical polymerization of dimethacrylate resin”. In: *Dental Materials* 34.9 (2018), pp. 1247–1252.
- [131] D. S. A. De Focatiis, C. P. Buckley, and F. Abraham. “Multi-axial viscoelastic deformation of carbon-black filled EPDM rubber”. In: *Constitutive Models for Rubber VI*. Ed. by G. Heinrich, M. Kaliske, A. Lion, and S. Reese. Dresden, Germany: Taylor & Francis, 2009, pp. 187–192.
- [132] R. N. Haward and G. Thackray. “The Use of a Mathematical Model to Describe Isothermal Stress-Strain Curves in Glassy Thermoplastics”. In: *Proceedings of the Royal Society A: Mathematical, Physical and Engineering Sciences* 302.1471 (1968), pp. 453–472.
- [133] J. S. Bergström and M. C. Boyce. “Constitutive modeling of the large strain time-dependent behavior of elastomers”. In: *Journal of the Mechanics and Physics of Solids* 46.5 (1998), pp. 931–954.
- [134] C. Prisacariu, C. P. Buckley, and A. A. Caraculacu. “Mechanical response of dibenzyl-based polyurethanes with diol chain extension”. In: *Polymer* 46.11 (2005), pp. 3884–3894.

- [135] D. S. A. De Focatiis and C. P. Buckley. “The Initiation of Environmental Stress Crazes in Polystyrene with Process Induced Anisotropy”. In: *Proceedings of the 22nd Annual Meeting of the Polymer Processing Society*. Yamagata, Japan, 2006.
- [136] D. J. Senden, J. A. Van Dommelen, and L. E. Govaert. “Strain hardening and its relation to Bauschinger effects in oriented polymers”. In: *Journal of Polymer Science, Part B: Polymer Physics* 48.13 (2010), pp. 1483–1494.
- [137] M. Rendek and A. Lion. “Amplitude dependence of filler-reinforced rubber: Experiments, constitutive modelling and FEM - Implementation”. In: *International Journal of Solids and Structures* 47.21 (2010), pp. 2918–2936.
- [138] D. Jalocha, A. Constantinescu, and R. Neviere. “Prestrain-dependent viscosity of a highly filled elastomer: experiments and modeling”. In: *Mechanics of Time-Dependent Materials* 19.3 (2015), pp. 243–262.
- [139] A. Lion. “On the large deformation behaviour of reinforced rubber at different temperatures”. In: *Journal of the Mechanics and Physics of Solids* 45.11-12 (1997), pp. 1805–1834.
- [140] H. Laurent, A. Vandenbroucke, G. Rio, and N. A. Hocine. “A simplified methodology to identify material parameters of a hyperelasto-visco-hysteresis model: Application to a fluoro-elastomer”. In: *Modelling and Simulation in Materials Science and Engineering* 19.8 (2011), p. 085004.
- [141] Q. Guo, F. Zaïri, and X. Guo. “A thermo-viscoelastic-damage constitutive model for cyclically loaded rubbers. Part II: Experimental studies and parameter identification”. In: *International Journal of Plasticity* 101 (2018), pp. 58–73.
- [142] D. S. A. De Focatiis. “Inverting Domes for Needle-less Powder Injection”. PhD thesis. Oxford: University of Oxford, 2003.
- [143] S. He, Y. Lin, L. Chen, S. Cao, J. Lin, and X. Du. “Improvement in thermal conductivity and mechanical properties of ethylene-propylene-diene monomer rubber by expanded graphite”. In: *Polymer Composites* 38.5 (2017), pp. 870–876.

- [144] K. George, C. Komalan, P. Kumar, K. Varughese, and S. Thomas. “Dynamic mechanical analysis of binary and ternary polymer blends based on nylon copolymer/EPDM rubber and EPM grafted maleic anhydride compatibilizer”. In: *eXPRESS Polymer Letters* 1.10 (2007), pp. 641–653.
- [145] M. Jaunich, W. Stark, and D. Wolff. “Comparison of low temperature properties of different elastomer materials investigated by a new method for compression set measurement”. In: *Polymer Testing* 31.8 (2012), pp. 987–992.
- [146] *ASTM D3191-10(2020), Standard Test Methods for Carbon Black in SBR (Styrene-Butadiene Rubber)—Recipe and Evaluation Procedures*. Tech. rep. West Conshohocken, PA: ASTM International, 2020.
- [147] V. A. Fernandes and D. S. A. De Focatiis. “The role of deformation history on stress relaxation and stress memory of filled rubber”. In: *Polymer Testing* 40 (2014), pp. 124–132.
- [148] R. D. Blevins. *Formulas for natural frequency and mode shape*. New York: Van Nostrand Reinhold Companyblishing, 1979.
- [149] N. Diercks, M. Johlitz, and J. Calipel. “The dynamic Mullins effect: On the influence of the Mullins effect on dynamic moduli”. In: *Proceedings of the Institution of Mechanical Engineers, Part L: Journal of Materials: Design and Applications* 230.3 (2016), pp. 705–716.
- [150] J. H. Cho and S. K. Youn. “A viscoelastic constitutive model of rubber under small oscillatory load superimposed on large static deformation considering the Payne effect”. In: *Archive of Applied Mechanics* 75.4 (2006), pp. 275–288.
- [151] Y. Liao and V. Wells. “Estimation of complex Young’s modulus of non-stiff materials using a modified Oberst beam technique”. In: *Journal of Sound and Vibration* 316.1-5 (2008), pp. 87–100.
- [152] M. Maciejewska, A. Sowinska, and J. Kucharsk. “Organic zinc salts as pro-ecological activators for sulfur vulcanization of styrene-butadiene rubber”. In: *Polymers* 11.10 (2019), p. 1723.
- [153] L. B. Tunncliffe. “Particulate Reinforcement of Elastomers at Small Strains”. PhD thesis. London: Queen Mary University of London, 2015.

- [154] J. W. ten Brinke. “Silica reinforced tyre rubbers”. PhD thesis. Enschede: University of Twente, 2002.
- [155] M. Hamzah and A. Alibadi. “Effect of Carbon Black Type on the Mechanical Behaviour of Elastomeric Material Under Dynamic Loading”. In: *AL-Qadisiya Journal For Engineering Sciences* 6.3 (2017), pp. 268–286.
- [156] N. Suphadon, A. G. Thomas, and J. J. Busfield. “Viscoelastic behavior of rubber under a complex loading”. In: *Journal of Applied Polymer Science* 113.2 (2009), pp. 693–699.
- [157] N. Suphadon. “The viscoelastic properties of rubber under a complex loading”. PhD thesis. London: Queen Mary University of London, 2010.
- [158] N. Suphadon, A. G. Thomas, and J. J. Busfield. “The viscoelastic behaviour of rubber under a small simple shear oscillation superimposed on a large pure shear”. In: *Polymer Testing* 29.4 (2010), pp. 440–444.
- [159] N. Suphadon, A. G. Thomas, and J. J. Busfield. “The viscoelastic behavior of rubber under a complex loading. II. The effect large strains and the incorporation of carbon black”. In: *Journal of Applied Polymer Science* 117.3 (2010), pp. 1290–1297.
- [160] W. Kuhn and O. Künzle. “Experimental Determination of the Dynamic Viscosity and Elasticity and also the Relaxation Time Spectrum of Rubber. III”. In: *Rubber Chemistry and Technology* 28.3 (1955), pp. 694–710.
- [161] S.-P. Li, G. Zhao, and H.-Y. Chen. “The Relationship between Steady Shear Viscosity and Complex Viscosity”. In: *Journal of Dispersion Science and Technology* 26.4 (2005), pp. 415–419.
- [162] G. E. Maddux, L. A. Vorst, J. F. Giessler, and T. Moritz. *Stress Analysis Manual*. Tech. rep. TECHNOLOGY INC DAYTON OH, 1969.
- [163] V. A. Fernandes and D. S. A. De Focatiis. “A swelling study of process-induced and deformation-induced anisotropy of filled rubbers”. In: *Constitutive Models for Rubbers IX*. Ed. by I. P. Bohdana Marvalova. 1st ed. London: CRC Press, 2015, pp. 141–146.

- [164] M. Itskov, A. E. Ehret, R. Kazakevičiute-Makovska, and G. W. Weinhöhl. “A thermodynamically consistent phenomenological model of the anisotropic mullins effect”. In: *ZAMM Zeitschrift für Angewandte Mathematik und Mechanik* 90.5 (2010), pp. 370–386.
- [165] Y. Merckel, J. Diani, M. Brieu, and J. Caillard. “Constitutive modeling of the anisotropic behavior of Mullins softened filled rubbers”. In: *Mechanics of Materials* 57.1 (2013), pp. 30–41.
- [166] M. Rebouah, G. Machado, G. Chagnon, and D. Favier. “Anisotropic Mullins stress softening of a deformed silicone holey plate”. In: *Mechanics Research Communications* 49 (2013), pp. 36–43.
- [167] J. L. Leblanc. “Large amplitude oscillatory shear experiments to investigate the nonlinear viscoelastic properties of highly loaded carbon black rubber compounds without curatives”. In: *Journal of Applied Polymer Science* 109.2 (2008), pp. 1271–1293.
- [168] K. Hyun, M. Wilhelm, C. O. Klein, K. S. Cho, J. G. Nam, K. H. Ahn, S. J. Lee, R. H. Ewoldt, and G. H. McKinley. “A review of nonlinear oscillatory shear tests: Analysis and application of large amplitude oscillatory shear (LAOS)”. In: *Progress in Polymer Science* 36.12 (2011), pp. 1697–1753.

A. Appendices

A.1 Thickness measurement - Lebedev and Ufliand theory kernels

The Lebedev and Ufliand theory [122] was leveraged to determine the thickness of the soft silicone-acrylate elastomer compounds. The kernels $K(\nu)$ and $\Omega(T)$ are essential for this process and are determined via eq. and . The numerical values of these kernels $K(\nu)$ and $\Omega(T)$ are tabulated in Tables A.1 and A.2, respectively.

Table A.1: Numerical values of the kernel $K(\nu)$.

ν	$p = 0.5$	$p = 1.0$	$p = 1.5$	$p = 2.0$	$p = 2.5$	$p = 3.0$	$p = 3.5$	$p = 4.0$	$p = 4.5$	$p = 5.0$	$p = 5.5$	$p = 6.0$	$p = 6.5$	$p = 7.0$	$p = 7.5$	$p = 8.0$
0.0	0.5838	1.1676	1.7514	2.3351	2.9189	3.5027	4.0865	4.6703	5.2541	5.8378	6.4216	7.0054	7.5892	8.1730	8.7568	9.3405
0.1	0.5828	1.1597	1.7249	2.2730	2.7986	3.2973	3.7647	4.1974	4.5925	4.9478	5.2618	5.5337	5.7632	5.9509	6.0977	6.2051
0.2	0.5798	1.1365	1.6486	2.0987	2.4739	2.7668	2.9755	3.1026	3.1547	3.1413	3.0734	2.9625	2.8199	2.6562	2.4805	2.3006
0.3	0.5750	1.0991	1.5308	1.8446	2.0326	2.1032	2.0756	1.9750	1.8267	1.6537	1.4740	1.3007	1.1422	1.0027	0.8838	0.7847
0.4	0.5682	1.0494	1.3834	1.5513	1.5707	1.4812	1.3281	1.1503	0.9755	0.8201	0.6909	0.5886	0.5103	0.4517	0.4082	0.3758
0.5	0.5597	0.9896	1.2195	1.2565	1.1578	0.9922	0.8143	0.6561	0.5303	0.4373	0.3718	0.3266	0.2952	0.2725	0.2552	0.2411
0.6	0.5495	0.9223	1.0516	0.9875	0.8268	0.6504	0.5014	0.3924	0.3192	0.2722	0.2417	0.2209	0.2054	0.1926	0.1814	0.1713
0.7	0.5378	0.8501	0.8896	0.7589	0.5816	0.4297	0.3239	0.2581	0.2189	0.1947	0.1781	0.1651	0.1540	0.1441	0.1351	0.1270
0.8	0.5247	0.7756	0.7406	0.5751	0.4100	0.2943	0.2259	0.1879	0.1657	0.1507	0.1388	0.1285	0.1193	0.1111	0.1038	0.0974
0.9	0.5103	0.7011	0.6089	0.4336	0.2946	0.2128	0.1702	0.1473	0.1325	0.1209	0.1110	0.1023	0.0946	0.0880	0.0821	0.0770
1.0	0.4948	0.6283	0.4961	0.3280	0.2187	0.1633	0.1363	0.1205	0.1088	0.0990	0.0904	0.0831	0.0767	0.0713	0.0665	0.0624
1.1	0.4783	0.5588	0.4020	0.2512	0.1690	0.1319	0.1133	0.1009	0.0908	0.0822	0.0749	0.0687	0.0634	0.0589	0.0550	0.0515
1.2	0.4611	0.4937	0.3252	0.1962	0.1361	0.1105	0.0963	0.0856	0.0767	0.0692	0.0630	0.0578	0.0533	0.0495	0.0462	0.0433
1.3	0.4433	0.4338	0.2636	0.1570	0.1135	0.0948	0.0829	0.0734	0.0655	0.0590	0.0537	0.0492	0.0454	0.0422	0.0394	0.0369
1.4	0.4251	0.3795	0.2149	0.1291	0.0973	0.0825	0.0720	0.0635	0.0565	0.0509	0.0463	0.0424	0.0392	0.0364	0.0339	0.0318
1.5	0.4065	0.3307	0.1768	0.1089	0.0851	0.0726	0.0630	0.0554	0.0493	0.0444	0.0403	0.0370	0.0341	0.0317	0.0295	0.0277
1.6	0.3878	0.2876	0.1471	0.0939	0.0753	0.0642	0.0556	0.0487	0.0433	0.0390	0.0354	0.0325	0.0300	0.0278	0.0260	0.0243
1.7	0.3691	0.2497	0.1242	0.0826	0.0673	0.0572	0.0493	0.0432	0.0384	0.0345	0.0314	0.0288	0.0265	0.0246	0.0230	0.0215
1.8	0.3505	0.2168	0.1064	0.0736	0.0605	0.0511	0.0440	0.0385	0.0342	0.0308	0.0280	0.0257	0.0237	0.0220	0.0205	0.0192
1.9	0.3322	0.1884	0.0925	0.0664	0.0546	0.0460	0.0395	0.0346	0.0307	0.0276	0.0251	0.0230	0.0212	0.0197	0.0184	0.0172
2.0	0.3141	0.1640	0.0816	0.0603	0.0495	0.0415	0.0356	0.0312	0.0277	0.0249	0.0227	0.0208	0.0192	0.0178	0.0166	0.0155

Table A.2: Numerical values of the kernel $\Omega(T)$.

T	$p = 0.5$	$p = 1.0$	$p = 1.5$	$p = 2.0$	$p = 2.5$	$p = 3.0$	$p = 3.5$	$p = 4.0$	$p = 4.5$	$p = 5.0$	$p = 5.5$	$p = 6.0$	$p = 6.5$	$p = 7.0$	$p = 7.5$	$p = 8.0$
0.0	1.530	2.354	3.321	4.322	5.324	6.323	7.318	8.311	9.301	10.290	11.278	12.265	13.250	14.234	15.218	16.202
0.1	1.529	2.349	3.308	4.303	5.300	6.294	7.284	8.272	9.257	10.242	11.224	12.206	13.186	14.165	15.144	16.122
0.2	1.527	2.333	3.272	4.247	5.228	6.206	7.181	8.154	9.124	10.093	11.061	12.027	12.992	13.956	14.919	15.882
0.3	1.523	2.308	3.212	4.154	5.105	6.056	7.006	7.953	8.898	9.841	10.783	11.723	12.662	13.600	14.537	15.473
0.4	1.518	2.273	3.130	4.023	4.930	5.841	6.753	7.663	8.571	9.477	10.381	11.283	12.184	13.084	13.983	14.882
0.5	1.511	2.229	3.026	3.854	4.700	5.555	6.413	7.272	8.129	8.984	9.838	10.690	11.540	12.389	13.237	14.085
0.6	1.503	2.177	2.903	3.651	4.416	5.194	5.978	6.766	7.554	8.342	9.129	9.914	10.698	11.481	12.262	13.042
0.7	1.494	2.118	2.763	3.416	4.081	4.756	5.439	6.129	6.822	7.517	8.213	8.909	9.604	10.299	10.992	11.685
0.8	1.484	2.054	2.612	3.157	3.702	4.249	4.801	5.357	5.917	6.480	7.045	7.612	8.180	8.749	9.318	9.888
0.9	1.472	1.986	2.452	2.884	3.297	3.698	4.092	4.482	4.868	5.251	5.632	6.011	6.389	6.766	7.141	7.516
1.0	1.460	1.916	2.290	2.608	2.889	3.142	3.374	3.588	3.787	3.973	4.147	4.311	4.465	4.611	4.748	4.878

A.2 Thickness Measurement - Lebedev and Ufliand theory verification

The thickness values obtained via the Lebedev and Ufliand theory were verified using a simple experiment. For the purpose of the experiment three acrylic weights measuring 3.44g, 6.39g and 10.24g in mass were laser cut. The essence of the experiment was to identify the thickness of the material at different forces and then extrapolate to identify the thickness at zero force, i.e., the actual thickness of the material. The different forces imposed on the specimen were achieved via the acrylic weights. Firstly, the thickness observed due to the force from the probe is noted, following this the acrylic weights were added on one at a time. In each case, the specimen were allowed to relax for a 2 minute period prior to recording the thickness. The relaxation period was required to allow the deformation seen by the specimen on application of force to saturate, for this purpose 2 minutes suffices. Two specimen, a 40/60 and 70/30 composition, were examined in this way.

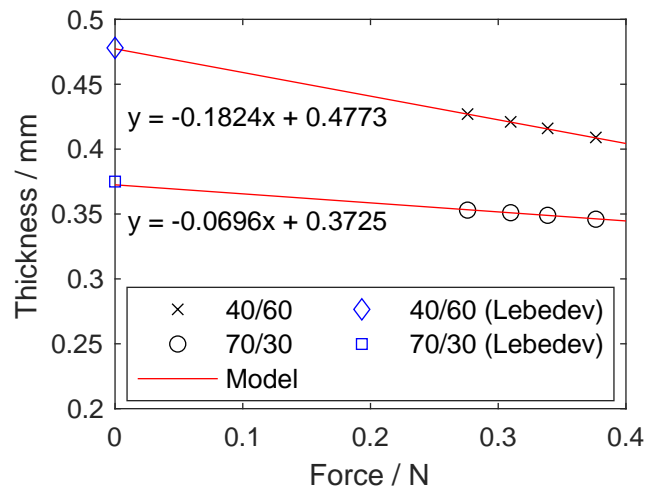


Figure A.1: A thickness versus force plot for different silicone/acrylate compositions. A linear model (red line) has been fitted to the experimental data (black symbols). The thickness values obtained via the Lebedev and Ufliand theory [122] have been highlighted using blue symbols.

Figure A.1 illustrates the thickness recorded by the gauge for a given force. Assuming a linear relationship between thickness and force, a linear

line is fitted to the data points. The line is extrapolated to find the thickness corresponding to a force of zero, this is the y-intercept of the thickness vs. force plot. The equations of the lines and the thickness obtained via the Lebedev and Ufliand theory [122] are also shown on the plot. The percentage difference between for the thickness obtained in this way and using Lebedev theory were minimal. For the 40/60 and 70/30 compositions, the percentage errors were 0.15% and 0.67%, respectively. This also illustrated that the theory is more accurate for softer material.

A.3 Width measurement

The width measurement was conducted using a HP Scanjet G4010 scanner and ImageJ software. Once the specimen is prepared, it is scanned at a resolution of 1200 dpi alongside a measure of known length, a ruler was used for this purpose as shown of Figure A.2. Following the scan, the image was analysed using the ImageJ software. The ruler was used to calibrate the image. A calibration factor of 47.2 pixels/mm was utilised for this work as shown in Figure A.3a. This provides a resolution of ~ 0.02 mm. The width of the specimen can then be determined by drawing straight lines on the specimen and measuring their length as illustrated in Figure A.3b. The beginning and the end of the lines are determined by eye by zooming into the area.



Figure A.2: A dumbbell shaped specimen cut for uniaxial tensile testing. The image was scanned using a HP Scanjet G4010 scanner at 1200 dpi.

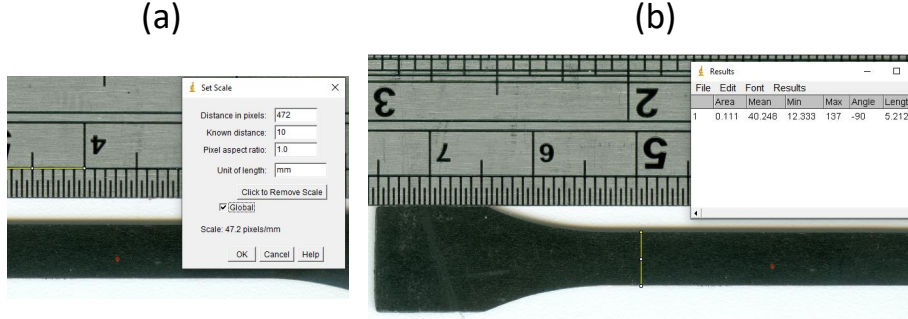


Figure A.3: a) The calibration of a scanned image by using a scale of known length, and b) the determination of the width of the specimen by drawing straight lines on the calibrated image.

A.4 Edwards-Vilgis - strain energy to stress

The method to determine stress σ from the strain energy function W was explained in the main text; however, the details were omitted. This is because numerical methods are typically utilised to obtain the stress from the strain energy functions, primarily since not all strain energy functions have an analytical solution or due to the complexity involved in determining an analytical solution. For the Edwards-Vilgis EV model [80], an analytical solution does exist; the details are stated below.

The EV strain energy function is defined as

$$W = W_C + W_S \quad (\text{A.1})$$

$$W_S = \frac{1}{2} N_S k T \left\{ \sum_{i=1}^3 \left\{ \frac{\lambda_i^2 (1 - \alpha^2) (1 + \eta)}{(1 - \alpha^2 \sum_{i=1}^3 \lambda_i^2) (1 + \eta \lambda_i^2)} + \log(1 + \eta \lambda_i^2) \right\} + \log(1 - \alpha^2 \sum_{i=1}^3 \lambda_i^2) \right\} \quad (\text{A.2})$$

$$W_C = \frac{1}{2} N_C k T \left\{ \frac{\sum_{i=1}^3 \lambda_i^2 (1 - \alpha^2)}{1 - \alpha^2 \sum_{i=1}^3 \lambda_i^2} + \log(1 - \alpha^2 \sum_{i=1}^3 \lambda_i^2) \right\} \quad (\text{A.3})$$

where W_C is the strain energy density due to cross-links, W_S is the strain energy density due to slip-links, N_C is the density of cross-links, N_S is the density of slip-links, α is a measure of inextensibility, η is a measure of slippage and λ_i represents the principle stretches λ_1 , λ_2 and λ_3 in the x, y

and z directions, respectively. To fit the EV model to the data, the model stress has to be determined.

Assuming incompressibility, i.e., that the volume remains unchanged, and symmetry, for a uniaxial tensile test the principal stretches λ_1 , λ_2 and λ_3 are

$$\lambda_1 = \lambda; \quad \lambda_2 = \lambda_3 = \lambda^{-1/2} \quad (\text{A.4})$$

where λ is the stretch imposed on the specimen during the test [9]. The first step is to substitute eq. A.4 into eq. A.1, this results in

$$W = W_C + W_S \quad (\text{A.5})$$

$$W_S = \frac{1}{2} N_S k T \left\{ \frac{(1 - \alpha^2)(1 + \eta)\lambda^2}{1 - \alpha^2(\lambda^2 + 2\lambda^{-1})(1 + \eta\lambda^2)} + \log(1 + \eta\lambda^2) \right. \\ \left. + \frac{2(1 - \alpha^2)(1 + \eta)\lambda^{-1}}{1 - \alpha^2(\lambda^2 + 2\lambda^{-1})(1 + \eta\lambda^{-1})} + 2\log(1 + \eta\lambda^{-1}) \right. \\ \left. + \log(1 - \alpha^2(\lambda^2 + 2\lambda^{-1})) \right\} \quad (\text{A.6})$$

$$W_C = \frac{1}{2} N_C k T \left\{ \frac{(1 - \alpha^2)(\lambda^2 + 2\lambda^{-1})}{1 - \alpha^2(\lambda^2 + 2\lambda^{-1})} + \log(1 - \alpha^2(\lambda^2 + 2\lambda^{-1})) \right\} \quad (\text{A.7})$$

The EV stress is then obtained by differentiation of eq. A.5 with respect

to λ , this results in

$$\sigma = \frac{dW}{d\lambda} = \frac{dW_C}{d\lambda} + \frac{dW_S}{d\lambda} \quad (\text{A.8})$$

$$\begin{aligned} \frac{dW_S}{d\lambda} = \frac{1}{2} N_S k T \left\{ \frac{2(1-\alpha^2)(1+\eta)\lambda}{1-\alpha^2(\lambda^2+2\lambda^{-1})(1+\eta\lambda^2)} + \frac{2\eta\lambda}{1+\eta\lambda} - \frac{2\eta\lambda^{-2}}{1+\eta\lambda^{-1}} \right. \\ \left. + \frac{\alpha^2(1-\alpha^2)(1+\eta)\lambda^2(2\lambda+4\eta\lambda^3-2\lambda^{-2}+2\eta)}{(1-\alpha^2(\lambda^2+2\lambda^{-1})(1+\eta\lambda^2))^2} + \frac{2\alpha^2(\lambda^{-2}-\lambda)}{1-\alpha^2(\lambda^2+2\lambda^{-1})} \right. \\ \left. - \frac{2(1-\alpha^2)(1+\eta)\lambda^{-2}}{1-\alpha^2(\lambda^2+2\lambda^{-1})(1+\eta\lambda^{-1})} \right. \\ \left. + \frac{2\alpha^2(1-\alpha^2)(1+\eta)\lambda^{-1}(2\lambda+\eta-2\lambda^{-2}-4\eta\lambda^{-3})}{(1-\alpha^2(\lambda^2+2\lambda^{-1})(1+\eta\lambda^2))^2} \right\} \quad (\text{A.9}) \end{aligned}$$

$$\begin{aligned} \frac{dW_C}{d\lambda} = \frac{1}{2} N_C k T \left\{ \frac{2(\lambda-\lambda^{-2})(1-2\alpha^2)}{1-\alpha^2(\lambda^2+2\lambda^{-1})} \right. \\ \left. + \frac{2\alpha^2(1-\alpha^2)(\lambda^2+2\lambda^{-1})(\lambda-\lambda^{-2})}{(1-\alpha^2(\lambda^2+2\lambda^{-1}))^2} \right\} \quad (\text{A.10}) \end{aligned}$$

A.5 Viscosity master curve - normalisation of error

The parameters for the viscosity master curve are obtained by minimising the error between eq. 4.13 and the experimental data. The experimental data in this scenario is an amalgamation of η_v obtained for all pre-deformation λ_{\max} explored. The amount of data available at lower and higher λ_{eff} values is limited. The RMS errors used in the minimisation process must therefore be weighted to account for limiting number of data points available at lower and higher values of λ_{eff} . The approach utilised was to minimise the RMS error normalised with respect to experimental data. Figure A.4 illustrates the models obtained *via* the minimisation of RMS error, i.e. no weighting factor, and *via* the minimisation of the normalised RMS error. The parameters for the two cases are shown in Table A.3. It can be observed that the models with and without weighting better represent the viscosity at lower and higher values of λ_{eff} , respectively. However, the model utilising the weighting factors is a fairer representation of the dataset and hence was chosen.

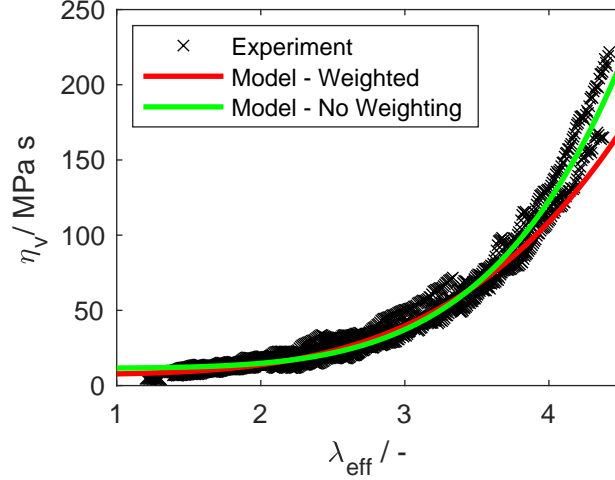


Figure A.4: A comparison of the model (lines) viscosity curves obtained due to the different minimisation schemes utilised.

Table A.3: Estimate ± 1 standard uncertainty for the coefficients of equation 4.13 describing the evolution of η_v as a function of λ_{eff} .

Coefficients	Model	
	No Weight	Weighted
C_{1,η_v}	(0.095 ± 0.005) MPa s	(0.411 ± 0.079) MPa s
C_{1,η_v}	5.099 ± 0.038	3.974 ± 0.148
C_{1,η_v}	(11.574 ± 0.170) MPa s	(7.379 ± 0.569) MPa s

A.6 Linear spring modulus

In order to find a suitable value for the linear spring modulus E , the loading portion of σ - σ_{EV} was used in a least squares algorithm against the numerical solution for eq. 4.8, for all values of λ_{max} explored. The corresponding fits have been illustrated in Figure A.5, the optimised value of E for each case has been tabulated in Table A.4. The value used in the model is the average of the E determined for all cases of λ_{max} explored. $E \pm$ two standard errors are quoted in section 4.5.4.

Table A.4: The optimised value for the linear spring modulus E for all cases of λ_{\max} explored.

Pre-deformation λ_{\max}	Linear Spring Modulus E
1.5	2.34
2.0	2.59
2.5	1.58
3.0	2.37
3.5	1.74
4.0	4.34
4.5	1.80
5.0	4.95
5.5	2.19
6.0	6.84
Mean	3.07
Standard Error	0.55

A.7 Set rate dependent viscosity

A drawback of the model proposed in chapter 4 is the inability of the model to capture the initial loading case. To overcome this problem, a set flow stress $\sigma_{f,\text{set}}$ was suggested. The viscosity η_{set} associated with $\sigma_{f,\text{set}}$ was assumed to be constant for simplicity. In this section a more complex model will be utilised to capture the full evolution η_{set} with stretch λ . A fourth order polynomial function, $\eta_{\text{set}} = 0.157\lambda^4 - 2.211\lambda^3 + 10.355\lambda^2 - 17.101\lambda + 9.261$ was fitted to the data and is illustrated in Figure A.6. The total model stress can then be obtained by adding $\sigma_{f,\text{set}}$ obtained from a η_{set} that evolves with λ to the sum of σ_{EV} and σ_{M} . The initial loading case was recomputed and the resulting response is shown in Figure A.7. The model is shown to be an excellent fit to the experimental data as expected.

A.8 EV parameter evolution

The evolution of the EV parameters for EPDM2 cyclic and pseudocyclic tests have been illustrated in Figs. A.8 and A.9, respectively. Eqs. 4.9-4.12 were fitted to describe the evolution, the corresponding coefficients (± 1

Table A.5: Estimate ± 1 standard uncertainty for the coefficients of equations 4.9 - 4.13 describing the evolutions of the elastic parameters: slip-link density N_S , chain inextensibility α , slip-link mobility η , the permanent set λ_{set} , and the viscosity η_v as a function of maximum stretch λ_{max} . These values are associated with EPDM2 cyclic test data.

Parameters	Coefficients	
$\log_{10}(N_S)$	C_{1,N_S}	-0.069 ± 0.005
	C_{2,N_S}	26.478 ± 0.020
α	$C_{1,\alpha}$	0.006 ± 0.001
	$C_{2,\alpha}$	-0.064 ± 0.010
	$C_{3,\alpha}$	0.417 ± 0.020
η	$C_{1,\eta}$	0.512 ± 0.028
	$C_{2,\eta}$	0.216 ± 0.021
λ_{set}	$C_{1,\lambda_{\text{set}}}$	0.107 ± 0.048
	$C_{2,\lambda_{\text{set}}}$	0.340 ± 0.067
η_v	C_{1,η_v}	(0.501 ± 0.102) MPa s
	C_{2,η_v}	5.095 ± 0.190
	C_{3,η_v}	(12.483 ± 1.012) MPa s

standard uncertainty) have been stated in Table A.5 and A.6 for EPDM2 cyclic and pseudocyclic tests, respectively. The coefficients corresponding to curves describing the EV parameter evolution for EPDM2, pseudocyclic case with a pause, and NBR are give in Table. A.7 and A.8, respectively.

A.9 Heat transfer calculations - adiabatic heating

The rate $\dot{\epsilon}$ required for adiabatic heating to occur is [10]

$$\dot{\epsilon} \gg \frac{\lambda_{\text{max}}}{\tau_{\text{cond}}} \quad (\text{A.11})$$

For EPDM2, λ_{max} is 6 and τ_{cond} obtained *via* eq. 5.1 is 0.63 s. This results in $\dot{\epsilon} \gg 7.94 \text{ s}^{-1}$.

Table A.6: Estimate ± 1 standard uncertainty for the coefficients of equations 4.9 - 4.13 describing the evolutions of the elastic parameters: slip-link density N_S , chain inextensibility α and slip-link mobility η , the permanent set λ_{set} and the viscosity η_v as a function of maximum stretch λ_{max} . These values are associated with EPDM2 pseudocyclic test data.

Parameters	Coefficients	
$\log_{10}(N_S)$	C_{1,N_S}	-0.071 ± 0.005
	C_{2,N_S}	26.491 ± 0.019
α	$C_{1,\alpha}$	0.005 ± 0.001
	$C_{2,\alpha}$	-0.058 ± 0.007
	$C_{3,\alpha}$	0.404 ± 0.013
η	$C_{1,\eta}$	0.634 ± 0.069
	$C_{2,\eta}$	0.274 ± 0.044
λ_{set}	$C_{1,\lambda_{\text{set}}}$	0.091 ± 0.044
	$C_{2,\lambda_{\text{set}}}$	0.371 ± 0.075
η_v	C_{1,η_v}	(0.536 ± 0.108) MPa s
	C_{2,η_v}	4.999 ± 0.190
	C_{3,η_v}	(11.974 ± 0.891) MPa s

A.10 Heat transfer calculations - accounting for conduction and convection

In the main text it was shown that the rate utilised in the experiment could result in a temperature rise, as it fell in the “nonisothermal/nonadiabatic” regime. Assuming that all the strain energy W generated is going towards increasing the temperature of the specimen, the temperature is seen to increase by ≈ 22 °C. A question that naturally follows is “how does W change due to conduction through the grips and convection to the environment?”. To answer this question, an incremental solution was implemented on MATLAB. Flow charts depicting the methodology are illustrated in Figure A.10. It can be observed that the methodology for conduction and convection are vastly similar. A number of assumptions have been made in these calculation, they will be stated in the appropriate sections.

The number of cycles in both loops are equivalent to one minus the size of the λ vector. At each interval, the change in time Δt is calculated by subtracting the time corresponding to the current interval to that of the pre-

Table A.7: Estimate ± 1 standard uncertainty for the coefficients of equations 4.9 - 4.13 describing the evolutions of the elastic parameters: slip-link density N_S , chain inextensibility α and slip-link mobility η , the permanent set λ_{set} and the viscosity η_v as a function of maximum stretch λ_{max} . These values are associated with EPDM2 pseudocyclic test including pauses.

Parameters	Coefficients	
$\log_{10}(N_S)$	C_{1,N_S}	-0.079 ± 0.017
	C_{2,N_S}	26.467 ± 0.072
α	$C_{1,\alpha}$	0.002 ± 0.001
	$C_{2,\alpha}$	-0.018 ± 0.012
	$C_{3,\alpha}$	0.309 ± 0.023
η	$C_{1,\eta}$	0.321 ± 0.114
	$C_{2,\eta}$	0.088 ± 0.113
λ_{set}	$C_{1,\lambda_{\text{set}}}$	0.089 ± 0.046
	$C_{2,\lambda_{\text{set}}}$	0.418 ± 0.081
η_v	C_{1,η_v}	(0.310 ± 0.078) MPa s
	C_{2,η_v}	6.021 ± 0.260
	C_{3,η_v}	(12.800 ± 0.977) MPa s

Table A.8: Estimate ± 1 standard uncertainty for the coefficients of equations 4.9 - 4.13 describing the evolutions of the elastic parameters: slip-link density N_S , chain inextensibility α and slip-link mobility η , the permanent set λ_{set} and of the viscosity η_v as a function of maximum stretch λ_{max} . These values are associated with NBR cyclic test data.

Parameters	Coefficients	
$\log_{10}(N_S)$	C_{1,N_S}	-0.134 ± 0.028
	C_{2,N_S}	26.955 ± 0.054
α	$C_{1,\alpha}$	-0.023 ± 0.014
	$C_{2,\alpha}$	0.028 ± 0.055
	$C_{3,\alpha}$	0.367 ± 0.053
η	$C_{1,\eta}$	0.746 ± 0.042
	$C_{2,\eta}$	0.370 ± 0.059
η_v	C_{1,η_v}	(4.039 ± 3.011) MPa s
	C_{2,η_v}	3.320 ± 1.011
	C_{3,η_v}	(1.699 ± 4.639) MPa s

vious interval. The strain energy W is then determined via Eq. 5.5, using the stress and stretch values corresponding to the current and previous intervals. A term to account for either the energy lost or gained *via* the environment Q_{conv} and *via* the grips Q_{cond} are subtracted from W at this stage. Q_{conv} and Q_{cond} are values obtained from the previous interval. Subsequently, the resultant strain energy is added to the sum of the strain energies from the previous intervals. During the first interval, the sum of the strain energies corresponding to the previous interval, Q_{conv} and Q_{cond} terms are set to zero, and are updated during each loop. This strain energy will be used to determine the change in temperature ΔT .

The change in temperature ΔT due to W is then determined via

$$\Delta T = \frac{W}{\rho C} \quad (\text{A.12})$$

A corrective temperature ΔT_{corr} term is introduced here to account for the change in temperature due to the two heat transfer processes considered. Similarly to Q_{conv} and Q_{cond} , ΔT_{corr} is from the previous interval. During the first interval, this term is set to a value of zero. The energy and temperature change due to conduction and convection lag behind the change in W and ΔT due to the work done on the material by the tensile tester.

The next step in the loop is to determine the rate at which energy is gained or lost due to conduction \dot{Q}_{cond} or convection \dot{Q}_{conv} . For convection, the convective surface area A_{conv} must be calculated, this changes throughout the mechanical test. The only known dimension is the length, which is simply the λ multiplied by the exposed length of the sample at the beginning of the test (~ 30 mm). To determine the convective surface area, the variation in width throughout the test is essential. To determine the width, the thickness is assumed to vary from 0.5 mm to 0.4 mm during loading, and in reverse for unloading. From this assumption, the width can be calculated by employing the constant volume assumption (the width (~ 5 mm) and thickness (~ 0.5 mm) of the specimen prior to the test is a known). This process is carried out at each interval.

For conduction through the grips, the contact area A_{cond} and the thickness, $2L_{\text{cond}}$, of the gripped region is assumed to remain the same throughout the tensile test. An illustration of the clamping region and the change in area following clamping can be found in Figure A.11. The geometry of the gripping region prior to the clamping process is obtained from the BS ISO 527-2 standard [126]. As shown on this figure, it is assumed that the thickness of

the specimen post clamping is reduced from 0.5 mm to 0.3 mm. Realistically the width and the height of the gripping region will also increase but for simplicity it is assumed that the width remains at 10 mm, the height is then determined to be ~ 14.2 mm by employing the constant volume assumption (the volume of the clamped region prior to clamping is known).

The heat dissipated due to conduction and convection are determined via

$$\dot{Q}_{\text{cond}} = \frac{k_t \Delta T A_{\text{cond}}}{L_{\text{cond}}} \quad (\text{A.13})$$

$$\dot{Q}_{\text{conv}} = h A_{\text{conv}} \Delta T \quad (\text{A.14})$$

\dot{Q}_{cond} has to be multiplied by a factor of four as each clamp has two surfaces in contact with the specimen and there are two clamps (one at the top and one at the bottom). By multiplying \dot{Q}_{cond} and \dot{Q}_{conv} by Δt and the reciprocal of the specimen volume, the change in energy per unit volume due to convection Q_{conv} and conduction Q_{cond} can be determined. Subsequently, ΔT_{corr} due to conduction and convection can then be determined *via* eq. A.12, Q_{cond} or \dot{Q}_{conv} is used in place of W .

The above process is repeated. The change in temperature due to conduction and convection are shown in Figure A.12. It can be observed that once conduction and convection are accounted for, the variation in the specimen temperature is significantly lower.

A.11 Theoretical density of SBR compounds

The theoretical density of a compound is determined by the summation of the multiple of the percentile contribution of the components of the compound by the corresponding densities. Typically elastomer composition is given in terms of parts per hundred rubber phr. The SBR compounds explored in this study were prepared as per the ASTM D3191 [146] standard. This standard specifies that for every 100 phr of SBR 1500 rubber, there is 3 parts of zinc oxide, 1 part of steric acid, 1.75 parts of sulfur and 1 part of TBBS. Additionally, there is also the carbon black, 40, 50 or 60 phr for this study. Another way to interpret this is that for every 100 grams of rubber, there is 3 grams of zinc oxide, 1 gram of steric acid, 1.75 grams of sulfur and 1 gram of TBBS.

Firstly, the volume V of the component in the compound is determined by dividing the mass of the component by its density ρ . The density of the

Table A.9: The ingredients and the corresponding values for parts, density ρ , volume V , volume fraction ϕ_{comp} and $\rho \times \phi_{\text{comp}}$ for the SBR compounds explored in this study.

Ingredient Name	Parts / phr	$\rho / \text{g}\cdot\text{cm}^{-3}$	V / cm^3	$\phi_{\text{comp}} / -$	$\rho \times \phi_{\text{comp}} / \text{g}\cdot\text{cm}^{-3}$
SBR 1500	100	0.935	106.952	0.807	0.755
Carbon Black	40	1.800	22.222	0.168	0.302
Zinc Oxide	3	5.610	0.535	0.004	0.023
Steric Acid	1	0.880	1.136	0.009	0.008
Sulfur	1.75	2.055	0.852	0.006	0.013
TBBS	1	1.280	0.781	0.006	0.008
$\Sigma(\rho \times \phi_{\text{comp}})$					1.108

components were provided by Dr Lewis Tunnicliffe. The volume fraction ϕ_{comp} is then determined by dividing the volume of the component by overall volume of the compound. The component density is then determined by the summation of the multiple of the volume fraction and density of each component. An example of the density calculation for a SBR compound containing 40phr of carbon black (either N234, N330 or N660) is provided in Table A.9. The density is $1.108 \text{ g}\cdot\text{cm}^{-3}$ in this instance. Note that a generic density is used for the carbon black here, a more accurate result will be obtained if the density of N234, N330 and N660 are considered.

A.12 Cyclic uniaxial tensile test

The stress-stretch response of the SBR compounds omitted from the main body of the thesis are presented in Figure A.13. These results were obtained via an Anton Paar Rheometer MCR 302 equipped with a SRF.

A.13 Reversible amplitude sweep

The Payne effect is reversible and it is illustrated by applying an amplitude sweep, followed by an amplitude sweep in reverse. A representative example was provided in the main body of the thesis using a SBR N330 50 phr compound. The results corresponding to remaining compounds are provided in

Figure A.14.

A.14 Filler volume fraction and effective surface area

The filler volume fraction ϕ can be determined from

$$\phi = \frac{\frac{\text{phr}_{\text{CB}}}{\rho_{\text{CB}}}}{\frac{\text{phr}_{\text{CB}}}{\rho_{\text{CB}}} + \frac{\text{phr}_{\text{SBR}}}{\rho_{\text{SBR}}} + \frac{\text{phr}_{\text{ZnO}}}{\rho_{\text{ZnO}}} + \frac{\text{phr}_{\text{SAcid}}}{\rho_{\text{SAcid}}} + \frac{\text{phr}_{\text{sulfur}}}{\rho_{\text{sulfur}}} + \frac{\text{phr}_{\text{TBBS}}}{\rho_{\text{TBBS}}}} \quad (\text{A.15})$$

This equation requires the amount of each ingredient relative to parts per hundred rubber and the density of the individual ingredients in the compound, these details are provided in Table A.9. The subscripts CB, ZnO and SAcid refer to carbon black, zinc oxide and steric acid, respectively.

The effective surface area SA_{eff} is determined from

$$\text{SA}_{\text{eff}} = \frac{\text{SA} \times \text{phr}_{\text{CB}}}{\text{phr}_{\text{rubber}}} \quad (\text{A.16})$$

where SA refers to the surface area of the filler in question. The N234, N330 and N660 fillers have a SA of 112, 75 and 34 m^2g^{-1} , respectively.

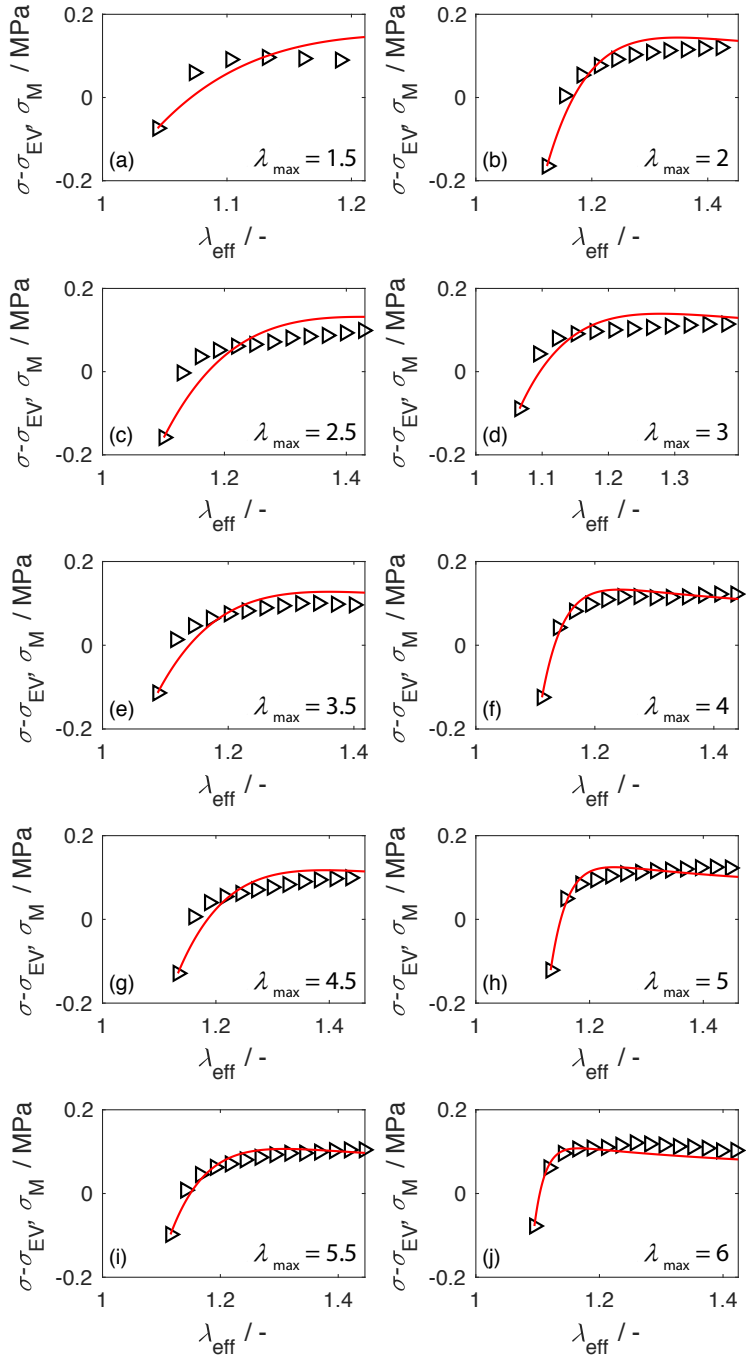


Figure A.5: Experimental (symbol) and model (line) third loop transient response for all values of λ_{\max} explored.

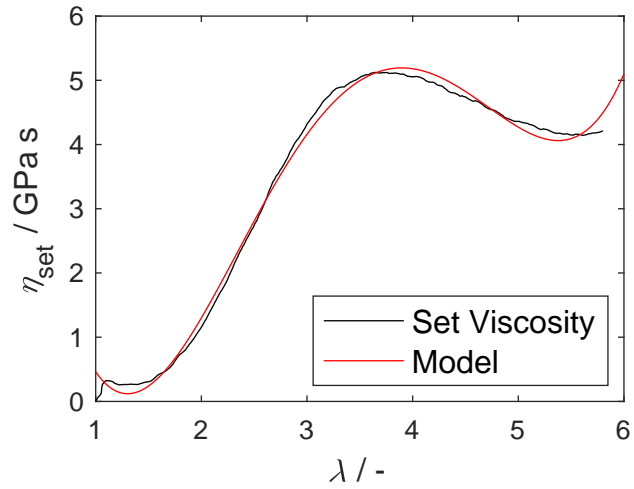


Figure A.6: The evolution of viscosity associated with set with increasing λ . A polynomial model of the fourth order is fitted to η_{set} and is represented as a solid red line on the plot.

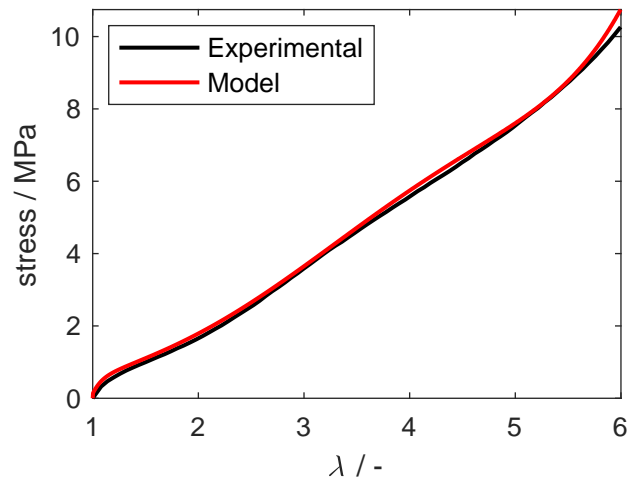


Figure A.7: A comparison of the experimental and model initial (or virgin) loading behaviour. The model stress is obtained by the summation of σ_{EV} , σ_{M} and $\sigma_{\text{f,set}}$. A variable η_{set} was utilised in the determination of $\sigma_{\text{f,set}}$.

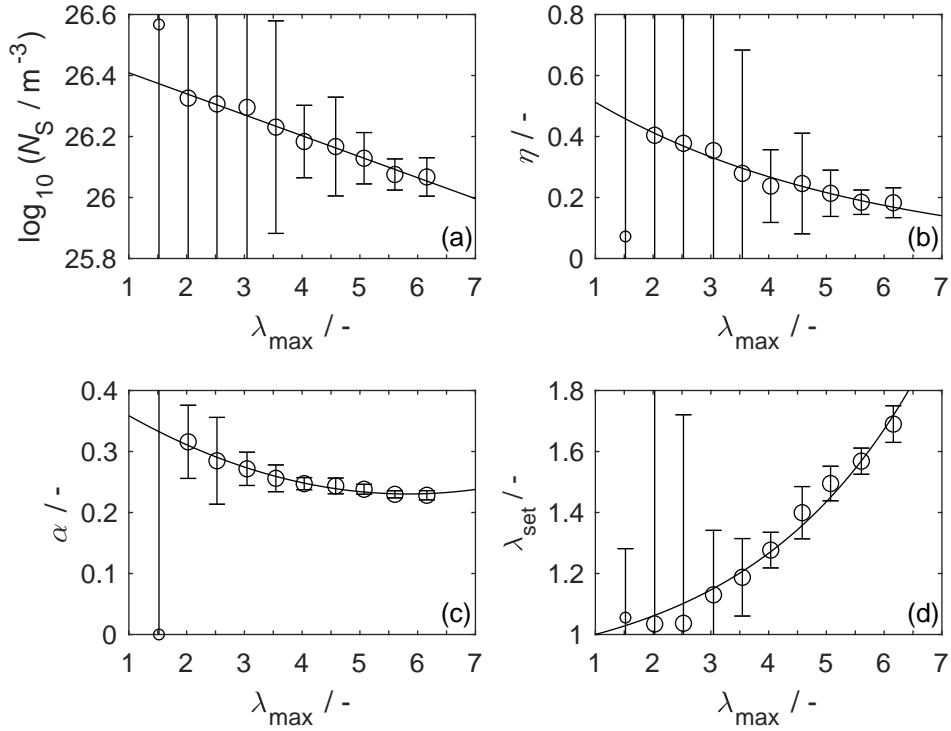


Figure A.8: The evolution of (a) slip-link density N_S , (b) slip-link mobility η , (c) chain inextensibility α (d) permanent set λ_{set} with pre-deformation λ_{\max} for EPDM2 specimen subjected to cyclic tests. The parameters extracted from the elastic contributions are shown as circles. The corresponding uncertainties (95% confidence interval) are also shown. To describe the evolution of these parameters, simple functions (lines) are fitted to the extracted parameter values as functions of λ_{\max} for $\lambda_{\max} \geq 2$ (larger circles).

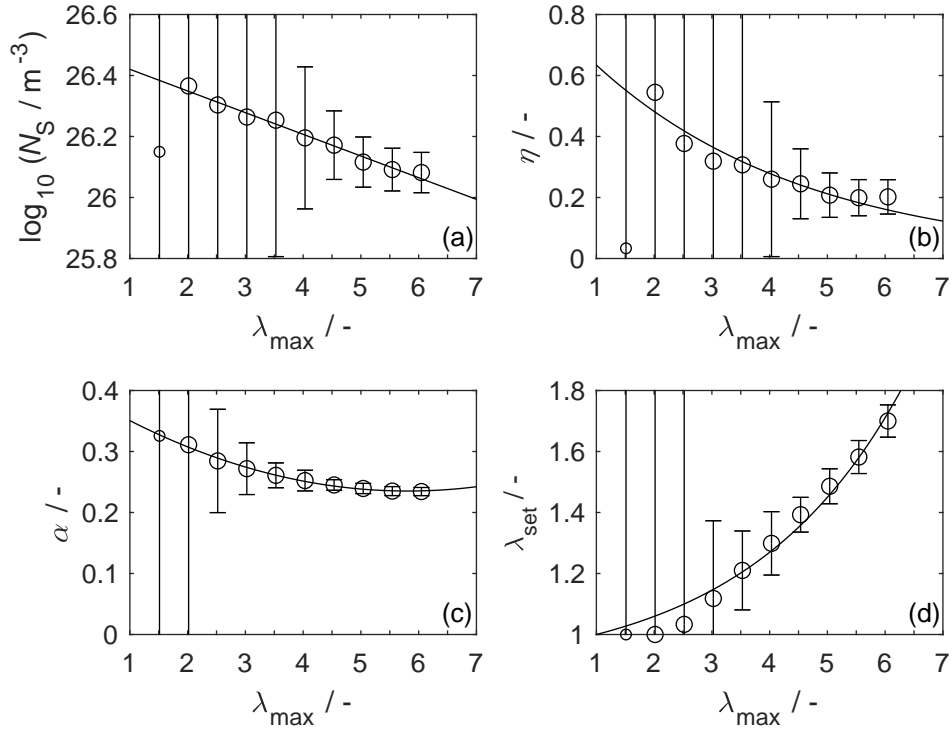


Figure A.9: The evolution of (a) slip-link density N_S , (b) slip-link mobility η , (c) chain inextensibility α (d) permanent set λ_{set} with pre-deformation λ_{\max} for EPDM2 specimen subjected to a pseudocyclic test. The parameters extracted from the elastic contributions are shown as circles. The corresponding uncertainties (95% confidence interval) are also shown. To describe the evolution of these parameters, simple functions (lines) are fitted to the extracted parameter values as functions of λ_{\max} for $\lambda_{\max} \geq 2$ (larger circles).

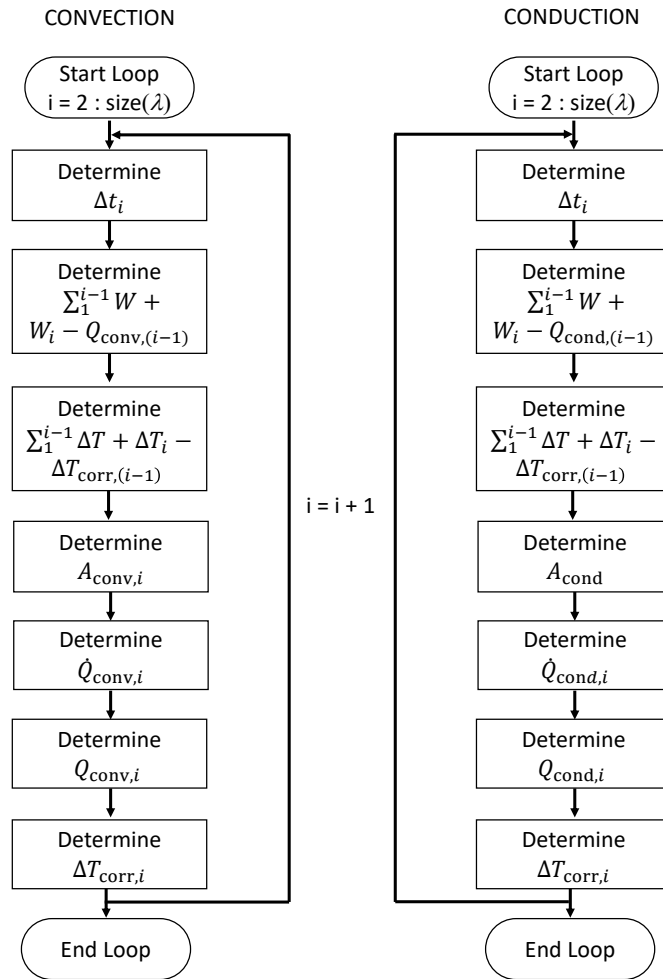


Figure A.10: A flow diagram highlighting the key steps involved in the solution implemented on MATLAB to determine the amount of heat dissipated via conduction through the grips and via convection to the environment.

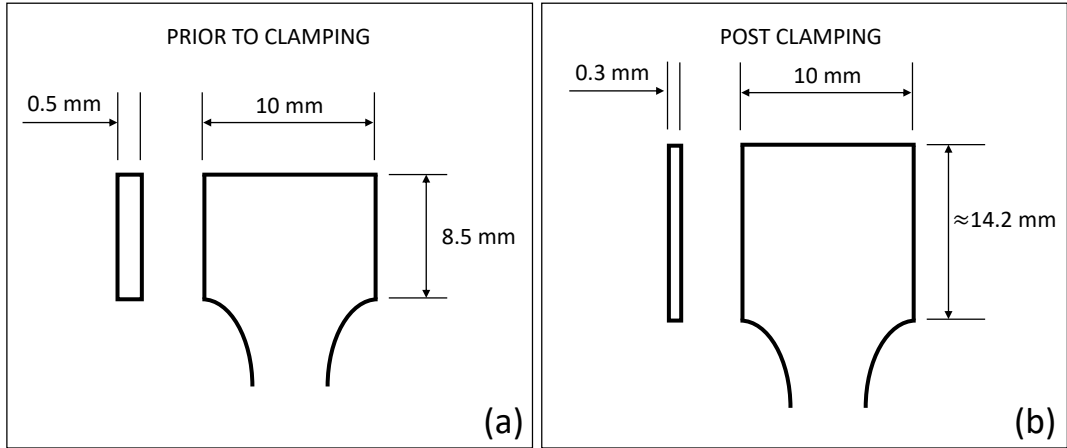


Figure A.11: The region of the specimen that will be gripped using the tensile tester clamps (a) prior to clamping, and (b) post clamping.

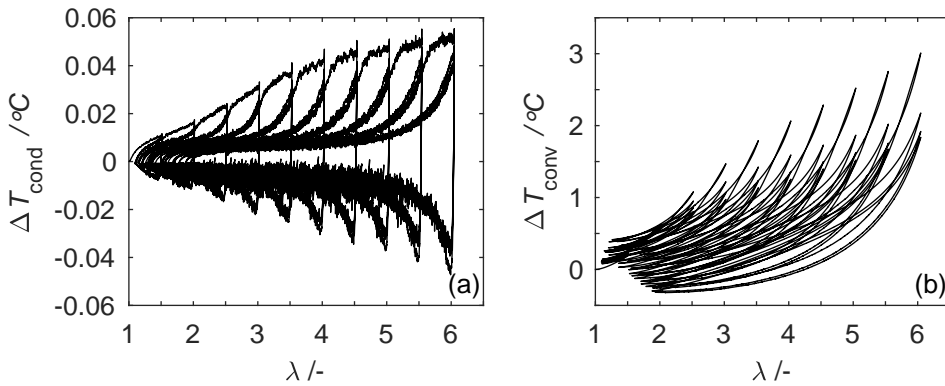


Figure A.12: The change in temperature ΔT experience by a specimen during a pseudocyclic tests when (a) conduction and (b) convection are accounted for.

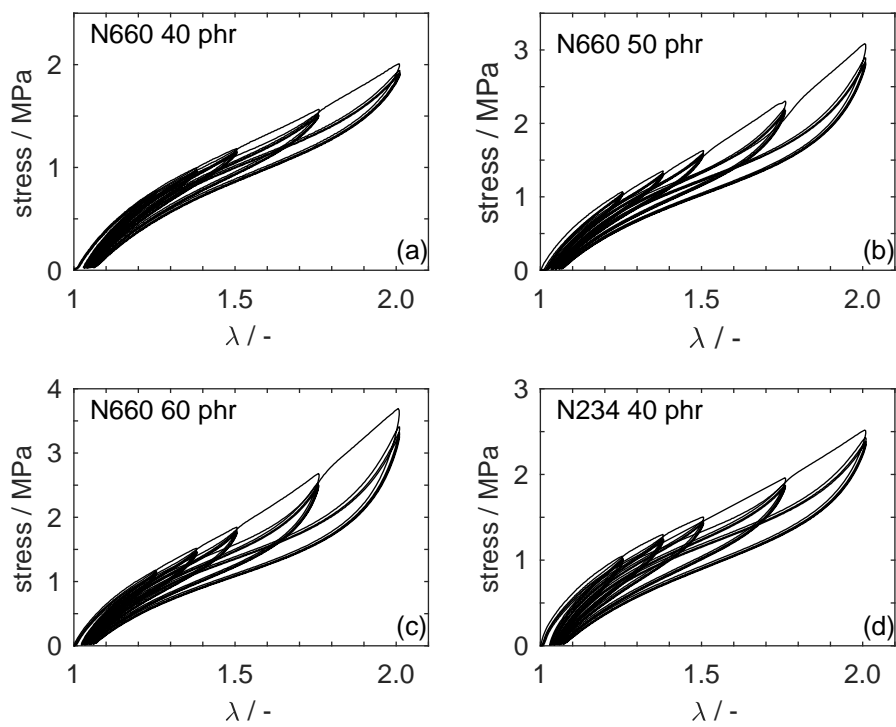


Figure A.13: The stress-stretch response of uniaxial cyclic tensile test of the SBR compounds omitted from the main body of chapter 6.

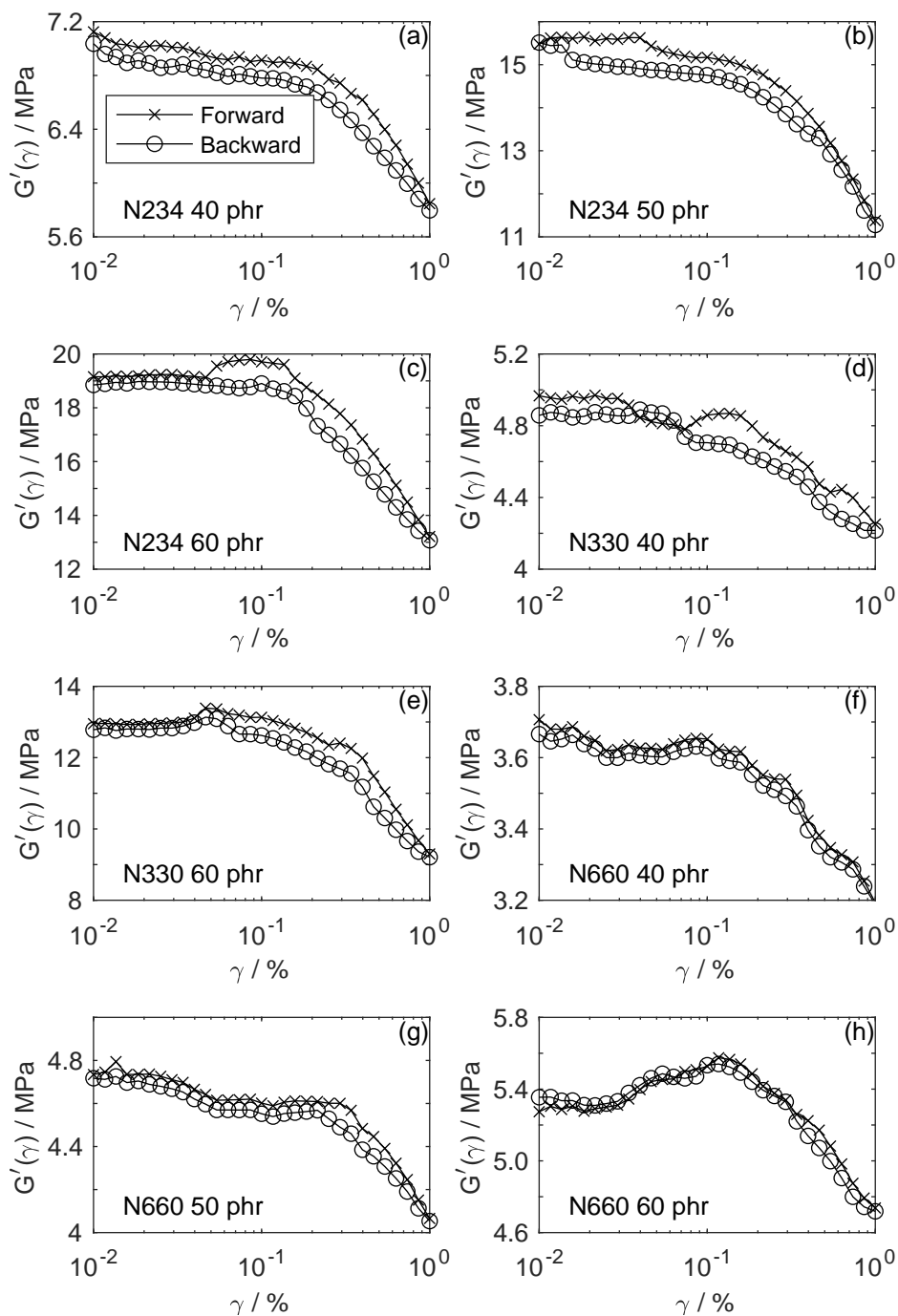


Figure A.14: Plot of the storage modulus against dynamic shear strain demonstrating the reversibility of the Payne effect for the SBR compounds omitted from the main body of chapter 6.